TU

TECHNISCHE UNIVERSITÄT WIEN

Dissertation

Design of a Hydrogen Peroxide based Miniaturized Bipropellant Thruster

ausgeführt zum Zwecke der Erlangung des akademischen Grades eines Doktors der technischen Wissenschaften unter Leitung von

Ao.Univ.Prof. Dipl.-Ing. Dr.techn. Karl Ponweiser
E302
Institut für Energietechnik und Thermodynamik

eingereicht an der Technischen Universität Wien
Fakultät für Maschinenwesen und Betriebswissenschaften

von

Dipl.-Ing. Mag. David Krejci
0325579
1120 Wien, Meidlinger Hauptstraße 7-9/2/43

Wien, am 30. Mai 2012

Acknowledgements

I would like to express my gratitude to the space propulsion team in
Seibersdorf for the collaboration, their support and contribution,
namely Dr. Alexander Woschnak and Dr. Carsten Scharlemann,
DI. Markus Schiebl, DI. Georg Decker and Univ.Prof. Dr. Martin Tajmar.
I want to further thank my advisor Prof. Dr. Karl Ponweiser, for his
continuous input to this thesis.

in cooperation with

Austrian Institute of Technology
former: **Austrian Research Centers Seibersdorf**
Space Propulsion and Advanced Concepts
2444 Seibersdorf

and

FOTEC Forschungs- und Technologietransfer GmbH
Aerospace Engineering
Viktor Kaplan-Straße 2
2700 Wiener Neustadt

Kurzfassung

Derzeitig verwendete, lagerfähige Raketentreibstoffe für Satellitenlageregelung werden aufgrund ihres Gesundheits- und Umweltgefährdungspotentials zunehmend in Frage gestellt. Dies erfordert die Entwicklung von neuartigen Triebwerken auf Basis weniger toxischer Treibstoffe. Dadurch können Sicherheitsmaßnahmen und somit Kosten reduziert werden. In der vorliegenden Arbeit wird ein miniaturisiertes Zweikomponententriebwerk auf Basis von Wasserstoffperoxid mit einem deutlich niedrigerem Gefahrenpotential entwickelt. Der im Vergleich zu herkömmlichen Zweikomponententriebwerken um eine Größenordnung reduzierte Schublevel mit einem Nominalschub von 1 N und die einhergehende Miniaturisierung stellen hohe Anforderungen an das Triebwerksdesign dar - vor allem in Bezug auf die Selbstzündungseigenschaft und an das instationäre Startverhalten des Triebwerks. Die Miniaturisierung ermöglicht jedoch eine in dieser Schubklasse bisher unerreichte Triebwerksleistung und dadurch ökonomischeren Treibstoffverbrauch.

Das entwickelte Triebwerk basiert auf einem abgestuften Triebwerkskonzept, in dem der flüssig gespeicherte Oxidator Wasserstoffperoxid zuerst in einer Dekompositionskammer katalytisch zu Wasserdampf und Sauerstoff zersetzt wird. Die auf diese Weise gewonnenen Heißgase werden daraufhin in der Brennkammer mit einem Treibstoff, Kerosin oder Ethanol, verbrannt. Ein besonderes Augenmerk liegt hierbei auf der Möglichkeit der automatischen Selbstzündung bei Einspritzung des Gemisches. Nach Abschluss der Verbrennung werden die Produktgase über eine Lavaldüse entspannt und dabei beschleunigt, um Schub zu generieren.

Im ersten Teil der Dissertation wird nach einer Einführung in das Themengebiet "Green Space Propulsion", hochkonzentriertes Wasserstoffperoxid als potentieller Oxidator vorgestellt und im Kontext derzeit verwendeter Treibstoffe diskutiert.

Ein thematischer Schwerpunkt der Arbeit liegt auf der katalytischen Zersetzung von Wasserstoffperoxid, sowohl auf theoretischer als auch experimenteller Basis. Eine Simulation, die den Einfluss der thermalen Massen von heterogenen Katalysatoren und der Dekompositionskammer auf die Dekomposition untersucht, wird erarbeitet. Dies liefert Designrichtlinien für Katalysatoren und Kammern. Weiters können anhand der Simulation spezifische Phänomene wie Katalysatorenüberladung und lokal inhomogene Temperaturverteilungen der Heißgase in der Dekompositionskammer erklärt werden. Die Gültigkeit der entwickelten Simulation wird durch Vergleich mit experimentellen Daten gezeigt. Auf experimenteller Basis werden anhand zweier Testmatrizen mit insgesamt 39 verschiedenen Katalysatorenkonfigurationen die Einflüsse verschiedener Katalysatorenparameter auf die Dekomposition untersucht. Die analysierten Designparameter umfassen Katalysatorentypen wie Monolithen, Pellets und Keramikschäume, verschiedene Monolithenlängen, Trägermaterialien und verschiedene aktive Materialien sowie Kanalgeometrien und Kanaldichten in monolithischen Katalysatoren. In Summe werden 121 Katalysatoren in mehr als 480 standardisierten Tests experimentell charakterisiert. Das zeitliche Startverhalten zeigt in den Tests Druckaufbau zu 90 Prozent des nominalen Kammerdrucks im Bereich von 350 bis 550 ms nach Kaltstart, und Temperaturanstiegszeiten von Umgebungstemperatur zu $T > 500$ °C von weniger als 1.6 s. Untersuchungen zur Lebensdauer von Katalysatoren zeigen erfolgreiche Zersetzung von bis zu 17.8 kg H_2O_2 für einen Katalysator.

Die Möglichkeit einer Selbstzündung des Zweikomponententreibstoffgemisches wird in einer modular aufgebauten Zündkammer für unterschiedliche Brennkammervolumina untersucht. Mithilfe eines speziell entworfenen Gegendruckverfahrens kann der Kammerdruck von den Treibstoffmassenflüssen unabhängig variiert werden. Dies erlaubt die Untersuchung des Zündverhaltens unter verschiedenen Kammerdrücken bei konstanten Massenflüssen ohne eine Änderung der Blendengeometrie nötig zu machen. Anhand einer Vielzahl erfolgreicher Selbstzündungen können, in Übereinstimmung mit gefundener Literatur, Zündlimits von Kerosin in zersetztem Wasserstoffperoxid als Funktion von Einspritztemperatur und Brennkammerdruck in einer miniaturisierten Brennkammer bestimmt werden. Zusätzlich kann die Möglichkeit der Selbstzündung von Ethanol in zersetztem Wasserstoffperoxid gezeigt werden.

Anhand der Ergebnisse der Dekompositions- und Zündstudien wird ein erstes Labormodel des Triebwerks entwickelt, um stationäre Verbrennungseigenschaften sowie Anfahr- und Zündverhalten des gesamten Systems zu untersuchen. Ein aktives Kühlungssystem für die Brennkammerwände wird implementiert, um längere Verbrennungsdauern zu ermöglichen. Dieser Testaufbau erlaubt die Untersuchung der Verbrennungseffizienz als Parameter des Einspritzverhältnisses, nachdem die Selbstzündlimits aus den Zündstudien für den veränderten Testaufbau reproduziert wurden. Neben der vollständigen Charakterisierung des Brennverhaltens für Kerosin kann die Selbstzündungseigenschaft des Triebwerkes mit Ethanol verbessert werden. Dies erlaubt die Untersuchung der Verbrennungseffizienz von Ethanol in zersetztem Wasserstoffperoxid als Funktion des Einspritzverhältnisses. Eine Vielzahl an Selbstzündungen mit beiden Treibstoffkombinationen zeigt gute Zündeigenschaften auch für Treibstoffgemische abseits des stöchiometrischen Verhältnisses. Zusätzlich kann dieses Triebwerk erfolgreich in gepulstem Modus betrieben werden. Tests mit einem verbesserten Katalysatordesign zeigen eine Verbesserung des Anfahrverhaltens mit reduzierter Zeit zum Erreichen von 500 °C in nur 1.36 s.

Anhand einer Simulation des thermalen Triebwerkbudgets wird ein strahlungsgekühltes finales Triebwerk entworfen. Der Heißgaswärmeübergang wird dabei basierend auf einem Modell der turbulenten Grenzschichten im Düsenhals des Triebwerks und anhand experimentell gewonnener Erkenntnisse erarbeitet. Pt-20%Rh wird als Brennkammernmaterial in Verbindung mit Nimonic für thermisch weniger belastete Komponenten wie die Dekompositionskammer ausgewählt. Die Funktionstüchtigkeit der Strahlungskühlung im Dauerbrennbetrieb wird durch Brenndauern von bis zu 30 s gezeigt. Verbrennungseffizienzen über 90 Prozent können, basierend auf gemessenen Brennkammerdrücken und Treibstoffmassenflüssen, bestimmt werden. Obwohl Strömungsablösung bei Standardumgebungstestbedingungen innerhalb der für Vakuumumgebung ausgelegten Düse auftreten, kann der gemessene Schub auf Vakuumumgebung rückgerechnet werden. Dies ergibt, abhängig vom getesteten Kammerdruck und Mischungsverhältnis, in Übereinstimmung mit dem angestrebten, nominalen Schub von 1 N, Schübe von 0.9-1.1 N. Untersuchungen des Pulsverhaltens im vorgewärmten Zustand zeigen Selbstzündungen auch für minimale Pulsdauern von 2 s und einhergehende minimal mögliche Impulse von 1 N s für den Zweikomponentenbetrieb. Das Triebwerk wird ohne auftretende Schäden über eine gesamte Zweikomponentenbrenndauer von 618 s mit 68 Selbstzündungen getestet.

1.   Introduction

The scope of the thesis is the design and development of a miniaturized high performance chemical bipropellant thruster operated with green propellants for satellite onboard propulsion. Due to increased awareness of environmental hazards such as toxicology and carcinogenicity of currently employed storable space propellants, interest in less toxic alternative propellants has aroused, necessitating the development of thrusters able to be operated with these propellants. The thruster designed and investigated in this thesis bases on highly concentrated hydrogen peroxide as oxidizer, which has drawn renewed attention to its potential ability to replace carcinogenic, hypergolic propellants, reducing production, storage and handling costs, while maintaining high performance. The thruster designed in this work is a miniaturized bipropellant engine in staged configuration, able to autoignite with easy to handle, low toxic fuels such as kerosene and ethanol.

The envisioned thrust level makes the thruster a potential candidate for onboard propulsion for both precision attitude control and as orbit maintenance propulsion system for small satellite missions. The target thrust level is one order of magnitude below commercially available bipropellant thrusters to date and competes with available monopropellant thrusters with reduced performance. This miniaturization, while posing inevitable difficulties to a high performance design, makes this thruster a potentially interesting, low cost propulsion option for a large variety of low thrust and precision propulsion applications.

The approach undertaken in the design of the propulsion system is based on both theoretical and experimental efforts. The theoretical work presented is guiding the experimental efforts, addresses specific issues arising during the design process and exploits possibilities of improving the design of the propulsion system. The latter is the case especially regarding the transient behavior of the thruster system, which has been identified as a key design parameter. The theoretical approach encompasses both numerical simulation studies for specific key issues as well as generally applicable, manageable analytical models. The experimental investigation undertaken comprises of a decomposition chamber for investigation of catalysts, an ignition chamber for autoignition studies and two experimental thrusters of different technology readiness levels.

The thruster designed in this work features a staged combustor configuration, in which the liquid oxidizer hydrogen peroxide is heterogeneously decomposed in a dedicated decomposition chamber, generating a high temperature oxygen/steam mixture. This gaseous oxidizer is then injected into the combustion chamber where it is combusted with the additionally injected liquid fuel. Autoignition capability of the thruster is aspired, meaning the ignition of the oxidizer/fuel mixture without external igniter.

The thesis is organized as follows:

The decomposition chamber and catalyst design is theoretically guided by a simulation focusing on the impact of structural mass on the decomposition performance. This allows the identification of various important design parameters, guiding the experimental investigation. In the experimental section, an exhaustive catalyst test matrix is investigated in a flow reactor specifically designed for catalyst investigation in a flow reactor environment similar to the final propulsion application. The experimental investigation includes the investigation of various different types of catalysts as well as the impact of honeycomb catalyst parameters, such as channel geometry and density, catalyst length, active material and wash coatings. In addition, various specific issues related to the design of the decomposition chamber are investigated on both theoretical and experimental level, such as catalyst overloading and radial exhaust temperature inhomogeneity.

In a second design step, autoignition of the propellant mixtures is investigated. A dedicated modular ignition chamber allows the investigation at different combustion chamber volumes. An additionally employed back-pressure device enables investigation at different chamber pressure levels which are varied independently from mass flow. It is therefore possible, to investigate the autoignition behavior of decomposed hydrogen peroxide and kerosene for a variety of temperature and chamber pressure levels for two miniaturized combustion chamber volumes at constant mass flows. In addition, the ability of autoignition of a mixture of decomposed hydrogen peroxide and ethanol is experimentally shown.

Steady state combustion behavior of both propellant mixtures is investigated in a dedicated, actively cooled thruster setup, allowing the investigation of combustion performance as a function of propellant mixture ratio. Findings from these investigations are used in the design of the final, fully operational thruster model. In addition, pulsing capability of the thruster is investigated. Additionally collected data on the autoignition behavior in off-design operation regarding the propellant mixture ratio showed reliable ignition capability of the thruster for both propellant combinations.

Guided by a thermal simulation of the overall thruster, a final miniaturized thruster incorporating all key components is designed. Based on numerical results, a radiative cooling approach is chosen, avoiding a negative impact of cooling technique on both performance and design complexity. This allows the design to satisfy both, the requirement of high performance comparable to larger thrusters, while low complexity of the combustion chamber satisfies the low cost approach for the overall propulsion system. The final thruster is thoroughly tested, validating the ability of the radiative cooling technique and allowing the determination of combustion performance and thrust generated.

1.1 Low thrust on-orbit propulsion

Active orbit control is required for a variety of on-orbit operation tasks, including orbit changes regarding altitude or inclination, attitude control, orbit maintenance maneuvers necessitated by non conservative influences on the orbit of the satellite, as well as orbit insertion and end of life de-orbiting maneuvers [1, 2, 3].

The velocity change Δv a thruster can deliver to a satellite is described by the Tsiolkovski equation, relating the thruster performance of specific impulse I_{sp} to the propellant consumption m_p and the spacecraft dry mass m_0 [3, 4]. The specific impulse is the quotient of propellant exhaust velocity and standard gravity, and is discussed in detail in section 1.2.3

$$\Delta v = I_{sp} g_0 \ln\left(\frac{m_0 + m_p}{m_0}\right)_. \tag{1.1}$$

g_0 refers to the standard acceleration of gravity. This basic correlation stresses the importance of increasing the specific impulse, and therefore the propellant exhaust velocity, to reduce launch costs by minimizing the satellites mass during launch or increasing the satellites operational life without increasing the propellant mass.

For on-orbit propulsion, a variety of different types of propulsion options are available, generally distinguished by the type of energy conversion to kinetic energy of the exhaust products. Various authors have published general classification schemes based on specific impulse and thrust level for different types of energy conversions, ranging from chemical, thermo-chemical and electrical to more advanced types such as thrusters based on nuclear fission. Such a classification published by Sutton and Biblarz [3] is shown in Figure 1.
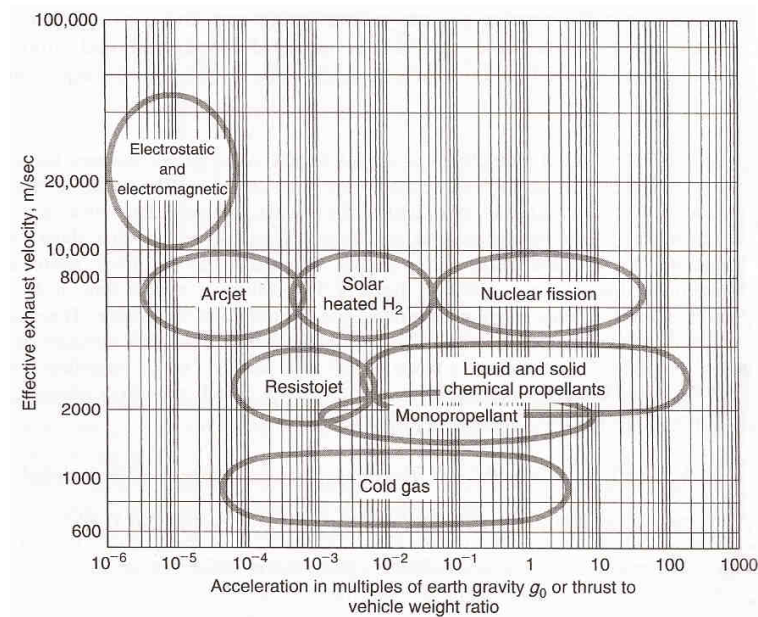
Figure 1 Exhaust velocities and thrust regimes for different types of thrusters, based on the type of energy conversion, Ref. 3

Whereas electrical propulsion features high specific impulse, only low thrust levels are currently achievable for power levels available on standard satellite buses. Rocket engines based on chemical energy conversion on the other hand generally feature high thrust levels, such as rocket engines employed in launch vehicles, but considerable reduced specific impulse, which is basically limited by the chemical energy stored in the propellants. Although concepts and experimental proofs are available for more advanced technologies such as large scale nuclear thrusters, these remain unavailable for commercial use in the near future due to a variety of issues. A more exhaustive discussion of this subject and description of the different thruster operation principles can be found in Ref. 3. A comprehensive overview on liquid propulsion history and developments around the world with a focus on large scale propulsion can be found in Ref 5.

For onboard propulsion applications including orbital change, maintenance and attitude control, high performance low thrust chemical propulsion guarantees a favorable tradeoff between long term employment due to economical propellant utilization and reasonable maneuver times. A long space heritage for chemical propulsion is generally considered as an additional asset.

In the special case of miniaturized satellites, requirements to the propulsion systems pose stringent limits concerning mass and size, demanding lower thrust levels while maintaining high specific impulses. Ref. 6 gives a review on propulsion requirements and options for microsatellites for orbit altitude change and orbit inclination change maneuvers. The authors stress the advantage of fast response times enabled by miniaturized chemical on-orbit propulsion compared to electrical propulsion approaches. Mueller et al. [7] discuss the requirements and propulsion options for even further miniaturized nanosatellites such as Cubesats with overall mass below 5 kg.
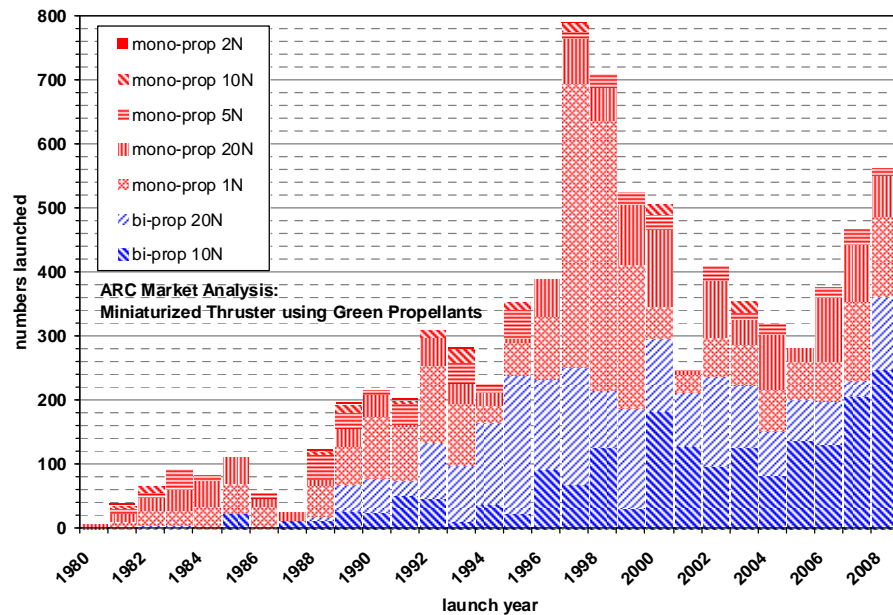
Figure 2: Low-thrust engines employed on commercial satellite buses, per launch year, Ref. 8

In the field of commercial satellites, a market analysis for onboard chemical propulsion systems performed by Woschnak [8] indicated a trend towards an increasing market for low thrust bipropellant systems since 1990, as can be seen in the analysis of low-thrust engines employed, listed per launch year in Figure 2. The data from Figure 2 also shows an increasing demand for 10 N engines, which currently constitute the smallest bipropellant thrust levels commercially available, compared to the 20 N thrusters in recent years. This can be explained by the decreased minimum impulse bits available for smaller thrust levels, assuming equal specific impulse, resulting in higher propellant utilization efficiencies in attitude control applications. Woschnak [8] also identified a significant market volume for 1 N monopropellant thrusters, whereas no heritage for bipropellant thrusters in this thrust level was found. A considerable demand for a thruster system combining the high performance of a bipropellant engine with the decreased thrust level of 1 N is therefore anticipated. The peak demand shown in the data in Figure 2 is caused by an increased launch volume caused by the Iridium constellation.

The thrust level of 1 N envisioned in this project compares to the thrust levels achieved by current monopropellant engines. Whereas state of the art hydrazine monopropellant thrusters achieve specific impulses in the range of $I_{sp} \approx$ 202-226 s at this thrust level [1], the miniaturized bipropellant thruster developed in this work aims at a specific impulse of $I_{sp} \approx$ 275-300 s.
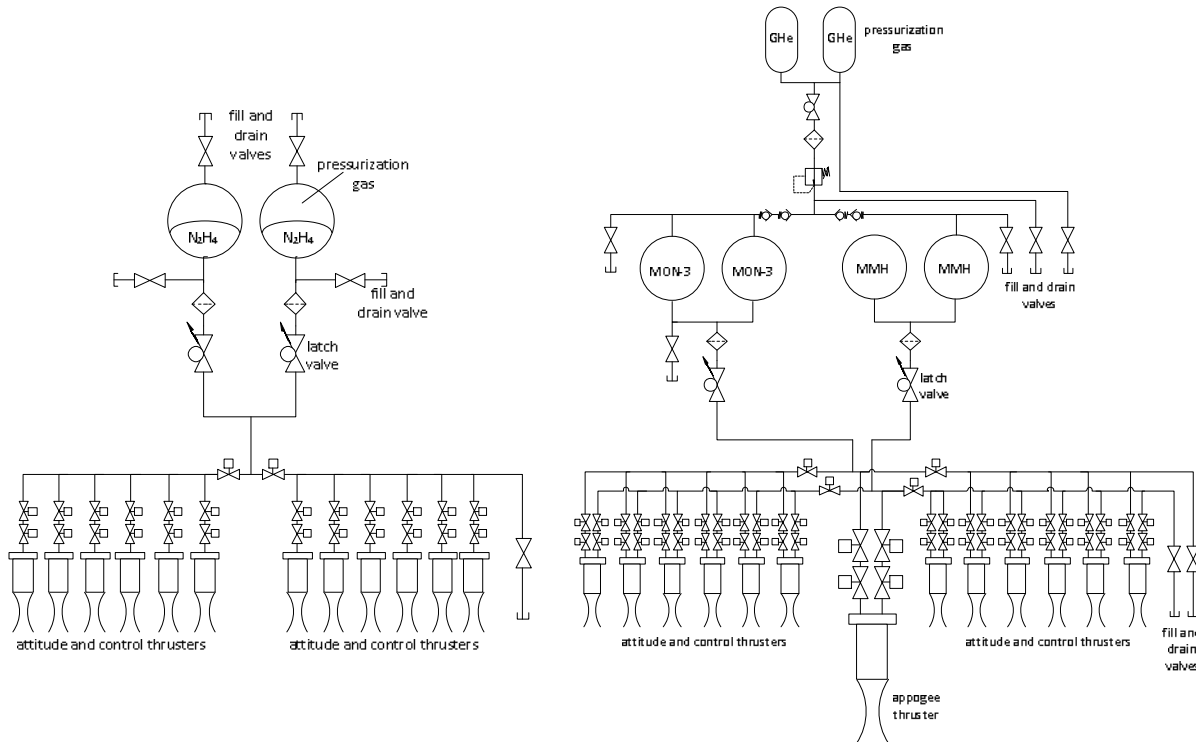
Figure 3: Fluid schematics of typical currently used monopropellant (left) and bipropellant (right) propulsion systems with redundant storage tank systems, according to Ref. 8

Figure 3 compares a typical attitude control monopropulsion system schematic to a bipropellant configuration including a high thrust apogee motor. Increasing the specific impulse by a change in propellant combination or thruster system reduces the propellant necessary to maintain equal total impulse, but potentially comes at the cost of increased

system mass. The latter is true for substituting a monopropellant based propulsion system by a bipropellant system, roughly doubling the tank and feed system components. In addition to the general increase in complexity for bipropellant systems, additional design issues may arise. These include shifts in the satellites center of mass due to oxidizer and fuel tanks being evacuated at different rates. Nevertheless, the favorable impact of increased thruster performance can result in an overall reduction of propulsion system mass for bipropellant systems, especially for large Δv applications. Sellers et al. [10] investigated a variety of different propulsion types on systems level and came to the conclusion of miniature bipropellant systems being the most cost efficient alternative for the investigated commercial small satellite mission.

1.2   Green Propulsion

Although considerable literature on the subject of green propulsion exists [9, 11, 12, 13, 14], lack of a common definition of the term "Green Propellants" persist. However, the website of the European Space Agency features a generally accepted definition of the term:

> *"A green propellant is one that has the potential to have reduced adverse impact (i.e. toxicity), either to the environment (planetary body) or to personnel with whom it may come into contact, whilst still having the performance to meet mission requirements."* [Ref . 15]

The general reference drawn in this definition by the word "reduced" is generally considered as referring to the currently used state-of-the-art propellants hydrazine and its derivatives. More precise definitions refer to the main impacts of substituting these propellant combinations with future "green propellants" as[1]:

-   Low toxicity: reduction of hazards during launch operation and reduced safety precautions during manufacture, handling and storage
-   Low pollution impact: reduced environmental impact on the ground and atmosphere and reduced contamination of satellite components in space
-   Lower cost: reduced overall cost due to reduced safety precautions throughout the propellant lifetime.

However, since high performance propellants are necessarily high energy density substances and ignition requirements favorable for thruster utilization somehow naturally interfere with the requirements for general safe substances, various authors have come to the conclusion that all propellant alternatives are in some way potentially harmful and toxic [16, 17]. These authors also stress their preference of the term "reduced-hazard propellants" instead of the widely used term "green propellants".

---

[1] European Space Agency: http://www.esa.int/, (last accessed: 3.5.2012).

Currently state of the art propellant Hydrazine (N_2H_4) and its derivatives Monomethyl-hydrazine (MMH) and Unsymmetrical Dimethylhydrazine (UMDH), which are often used in mixtures to improve physical properties, are widely regarded as highly toxic and carcinogenic [18], or as Bombelli et al. [19] phrased:

> *"Human exposure to hydrazine and its vapours is categorised as a 'catastrophic' hazard, the consequences of which lead to loss of life, permanently disabling injury or occupational illness."* [Ref. 19].

To assess the validity of referring to an alternative propellant as "reduced-hazard propellant" with respect to currently used propellant combinations, it is useful to compare risk classifications of these substances to another. An exhaustive effort in the classification of potential reduced-hazard propellants has been performed in Ref. 13, where also the issue of missing or wrong data found in literature is addressed. The main results regarding hydrogen peroxide, compared to hydrazine, are summarized hereafter.

The classification regarding toxicity was evaluated using, amongst others, the EU Hazard Statements categories[2] [13]. The leading parameters used in this classification are listed and described in Table 1.

<div align="center">Table 1 EU Hazard Statements categories, Ref. 13</div>

LD_{50} oral (mg/kg):	The oral LD_{50} is the single dose associated with a 50 % chance of death within two weeks
LD_{50} skin (mg/kg):	The skin (dermal) LD_{50} is the single dose associated with a 50 % chance of death within two weeks
LC_{50} inhalation (ppm):	The LC_{50} is the concentration in air over a period of four hours associated with a 50 % chance of death within two weeks

The assessment regarding carcinogenicity is based on the categories imposed by the IARC (International Agency for Research on Cancer, World Health Organization)[3]. The classification imposed by the State of California for assessment of drinking water, called Proposition 65, is included in the assessment as an example of a very cautious approach to the classification of chemical substances[4].

A comparison of available data for highly concentrated hydrogen peroxide to hydrazine is shown in Table 2. For each parameter listed in Table 2, the classification according to the EU Hazard Statements categories is displayed in the subsequent line. In addition to the classifications described above, the vapor pressure at standard room temperature is listed in the bottom line, since evaporation is strongly related to the problematic of inhalation of stored propellants. The problematic of properly assessing the danger from evaporated propellant is

---

[2] European Union: Directive 2008/112/EC of the European Parliament and of the Council of 16 December 2008, L 345/68, Official Journal of the European Union, http://eur-lex.europa.eu/LexUriServ/LexUriServ.do?uri=OJ:L: 2008:345:0068:0074:en:PDF , (last accessed: 24.4.2012).
[3] International Agency for Research on Cancer, IARC Monographs on the Evaluation of Carcinogenic Risks to Humans, http://monographs.iarc.fr/ENG/Classification/index.php, (last accessed: 24.4.2012).
[4] Office of Environmental Health Hazard Assessment: Proposition 65, http://oehha.ca.gov/Prop65.html, (last accessed: 24.4.2012).

discussed in Ref. 13. From this discussion it can be concluded that the resulting hazardous effect in case of low LC_{50} values is considerable increased for high vapor pressure. Accordingly, inhalation hazards during propellant handling may be considerably reduced in the case of low vapor pressure, even in the case of low LC_{50} values.

In addition to hydrogen peroxide and hydrazine, values for hydrazine derivates MMH and UDMH are shown in Table 2, as are for Dinitrogen Tetroxide (NTO), if available. The latter is used as oxidizer in bipropellant engines together with hydrazine, MMH or UDMH [3]. In addition, toxicity values for potential fuels for reduced hazard bipropellant propulsion are given, if available.

Table 2 Propellant toxicity comparison

		Hydrogen Peroxide H_2O_2	Hydrazine N_2H_4	MMH	UDMH	NTO	Jet A-1	Ethanol
LC_{50} inhalation	ppm	> 2876 [20] (90wt. % conc.)	330 [22], 570 (rat) [18]	34 [13]	252 [13]	88 [13]	830 [13]	46500 [13]
	Class *)	4: "Harmful if inhaled"	2: "Fatal if inhaled"	1: "Fatal if inhaled"	2: "Fatal if inhaled"	1: "Fatal if inhaled"	-	5: „Precaution"
LD_{50} Oral	mg/kg	> 805 [20] (70wt. % conc.)	60 - 200 [18, 23]	32 [13]	60 [13]	-	5000 [13]	7060 [13]
	Class *)	4: „Harmful if swallowed"	3: „Toxic if swallowed"	2: "Fatal if swallowed"	3: „Toxic if swallowed"	-	5: „Precaution"	5: „Precaution"
LD_{50} Dermal	mg/kg	2000 (mouse) [20] (90% conc.)	91 - 290 [23]	95 [13]	1060 [13]	-	>2000 [13]	20000 [13]
	Class *)	4: „Harmful in contact with skin"	2: „Fatal in contact with skin"	2: „Fatal in contact with skin"	4: "Harmful in contact with skin"	-	5: „Precaution"	5: „Precaution"
Carcin.	IARC	3: "Agent is not classifiable as to its carcinogenicity to humans."	2B: "Agent is possibly carcinogenic to humans"			-	-	1: "carcinogenic to humans"§)
	Prop. 65	Not listed	Cancer	Cancer	Cancer	Not listed	Not listed	Cancer §)
Evaporation at T = 298 K	p_{vap} [Pa]	1266	20631	6426	1895	141343	~10000	6580

Annotations: *) Classified by EU Hazard Categories Classification
                        §) if consumed as a beverage

Table 2 shows the reduced toxicity and reduced risk classification regarding carcinogenicity for hydrogen peroxide compared to the standard monopropellant hydrazine and its derivatives. The significantly lower vapor pressure of hydrogen peroxide additionally reduces the evaporation and the possibility of inhalation of the propellant, compared to hydrazine. The reduced toxicity of hydrogen peroxide compared to the standard fuel hydrazine is further discussed in Ref. 18. As for the potential fuels kerosene and ethanol, lowest risk classification is found for the data available. However, ethanol is classified as carcinogenic, but this classification specifically states that this is based on a consume of ethanol in the form of beverages, making the classification obsolete for an assessment of rocket fuels.

A detailed discussion of the preliminary assessment of a large variety of propellants, based on toxicity, storability and performance is given in Ref. 14. This assessment led to the propellant combinations hydrogen peroxide/kerosene and hydrogen peroxide/ethanol as candidate propellants for further investigation on propulsion system level, performed in this work.

1.2.1. High grade hydrogen peroxide

The decomposition of highly concentrated hydrogen peroxide has a long heritage as propulsion and power source in aerospace applications. It has been employed in the ME-163 fighter plane, in the steam generator system of the A-4 (V-2) missile and Redstone rocket, as steam source and propellant for the reaction control system of the X-15 experimental aircraft, in the reaction control system, among others, of the Mercury, Centaur and Soyuz programs and as main propulsion system of the British Black Arrow missile [24, 25, 26, 27, 28, 29, 30].

Recent applications are found in low thrust engines like monopropellant engines typically used for on-orbit propulsion [24, 31, 32]. Especially system considerations from ongoing miniaturization make hydrogen peroxide thrusters a candidate for low-toxic, low-cost propulsion, featuring easily storable propellant while allowing high performance [14, 18, 33, 34, 35, 36, 37, 40]. Reviews on the historical use of hydrogen peroxide as a storable oxidizer for spacecraft propulsion can be found in Ref. 41, 42 and 43. Wernimont [18] stresses the favorable impact of using hydrogen peroxide as propellant in the case of miniaturized propulsion systems.

Storability and material compatibility of hydrogen peroxide, compared to hydrazine, are discussed in Refs. 18, 38, 40, 43 and 44. Especially the latter source gives valuable detailed information on test setup and different materials used, although only storability of non-stabilized hydrogen peroxide was investigated. Ref. 18 reported successful storage tests of 3 years in sealed containers and up to 17 year long storage in a vented storage container without significant change in concentration in 1965. Storability tests based on gravimetric measurements of the storage containers (approximately total weight: 1.8kg) at defined ambient conditions for a three year duration performed within this project could not identify any measurable change in concentration for storage in refrigerated, passivated aluminum containers. Ref. 40 reports no measurable performance decrease for on-orbit thrusters employed in the Hughes-NASA SynCom II satellite after one year of operation compared to the performance achieved 24 hours after launch, validating the ability of on-board storability for 90 wt.% hydrogen peroxide in this timeframe. Other satellites employing hydrogen peroxide monopropellants include the satellite Early Bird, which was in operation for 5 years [38].

The decomposition of hydrogen peroxide yields a high temperature mixture of steam and oxygen, which can be used in a monopropellant configuration to generate thrust by expansion

though a nozzle [24, 45], or in a bipropellant configuration as oxidizer source for combustion with a proper fuel.

Besides efforts undertaken to improve the performance of hydrogen peroxide monopropellant thrusters [27, 31, 35, 36, 37, 77, 78], a variety of scholars investigated hydrogen peroxide based bipropellant engines for a large range of thrust levels. A short overview on current research activities is given hereafter.

Scholars at the Purdue university are investigating the design of a rocket engine for kerosene-hydrogen peroxide mixtures with mass flow rates in the order of 1 kg s^{-1}, successfully achieving autoignition [46, 47, 48].

Wernimont and Duran [49] presented test results of a 1.1 kN thruster utilizing 90 wt.% hydrogen peroxide in combination with kerosene, developed by General Kinetics. Hydrogen peroxide based propulsion efforts conducted at General Kinetics resulted in a variety of thrusters at different thrust levels. This includes monopropellant thrusters featuring nominal vacuum thrust levels ranging from ~26 N to ~670 N, and bipropellant thrusters with kerosene ranging from ~1.1 kN to ~4.4 kN.

Lederbuhr et al. [50] published literature on the development of a pump-fed thruster using 90 wt.% hydrogen peroxide and kerosene with a targeted thrust level of 1.2-1.3 kN at the Lawrence Livermore National Laboratory, stressing the cost reduction in both experimental investigation and operation in comparison to earlier studies utilizing hydrazine as propellant.

In the UK, Musker et al. [51] investigate a hydrogen peroxide based staged combustor concept with autoignition capabilities. Like a variety of other authors, they employ the concept of starting the thruster by a warming pulse to enhance catalyst performance.

Scholars at the Dalian Institute of Chemical Physics [52] investigated the ability of hypergolic propulsion by H_2O_2/kerosene mixtures with additives and reported successful pulsing tests in preheated configurations with pulse duration in the order of 10 ms at mass flows of ~16 g s^{-1}.

Developments on hydrogen peroxide based bipropellant thrusters at low thrust levels include efforts undertaken by Surrey space center (UK), where a 40 N bipropellant thruster based on 90 wt.% hydrogen peroxide and kerosene was developed and test-fired in 2002 [53].

Besides conventional manufacturing techniques, a new approach for miniaturized thrusters has emerged, based on microelectromechanical systems (MEMS) technology at significantly reduced geometrical scales in the order of hundreds of micrometers. Thrusters investigated include cold gas thruster, monopropellant and bipropellant engines. Hitt et al. [54, 55] have investigated the design of a MEMS based hydrogen peroxide monopropellant thruster, reporting considerable difficulties in achieving high decomposition efficiencies. Ref. 56 specifically addresses the problem of achieving high decomposition efficiencies in MEMS scale hydrogen peroxide propulsion and presents efforts of designing an electrically heated porous catalyst bed. The possibility of bipropellant propulsion based on MEMS technology in

a regeneratively cooled configuration has been shown by scholars at the Massachusetts Institute of Technology for a gaseous oxygen-methane propellant combination [57]. In addition, various scholars investigated a variety of issues arising for MEMS based propulsion systems, such as adapted nozzle designs and thermal coupling of the thruster [58, 59, 60, 61].

To the best of the author's knowledge, no green bipropellant engine miniaturized to a thrust level of 1 N has been developed or investigated anywhere.

1.2.2. Staged thruster concept and thrust generation

Using hydrogen peroxide as oxidizer in a bipropellant thruster configuration has been studied in two principal configurations: direct injection of the undecomposed hydrogen peroxide into the combustion chamber and staged combustion with a separate decomposition of the hydrogen peroxide prior to the injection into the combustion chamber. The main advantage of the latter configuration is the ability to autoignite the combustion process, facilitated by the high temperature decomposition products. A comparison and discussion of both configurations is given in Ref. 62.
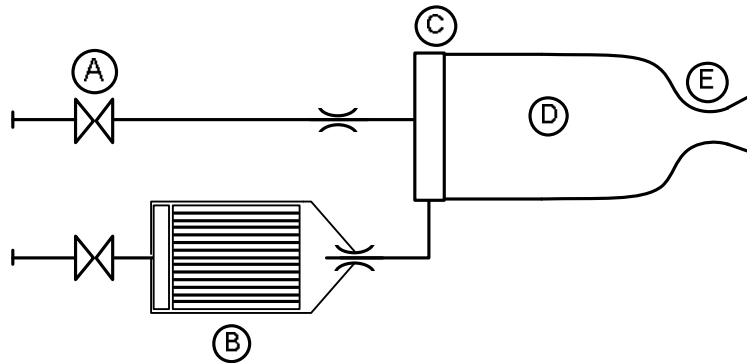
Figure 4: Main components of a staged bipropellant thruster

In a staged bipropellant system as shown in Figure 4, the hydrogen peroxide is decomposed in a decomposition chamber (B) by a catalyst into steam and oxygen at elevated temperatures (T = 690 °C for 87.5 wt.% H_2O_2), before it is injected (C) into the combustion chamber (D). The high temperature of the decomposition products enables autoignition with an additionally injected fuel (A: kerosene, ethanol, etc.) at design chamber pressure. Experimental investigations within this work showed autoignition thresholds at chamber pressures before ignition of 4.7-22 bar for temperatures of T = 330-430 °C for kerosene Jet A-1 and T = 590-615 °C at ignition pressures of 15-22 bar for ethanol for the given combustion chamber design. The combustion products are then expanded through a converging-diverging nozzle (E) to high exit velocities, guaranteeing high specific impulse. In this work, a nominal thrust of 1 N is aimed at for a bipropellant thruster system with autoignition capability suited for the increasing market of small satellites [63, 64, 65, 66].

Figure 5: Stationary thruster schematics

The thrust generated by a thruster shown in Figure 5 can be derived by a control volume analysis. The momentum equation is given by

$$\frac{\mathrm{d}}{\mathrm{d}t}\int_{CV}\rho\vec{u}\mathrm{d}V+\int_{CS}\vec{u}\rho(\vec{u}\cdot\vec{n})\mathrm{d}A=\sum\vec{F}.$$

(1.2)

CV and CS refer to the control volume and the control surface of the volume, with surface normal $\vec{n}$ respectively. ρ refers to the density, whereas $\vec{u}$ refers to the velocity of the working fluid. The first term in 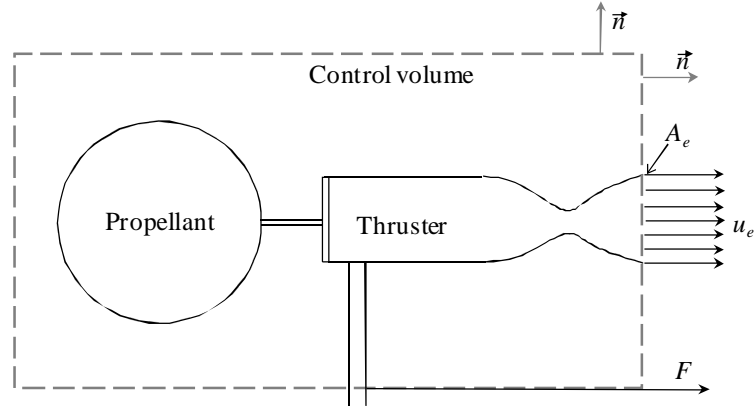the momentum equation is the instationary term of rate of change in momentum within the control volume, whereas the second term refers to the convective transport of the momentum out of the control volume. Conservation of momentum is given by introducing the sum over all forces acting on the thruster, such as the force F reacting to the thrust shown in Figure 5.

Solving the momentum equation for the control volume indicated in Figure 5 for the stationary case with vanishing gradient with respect to time, gives the sum of all forces acting on the thruster to maintain its position in a vacuum environment

$$\sum\vec{F}=\int_{CS}\vec{u}\rho(\vec{u}\cdot\vec{n})\mathrm{d}A.$$

(1.3)

According to Figure 5, all forces act normal to the control volume surface, and Eq. (1.3) therefore becomes, for the only forces acting through the control volume being the reaction force F and the pressure forces at the nozzle exit plane

$$\int_{CS}\vec{u}\rho(\vec{u}\cdot\vec{n})\mathrm{d}A=F-A_e p_e+A_e p_a.$$

(1.4)

with p_e being the homogeneous exit pressure at the nozzle exit plane and p_a the ambient pressure. Assuming homogeneous exit velocity u_e normal to the control volume surface, Eq. (1.4) becomes

$$\rho u_e^2 A_e=F-A_e p_e+A_e p_a.$$

(1.5)

Since the propellant mass flow can be expressed as $\dot{m}_p = \rho u_e A_e$, the thrust produced by the engine shown in Figure 5 becomes:

$$F = \dot{m}_p u_e + (p_e - p_a) A_e .$$
(1.6)

1.2.3. Performance characteristics

Theoretical performance achievable for propellant combinations using hydrogen peroxide as oxidizer have been calculated using NASA Chemical Equilibrium and Applications (CEA) code [92], which is described in more detail in section 0. The specific impulse is used as a figure of merit for theoretically achievable propellant performance. The specific impulse is the total impulse achieved per unit weight of propellant and is defined as the quotient of thrust F produced by an engine and the propellant mass flow $\dot{m}_p$ necessary to achieve the thrust [3]

$$I_{sp} = \frac{\int F \mathrm{d}t}{g_0 \int \dot{m}_p \mathrm{d}t} .$$
(1.7)

g_0 refers to the standard acceleration of gravity. In a liquid propulsion system with no external energy added to the exhaust, the ideal specific impulse thus describes the conversion of chemical energy stored in the propellants into thrust.

The performance calculations presented in this section were performed assuming frozen flow downstream of the throat area, a combustion chamber pressure of 10 bar and expansion to vacuum for a nozzle area expansion ratio of $\varepsilon = 40$. These calculation parameters comply with the standardization scheme outlined in Ref. 68 and therefore allow comparison to performance characteristics published for other propellant combinations [14, 68]. Figure 6 shows a comparison of specific impulse theoretically achievable for various fuels combined with 90 wt.% hydrogen peroxide as oxidizer. Stoichiometric mixture ratios, that are the mixture ratios featuring highest combustion temperatures, are indicated by black round markers.

Note that Figure 6 compares only specific impulse, neglecting any other issues possibly arising for these fuels like autoignition capability and storability issues in the expected temperature regimes, such as propellant freezing or high vapor pressure. These physical parameters for a large variety of potential fuels have been published in Ref. 13.

Figure 6 Specific impulse comparison for selected fuels combusted with 90 wt.% H_2O_2, frozen flow, $\varepsilon = 40$, black markers refer to stoichiometric mixture ratio

For the overall propulsion system, not only thruster related performance parameters are of interest, but figures of merit describing the performance of the overall system, including the propellant storage system. Under the assumption of volume reduction being the most stringent requirement for onboard propulsion systems, the specific impulse density describes the overall thruster performance incorporating propellant storage volume. The specific impulse density is defined as [68]

$$I_{sp}^V = \frac{\rho_p}{\rho_{H_2O}} I_{sp} \; . \tag{1.8}$$

ρ_{H2O} refers to the reference density of water at standard conditions and is introduced to maintain the unit of the density specific impulse in seconds. ρ_p refers to the mean density of the propellants according to the oxidizer to fuel mixture ratio $O/F = \dot{m}_{ox}/\dot{m}_{fu}$

$$\rho_p = \frac{\rho_{ox}\rho_{fu}\left(1+O/F\right)}{\rho_{ox} + \rho_{fu}O/F} \; . \tag{1.9}$$

The specific impulse density was evaluated for a tank pressure of 20 bar. Since ethylene remains gaseous under this condition at reference temperature, the corresponding specific impulse density is considerable decreased and is therefore not shown in the comparison in Figure 7. Due to the high density of kerosene compared to other potential propellants, highest volume specific impulse values are achieved for this propellant combination.
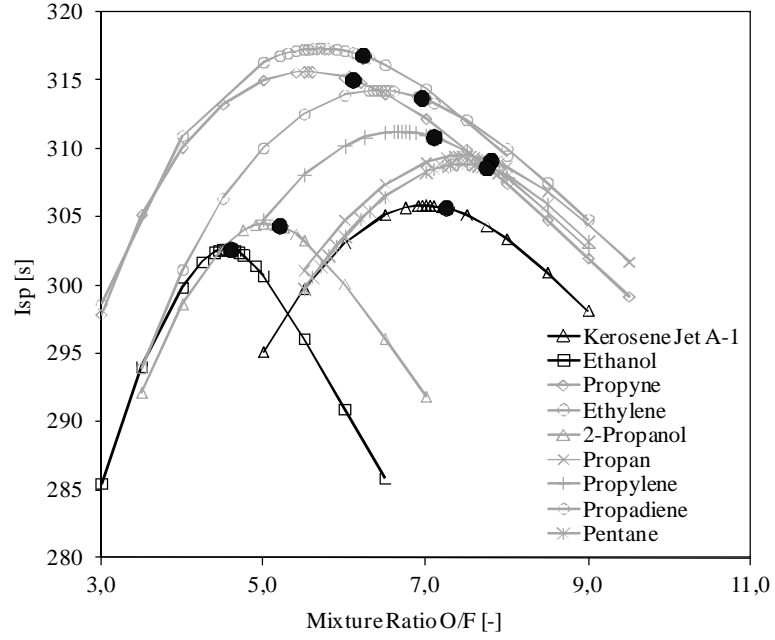
14

Figure 7 Specific impulse density comparison for selected fuels combusted with 90 wt.% H_2O_2, frozen flow, $\varepsilon = 40$, black markers refer to stoichiometric mixture ratio

A tradeoff between performance, toxicity, handling issues and storability led to the choice of ethanol and kerosene as possible fuels for hydrogen peroxide based bipropellant propulsion for further investigation [13, 33].

The influence of oxidizer concentration on thruster performance is compared in Figure 8 for 90 wt.% H_2O_2 and 100 wt.% H_2O_2 for the two fuels investigated in this work.
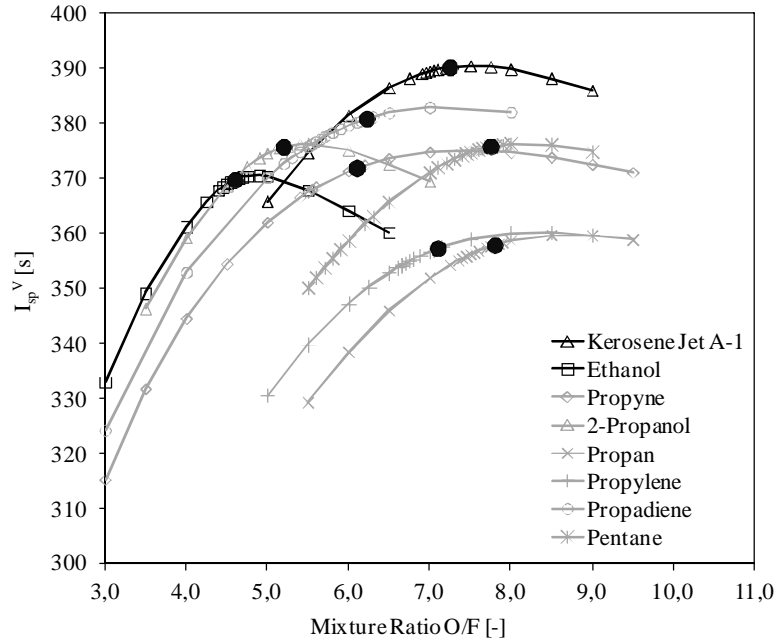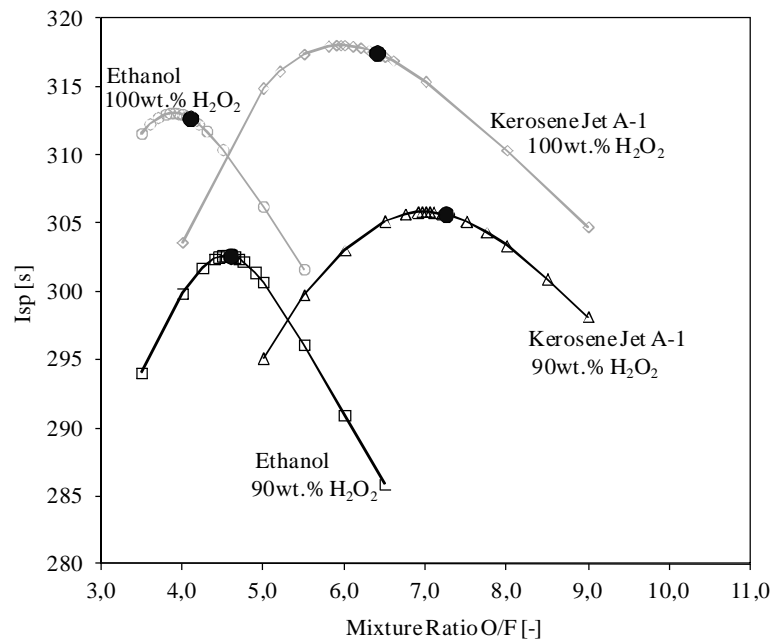

Figure 8 Specific impulse comparison for selected fuels combusted with 90 wt.% and 100 wt.% H_2O_2, frozen flow, $\varepsilon = 40$, black markers refer to stoichiometric mixture ratio

1.2.4. Hydrogen peroxide phase diagram

An early work summarizing main physical and chemical properties of highly concentrated hydrogen peroxide has been published by Shanley and Greenspan [39]. Ignition limits for hydrogen peroxide have been investigated by Satterfield et al. [69]. Early comprehensive compendia on hydrogen peroxide have been published in References 25 and 91, and, in reference to propulsion applications, in Ref. 30.

The phase diagram of hydrogen peroxide in aqueous solution with relevant physical states indicated is shown in Figure 9. Whereas low temperature behavior is well studied [71, 72, 73, 29, 74, 25], collecting data on bubble point and dew point curves caused considerable efforts due to the inherent presence of thermal decomposition at elevated temperatures for low purity concentrations, leading to considerable uncertainties in experimental data available concerning the concentrations investigated. Ref. 75 conducted a review on experimental data, identifying Ref. 76 to contain the most reliable experimental data available. A negative deviation from Raoult's law has been observed for aqueous hydrogen peroxide solutions, leading to an overestimation of calculated partial pressures for an ideal solution. Therefore, vapor pressure relations have been extrapolated from experimental data [75, 76].
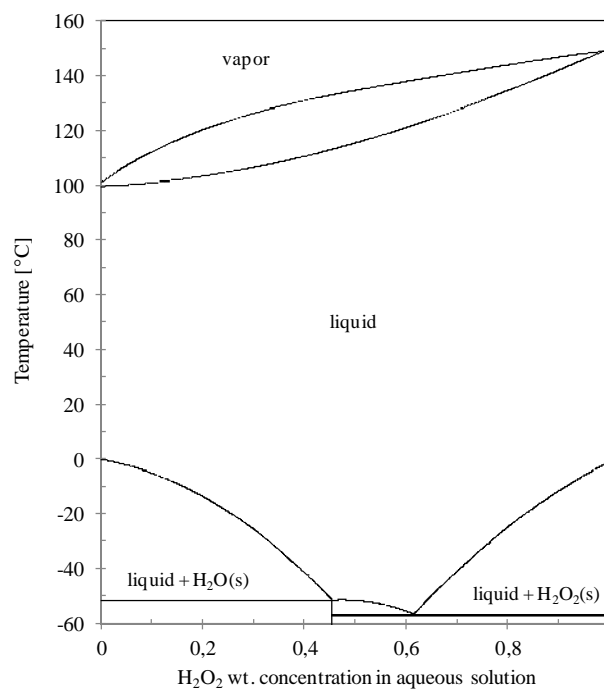
Figure 9 Phase diagram of hydrogen peroxide in aqueous solution, reproduced from data of Ref. 25, 29, 71, 72, 73, 74, 75, 76

The phase diagram for standard pressure conditions is shown in Figure 9 based on experimental and derived data from Ref. 76 and 75 (bubble and dew point curve) and Ref. 25, 71, 72, 73, 74 and 75 for liquid-solid phase change data. The data given in Ref. 75 allowed calculation of the liquid-vapor phase change data at elevated pressures, as necessary in the decomposition simulation presented in section 2.3.2.1.

2.   Decomposition chamber

In past chemical propulsion applications utilizing heterogeneous hydrogen peroxide decomposition, a variety of different catalyst carrier materials have been employed. These include screens [25, 30], packed metal-oxide pellets [77], fine grains [79], gauzes [27], porous foams [80] or monoliths with defined flow channels [81] as supporting structures. The catalytic material is usually applied onto the surface of the carrying structure. Thus, this structure is supposed to provide as much surface as possible while avoiding to large volumes of the overall catalyst, maintaining mechanical stability and guaranteeing enduring contact of the hydrogen peroxide to the catalytic material. The advantage of increasing the surface of the supporting structure by coating is discussed for the example of Ag supported by Al_2O_3 compared to pure silver in Ref. 82 and 83. Other important design issues include a uniform flow path, the avoidance of large pressure drops due to friction caused by large internal surfaces, and shortening time periods until decomposition at high efficiency is achieved after system start up, to enable pulsed operation.

Since the discovery of hydrogen peroxide decomposition, over hundred materials able to trigger decomposition were identified [25, 84, 85, 86]. Several studies investigated manganese based catalysts used to decompose highly concentrated hydrogen peroxide, indicating a strong dependence of catalytic behavior on supporting material [87]. Ref. 83 presents a comprehensive examination of different active materials such as Al, MnO_x, Pt, Ir and Pt-Sn.

In this work, focus will be laid on the experimental investigation of two different active materials identified as promising catalyst materials in previous studies [82, 83, 87, 88, 90], applied to a variety of different catalyst configurations and washcoatings. The experimental approach and results are discussed in section 4.2.

In a staged propulsion system, the decomposition of the hydrogen peroxide plays a crucial role: Immediate start up is necessary to guarantee fast pressure and temperature build-up to reach the autoignition threshold, as is high stationary performance in order to fully utilize the stored chemical energy and guarantee satisfying performance throughout the required lifetime. Therefore, a thorough understanding of the processes in the catalyst and catalyst chamber and the impact of thermal losses to the structure are of great interest. The latter is especially important in the case of miniaturization, which eventually increases the impact of thermal losses to the external environment.

After discussing the decomposition of hydrogen peroxide on a general basis, introducing an easy to handle analytical expression for the adiabatic decomposition temperature, a more complex approach based on a numerical simulation of the impact of structural design of both catalyst and decomposition chamber on decomposition performance is presented.

2.2. Adiabatic decomposition temperature

This section describes a simple analytical way of approximating the adiabatic decomposition temperature of hydrogen peroxide diluted in water for the case of ideal decomposition. The decomposition of one mole of pure hydrogen peroxide can be phenomenologically described by [88, 91]:

$$H_2O_2(l) \rightarrow H_2O(l) + \frac{1}{2}O_2(g) + \Delta q$$

$$\Delta_r H = -97.1kJ + \int_{298.15K}^{T_{Final}} \Delta c_p \, dT \, . \tag{2.1}$$

The letters in brackets indicate the state of the substance, i. e. liquid or gaseous. The total enthalpy gained from the decomposition of one mole of hydrogen peroxide is reduced by the energy needed to evaporate the produced and remaining water. The mass concentration of initial hydrogen peroxide is expressed as a function of the initial masses of the compounds:

$$x_{H_2O_2} = \frac{m_{H_2O_2}}{m_{H_2O_2} + m_{H_2O}} \, . \tag{2.2}$$

The difference in enthalpy for one mole of hydrogen peroxide diluted in water to the mass concentration $x_{H_2O_2}$, can thus be rewritten as, for fully evaporated products, for concentrations higher 61 wt.%:

$$\Delta H = -53.13\text{kJ} + \frac{M_{H_2O_2}}{M_{H_2O}}\left(\frac{1}{x_{H_2O_2}} - 1\right)44.00\text{kJ} \, . \tag{2.3}$$

The resulting heat release is calculated by the first law of thermodynamics

$$\Delta q = \Delta h + \int_{T_{298.15}}^{T_{Final}} c_P \, dT \approx c_P \left(T_{Final} - T_{298.15}\right) \, . \tag{2.4}$$

With the assumption of vanishing Δc_p, the change in mixture temperature caused by decomposition can be approximated by

$$\Delta T = \frac{53.13 \cdot 10^3 + \dfrac{M_{H_2O_2}}{M_{H_2O}}\left(\dfrac{1}{x_{H_2O_2}} - 1\right)44.00 \cdot 10^3}{\left[M_{H_2O_2}\left(\dfrac{1}{x_{H_2O_2}} - 1\right) + M_{H_2O}\right]c_P^{H_2O(g)} + \dfrac{1}{2}M_{O_2}c_P^{O_2(g)}} \, . \tag{2.5}$$

Figure 10 shows the adiabatic decomposition temperature of the evaporated products according to Eq. (2.5). The results from this simple correlation can be compared to numerical solutions gained by NASA Chemical Equilibrium and Applications (CEA) code [92], and results provided by Degussa and General Kinetics [93]. These results incorporating alterable specific heat capacity, yield, for 90 wt.% concentrated hydrogen peroxide a temperature of $T_{dec} \approx 740\text{-}756$ °C, whereas Eq. (2.5) results in $T_{dec} \approx 753$ °C. Thus, the analytical relation in Eq. (2.5) yields results in reasonable accuracy.
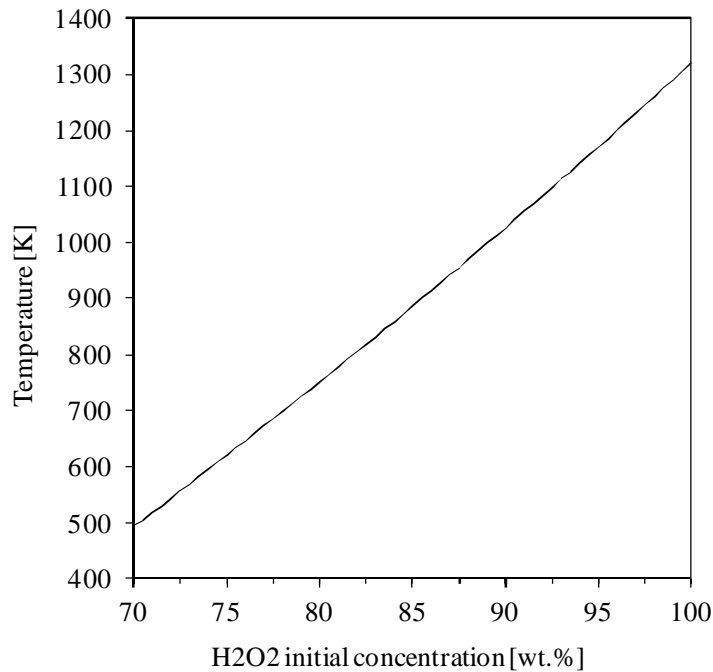
Figure 10 Adiabatic decomposition temperature of hydrogen peroxide as function of initial weight concentration, Eq. (2.5)

The resulting adiabatic mixture decomposition temperature for incomplete decomposition as a function of decomposition efficiency is shown in Figure 11. Decomposition efficiency is defined as the weight fraction of hydrogen peroxide decomposed, which equals unity for fully decomposed hydrogen peroxide, whereas an efficiency of zero depicts the total absence of decomposition. The temperature shown in Figure 11 corresponds to a chamber pressure of 10 bar and an initial hydrogen peroxide weight concentration of 87.5 wt.%. The method used to derive the adiabatic mixture temperature is based on the assumption of thermal equilibrium. Undecomposed hydrogen peroxide is therefore evaporated for temperatures above 425 °C, lowering the resulting adiabatic decomposition temperature.
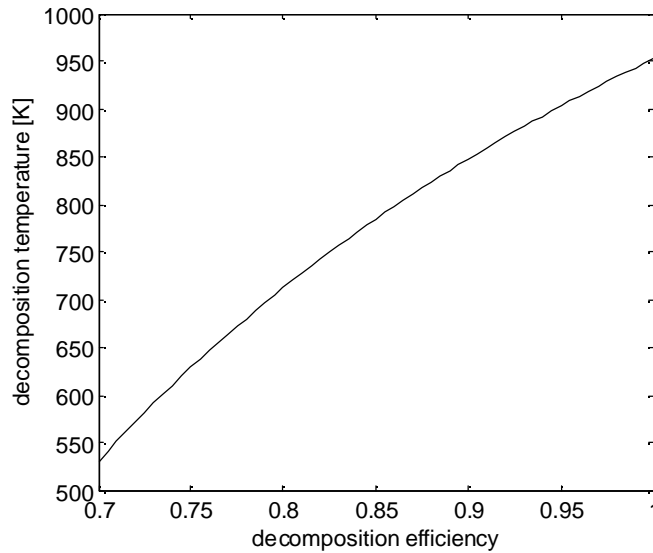
Figure 11 Resulting adiabatic decomposition temperature as a function of decomposition efficiency for $p_c = 10$ bar and 87.5 wt.% hydrogen peroxide concentration

2.3. Simulation

2.3.1. General considerations

In the following, the modeling efforts undertaken to investigate the impact of non-adiabatic coupling of the fluid flow within a heterogeneous honeycomb type catalyst to the catalysts structure and the decomposition chamber, is outlined. The hydrogen peroxide is injected into the different channels of the catalyst using a porous element injector mounted directly onto the catalysts face. The pressure drop within the injector prevents coupling of the flows between the different channels. Thus, the flow within each channel is treated as independent from other channels upstream of the catalysts exit face, except for thermal coupling via the catalysts structure.

The model presented hereafter bases on the following approximations:

- Homogeneous fluid distribution over the catalyst face, the mass flow through one catalyst channel is equal to the total injected mass flow divided by the number of channels.

- Homogeneous distribution of chemical species in the plane normal to the flow direction within the channel. Mass transport of chemical species to the channel walls is incorporated in the frequency factor in the Arrhenius equation.

- Large Péclet number for mass diffusion $\mathrm{Pe} = D_H u / \hat{D}$ shows convection to be the dominant process of mass transport and justify omission of diffusion processes of chemical species and thermal energy in the main flow direction in a first approximation. Thus, mass transport is described as convective process only. Therefore, a change in density of chemical species is caused by chemical reaction and thermal losses to the structure only [94].

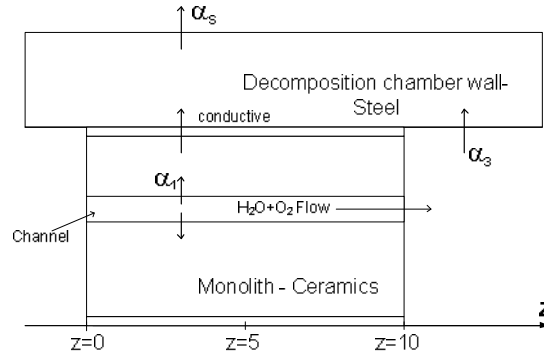Figure 12 Coupling of flow in channel to solid domain by convective heat loss

The decomposition process of liquid hydrogen peroxide into water vapor and gaseous oxygen is described phenomenological by

$$H_2O_2 \rightarrow H_2O + \frac{1}{2}O_2 + \Delta q .$$ (2.6)

In a batch reactor, a certain initial concentration of hydrogen peroxide in the presence of a catalyst will behave according to a first order reaction [25, 90, 55, 95] with the mole balance:

$$\frac{d[H_2O_2]}{dt} = -k[H_2O_2] ,$$ (2.7)

where the square brackets indicate the concentration of the species. The rate of reaction k indicates both the probability of contact between hydrogen peroxide and catalytic molecules and the probability of chemical reaction taking place. The rate of reaction k is described by the Arrhenius equation [55, 96], reflecting a strong dependence on temperature:

$$k = A_0 \exp(-\frac{E_a}{RT}) .$$ (2.8)

The constant A_0 denotes the pre-exponential factor, also called frequency factor, and is a measure of the number of contacts of hydrogen peroxide and catalytic molecules per second. The frequency factor is influenced by the flow behavior, such as the radial diffusivity of hydrogen peroxide molecules within the given channel and time of contact with catalytic molecules. Since this parameter is influenced by a series of complex processes, including orientation on molecule level, the ability to theoretical determine this parameter in sufficient accuracy for the given catalyst configurations is limited, and thus fitting to experimental results for the specific catalyst design is preferred.

Models of thermal decomposition indicate an activation energy in the liquid phase in the order of $E_a \approx 200$ kJ mol^{-1} [96]. Ref. 97 found decomposition rates for 90 wt.% hydrogen peroxide to be in the range of $k = 3 \cdot 10^6 \, \text{s}^{-1}$ to $k = 5 \cdot 10^6 \, \text{s}^{-1}$. This is compared to significantly lower

activation energy in the liquid phase of $E_a \approx 50$ kJ mol^{-1} for catalytic decomposition in the presence of a MnO$_x$ based catalyst [98, 99].
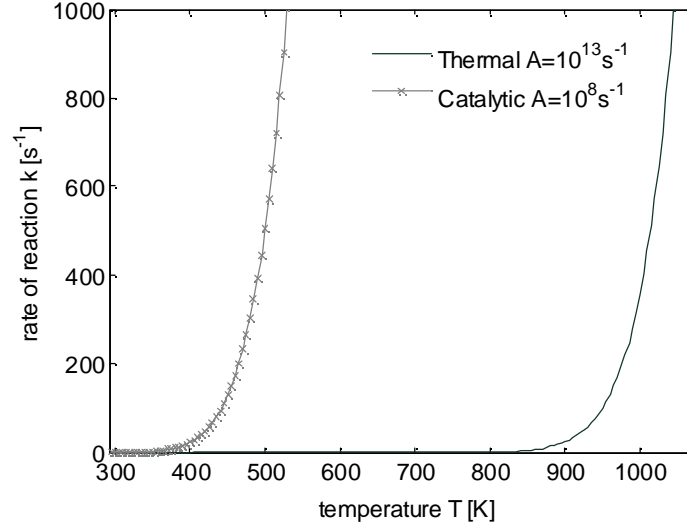
Figure 13 Rate of reaction for one mole of hydrogen peroxide for $A_0 = 10^8$ s^{-1} and E_a=50.7 kJ mol^{-1} compared to rate of thermal decomposition with $A_{thermal} = 10^{13}$ s^{-1} and $E_a = 200$ kJ mol^{-1}[96].

Figure 13 shows the rate of reaction on a molar basis as a function of temperature for the frequency factor $A_0 = 10^8$ s^{-1} compared to the thermal decomposition rate, calculated with parameters from Ref. 96. The behavior of rates of reaction justifies neglecting the contribution from thermal decomposition, as the rate of catalytic decomposition diverges at far lower temperatures. Note that the catalytic rate is much higher at low temperatures even for lower frequency factors. Nevertheless, thermal decomposition can help increasing decomposition efficiency in the case of poor contact between the hydrogen peroxide and the catalyst surface (low frequency factor).

2.3.2. Lumped parameter fluidic model

In this section, a simple approach to model the fluid within the catalyst is presented. This model will later act as a boundary condition for the solid domain simulation. In a heterogeneous catalyst with hydrogen peroxide entering one face and the reaction products exiting the catalyst at the opposite face, a velocity, averaged over the channel cross section A_C, can be introduced for the assumption of constant densities over the channel cross section A_C.

$$\bar{u}_{(z)} = \frac{1}{A_C} \int u_{(z)} \mathrm{d}x \mathrm{d}y .$$ (2.9)

Thus, average velocity $\bar{u}$ is dependent on stream position z only.

Introducing a mean velocity for a two phase mixture introduces certain approximations regarding the type of flow occurring in the micro channel [100]. As found later by the model presented hereafter, superficial gas velocities are in the order of 1-2 meter per second. For the given fluid densities occurring in the system, flow pattern maps [101, 102, 103, 104, 105] suggest plug flow to be a reasonable approximation. Eq. (2.7) thus becomes

$$\frac{dn_{H_2O_2}}{dz} = -\frac{k}{\bar{u}} n_{H_2O_2} .$$
(2.10)

In this approximate model, the velocity is determined by the conservation of mass:

$$\frac{\partial}{\partial z} (\bar{\rho} \bar{u} A_C) = 0.$$
(2.11)

Experimental investigation justifies the approximation of constant chamber pressure to simplify the simulation and reduce calculation efforts [107, 106]. In this case, the mean density, determined by the weighted sum of all occurring species, is a function of temperature only:

$$\bar{\rho} = \sum_i m^i \bigg/ \sum_i \frac{m^i}{\rho^i} ,$$
(2.12)

where the sums extend over all species in gaseous and liquid state. The individual gaseous species densities are approximated by the equation of state of an ideal gas, liquid species are approximated to be incompressible.

In the process of temperature increase of the mixture due to heat release by the decomposition, different evaporation temperatures of water and hydrogen peroxide will lead to a shift in concentration of the liquid and gaseous compounds according to the two species phase diagram (Figure 9). The evaporation process and a possible approximation are discussed in detail in the sections hereafter.

The specific heat capacities for the chemical species are described by the Shomate Equation, in J mol^{-1} K^{-1} [25]:

$$c_P = A + Bt' + Ct'^2 + Dt^3 + Ct'^{-2} ,$$
(2.13)

for $t'=T/1000$K, with T given in Kelvin. The parameters A to E are given in Table 3. The heat capacity of liquid hydrogen peroxide is assumed to be constant at $c_P^{H2O2} = 88.1959$ J mol^{-1} K^{-1} according to Ref. 91.

Table 3 Parameters for Shomate Equation

Species	State	A	B	C	D	E	Ref
H_2O	liquid	-203.606	1523.29	-3196.413	2474.455	3.855326	[25]
H_2O	gaseous	30.092	6.832514	6.793435	-2.53448	0.082139	[25, 108]
H_2O_2	gaseous	34.25667	55.18445	-35.15443	9.08744	-0.422157	[25]
O_2	gaseous	29.659	6.137261	-1.186521	0.095780	-0.219663	[25]

The mean heat capacity of the mixture per kg is given, for specific heat capacities converted to $J\ kg^{-1}\ K^{-1}$:

$$\bar{c}_p = \frac{\sum_i c_p^i m^i}{\sum_i m^i}.$$

(2.14)

The conservation of energy gives:

$$Q_{Source} + Q_{Loss} + Q_{Sink} = 0.$$

(2.15)

The source term in Eq. (2.15) describes the energy release by decomposition of hydrogen peroxide which is described in Eq. (2.6). The term denoted Q_{Loss} includes thermal losses to the surrounding structure by convective heat transfer from the fluid to the monolith with α being averaged over the channel perimeter, for square channel cross section

$$Q_{Loss} = \alpha_{(z)} 4\sqrt{A_C}\, dz \left(T_{(z)} - T_{W(z)} \right).$$

(2.16)

The term Q_{sink} in Eq. (2.15) describes the increase of enthalpy of the fluid cell due to temperature increase or evaporation. Two different approaches for modeling the evaporation behavior of the system are given in the following sections.

The governing equations for the remaining chemical species are directly determined by Eq. (2.10):

$$\frac{dn_{H_2O}}{dz} = -\frac{dn_{H_2O_2}}{dz}$$

$$\frac{dn_{O_2}}{dz} = -\frac{1}{2}\frac{dn_{H_2O_2}}{dz}.$$

(2.17)

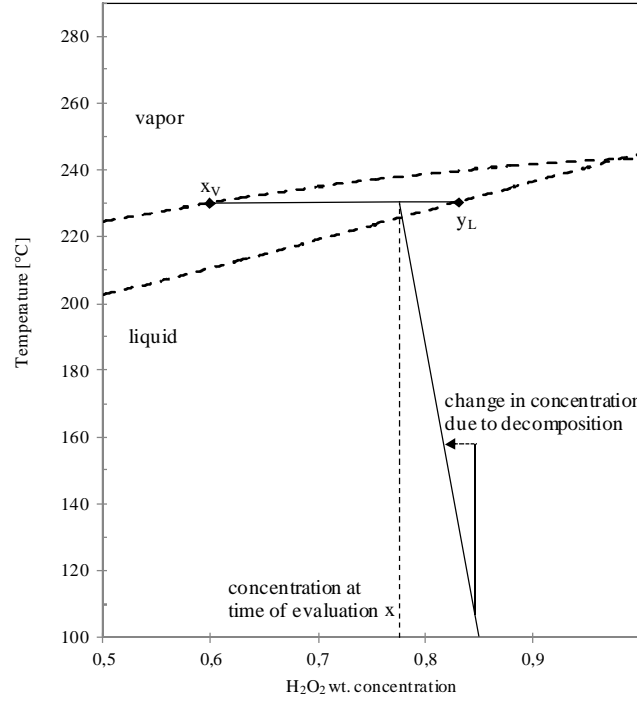### 2.3.2.1. Evaporation according phase diagram

Figure 14 Shift in liquid and vapor concentration according to phase diagram

Evaporation according to the binary phase diagram of hydrogen peroxide in aqueous solution leads to a shift in concentration in the liquid and the vapor phase. Since the third species O_2 only exists in gaseous state at the pressures and temperatures involved, reduction to the binary phase diagram is valid. Evaporation of species at a given temperature occurs according to the intersection of the isotherm line with dew point and the bubble point curve, denoted x_V and y_L in Figure 14 respectively. At a given temperature T, the fractions of evaporated water x^{H2O} and hydrogen peroxide x^{H2O2} become:

$$x^{H_2O} = \frac{x - x_V}{y_L - x_V}, \quad x^{H_2O_2} = \frac{y_L - x}{y_L - x_V}. \tag{2.18}$$

Due to continuing decomposition during evaporation, the concentration at time of evaluation x has to be updated for each time step. The energy balance in Eq. (2.15) then becomes:

$$-\Delta q \frac{dn_{H_2O_2}}{dz} = -\frac{dQ_{loss}}{dz} + \overline{c}_p \overline{m} \frac{dT}{dz} + \left(x^{H_2O} h_{H_2O}^{vap} + x^{H_2O_2} h_{H_2O_2}^{vap} \right) \frac{\partial \left(n_{H_2O(l)} + n_{H_2O_2(l)} \right)}{\partial T} \frac{dT}{dz}. \tag{2.19}$$

The specific heat $\overline{c}_p$ and the mass $\overline{m}$ refer to the mixture. The gradient of total amount of substance evaporated with respect to the temperature can be substituted in a linear approximation by a quotient of remaining liquid amount of substance divided by the temperature difference until evaporation is completed:

$$\frac{\partial \left(n_{H_2O(l)} + n_{H_2O_2(l)}\right)}{\partial T} \rightarrow \frac{\Delta \left(n_{H_2O(l)} + n_{H_2O_2(l)}\right)}{\Delta T} = \frac{n_{H_2O(l)} + n_{H_2O_2(l)}}{T_{dew(x)} - T} \qquad (2.20)$$

.

The change in gaseous species is then calculated according to:

$$\frac{dn_{H_2O(g)}}{dz} = x^{H_2O} \frac{n_{H_2O(l)} + n_{H_2O_2(l)}}{T_{dew(x)} - T}$$

$$\frac{dn_{H_2O_2(g)}}{dz} = x^{H_2O_2} \frac{n_{H_2O(l)} + n_{H_2O_2(l)}}{T_{dew(x)} - T} \qquad (2.21)$$

.

The adiabatic solutions for temperature and species mass distribution as a function of channel position are shown in Figure 15 for a sample simulation utilizing the parameters from Table 6 for an increased initial hydrogen peroxide concentration of 92 wt.%.
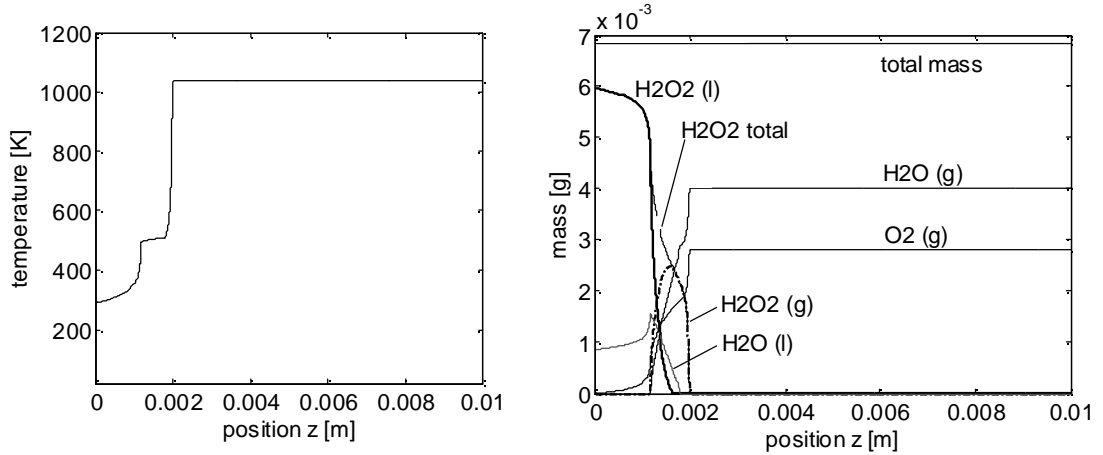
Figure 15 Phase diagram evaporation model: temperature (left) and species (right) distribution

Since high integration accuracies are necessary to determine the successive shifts in liquid and vapor concentration during evaporation according to the method presented in this section, an alternative approach of more approximate nature to reduce calculation complexity is presented hereafter.

2.3.2.2.   Monospecies evaporation approximation

The general idea of this approach is to divide the evaporation process into two single species evaporation processes of pure water and pure hydrogen peroxide at their dedicated boiling temperatures: only the species whose boiling point is reached with increasing temperature takes part in the evaporation process, with the remaining species staying in its original state. This way, the process of temperature increase can be divided into five delimited, successive regimes. These are separated by the boiling temperatures $T_{H_2O}^{boil}$ and $T_{H_2O_2}^{boil}$, which are given by the intersection points of bubble point and dew point temperature curves at zero and 100

percent concentration respectively (Figure 9). The strong approximations introduced by the assumption of single phase evaporation regimes are later justified by the narrow zone in which evaporation is present compared to the overall catalyst, thus introducing negligible approximations to the overall thermal investigation.

The boiling temperatures for the pure species as function of pressure are determined by the expressions given for vaporization pressure. The vapor pressure for water is commonly described by the Antoine Equation [108]:

$$\log \frac{p}{\text{bar}} = A - \frac{B}{T/\text{K} + C} \quad (2.22)$$

The vapor pressure relation for pure hydrogen peroxide is found in Ref. 25 as:

$$\log \frac{p}{\text{mm Hg}} = A - \frac{B}{T/\text{K}} - \frac{C}{\left(T/\text{K}\right)^2} \quad (2.23)$$

The parameters A, B and C are listed in Table 4.

Table 4 Parameters for vapor pressure expressions

Species	A	B	C	Ref
H_2O	3.55959	643.748	-198.043	[25]
H_2O_2	8.92536	2482.60	24675	[108]

In this approach, the fluid undergoes two different regimes during temperature increase (depicted in Figure 16):

I. Absence of phase changes, heat released by decomposition leads to an increase in temperature of the mixture and thermal losses. These are defined by either "all liquid" ($T < T_{H_2O}^{boil}$), "H_2O_2 liquid, H_2O gaseous" ($T_{H_2O}^{boil} < T < T_{H_2O_2}^{boil}$) or "all gaseous" ($T > T_{H_2O_2}^{boil}$:). The energy equation then becomes:

$$\Delta q \frac{dn_{H_2O_2}}{dz} = -\frac{dQ_{loss}}{dz} + \bar{c}_p \bar{m} \frac{dT}{dz} \quad (2.24)$$

The specific heat $\bar{c}_p$ and the mass $\bar{m}$ refer to the mixture.

II. Regimes in which one of the mixture component is changing its physical state. These are given by either "H_2O_2 liquid, H_2O evaporating" ($T = T_{H_2O}^{boil}$) or "H_2O_2 evaporating, H_2O gaseous" ($T = T_{H_2O_2}^{boil}$). In this regime, temperature remains constant, the energy equation becomes

$$q \frac{\mathrm{d}n_{H_2O_2}}{\mathrm{d}z} = -\frac{\mathrm{d}Q_{loss}}{\mathrm{d}z} + h_n^{vap} \frac{\mathrm{d}n}{\mathrm{d}z} \quad .$$

(2.25)

n and vaporization enthalpy h_n^{vap} refer to the species taking part in the evaporation process.

Five regimes are distinguished, two of them caused by evaporation of water and hydrogen peroxide, and three regimes of temperature increase without phase changes.

The lumped parameter model outlined in this section thus consists of three leading equations which are summarized in Table 5. Since Q_{loss} is dependent on the structural wall temperature of the catalyst channel, this set of equations has to be solved iteratively together with the structural model.

Table 5 Lumped parameter model leading equations, monospecies evaporation model

Designation	Equation
Rate of decomposition	$\dfrac{\mathrm{d}n_{H_2O_2}}{\mathrm{d}z} = -\dfrac{k}{\bar{u}} n_{H_2O_2}$
Balance equation of decomposition	$H_2O_2(l) + xH_2O(l) \rightarrow (x+1)H_2O(l) + \dfrac{1}{2}O_2(g)$ $\Delta_r H = 97.1\,\mathrm{kJ\,mole}^{-1}$
Conservation of energy	$Q_{Source} + Q_{Loss} + Q_{Sink} = 0$
- Evaporation processes:	$\Delta q \dfrac{\mathrm{d}n_{H_2O_2}}{\mathrm{d}z} = -\dfrac{\mathrm{d}Q_{loss}}{\mathrm{d}z} + h_n^{vap} \dfrac{\mathrm{d}n}{\mathrm{d}z}$
- Absence of evaporation:	$\Delta q \dfrac{\mathrm{d}n_{H_2O_2}}{\mathrm{d}z} = -\dfrac{\mathrm{d}Q_{loss}}{\mathrm{d}z} + \bar{c}_p \bar{m} \dfrac{\mathrm{d}T}{\mathrm{d}z}$

The resulting adiabatic solutions for temperature and species mass distribution as a function of channel position are shown in Figure 16 for a sample simulation utilizing the same input parameters as for Figure 15.

Comparison of Figure 15 to Figure 16 shows only minor impact on the simulation results regarding the thermal distribution due to the narrow distance in which evaporation occurs. Therefore, the significantly reduced calculation efforts justify the employment of the approximate approach in the simulation hereafter.
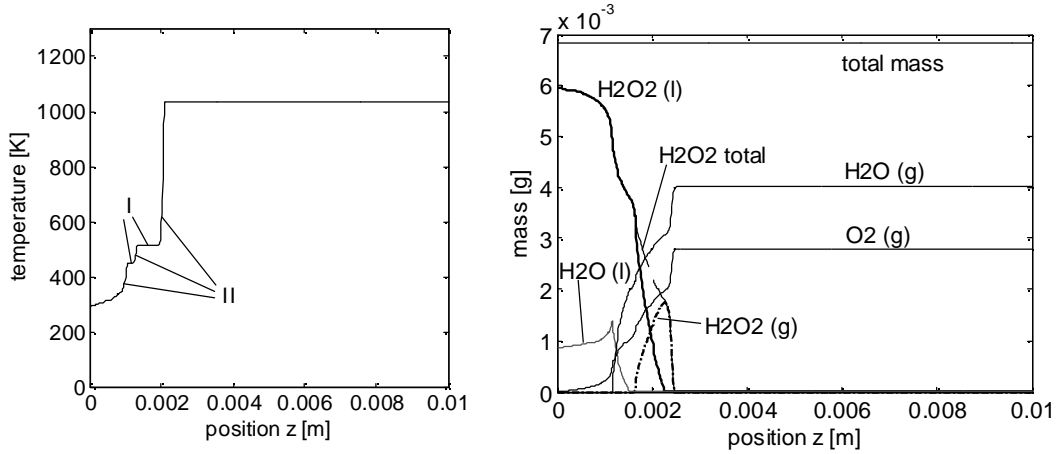
Figure 16 Monospecies evaporation model: temperature (left) and species (right) distribution

2.3.3. Solid domain model

The loss term Q_{loss} in the non-adiabatic fluid model couples the fluid model to the solid domain, which comprises of the catalyst structure and the surrounding decomposition chamber.

Conservation of energy expressed in form of a generalized transport equation for a scalar Φ is given by [109]

$$\frac{\partial(\rho\Phi)}{\partial t} + \mathrm{div}\left(\rho\vec{u}\Phi\right) = \mathrm{div}\left(\Gamma_\Phi \mathrm{grad}(\Phi)\right) + S_\Phi \,, \tag{2.26}$$

where the first term on the left hand side denotes the instationary term. Since the convective term equals zero, and in the absence of any sources S_Φ, only the diffusion term on the right hand side is considered. For an analysis of heat flow within a solid structure, the conservation of energy becomes, without boundary conditions:

$$\frac{\partial(\rho c_p T)}{\partial t} = \mathrm{div}\left(\lambda \cdot \mathrm{grad}(T)\right) \tag{2.27}$$

The thermal field of the structural domain of both the catalyst and decomposition chamber is calculated using a 3-dimensional Finite Element (FEM) solver (Ansys Multiphysics). The FEM adaptive mesh utilizing rotation symmetry, with the boundary condition of vanishing gradients at the cut areas, is shown in Figure 17.
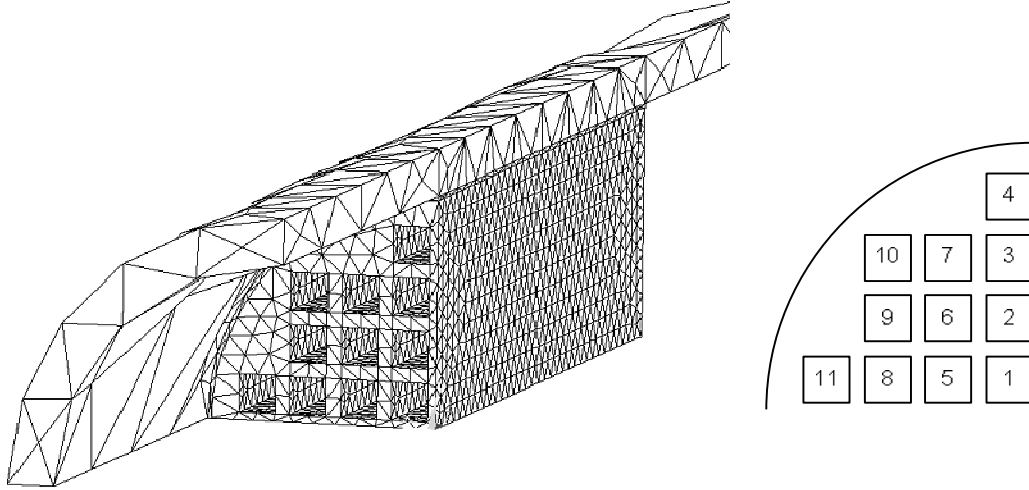
Figure 17 Depiction of FEM mesh of catalyst and decomposition chamber utilizing symmetry (left) and channel numbering (right)

The solid domain includes a monolith featuring a given number of squared channels, linked to the surrounding steel cladding by a thin gap described by thermal conductivity λ_2 as shown in Figure 18. This gap represents the nature of thermal insulation achieved by the decomposition chamber design. Thermal analysis was conducted for either good thermal insulation, achieved by a thin layer of steam separating the monolith (λ_1) from the steel cladding (λ_3), or by strong thermal coupling, simulated by perfect contact of the monolith to the steel cladding. The latter case was simulated by neglecting any surface roughness and hence total contact of the monoliths outer surface to the steel cladding, which was simulated by $\lambda_2 = \lambda_3$.
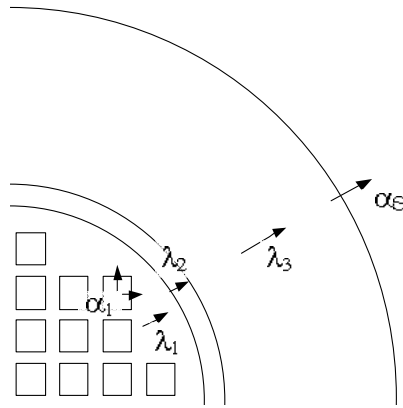
Figure 18 Boundary condition for FEM simulation, front view

The heat loss of the fluid to the catalyst structure is assumed to be solely caused by convective losses (convective heat coefficient α_1 in Figure 12). Fluid flow in the channel, changing from liquid to mixed and then gaseous state, leads to a convective boundary condition at the channel walls. The flow analysis showed Reynolds numbers Re < 2300 for the fully liquid and fully vaporized domain and therefore laminar flow is assumed. For this case, the solution of the Nusselt number becomes $Nu_D = 4.36$ (assuming constant heat flux on the surface). Literature on two phase flow indicates the concept of laminar boundary layer introducing a strong approximation if evaporation is present. Although expressions exist on film and bulk

boiling in channels based on the Martinelli parameter [102, 110, 111], these are based on thermal fluxes into the heated fluid from channel walls, governed by an appointed heat flux density [102]. As it is not self-evident whether these correlations can be applied to the present case, an interpolation of laminar film coefficients will be used in this model instead. As bubble formation is known to increase convective heat transfer, this approximation underestimates the heat loss and therefore sets a lower limit for the thermal impact of catalyst structure on decomposition performance. Additional boundary conditions to the solid thermal simulation are shown in Figure 12 and Figure 18 and comprise of a convective heat flux downstream of the catalyst to the decomposition chamber wall (α_3 in Figure 12) and a free convection boundary condition at the outer surface of the decomposition chamber (α_S in Figure 18).

2.3.4. Iterative coupling of models

The coupled simulation is solved iteratively. The simulation is described as a quasi steady chemical-fluid dynamic simulation coupled by the heat flow through the catalyst channel walls to a fully transient structural domain simulation which is solved iteratively, as depicted in Figure 19. Converged solutions for a time step are stored and act as initial condition for successive iterations in time.
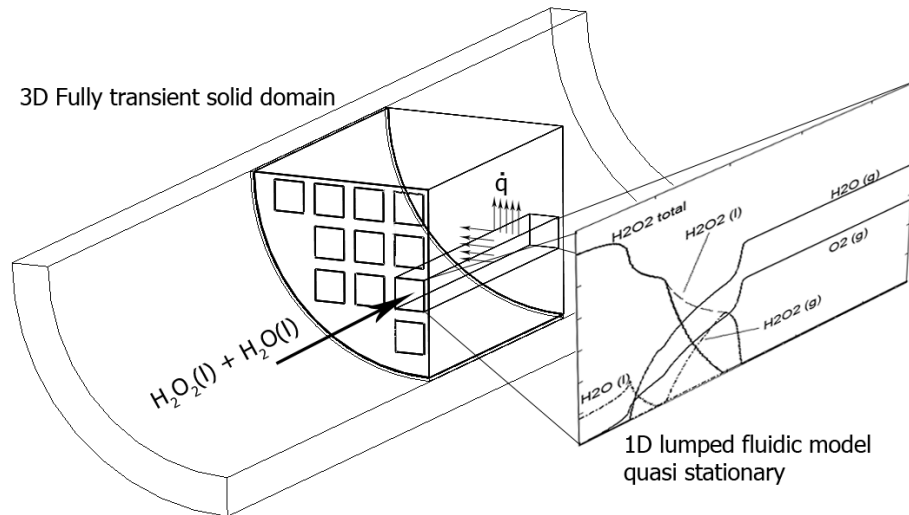

Figure 19 Coupling schematics of quasi-stationary lumped parameter model evaluated for each channel acting as boundary condition for transient solid domain simulation

Since each models boundary condition is determined by the result of the other model, it is intuitively that this simulation can only be solved iteratively. This is accomplished by the following solving procedure, outlined for one time step:

1) Starting with an adiabatic one-dimensional lumped parameter fluid analysis solved in MATLAB for each channel.

2) The resulting temperatures as function of monolith position z are transferred to the structural model in the FEM solver and act as convective boundary condition on the walls of each corresponding channel. The film coefficients are readily determined by the fluid dynamic model.

3) The structural domain model is solved and the results are transferred to MATLAB, where Q_{loss} (Table 5) is calculated using previous iteration results and the structural thermal field from the FEM solver. A film coefficient is derived from results of previous iteration.

4) The lumped parameter fluid dynamic model is solved in MATLAB for each channel, incorporating Q_{loss}.

5…i-1)   Steps 2 to 4 are repeated until convergence, defined as the sum of the square errors of chemical temperature distributions of actual to previous iteration, is achieved.

i) Results are stored and used as initial condition for the next time step.

The block diagram in Figure 20 shows the fully transient simulation procedure.

Inlet flow condition
T_i, p_i, m_i H_2O_2 Conc.

Time=0...Endtime by interval t_{step}

MATLAB ODE Solver

Channel No. = 1

Determining physical fluid/gas properties

Determining regime of physical state of mixture (evaporation plateaus)

Decomposition balance equations for all species

$$\frac{dn}{dz} = -\frac{k}{u}n$$

Determining temperature of fluid/gas $T_{(t)}$ incorporating thermal losses determined by FEM analysis of previous iteration

1D flow model, determining fluid/gas valocities and film coefficent

Channel No. = Max ?   No   Yes

solving for dz (ODE15s solver for stiff equations)

Increase Channel No.

Increase Time by t_{step}

$\dot{Q}_{loss}$
T_{Wall}

$T_{(x, Ch No.)}$
$\alpha_{(v(x), Ch No.)}$

FEM Thermal analysis

3D thermal model, channel wall boundary conditions (hotgas temperature and film coefficient) from Matlab solver

Determining wall temperature distribution and thermal losses for each channel

$\dot{Q}_{loss}$
T_{Wall}

$(\Delta T_{Error})^2 < Limit$?   No   Yes

Initial condition for structural analysis

Stored structural temperatur from evaluation (Time-t_{step})

Storing structural temperature Result to be used as initial condition in succeeding timestep

Time=Endtime?   No   Yes

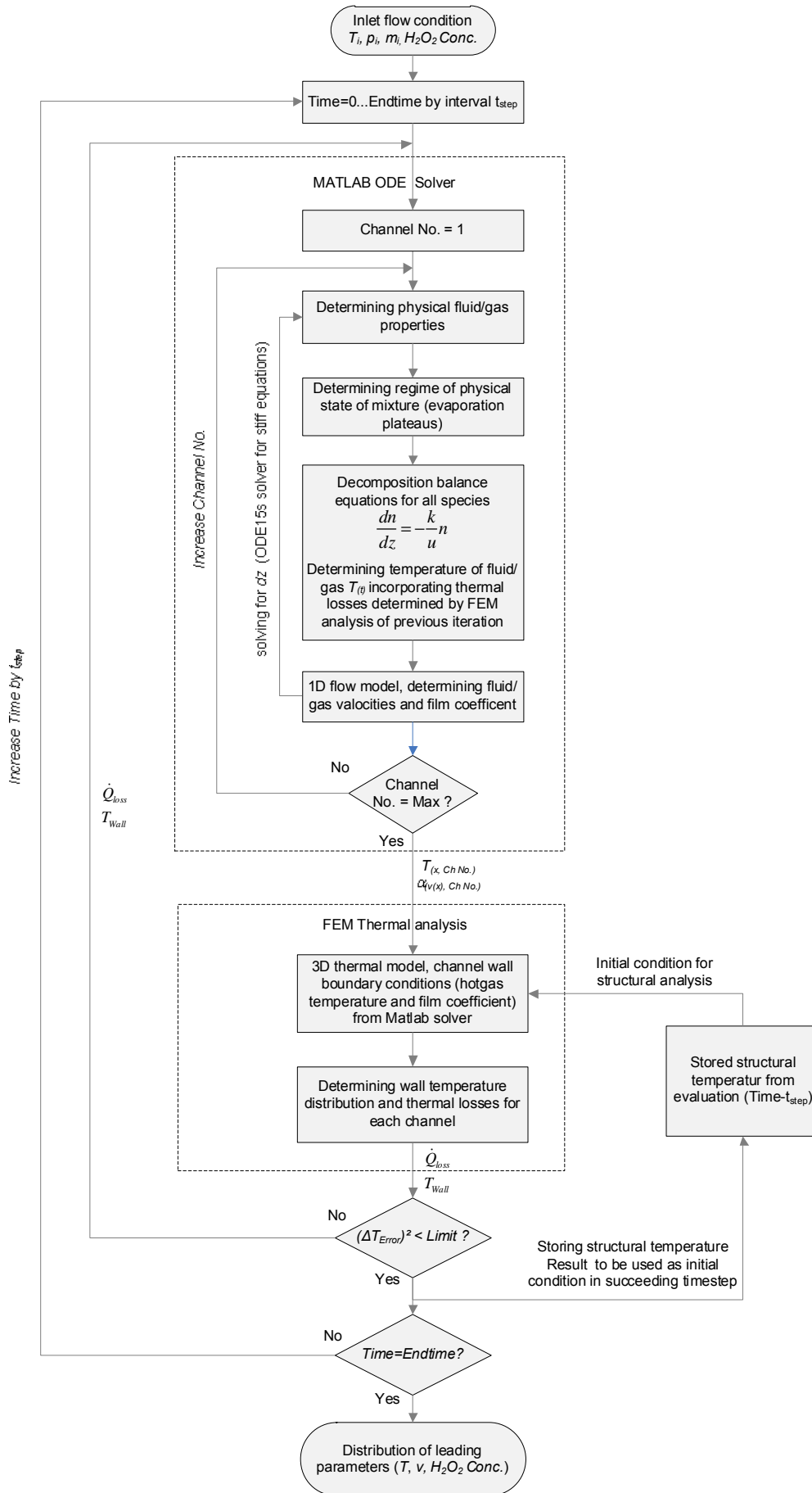Distribution of leading parameters (T, v, H_2O_2 Conc.)

Figure 20 Flow diagram of transient decomposition simulation

Another way of representing the coupling of the models is to illustrate the spatial and temporal calculation points. Figure 21 shows the points of calculation in temporal (*n-1, n, n+1,…*) and spatial dimension (*j-1, j, j+1,…*). Black markers refer to calculation points of the fluid-chemical domain, whereas grey markers indicate the structural domain. The arrows indicate integration direction in the fluid-chemical model.

The calculation of the system at time *n* bases on the solution of the structural model at time *n-1*. The fluid model at point (*n, j*) is dependent on both the fluid model (*n, j-1*) and the structural domain points (*n, j-1*), (*n, j*) and (*n, j+1*). Once the system has reached convergence at time *n*, the system is solved for *n+1*, based on the structural solution at *n*.
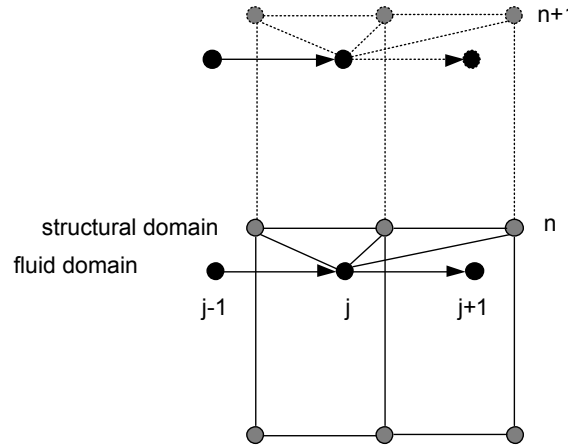

Figure 21 Calculation points of transient decomposition simulation

2.3.5. Simulation results

Table 6 Simulation parameters

Parameter	Value	Dimension	Comment
x_{H2O2}	87.5	%	Hydrogen peroxide weight concentration
p_c	$12 \cdot 10^5$	Pa	System pressure
No. of channels	44	-	Number of channels
$\dot{m}$	0.3	g s^{-1}	Mass flow of diluted hydrogen peroxide
R_M	$6.25 \cdot 10^{-3}$	m	Monolith radius
L_M	$20.0 \cdot 10^{-3}$	m	Monolith length
a_M	$1.1 \cdot 10^{-3}$	m	Channel side wall
d_w	$0.39 \cdot 10^{-3}$	m	Monolith minimum wall thickness
s_{gap}	$0.12 \cdot 10^{-3}$	m	Gap between monolith and chamber cladding
$s_{cladding}$	$1.28 \cdot 10^{-3}$	m	Decomposition chamber wall thickness
α_S	1	W m^{-2} K^{-1}	Insulated decomposition chamber
E_a	$50.2 \cdot 10^3$	J mol^{-1}	Energy of activation for hydrogen peroxide in the presence catalytic material MnO$_x$
A_0	$1.1 \cdot 10^8$	s^{-1}	Pre-exponential factor[1]
Gap material (λ_2)	Water Vapor	-	Good thermal insulation of the monolith
T_{init}	295	K	Initial temperature of monolith and structure
$T_{init, H2O2}$	295	K	Temperature of injected fluid at catalyst face

Annotations: [1] The pre-exponential factor is experimentally determined as outlined in section 2.3.6.4.

This section summarizes selected results for a simulation with input parameters resembling the standard experimental investigation chamber described in section 4.2. These input parameters are summarized in Table 6.

Figure 22 shows the structural temperature distribution for the near stationary case for a $L_M = 20$ mm catalyst after 200 seconds, corresponding to the final stage of a standard catalyst test. As can be seen for the chemical distributions displayed in Figure 23, all the hydrogen peroxide is decomposed within a narrow zone near the entrance of the catalyst for the stationary case. At this stage, the spatial temperature transient from initial low temperatures to high temperatures occurs within this zone, as can be seen by the temperature distribution in Figure 24. In this plot, the fluid temperature of one centrally located channel (No. 1 in Figure 17, right) is compared to the structural temperature of the channel surface, averaged over the channels perimeter.
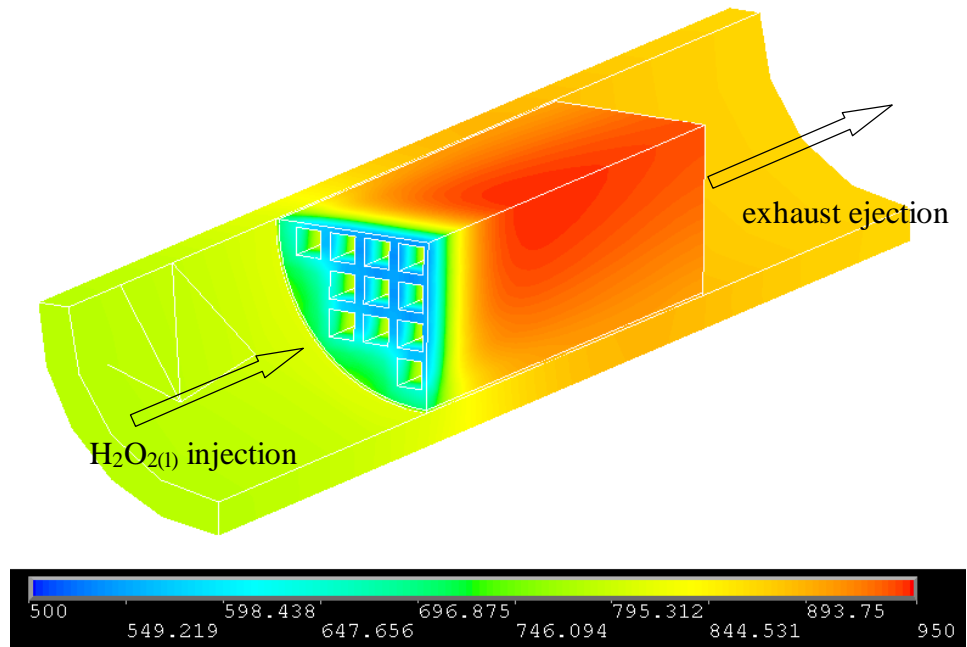

Figure 22 Solid temperature distribution of catalyst and chamber wall, $L_M = 20$ mm, $R_M = 6.25$ mm. Temperatures are in Kelvin

The completion of the decomposition just downstream of the inlet region is however only the case in the stationary case, when the structural temperature of the catalyst is high and heat loss of the fluid to the structure is accordingly small. In the transient case, the region of temperature transient can be significantly further downstream and decomposition might not be completed within the catalyst channel upstream of the catalysts exit.
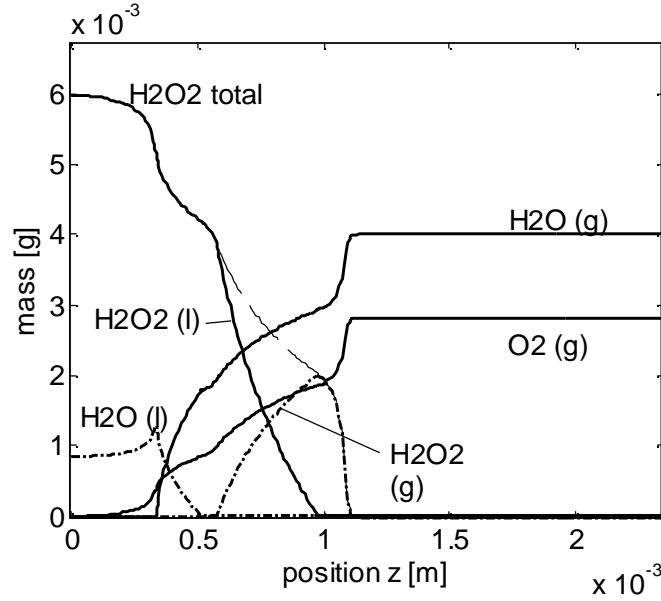
Figure 23 Mass distribution along the channel axial position in the region just downstream of injection ($z = 0$), physical state of species is indicated in brackets

Figure 24 compares the temperature solution of the lumped fluidic model of a centrally located channel to the solid domain channel wall temperature, averaged over the channels perimeter. Comparison to the adiabatic solution found by Zhou and Hitt [55] yields good agreement to the temperature profile they presented for micro-catalysts obeying Arrhenius law.
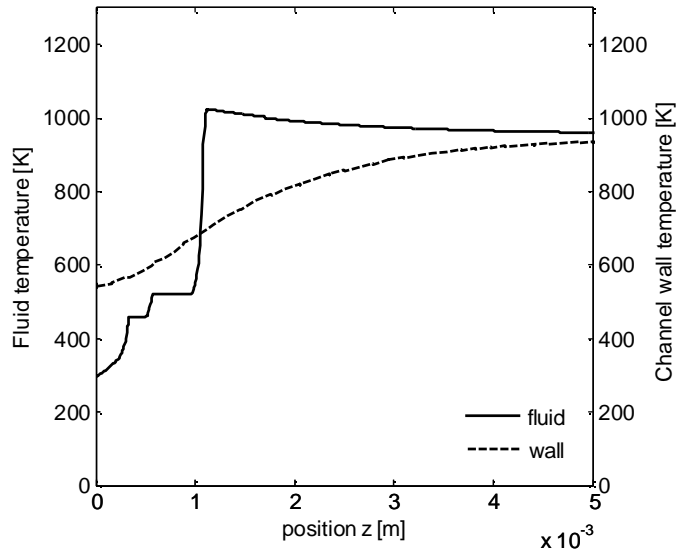

Figure 24 Fluid temperature of centrally located channel (solid line) compared to surface temperature of channel side wall (dashed line), simulation regimes indicated: I: temperature increase, II: evaporation

It is interesting to notice the entrance section of the monolith, where axial heat flux within the solid domain cause the monolith structures temperature to be above the entering fluid temperature. This leads to a preheating of the incoming hydrogen peroxide, causing both an acceleration of the decomposition process and an increase of peak decomposition temperature

above the theoretical decomposition temperature since initial hydrogen peroxide temperature is increased before decomposition occurs.

Figure 25 shows results from a fully transient simulation at time steps of 1.5 s and 5.25 s. The figures compare the converged results for central channel 1 to the structural wall temperature of the corresponding channel. The results show rapid decomposition of the hydrogen peroxide being fully completed within the entrance section of the catalyst. For small t, the monolith structure is then cold compared to the decomposition products. Convective cooling with large thermal fluxes, caused by high flow velocities in the order of meters per second, the large internal channel surface area compared to cross section and the excessive temperature difference lead to significant temperature decrease before the fluid exits the channel. In the case of $t < 1.5$ s, back condensation may occur (not modeled in this simulation) with mixing and re-evaporation phenomena downstream of the catalyst. At this stage, the measured mean temperature resembles the evaporation temperature of water.
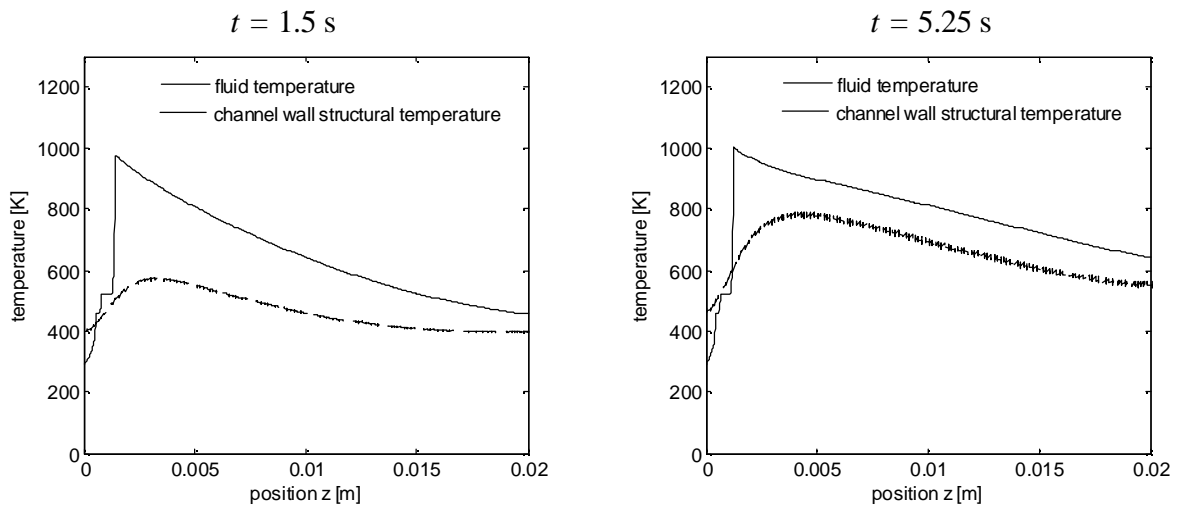

Figure 25 Temperature distribution and solid domain response at different simulation times t

Figure 25 shows the favorable impact of shortening catalyst length on transition time, as long as chemical reaction remains fully completed upstream of the catalyst exit face.

The evolution of structural temperature fields in the transient case is shown for selected time steps in Figure 26. Due to large heat flux into the monolith structure, the catalysts temperature rapidly increases in time, leading to decreased cooling of the exhaust gas stream and to an increased mean exit temperature.
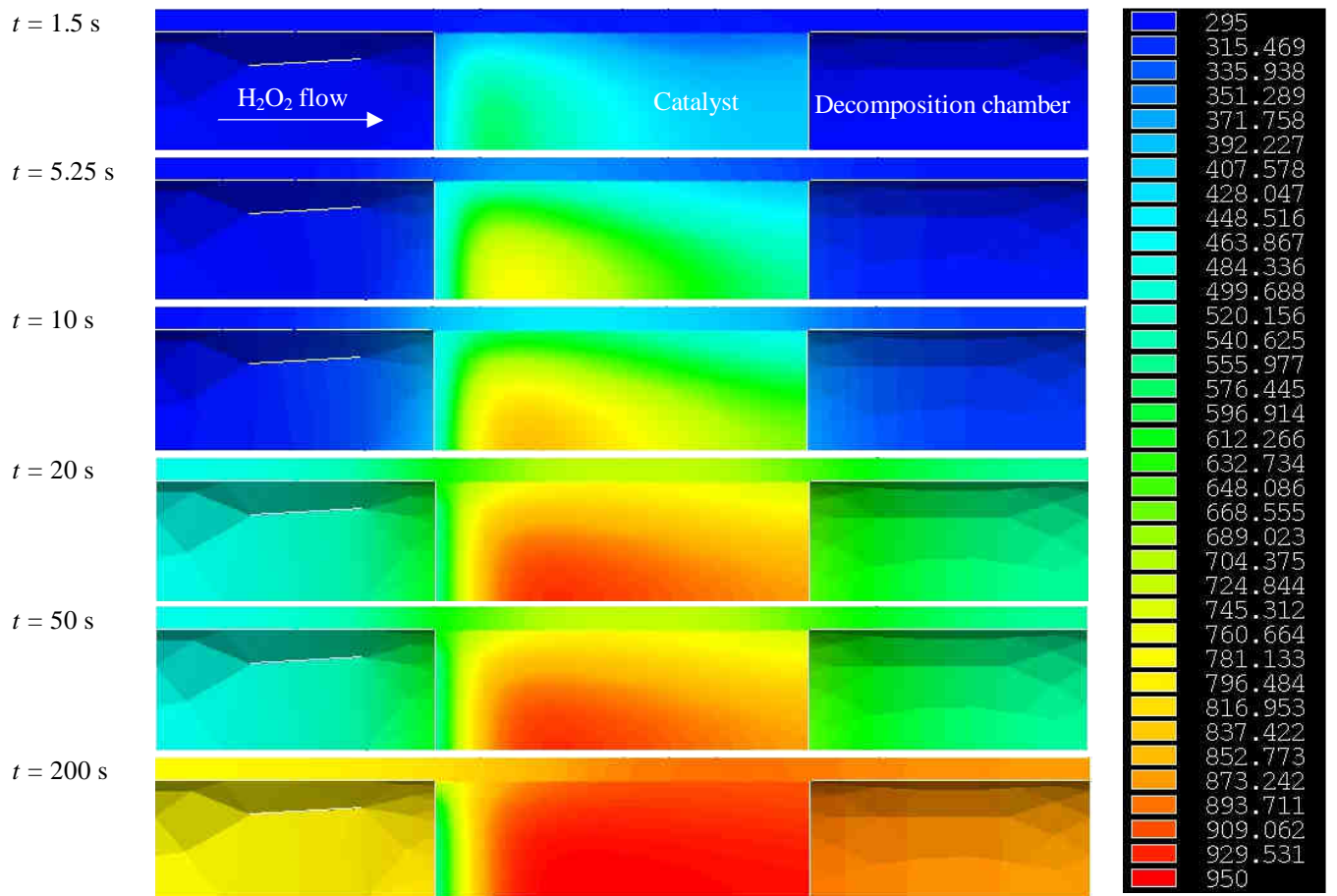
Figure 26 Evolution of structural temperature fields in a transient analysis

2.3.6. Comparison to experimental results

In this section, simulation results are compared to experimental results. A description of the experimental setup, test procedures and data acquisition is found in section 4.2.

Figure 27 shows a comparison of the simulation results to experimental data from four successive tests with catalyst C2-1 of L_M = 10 mm length. Experimental and simulated temperatures are given for centrally located channels. The general good accordance in both the transient and the stationary case validates the modeling efforts presented above. The exit temperatures are close to the theoretically achievable decomposition temperature of T_{dec} = 695.23 °C for 87.7 wt.% concentrated hydrogen peroxide, which is the simulated value for adiabatic conditions (not shown in Figure 27) or can be calculated by NASA chemical equilibrium code CEA for full decomposition [92]. To avoid influences from cold chamber walls on the temperature measurements, thermal shielding of the thermocouple has been employed in the measurements as discussed in section 4.2.6.1. The validation accuracy however remains limited by the experimental test-to-test variation.
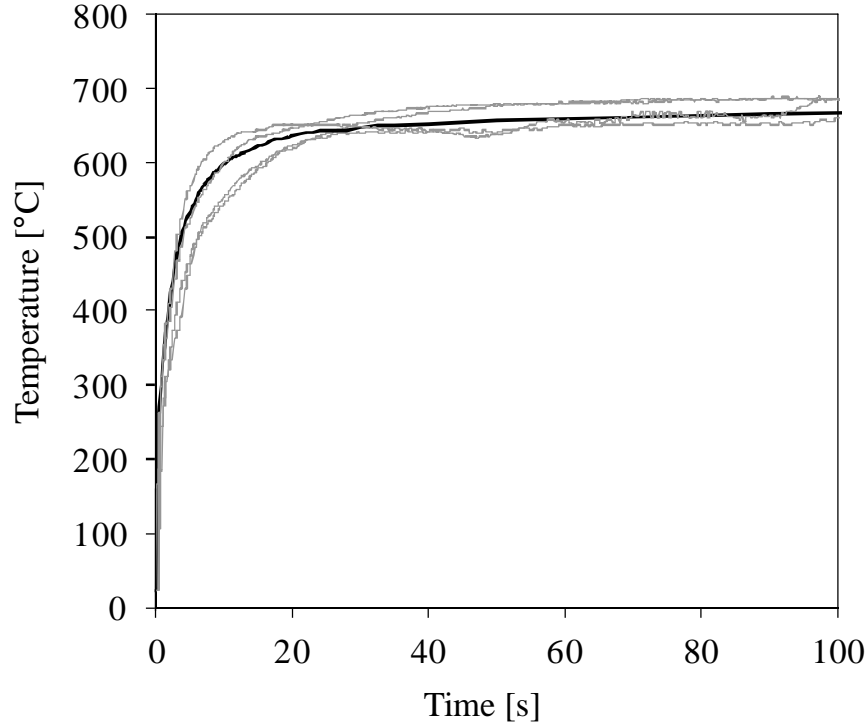
Figure 27 Experimentally determined exhaust temperature time traces (solid gray lines) compared to simulation results: $A_0 = 10^8 \, s^{-1}$ (solid black line) for catalyst length $L_M = 10$ mm.

One aspect which appears in both the simulation results and in the experimental data is especially worth emphasizing: the results for the channels in the center of the catalyst indicate final decomposition temperatures higher than the ideal adiabatic temperature (as calculated by NASA CEA code to be $T_{dec} = 670.7$ °C for *86.7* wt.% hydrogen peroxide [92]). Ventura et al. have measured the temperature of decomposed hydrogen peroxide as a function of the hydrogen peroxide inlet temperature [112]. Their measurement indicate that that final decomposition temperatures increase nearly 1.6 °C for every 1.0 °C increase in the inlet temperature of the liquid hydrogen peroxide, caused by temperature dependency of physical properties. Furthermore, an increased decomposition temperature has been experimentally observed as described in the experimental section 4.2.4.2 for a thermocouple located just downstream of the centrally located channels. These findings can be explained in this simulation by two effects caused by the interaction of fluid dynamical and structural domain:

The axial heat flux within the monolith from high temperature exit region to low temperature entrance region of the fluid, leads to a certain preheating of the liquid hydrogen peroxide solution in the entrance region. Thus, hydrogen peroxide temperature can be higher before decomposition than the temperature of the fluid entering the monolith. Temperature increase from decomposition will then add a given temperature difference to this preheated temperature.

Radial inhomogeneity of heat fluxes, both from the fluid to the catalyst walls and vice versa lead to significant lower temperatures for fluids in channels located near the perimeter of the catalyst, compared to centrally located ones. Centrally located channels experience a heat flux input into the fluid near the entrance while featuring significant smaller losses in temperature

at the high temperature exit region, where the temperature gradient to cold structure is small compared to the one for channels located in the monolith outer region. This way, a certain heat flux from channels in the perimeter region of the catalyst to centrally located channels is accomplished, leading to high central exit temperatures and temperatures well below the adiabatic case for channels located at the outer regions of the catalyst. Thus, the net heat flux for centrally located channels is orientated towards the fluid, while in opposite direction for channels located further outwards. The caloric mean temperature approaches the ideal adiabatic decomposition temperature for the stationary case, elucidating the overall conservation of energy. The existence of such a significant radial temperature gradient is investigated in detail both by simulation efforts in section 2.3.6.5 and experimentally in section 0.
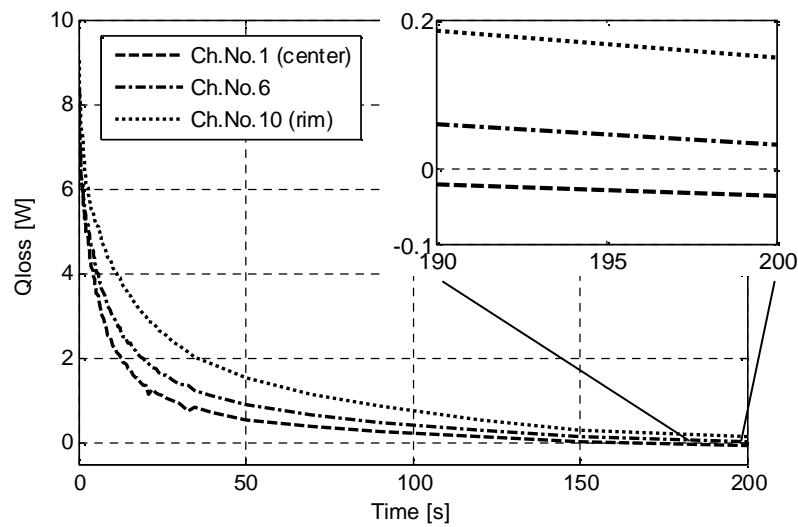

Figure 28 Transient total heat loss for selected channels over the catalyst length as a function of time

Figure 28 shows the total heat flux as a function of time for selected channels, integrated over the entire channel surface. A positive value indicates "losses", i.e. heat flux from the fluid into the monolith structure. Heat losses are largest for the transient time period, as structural temperatures remain low in the initial phase, compared to hot gaseous temperatures. For the near stationary condition, this heat flux, which is the sum of all heat fluxes from the fluid and into the fluid of a channel, becomes negative for the centrally located channel as shown in the detailed view, indicating a net heat flux from the structure into the fluid. In this case overheating of the exhaust, surpassing the ideal decomposition temperature, is occurring for this channel. For the channel located at the catalysts perimeter, the stationary heat flux approaches a positive value, thus energy losses from the fluid into the structure. The negative heat flux for the centrally located channel can explain, as discussed above, decomposition temperatures locally exceeding the ideal adiabatic decomposition temperature.

The mean heat flux over all channels remains positive and is equal to the heat loss caused by the heat sinks of monolith and decomposition chamber structure.

The heat flux density from the fluid into the monolith structure averaged over all channels shows a short, significant peak to $\dot{q} \approx 100$ kW m^{-2} and is quickly reduced to $\dot{q} \approx 6.25$ kW m^{-2}

for the near stationary case at $t = 200$ s. Although experimental setups vary significantly, the stationary case can be compared to measurements performed by Satterfield and Audibert [113], who determined heat fluxes in a variety of experiments, inserting a catalyst into a hydrogen peroxide reservoir, to range from $\dot{q} \approx 0.95$ kW m^{-2} to $\dot{q} \approx 2.4$ kW m^{-2}. However, these experiments have been performed in the absence of a forced convective flow, which significantly increases the heat loss in the flow reactor investigated in this work.

2.3.6.1.   Impact of catalyst length on decomposition performance

The simulation was used to investigate the impact of a variety of catalyst design parameters such as thermal carrier material properties and geometrical properties on decomposition performance, with a special focus on the transitional behavior of the decomposition after cold start. Figure 29 shows a sample analysis regarding the length of the catalysts. In this simulation, the transitional decomposition temperatures for centrally located channels are compared for two different catalysts with length $L_M = 20$ mm and $L_M = 10$ mm. The pre-exponential factor used for the simulation was chosen in accordance to the experimentally for this catalyst configuration determined factor (section 2.3.6.4). This is of special importance, since the ratio of catalyst length and timescale of chemical reaction determine whether the decomposition is completed before the fluid exits the catalyst and necessarily sets a lower limit for catalyst length.
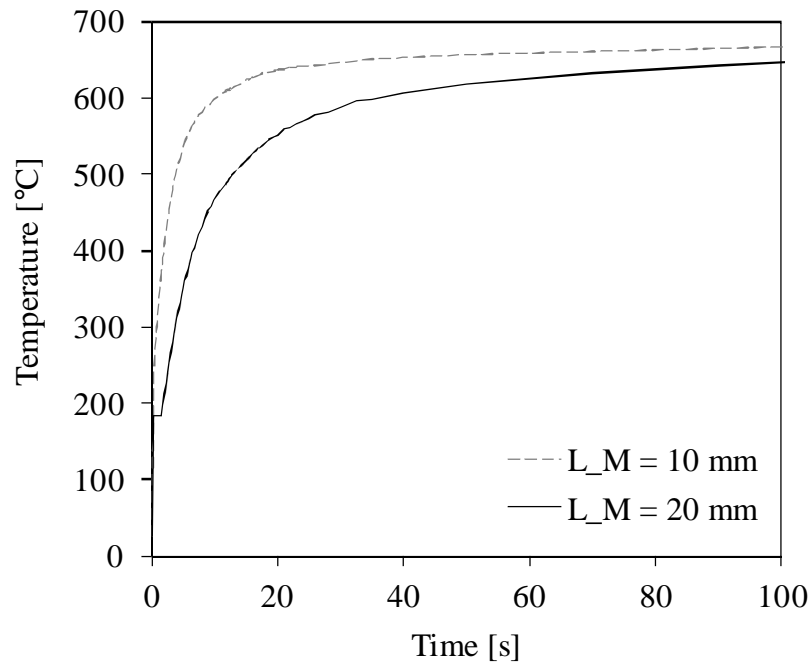

Figure 29 Comparison of simulated exhaust temperature profiles for different catalyst lengths

Figure 29 shows the favorable impact of shortening the monolith length from $L_M = 20$ mm to $L_M = 10$ mm due to the reduction of large internal surface area in the region of high temperature flow, preventing excessive heat losses to the catalyst structure in the early transitional stage. In the example above, reduction of the transition times, that is the time to

surpass $T_{dec} = 500$ °C, are reduced from $t_{500} = 12.75$ s for the $L_M = 20$ mm catalyst to $t_{500} = 3.85$ s for the $L_M = 10$ mm catalyst. This compares to an experimentally found decrease in mean transition times from $t_{500} = 18.85$ s for $L_M = 20$ mm catalysts to $t_{500} = 8.72$ s for $L_M = 10$ mm monoliths (Figure 106). While the relative difference corresponds well to the simulated results, these experimental absolute transition times are larger for both configurations compared to the simulation results. This can be explained by a certain error afflicted to the experimental measurement due to the experimental setup, as discussed in section 4.2.6.1. Transition time measurements in an advanced experimental setup revealed transition times of $t_{500} = 1.56$ s for a $L_M = 10$ mm monolith.

The simulation was thus able to accurately predict a reduction in transition times for shorter catalysts which could then be verified experimentally. Another design change predicting favorable impact on transient performance was the reduction of thermal mass by reducing monolith wall thickness, which was experimentally shown in section 4.4.3.6.

2.3.6.2.   Impact of thermal mass of decomposition chamber

The simulation presented in this chapter allows for the investigation of the impact of design parameters such as decomposition chamber mass on decomposition performance. This allows for a direct input to the design of a high performance decomposition chamber with particular focus on reducing start-up times.

The input parameters for the simulations presented in this chapter have been chosen to match the experimental decomposition chambers investigated in section 4.2.6.6.

Figure 30 shows simulated results for two different chamber designs. No flanges or differences other than chamber wall thickness are modeled for simplicity purpose. The simulated "Chamber L" is modeled with a steel tube thickness of 13.5 mm, matching the experimental chamber with equal designation. The chamber designated "Chamber S" in the experimental setup matches the standard decomposition chamber used for all simulation purposes with 1.28 mm thickness of the cylindrical steel tube. As the large thermal mass of the increased chamber wall thickness leads to a significant thermal gradient within the catalyst, temperatures from a channel close to the chamber wall (denoted number 11 in Figure 17) at the catalyst exit plane are plotted in addition to the near central axis exhaust (denoted number 1 in Figure 17). Since temperatures are lowest in the channels located at the catalysts perimeter, these act as the limiting factor in the transient behavior and are therefore of great interest.

A comparison to the experimental data in Figure 122 shows an overestimation of the centrally located temperatures, although the general trend of significantly lower exit temperatures for the large chamber is reproduced. If one additionally allows a certain mixing of the central exhaust gas with the flow from the larger number of outer channels (not modeled), one will find a significantly reduced temperature downstream of the catalyst which is located

somewhere in between the two simulated results obtained for the central and outer channel exhaust temperature.

Even significant deviations in the comparison to experimental results are present due to the utilization of a largely simplified solid model structure and uncertainties in the thermal contact properties between catalyst and chamber wall, the strong impact of increasing thermal mass on decomposition performance according to the trend in the experimental results is apparent. This shows the significant impact of thermal mass of the decomposition chamber on decomposition performance.
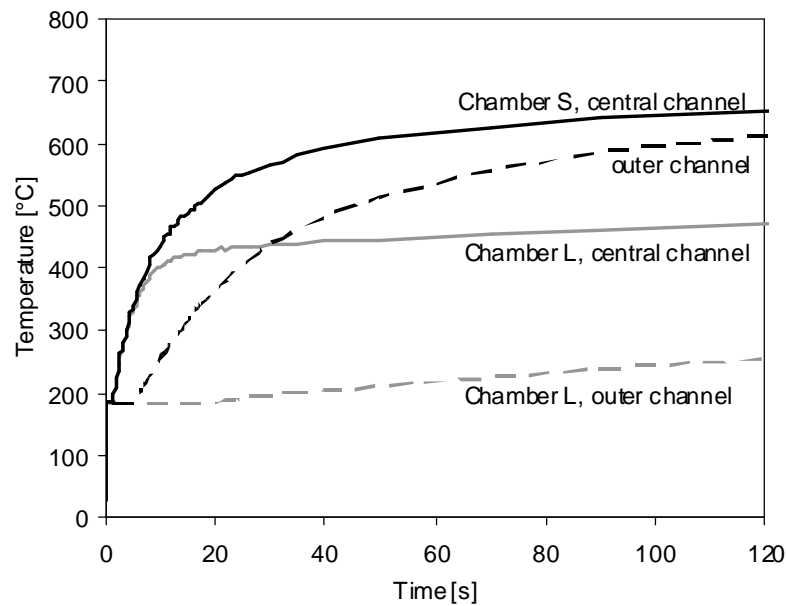

Figure 30 Simulated exhaust temperature profiles for different chamber designs for a central channel and a channel close to the catalysts perimeter close to the decomposition wall

2.3.6.3. Preheated catalyst

In the case of a preheated catalyst, the catalyst is at high temperature while hydrogen peroxide is injected at ambient temperature. In this case, hydrogen peroxide entering the monolith in liquid state is additionally heated, decomposition rates are increased, and losses are reduced as the difference in temperature from hot gas to chamber wall is decreased. The behavior of a catalyst in preheated configuration has been experimentally investigated in section 4.2.6.7.

Figure 31, left hand side, shows the initial transient result for a catalyst which was modeled with initial temperature of 300 °C, compared to a non preheated catalyst (right hand side). As expected, the results indicate strongly reduced transition times for preheated catalysts, compared to the case of initial ambient temperature (22 °C). A comparison to the experimental data presented in section 4.2.6.7 shows the good agreement of the simulation results regarding the greatly reduced transition times for the preheated catalyst.
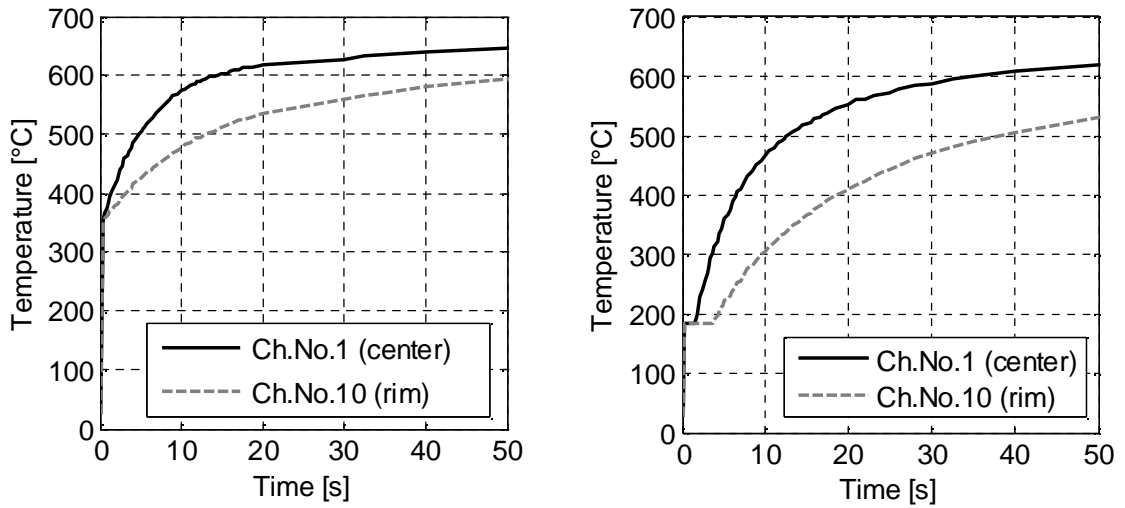
Figure 31 Simulated preheated start-up behavior (left) and non-preheated case (right), catalyst length $L_M = 20$ mm

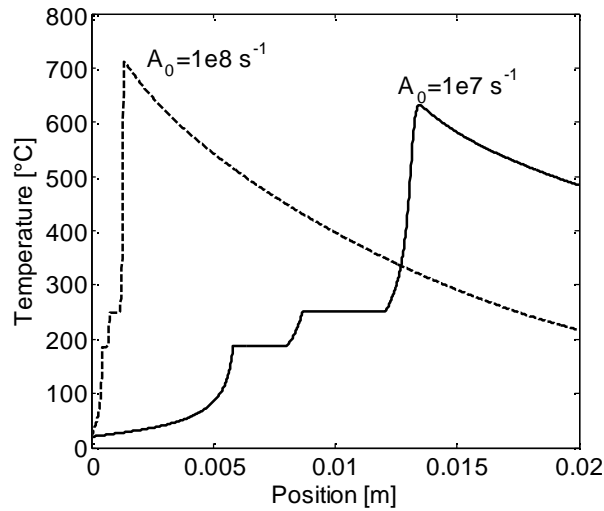#### 2.3.6.4. Impact of frequency factor – overloading results

Figure 32 Fluid temperature distribution of central channel 1 for different frequency factors in the initial transient case as a function of axial position

The order of magnitude of the frequency factor allows identifying two types of reactions: chemically and thermally limited. In the former case, the speed of chemical reaction is slow (A_0 small). In the initial phase, this causes the fluid to exit the catalyst partially undecomposed, which yields low decomposition temperatures. The latter limitation leads to a significant decrease in exhaust temperature due to thermal losses to the initially cold catalyst structure. In this case, full decomposition upstream of the catalyst exit plane takes place. Figure 32 shows the temperature distribution for frequency factors of $A_0 = 10^7$ s^{-1} and $A_0 = 10^8$ s^{-1} for the centrally located channel No. 1 (Figure 17), five seconds after hydrogen peroxide injection. Full decomposition upstream of the catalyst exit plane takes place in both cases. With increasing time, the region of temperature transition moves further upstream, and the

increasing structural temperature of the chamber walls leads to a decrease in the heat loss of the exhaust gases, yielding higher exit temperatures.

An estimation of the order of the frequency factor for the given decomposition configuration can be gained by investigation of the overloading behavior of the catalyst. Since the simulation predicts a rapid drop in catalyst performance for surpassing a certain mass flow threshold, depending on the ratio of rate of decomposition to mass flow, a certain conclusion on the frequency factor can be drawn from experimental overloading data. Such experimental overloading experiments have been conducted and are described in section 0 using the test apparatus described in section 4.2.1. The results gained are reproduced in Figure 33 and are compared to results from simulations for different frequency factors.
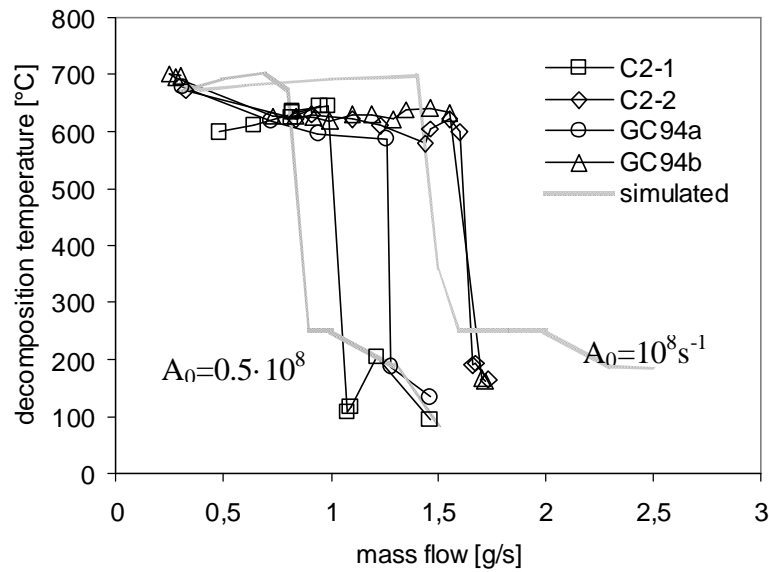

Figure 33 Experimental found overloading effect of catalysts (solid line) compared to simulated overloading for two different frequency factors as indicated (gray lines)

Although significant deviation in the absolute values of overloading thresholds for the tested catalysts exists, the rapid drop in exhaust temperature for surpassing the mass flow threshold compares well to the simulated results from the lumped parameter model, indicated by gray lines for frequency factors of $A_0 = 0.5 \cdot 10^8$ s^{-1} and $A_0 = 10^8$ s^{-1}. The deviation of overloading threshold in the experimental data is not related to the type of measurements (ramped (GC94a and GC94b) versus individual (C2-1 and C2-2) tests) or the channel density of the catalyst (304 cpsi for C2-1 and C2-2 versus 635 cpsi for GC94a and GC94b). These procedures are described in detail in section 0.

Figure 34 shows the catalyst structural temperature distributions in the stationary case for different mass flows, including the case of "overloading", all for a frequency factor of $A_0 = 10^8$ s^{-1}. The displacement of high temperature region further downstream for increasing mass flow until complete "overloading" of the catalyst occurs can easily be seen.
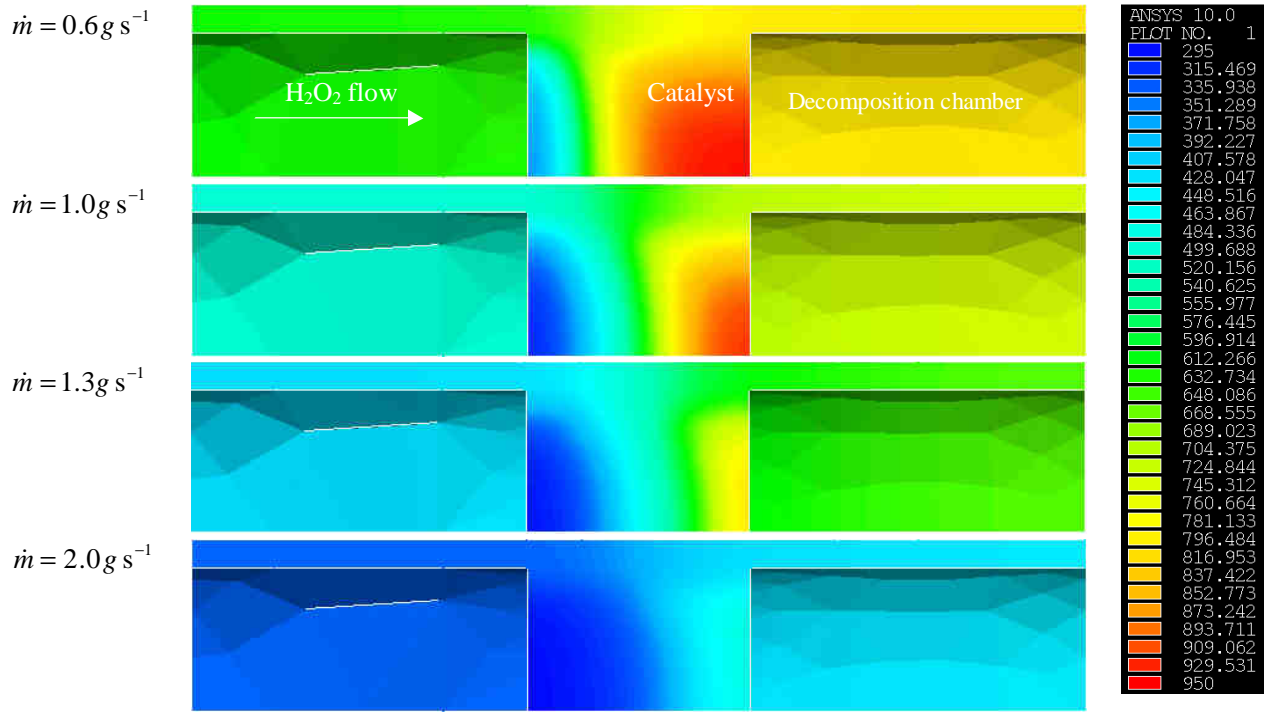
$\dot{m} = 0.6\,g\,\mathrm{s}^{-1}$

$\dot{m} = 1.0\,g\,\mathrm{s}^{-1}$

$\dot{m} = 1.3\,g\,\mathrm{s}^{-1}$

$\dot{m} = 2.0\,g\,\mathrm{s}^{-1}$

Figure 34 Structural temperature fields during overloading of catalysts in Kelvin

2.3.6.5. Radial inhomogenities of exhaust temperature

The simulation predicts the presence of a radial temperature gradient in the catalyst exhaust as discussed in section 2.3.6. This temperature gradient could then be verified by an experimental effort dedicated to measure radial temperature distributions of the catalyst exhaust. The experimental setup and procedure as well as the experimental results are described in section 0.

Figure 35 shows results from the simulation (solid gray line) compared to experimental values (black markers). However, although the general behavior of radial distribution agrees to the experimental results, the gradient in temperature is underestimated by the model. The recorded radial temperature distribution is the product of various factors, with thermal heat losses to the structural domain being one among others. One other potential influence is a non-uniform distribution of the fluid by the injector, with an excess in mass flow for the centrally located channels. The resulting radial exhaust temperature distribution for an inhomogeneous mass flow distribution with an excess in mass flow of a factor of two for the central channel and accordingly small mass flow for the perimeter channels, is shown in Figure 35. The total mass flow through the catalyst is again 0.3 g s^{-1}. This result explains the decrease of exhaust temperature in the outer channels well, but shows again an underestimation of temperature excess in the central exhaust region. This result thus indicates that even in the stationary case, the injection method employed potentially leads to a non-negligible inhomogeneous mass flow distribution.
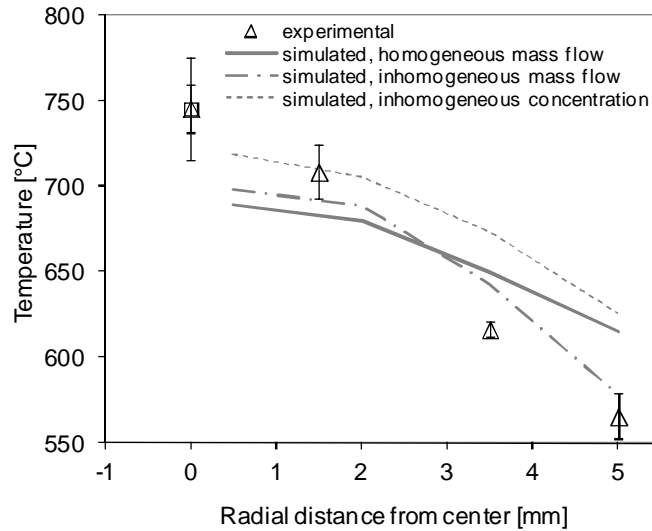
Figure 35 Simulation of radial exhaust temperatures gradient: homogeneous mass flow (solid gray line), inhomogeneous mass flow and concentration (dashed gray lines) compared to experiment (black markers).

The underestimation of central exhaust temperature excess by the simulation can be explained by two assumptions used in the modeling approach: Firstly, the model of the structural domain does not incorporate the injector. As the injector is placed upstream of the catalyst in direct contact to both the catalyst and the chamber structure, a preheating of the injected undecomposed hydrogen peroxide is expected from this configuration, augmenting the effect of temperature increase.

Secondly, besides the nature of the solid domain model, the general underestimation of the temperature excess in the central channels is additionally impacted by an underestimation of thermal conductivity properties. The results displayed in Figure 35 have been determined by neglecting any contribution of the washcoating to the thermal conductivity of the catalyst. Peng and Richardson [114] however showed that applying γ-Al_2O_3 washcoating increased thermal conductivity of their ceramic based catalysts by a factor of two. It can therefore be assumed that the results given present a lower boundary of impact of thermal coupling on decomposition performance.

Another potential explanation of the measured radial temperature inhomogeneity is a potential radial shift in hydrogen peroxide concentration during injection, resulting in higher concentrated central flow and diluted flow near the chamber walls. Results for this scenario are shown in Figure 35 for a maximum shift in concentration of +5 wt.% for the central channel and linear decreasing concentration with increasing radius, labeled "inhomogeneous concentration". The concentration averaged over the entire catalyst remained 87.5 wt.%. While this assumption is able to better explain the temperature excess for the central channels, it does not comply with the temperature drop in the vicinity of the wall.

2.3.7. Concluding remarks

A simulation dedicated to the interaction of a one dimensional fluid-chemical model simulating hydrogen peroxide decomposition and a heterogeneous monolith type catalyst and decomposition chamber has been developed. The simulation allowed determining the concentration of each chemical species, flow parameters and temperature as function of position between monolith entrance and exit plane for each channel in the monolith. A single species evaporation approximation was presented and justified, yielding dedicated evaporation regimes and associated temperature plateaus. The simulation was designed to investigate the impact of decomposition chamber and catalyst structure on the performance of hydrogen peroxide decomposition for miniaturized geometries.

Time and space resolving simulation of the decomposition allowed investigation of the impact of various design parameters on the resulting exhaust gas temperature, which is of great importance for the downstream propulsion system components. These investigations showed the great importance of the thermal mass of the monolith and the heat flux from the fluid to the decomposition chamber structure, especially regarding fast transition times.

The model was found to accurately predict the general transitional and stationary behavior of decomposition exhaust temperatures. The accuracy of the model was verified by comparing the predictions with experimental data. Variation of test parameters such as the catalyst length and initial catalyst temperature were conducted. The predictions of the model for this cases have been found to accurately describe the impact of the given parameter changes and yielded design guidelines for both catalyst and decomposition chamber designs.

Investigation of decomposition behavior as a function of mass flow predicted a rapid decrease in decomposition efficiency for mass flows above a certain threshold. In this case, the catalyst was not able to fully decompose the high hydrogen peroxide load, leading to incomplete evaporation of the exhaust and therefore to a drastic decrease in decomposition temperature below 200 °C. The threshold for "overloading" the given catalyst was found experimentally for catalysts of L_M = 10 mm to occur at mass flows of 1-1.7 g s^{-1}. Comparison to the simulation showed accurate prediction of the sudden temperature drop in case of catalyst overloading and allowed for an estimation of the frequency factor in the Arrhenius equation for the given decomposition configuration.

Another major finding from the model was the prediction of a radial gradient in temperature of the decomposition products downstream of the catalyst. This finding implies significantly reduced temperatures in the outer radial regions, which is of general importance because many experimental setups determine catalyst performance using a centrally located temperature measurement, causing potential overestimations. The existence of such a temperature gradient has been experimentally verified.

3. Thrust chamber
3.2. Thrust chamber introduction

The purpose of the thrust chamber in a staged combustor configuration is to enable and sustain combustion of the injected propellants at high efficiency and accelerate the product exhaust gases to high exhaust velocities by expansion. The heat release from combustion is thus translated into kinetic energy of the exhaust gas, resulting in thrust. For the specific configuration employed, the ability to ignite the combustion process without external help poses an additional requirement to the thrust chamber design.

Thrust chamber geometries are generally driven by thrust level and propellant choice and vary significantly in scale. Exhaustive literature is available on the design of bipropellant thrust chambers [1, 3, 4, 79, 115]. Early design guidelines based on the concept of characteristic length are found in Ref. 116. Large thrust chambers using kerosene as fuel have been employed in combination with liquefied oxygen (LOX) in various launch vehicles, including the Saturn-V main engine (F-1) which used RP-1 as fuel [115]. Ethanol as fuel in combination with LOX was employed in the German A-4 (V-2) missile and in early thrust chambers constructed in both the US and UdSSR [5].

In the specific field of thrust chambers adapted for staged combustor configurations of hydrogen peroxide based bipropellant propulsion, fewer scholars published work on the design of such combustors. Recently published literature includes:

Wernimont and Duran [49] reported on the development of a 1.1 kN thruster utilizing 90 wt.% hydrogen peroxide thruster in combination with kerosene and published results of successful autoignition and combustion at high efficiencies.

Scholars at the Purdue university investigated autoignition behavior of kerosene-hydrogen peroxide mixtures in their efforts of designing a thruster fuelled with green propellants at mass flow rates in the order of kg s^{-1} [46, 47, 48]. Their literature gives both exhaustive reviews on hydrogen peroxide based propulsion efforts and guidelines for combustor design, although at significantly elevated thrust and mass flow levels compared to the design investigated in this thesis.

In their effort of designing a hydrogen peroxide based bipropellant thruster for design thrust levels of 220 N, Musker et al. [51] designed a thrust chamber able to autoignite with kerosene. Published work presents various and evaluates the impact of various different injection techniques based on spray injection.

Ju and Maruta [117] give a review on technology development and research in the emerging field of MEMS based combustor designs. They discuss a variety of approaches and difficulties arising from highly miniaturized combustor design.

3.3. Thermophysical fuel properties
3.3.1. Kerosene Jet A-1

Jet aviation fuels have a long history in air-breathing propulsion, with Jet A-1 being the standard aviation jet fuel worldwide, with exception of the USA. Edwards [118] published a comprehensive historical review on kerosene for jet and rocket propulsion. He stresses the favorable impact of high liquid density of kerosene for storage purposes, as discussed in section 1.2.3.

In his survey of possible high performance propellant combinations, Edwards [118] points to the combination of undecomposed hydrogen peroxide and kerosene as "storable, relatively nontoxic" propellant combination with comparable performance to nitrogen tetroxide and hydrazine.
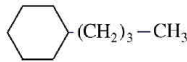
While the precise composition of kerosene varies with different crude oils used in the processing of the fuel, its average composition and physical parameters are given in Table 7, derived from Ref. 119, where a thorough discussion of additional properties and comparison to other fuel specifications can be found.

Table 7 Jet A-1 composition and physical parameters, from Ref. 119

Approx. formula	$C_{11}H_{21}$	Average composition	
H/C ratio	1.91	Aromatics, vol.%	18
Boiling range, K	439-539	Cycloparaffin, vol.%	20
Freezing point, K	222	Paraffins, vol.%	60
Flash point, K	326	Alkenes, vol.%	2
Specific gravity at 289 K	0.81	Sulfur, ppm	490
Critical temperature, K	683		
Critical pressure, MPa	2.344		

Kerosene components can be divided into five major compound classes: paraffins, isoparafins, cycloparaffins, alkenes and aromatics, whose atomic structures are depicted in Table 8.

Table 8 Classes of hydrocarbon compounds, from Ref. 119

Due to its multicomponent composition, kerosene features a two-phase evaporation region, as shown in Figure 36 for Jet A, which shows similar evaporation characteristics as Jet A-1. A more detailed review on vapor pressure correlations and flash point properties of Jet A-1 can be found in Ref. 120.
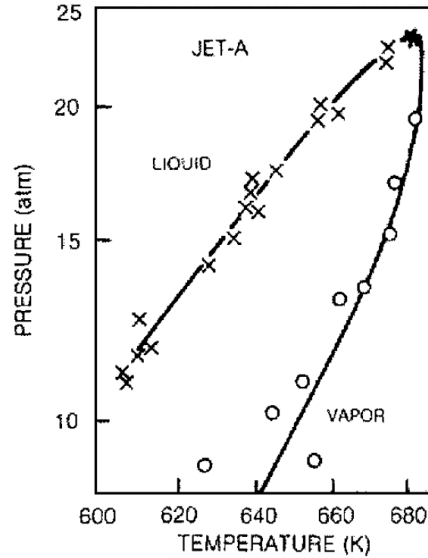

Figure 36 Two-phase evaporation regime of kerosene Jet A [119]

Edwards [118] discussed the problematic of deposition for kerosene above 150 °C. For higher temperatures, thermal oxidative degeneration occurs, since oxygen residuents in the kerosene start to react with hydrocarbons, forming peroxides and eventually deposits. Although this deposition ceases on complete consumption of the oxygen, deposition may lead to clogging of small geometries, as employed in the fuel injector. Thus, cooling of the fuel injector capillary has to be maintained.

3.3.2. Ethanol

Ethanol, or ethyl alcohol, was first used as rocket propellant in the German A-4 (V-2) missile, which employed a 75 % diluted ethanol/water mixture in combination with LOX as oxidizer [118]. The main purpose of diluting the fuel was to lower the combustion temperature and therefore the thermal load to the thrust chamber. Asides from rocket propulsion, ethanol is regarded as a candidate for low-pollution air-breathing propulsion [121, 122, 123, 126].

Ethanol is a hydroxyl as it features a –OH group with corresponding molecular dipole moment. Its physical properties at standard conditions are given in Table 9. Instead of its low freezing point, the pour point temperature, that is the temperature at which ethanol loses its flow characteristic, is given. Additional thermophysical parameters of ethanol are listed in Ref. 108.

Table 9 Ethanol physical parameters

Parameter	Value	Ref.
Formula	C_2H_5OH	[122]
Molecular weight	46	[122]
Boiling point, K	351	[122]
Pour point, K	115.8	[123]
Flash point, K	286-287	[123]
Specific gravity at 293 K, -	0.7908	Append. X.3
Purity, vol. %	99.98	Append. X.3
Vapor pressure at 293 K, kPa	5.87	[108]
Critical temperature, K	514	[108]
Critical pressure, MPa	63	[108]

Ethanol features a low vapor pressure, leading to non-negligible evaporation at standard conditions. Its vapor pressure in bar, expressed as Antoine equation, is given by [108]

$$\log_{10}\left(\frac{p}{\text{bar}}\right) = 5.37229 - \frac{1670.409}{T/\text{K} - 40.191}.$$

(3.1)

A variety of literature on ignition and combustion of ethanol in air is available, as discussed in section 3.4.1, including Ref. 124, 125 and 126.

3.4. Combustion chamber and injector design

The dimensionless Damköhler number [127] can be interpreted as the ratio of timescales of a velocity of chemical reaction and a velocity of diffusion. It can therefore be defined as the ratio of shear layer residence time after mixing and evaporation and the ignition delay

$$\text{Da} = \frac{\tau_r}{\tau_i}.$$

(3.2)

The residence time τ_r is usually expressed by the quotient of a characteristic length scale L and a characteristic velocity u and can be approximated by the residence time within the shear layer τ_{sl} as [128, 129]

$$\tau_r \sim \tau_{sl} = \frac{2L}{u}.$$

(3.3)

Zukoski [131] and Zukoski and Marble [132, 133] proposed a simple relation of timescales as limit for flame blowoff as

$$\frac{u\tau_i}{L} = 1.\qquad\qquad(3.4)$$

With u_g being the gas velocity, τ_i the ignition time and L a characteristic length, usually the length of the recirculation zone. Using Eq. (3.3), this criterion becomes essentially Da = 2.
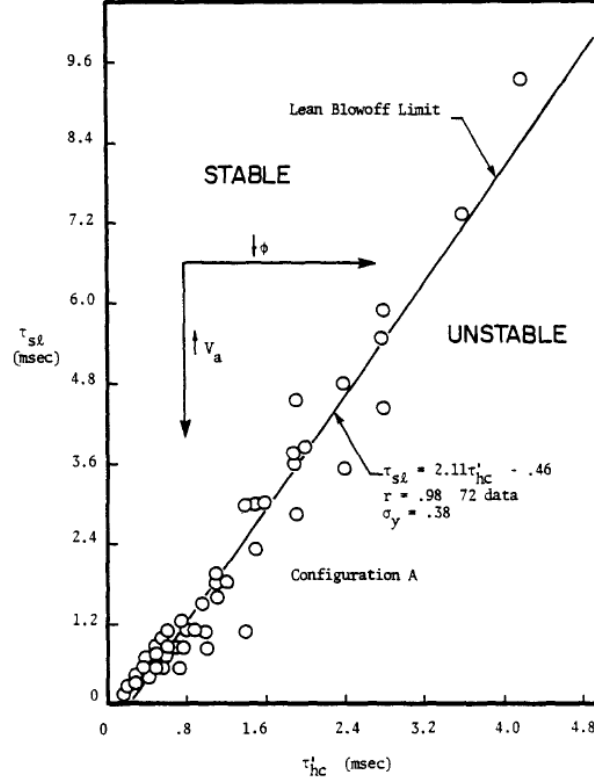

Figure 37 Stable flame as a function of ratio of shear layer residence time and mixing time [128]

Plee and Mellor [128] conducted early studies on bluff body flame stabilization based on ignition delay and mixing times. In this study, the ignition delay times were determined from an experimentally determined overall rate of reaction. Mixing time was defined by a basic estimate of the residence time in the shear layer of the bluff body by Eq. (3.22). Their results are shown in Figure 37 as a function of shear layer residence time τ_{sl} and mixing time τ_{hc}. This points to a limit of Da ~ 2, that is larger shear layer residence time than ignition delay times.

A variety of ignition studies for hydrocarbons in air exists, mostly for lean natural gas turbine combustors and for scramjet combustors [129, 130, 134, 135, 136, 137, 138], investigating ignition delay. The ignition delay is usually expressed as Arrhenius correlation utilizing a global energy of activation, and experimentally fitted coefficients j, m and n. [C_{fu}] refers to the concentration of the fuel [48]

$$\tau_i = A\, e^{\frac{E_a}{RT}} \left[C_{fu} \right]^j \left[O_2 \right]^m p^n .\qquad\qquad(3.5)$$
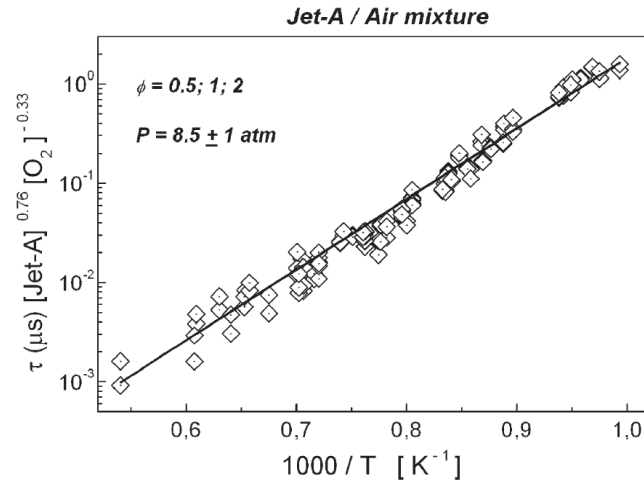
53

Figure 38 Sample ignition delay time plot for Jet A/air mixtures, from Ref. 134

Dean et al. [134] for example derived a correlation of ignition delay from experimental data for Jet-A/air mixtures, shown in Figure 38, where ignition delay is given in seconds

$$\tau_i = 1.41 \cdot 10^{-13} [Jet-A]^{-0.76} [O_2]^{0.33} e^{\frac{16386}{T}} . \tag{3.6}$$

The concentrations [Jet-A] and [O_2] are given in mole m^{-3}. For ignition conditions targeted in this work, ignition delay times in the order of < 10 µs are expected according to Eq. (3.6). Note however that this does not imply mixing and evaporation which may occur at significantly increased timescales.
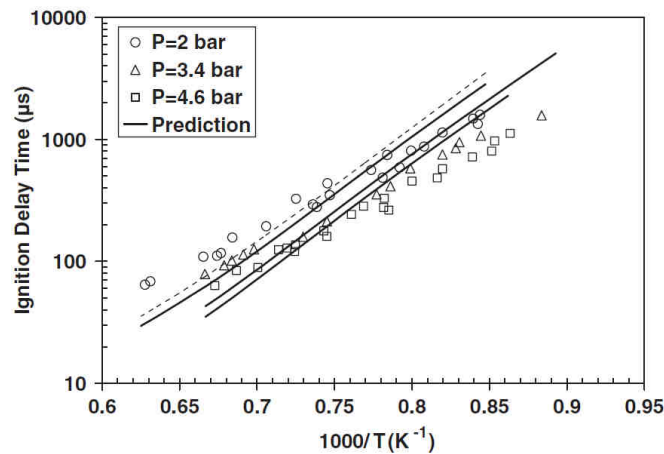

Figure 39 Sample ignition delay time plot for ethanol/air mixtures, from Ref. 126

Data on ethanol ignition characteristics and flames have been published by a variety of scholars [124, 125, 126]. Saxena and Williams [126] for example provide ignition delay times as well as laminar flame speeds as a function of equivalence ratio. Their calculated data is shown in comparison to experimental data in Figure 39. Yates et al. [125] give ignition delay times for ethanol in the expected temperature range in the order of milliseconds. Although test results at decreased pressure are shown in Figure 39 compared to the ignition delay results presented for kerosene, a significant increase in ignition delay is apparent for ethanol, hampering autoignition capability.
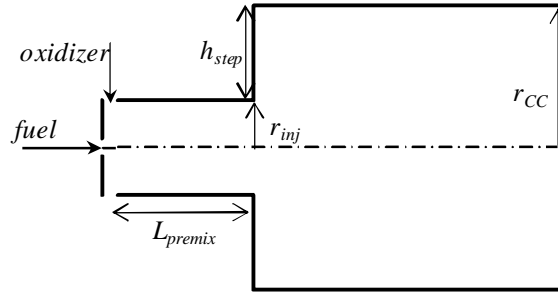
3.4.1. Premixing chamber design

Figure 40 Combustion chamber geometrical parameters

In the premixing chamber, the tangentially injected swirling gaseous oxidizer is mixed with the axially injected liquid fuel. The different injector designs are presented and discussed in the experimental sections of the individual thruster configurations in section 4. The swirl injector designs are additionally described in section 3.6.3.1.

Various authors have pointed to the importance of initial droplet radius for fuel evaporation [4, 140, 141]. In the absence of a gaseous oxidizer stream, expressions based on the Weber number, with the characteristic dimension D_H equal to the injection capillary inner diameter and σ the surface tension of the fuel [178]

$$We = \frac{u_{fu}^2 \rho_{fu} D_H}{\sigma} < 8 \tag{3.7}$$

indicate Rayleigh break-up region [179]. According to Ref. [179], typical droplet dimensions found in this region are 1.9 times the injection orifice diameter, and therefore can be estimated as $d_d \approx 360$ μm. Note however that various sources indicate reduced droplet radii of 1-2 orders of magnitude for incident high velocity gas streams [143, 180, 181, 182, 183, 184, 185, 186, 187].

Kihm et al. [181] compared the validity of simple analytical correlations for mean droplet radii for fluids injected into cross flowing gas streams to experiments. For high speed gas streams, they give the correlation:

$$\bar{r}_d = \frac{65.3}{2} \frac{\mu_{fu}^{\frac{2}{3}} \left(\dfrac{\sigma_{fu}}{\rho_{fu}} \right)^{\frac{1}{3}}}{\left(\rho_{ox} u_{ox,inj}^2 \right)^{\frac{2}{3}}} \tag{3.8}$$

,

where $u_{ox,inj}$ refers to the tangential injection velocity of the oxidizer, which is approximated by the flow velocity within the tangential injection channels. Table 10 shows initial droplet radii for both fuels, in the case of the DM and EBB thruster injector geometries, which satisfy the assumption of cross-injection. Values were derived assuming fuel mixture ratio according to maximum specific impulse at target mass flow rates.

Table 10 Initial droplet radii in µm for injection at maximum mixture ratio, from Eq. (3.8)

	EBB injector	DM injector
Kerosene	59	36
Ethanol	40	25

Li et al. [180] studied diesel fuel droplet injection in a swirl type atomizer with injected high speed air at 500 K to enhance evaporation and found mean droplet diameter in the order of 10 µm.

When determining the droplet residence time within the premixing chamber, a proper choice of flow velocity is necessary. The low speed liquid droplet flow is introduced into the high velocity gaseous oxidizer stream, which accelerates the droplet. The lower boundary for the axial droplet velocity is therefore given by the absence of any acceleration processes without evaporation. In this case, the axial fuel injection velocity is given by fuel injector properties only:

$$u_{fu,ax} = \frac{\dot{m}_{fu}}{\rho_{fu,liq} r_{cap}^2 \pi} \, , \tag{3.9}$$

which is in the order of $u_{fu,ax} \approx 0.7 - 1.3 \, \mathrm{m\,s^{-1}}$ for liquid fuel, depending on injector configuration (described in sections 4) and fuel type, increasing to $u_{fu,ax} \approx 2 - 8 \, \mathrm{m\,s^{-1}}$ for fully evaporated fuel in the premixing chamber without any influence of the oxidizer.

Acceleration of droplets injected into high velocity gas streams has been extensively studied [188, 189, 190] and is usually expressed in terms of the dimensionless drag coefficient C_D. The acceleration $\mathrm{d}u_d/\mathrm{d}t$ of a liquid droplet exposed to a gaseous steam of velocity u_{ox} becomes

$$\frac{\mathrm{d}u_d}{\mathrm{d}t} = \frac{3\rho_{fu}u_{ox}^2}{2r_d \rho_{ox}} C_D \, . \tag{3.10}$$

With experimental studies indicating values for C_D ranging from 2.1-2.9 for droplets injected into air streams [189]. Eq. (3.10) leads to accelerations in the order of $\mathrm{d}u_d/\mathrm{d}t > 10^6 \, \mathrm{m\,s^{-2}}$, which is in accordance to Ref. 189. This points to the fact that droplet residence time should be evaluated by gaseous oxidizer velocities rather than liquid injection velocity, which leads to significantly reduced residence times.

Droplet evaporation can be modeled assuming convective heat transfer from the surrounding gas to the liquid droplet:

$$\dot{q} = \alpha A_d \Delta T \,, \tag{3.11}$$

with the droplet surface A_d varying in time, and the convective heat transfer coefficient determined by Nusselt correlation. The change in mass of the droplet is given by the evaporating mass flow rate:

$$\frac{\mathrm{d}m_d}{\mathrm{d}t} = -\dot{m}_{vap} \,. \tag{3.12}$$

Assuming equilibrium evaporation, the energy balance at the surface of the fuel droplet, based on the heat flux $\dot{Q} = \dot{m}_{vap} h^{vap}$ caused by evaporation at an evaporation mass flow rate $\dot{m}_{vap}$ and positive heat flow from ambient hot gas, described by Fourier's law, becomes

$$\dot{m}_{vap} h^{vap} = 4\pi r_d^2 \alpha \left(T_{ox} - T_{boil,fu} \right) \,. \tag{3.13}$$

The convective heat transfer coefficient is approximated using Dittus-Boelter correlation for fully turbulent flow:

$$\alpha = 0.023 \, \mathrm{Re}^{4/5} \, \mathrm{Pr}^{0.4} \,, \tag{3.14}$$

where the hydraulic diameter appearing in the Reynolds number $\mathrm{Re} = \rho u D_H / \mu$ is $D_H = 2r_d$ and therefore dependent on time. According to the earlier discussion on droplet velocity, the velocity is chosen equal to the oxidizer gas velocity in the premixing chamber.

The mass of a droplet is dependent on the third power of the radius $m = 4\pi \rho r_d^3 / 3$. Eq. (3.13) allows to determine the change in droplet radius

$$\frac{\mathrm{d}r_d}{\mathrm{d}t} = -\frac{\alpha}{\rho_{fu} h^{vap}} \left(T_{ox} - T_{boil} \right) \,, \tag{3.15}$$

where the density ρ_{fu} refers to the liquid density of the droplet. Eq. (3.15) has been derived under the assumption of constant droplet temperature during evaporation, implying vanishing temperature gradients within the droplet. The evolution of droplet radius in time becomes:

$$r_{d(t)} = r_{d(t=0)} - \frac{\alpha}{\rho_{fu} h^{vap}} \left(T_{ox} - T_{boil} \right) t \,. \tag{3.16}$$

Eq. (3.16) can be solved for different initial droplet radii, and time necessary for full evaporation can be determined. Manipulating the time necessary for evaporation with the gas

velocity in the premixing chamber allows for the determination of premixing chamber length necessary to evaporate a droplet with initial radius $r_{d(t=0)}$. The distance necessary for full evaporation is shown in Figure 41 as a function of initial droplet radius in comparison to a different evaporation model described hereafter.

Hill and Peterson [4] presented expressions based on the work of Spalding [139] to estimate droplet evaporation using the droplet drag coefficient [4]

$$C_D = \frac{9}{2}\frac{c_{p,vap}\mu}{\lambda B}, \quad with\ B = \frac{c_{p,vap}(T_{ox}-T_{boil,fu})}{h^{vap}}$$ (3.17)

Assuming isentropic flow, the length for vanishing droplet radius is given by [4]

$$L = r_{d,init}^2 \frac{u_{d,init}\ \dfrac{\rho_{vap}A_C}{\dot{m}}+\dfrac{3C_D}{10}}{2+C_D}\frac{\dot{m}}{A_C}\frac{\rho_l}{\rho}\frac{c_{p,vap}}{\lambda}\frac{1}{\ln(1+B)}$$ (3.18)

Hill and Peterson [4] however stress that the theory utilized to derive Eq. (3.18) does not constitute a quantitatively exact theory but rather gives a guideline on the order of magnitude. To adapt Eq. (3.18), which is only valid for droplet injection in the absence of a hot gaseous stream, to the configuration investigated, the droplet injection velocity $u_{d,init}$ is substituted by the gaseous stream velocity in the premixing chamber, implying instantaneous acceleration of the droplet to gaseous velocities after injection, constituting a worst scenario. Figure 41 shows the necessary premixing chamber length for kerosene injection in the DM injector configuration as a function of initial droplet radius r_d.
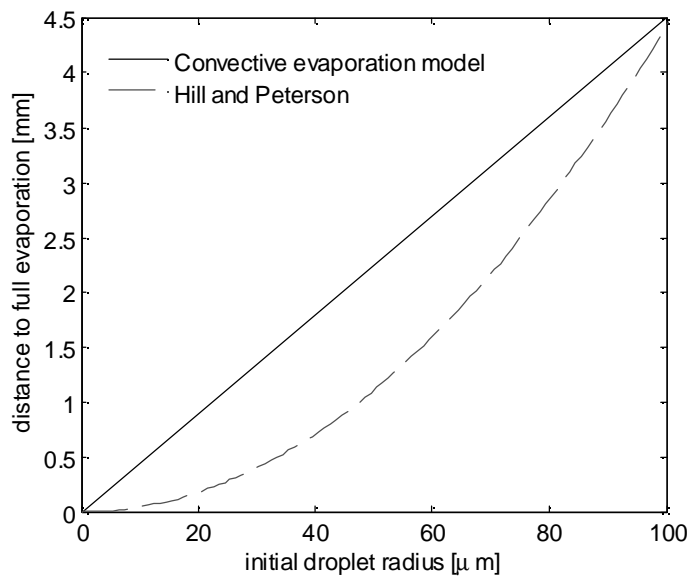

Figure 41 Flow length for full droplet evaporation as a function of initial droplet radius, comparison of models

The results presented in Figure 41 show that both, the convective evaporation model and the droplet evaporation theory by Spalding [139], presented by Hill and Peterson [4], indicate complete droplet evaporation for initial droplet radii expected from Table 10 at distances in the order of millimeters.

Kryukov et al. [140] and Sazhin et al. [141] have studied droplet evaporation according to kinetic droplet evaporation theory, basing the evaporation mass flow j_{lg} on the partial pressures of the liquid-gas mixture, allowing variable droplet temperature.

The evolution of a fuel droplet diameter according to the kinetic droplet theory in case of evaporation is given, similar to Eq. (3.12), by [140, 141]:

$$\frac{\mathrm{d}r_d}{\mathrm{d}t} = -\frac{j_{\mathrm{lg}}}{\rho_l},$$

(3.19)

where ρ_l is the liquid droplet density and j_{lg} is the mass flux density leaving the droplet due to evaporation. The simplest approximation to this mass flux is derived assuming Maxwellian molecular fluxes for both incoming and outgoing fluxes at the temperatures T_∞ and T_{surf} respectively and is known as Hertz-Knudsen-Langmuir correlation [140]:

$$j_{\mathrm{lg}} = \frac{\beta_m}{\sqrt{2\pi R}} \left(\frac{p_s}{\sqrt{T_{surf}}} - \frac{p_\infty}{\sqrt{T_\infty}} \right),$$

(3.20)

where R is the gas constant, p_s refers to the saturated fuel vapor partial pressure at T_s, p_∞ refers to the vapor partial pressure at the free gaseous stream with temperature T_∞. β_m is the evaporation coefficient referring to the proportion of gas particles absorbed by the droplet and remains widely unknown. However, Ref. 140 gives a discussion on reasonable values ranging from $\beta_m = 0.05\text{-}0.5$.

The temperature within the droplet can be approximated, neglecting internal temperature gradients, by [140, 141]

$$\frac{\mathrm{d}T_d}{\mathrm{d}t} = \frac{3}{c_{p,l}\rho_l r_d} \left(\alpha \left(T_\infty - T_{surf} \right) - j_{\mathrm{lg}} h^{vap} \right),$$

(3.21)

with c_p being the specific heat capacity, α is the convective heat coefficient and h^{vap} the enthalpy of evaporation. The partial pressures are determined using Clausius-Clapeyron correlation.

Figure 42 shows the solution regarding droplet radius and temperature for injected kerosene Jet A-1 for an initial droplet radius of 35 μm, according to Table 10 for kerosene Jet A-1 in the DM injector configuration for $\beta_m = 0.5$. This shows full evaporation 1.8 ms after injection.
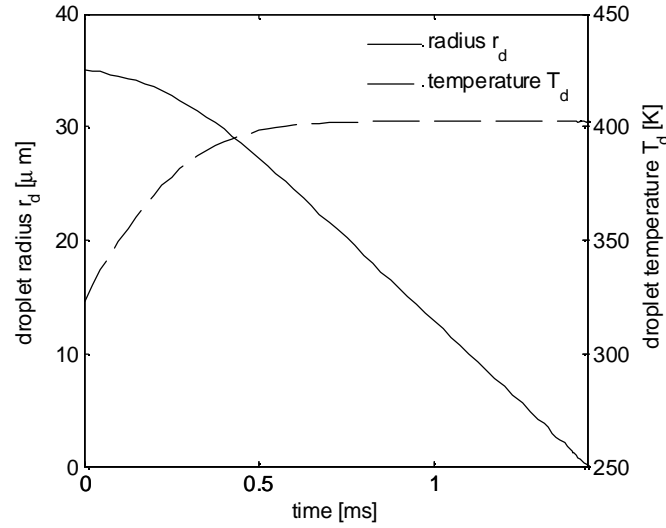
Figure 42 Kerosene Jet A-1 droplet evolution in premixing chamber, based on initial droplet radius $r_d = 36$ µm

The total time for evaporation for kerosene injected into a decomposed hydrogen peroxide exhaust stream is shown in Figure 43 as a function of initial droplet radius. An initial droplet radius of $r_d = 180$ µm would correspond to Rayleigh jet break-up in the absence of a gaseous stream.

Depending on the configuration employed, gaseous oxidizer axial flow velocities range from 60 m s^{-1} in the premixing chamber to ~5 m s^{-1} in the combustion chamber, and would result in residence times one order of magnitude below the evaporation times presented in Figure 43.
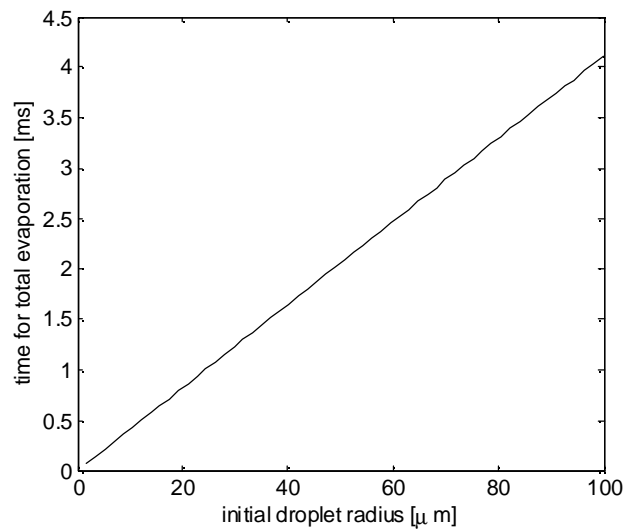
Figure 43 Droplet evaporation time as a function of initial droplet radius

However, since this model predictions differ significantly from previously presented models, the exact regime of operation remains rather uncertain. Therefore, residence times for droplets have been additionally increased using a swirl flow over a backward facing step to guarantee evaporation and combustion of the fuel [142] as well as high temperature backflux to enhance evaporation. This is discussed in the section hereafter. Zuo and Van den Bulck [143] showed the beneficial influence of oxidizer swirl flow on mixing and residence time.

Table 11 gives the premixing chamber lengths for the different combustion chamber geometries leading to successful ignitions in the experimental section 4. However, a successful ignition does not necessarily indicate total evaporation within the premixing chamber, since evaporation can also occur further downstream within the combustion zone in the swirl shear layer or beyond. In addition, total evaporation may not be required, since combustion can also occur as droplet combustion with oxidizer diffusion into the remaining droplet [144, 145].

Table 11 Premixing chamber lengths for different combustion configurations

Configuration	Premixing chamber length [mm]
Ignition chamber	3.4
EBB thruster	1.8
DM thruster	1.4

3.4.2. Backward facing step and swirl flow

The high gaseous velocities of the oxidizer require flame stabilization to avoid blow-off of the flame. In the current thruster design, a backward facing step was designed to induce a turbulent shear layer, stabilizing the flame. This concept has been widely used to stabilize gaseous premixed flames [146, 147, 148]. Recirculation zones induced by the sudden increase in flow cross section facilitate mixing of recirculated hot combustion gases with the injected propellants, increasing mixture temperatures and therefore sustaining stable combustion. Huang and Yang note that:

> *"The flow region of vortex breakdown provides the dominant flame stabilization mechanism, and is characterized by the existence of internal stagnation points and reversed flows."* [Ref.148, p. 300].

The benefit of recirculation zones for combustion processes roots in the recirculation of heat and active chemical species to the root of the flame.
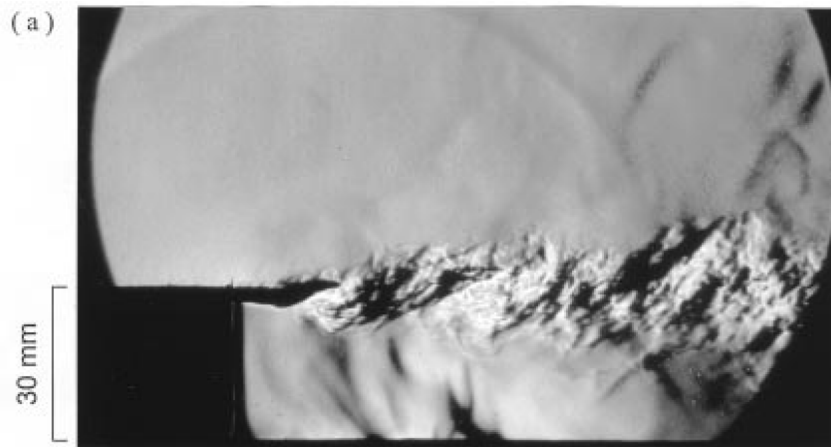

Figure 44 Schlieren photograph of a methane-air shear layer flame downstream of a backward facing step, dark zones indicate both turbulent shear layer and recirculation flames [146]

In a study of flame extinguishing, Takahashi et al. [146] presented Schlieren photographs of methane-air flames stabilized by a backward facing step, as shown in Figure 44. The dark zones in the flow indicate flames and are visible both in the turbulent shear layer and the recirculation zone at the bottom. Note that there is no swirl flow involved in this study. The shear layer therefore extends parallel to the flow from the premixing chamber. The leading parameters in the image shown in Figure 44 are the axial injection velocity of the propellant mixture in the premixing chamber of 7.1 m s^{-1} and the backward facing step height of $h = 32$ mm.

The time scale of the fluid mechanical residence time expressed as the ratio of a characteristic length and a velocity scale [128, 129].

$$\tau_{sl} = \frac{2L}{u} .$$
(3.22)

This simple relation is dependent on step height h and velocity at the edge u only and neglects any other geometrical influences such as chamber length. However, while the strongly simplifying nature of this relation is obvious, it is still used to guide the chamber design in absence of more detailed descriptions [46, 47, 149]. In literature, the characteristic length scale L is usually taken equal to the height of the backward facing step $L = h_{step}$, with geometrical parameters indicated in Figure 40.

$$\tau_{sl} = \frac{2h_{step}}{u} = \frac{2(r_{CC} - r_{inj})}{u} .$$
(3.23)

Neglecting any contribution from the swirl flow by using the axial injection velocity

$$u = u_{ax} = \frac{\dot{m}_p}{r_{inj}^2 \pi \rho} ,$$
(3.24)

the shear layer residence time becomes maximum for $d\tau_{sl}/dr_{inj} = 0$ [46, 149]

$$r_{inj} = \frac{2}{3} r_{CC} .$$
(3.25)

To account for combustion chamber length L_{CC}, Prior et al. [150] proposed the utilization of the reattachment length L_r as characteristic length scale. The reattachment lengths for backward facing step configurations have been exhaustively studied both on experimental and theoretical basis, with recent literature primarily focusing on large eddy simulation approaches [151, 152, 153, 154]. The reattachment length for a non-swirling flow over a backward facing step can be estimated by [150]:

$$L_r = 8.72 h_{step} \left(1 - e^{-\frac{2L_{CC}}{r_{cc}}} \right) \tag{3.26}$$

This reattachment length becomes $L_r \approx 23.5$ mm and $L_r \approx 24.4$ mm for the DM and EBB thruster respectively. Note however these reattachment lengths have been derived in the absence of swirl flow.
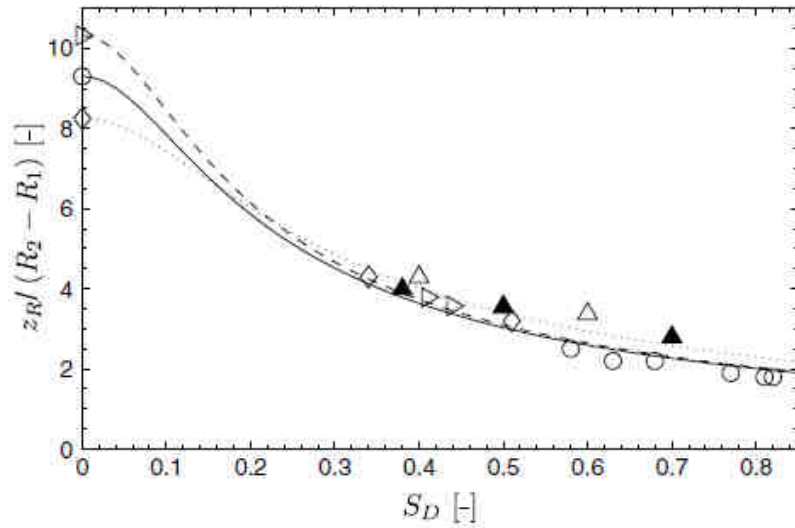

Figure 45 Reattachment length as a function of local swirl number [155]

Vaniershot and Van den Bulck [155] investigated the influence of local swirl number S_D on the reattachment length in case of a sudden expansion of the flow cross sectional area. Their findings are shown in Figure 45 in nondimensionalized form. For the given injector configuration (section 3.6.3.1), they reported a maximum shortening of the reattachment length to $\sim 0.2L_r$ for $S = 0.85$. Based on interpolation of these findings, reattachment lengths in the order of $L_r < 5$ mm are expected for the combustion chamber geometries investigated.
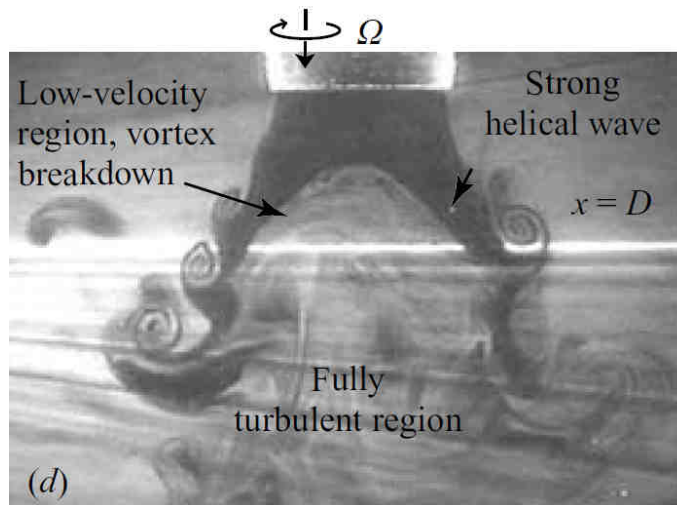
Figure 46 Vortex break up for $S = 1.03$, Re = 1000, $u_{ax} = 2.74$ cm s^{-1}, Ref. 156

Liang and Maxworthy [156] studied the entrainment of vortex injector swirl flows into the ambient chamber gases and found that:

"Swirl expanded the mixing region so that the jet spread faster than a non-swirling one, and the entrainment of ambient fluid was higher. The laminar region became shorter at larger swirl number, and the fully turbulent region was located further upstream" [Ref. 156, p. 126].

They state that the turbulent region was located at $x \sim 3D$ for a Swirl number of $S = 0.44$. It can thus be concluded, that the higher Swirl numbers of the injector configurations investigated in this work result in a swirl breakdown regions significantly upstream of $x < 3D$, which is in concordance with the findings from Ref. 155.

The increase in PVC central body for increased swirl numbers have been investigated and confirmed by various scholars [157, 158, 160, 163].

Huang and Yang [148, 147] studied turbulent combustion processes in the presence of a swirl injector in combination with a backward facing step configuration in gas turbines, combusting natural gas and air. In agreement with results from other authors, they found the zone of combustion located at the region of large vortex break up, where the large vortex flow induced from the swirl injector breaks up into small eddies due to the sudden increase in flow area downstream of the backward facing step. The small eddies lead to both a thorough mixing of the combustion components as to large residence times, thus facilitating combustion [159]. The presence of a swirl flow in a configuration with a backward facing step introduces an additional recirculation zone along the central axis of the combustion chamber, downstream of the backward facing step. The stream lines of a swirl injector geometry featuring a backward facing step are shown in Figure 47 with identified flow structures. Although the geometry used in this work features no injector center body, the flow structures in the region of the backward facing step are similar to the gas burner shown in Figure 47. The findings presented have been confirmed by various authors [161].
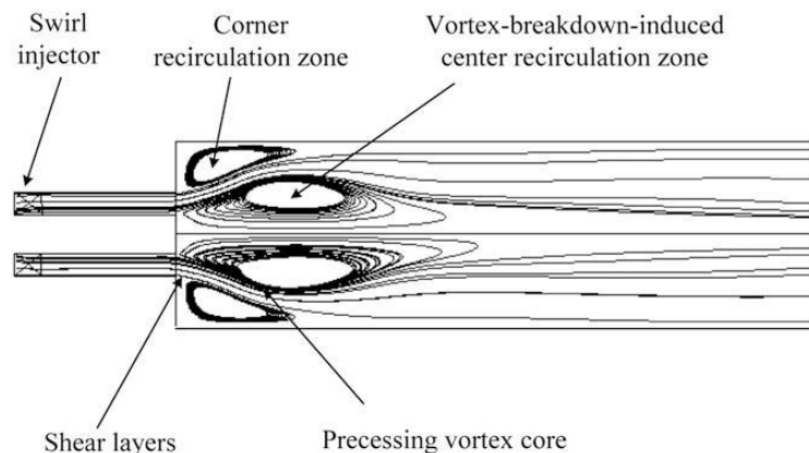

Figure 47 Stream lines for swirl injection and backward facing step configuration, from Ref. 148

Figure 48 shows a more detailed result with indicated local swirl numbers. This plot shows the shift of maximum tangential velocities to larger radial positions downstream of the backward-facing step, as well as backflux in the central body flow structure.
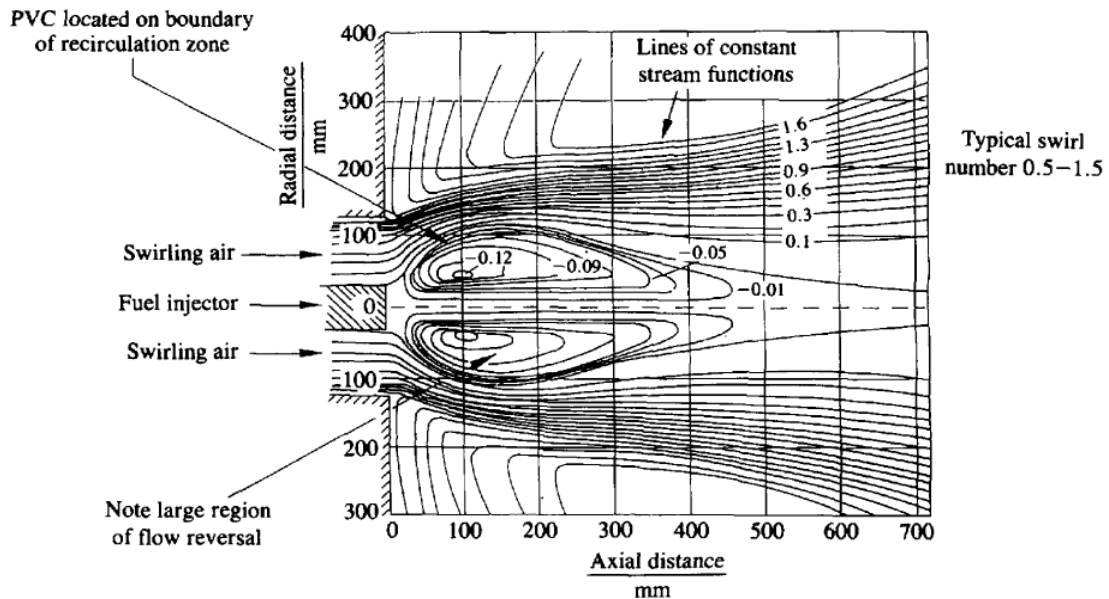

Figure 48 Stream lines for swirl injection and backward facing step configuration, larger dimensions with swirl number $S = 1.57$, from Ref. 162

Syred [162] describes the effect of backflux as a result of a centrifugal pressure gradient caused by the tangential injection velocity profile. The axial decay of this tangential velocity causes a decay of the centrifugal pressure gradient in axial direction. This again causes an axial pressure gradient orientated towards the injector, causing backflux. This is depicted schematically in Figure 49, with $\overline{w}$ indicating tangential and $\overline{u}$ indicating axial velocity, whereas pressure is indicated by $\overline{p}$.
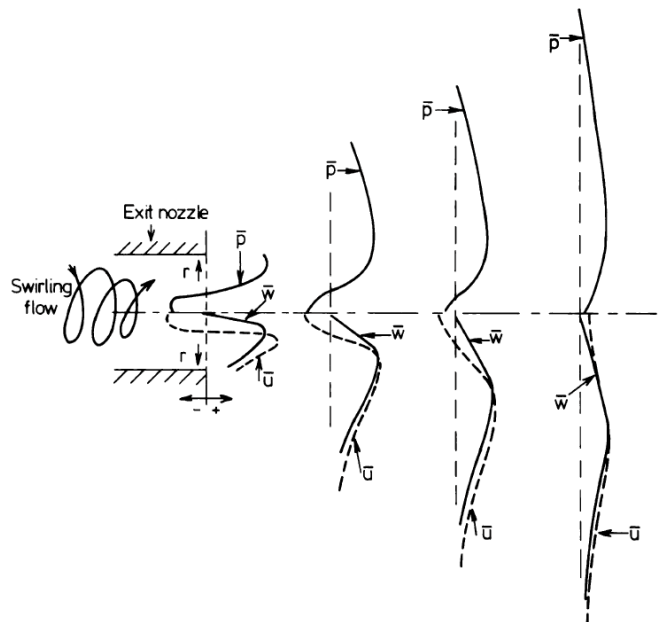
Figure 49 Schematics of interaction of swirl decay and pressure gradient causing backflux, from Ref. 162

Ranga Dinesh, Kirkpatrick and Jenkins [157] studied swirl flow fields downstream of a backward facing step for different swirl numbers on a numerical basis. They showed that increasing the swirl number for fixed configuration led to a widening of the PVC structure with respect to the central axis. The resulting velocity fields for the case of axial and tangential injection flow velocities of $u = 13$ m s^{-1} and $w = 26$ m s^{-1} respectively are shown in Figure 50. Negative values of axial velocity show the recirculation of downstream, potentially hot, combustion gases, which are essential for sustaining a stable combustion.
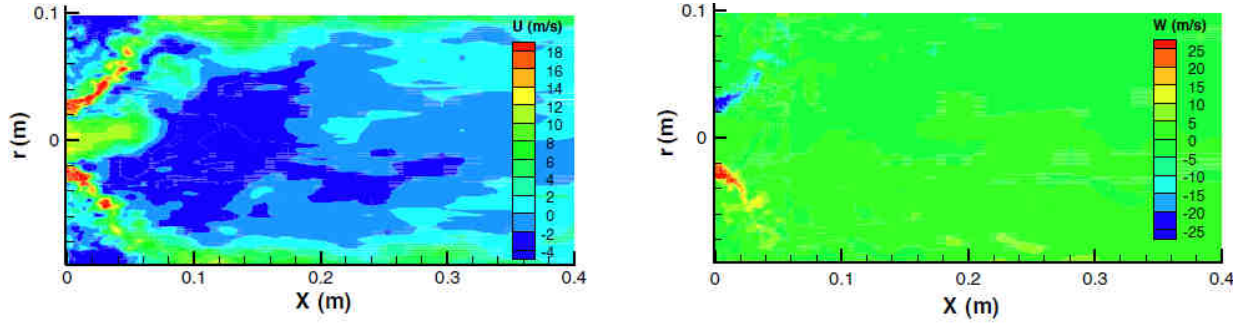
Figure 50 Axial (u, left) and tangential (w, right) flow velocities for injection conditions of $u_0 = 13$ m s^{-1} and $w_0 = 26$ m s^{-1}, from Ref. 157

A variety of investigations of combustion processes in swirl configurations featuring a backward facing step are available in literature, mostly for natural gas burners [148, 147, 157, 164, 165, 166, 167, 168]. Major findings applicable to the given application are discussed hereafter.
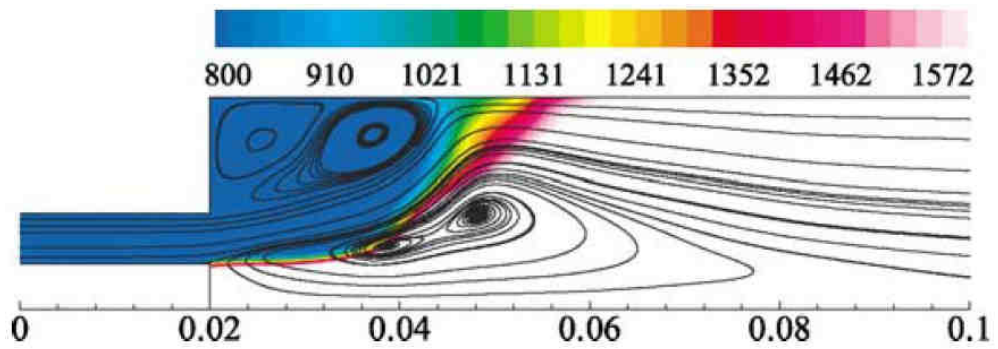

Figure 51 Temperature increase from combustion for swirl injection, from Ref. 147

Results from combustion modeling done by Huang and Yang [148] suggest a narrow zone of temperature increase along the zone of eddy break up, as shown in Figure 51. These findings have been proven experimentally, as can be seen in Figure 52, where a visual image of the flame front in a swirl combustion downstream of the backward facing step is shown. The narrow flame front at the vortex breakdown zones is in good accordance with Figure 51.
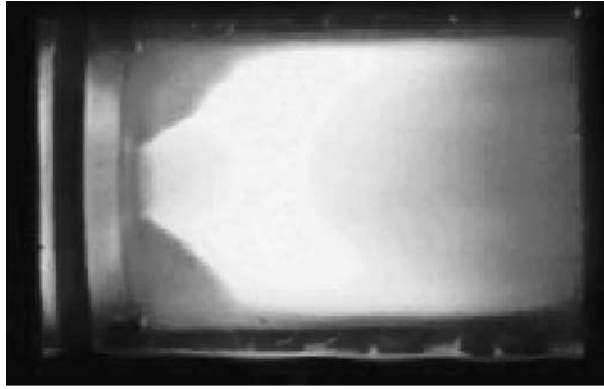
Figure 52 Natural gas combusted in a swirl air lean mixture, from Ref. 147

LaBry et al. [177] investigated lean swirl stabilized combustion of C_3H_8 with similar backward facing step burner configuration. Figure 53 shows the flame front again in the region of vortex breakdown.

The behavior of combustion outlined above will be modeled in a first approximation by a linear interpolation of stagnation temperature increase in the region of $z < L_r$ (Figure 45) of the combustion chamber from injection temperature to combustion temperature.
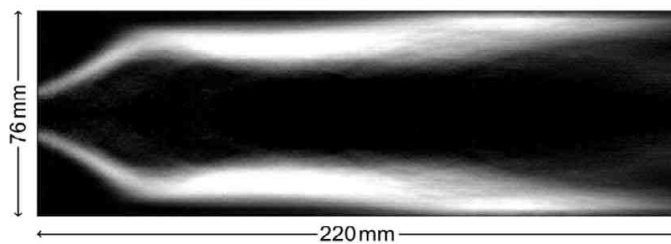
Figure 53 Propane gas combusted in a swirl air lean mixture, from Ref. 177

3.5. Bipropellant autoignition

Autoignition is defined as the ability to initiate bipropellant combustion without any external ignition devices, such as spark generators. This typically involves the injection of fuel into an oxidizer stream at pressure and temperature conditions above a certain threshold limit, and has been exhaustively studied for scramjet engines and air-kerosene mixtures [135, 169, 170, 171]. In the combustion chamber configuration with swirl injection and backward facing step, the main challenge is to meet combustion conditions within the shear layer without the favorable contribution of recirculating hot combustion gases in the recirculation zones.

It is therefore crucial to surpass the autoignition temperature not only in local zones by the favorable recirculation of combustion gases, but to achieve this condition by injecting high temperature oxidizer only.

Walder et al. [48, 172, 173, 174] published early work on the autoignition behavior of kerosene in decomposed hydrogen peroxide and proposed the empirically found correlation

$$\ln\left(L^* p^{m'}\right) = \frac{K}{T_0} + L' ,$$
(3.27)

relating the autoignition temperature limit to the combustion chamber pressure. With *K, L'* and *m* = 1.15 as empirical constants. Walder found constants fitted to experimental data to be *K* = 3720 and *L'* = -2.62.

Schiebl [149, 175] showed that the empirical constant *L'* is a parameter dependent on initial gas temperature, *O/F* ratio, specific heat, mean molar mass and isentropic exponent

$$L' \to L'_{\left(T_0, O/F, c_p, \gamma\right)} .$$
(3.28)

The analytical model presented in Ref. 149 focuses on the special issue of thermal losses in case of miniaturized combustion, where thermal losses become increasingly important. This model could be validated by the experimental results from section 4.3.3.2.

Sadov and Prokhorov [176] provided experimental data on temperature and pressures necessary to achieve autoignition for decomposed hydrogen peroxide and kerosene in a study of starting units for large scale combustion chambers. The results shown in Figure 54 have been determined using a nominal oxidizer mass flow of 8.5 g s^{-1}. In the discussion of their results, they pointed to the fact that the dependency of autoignition behavior on pressure and temperature can be estimated by a simple relation for the residence time τ_r of the propellant mixture within the combustion chamber, without any influence from a shear layer that governs the residence time necessary for ignition

$$\tau_r = \frac{V_{CC} p_{CC}}{\dot{m}_p R T_{inj}} .$$
(3.29)

Since the data they collected showed no successful autoignition events for temperatures below 500 °C, Sadov and Prokorov concluded that autoignition was only possible for initial hydrogen peroxide concentrations above 80 wt.% for the given chamber pressures.
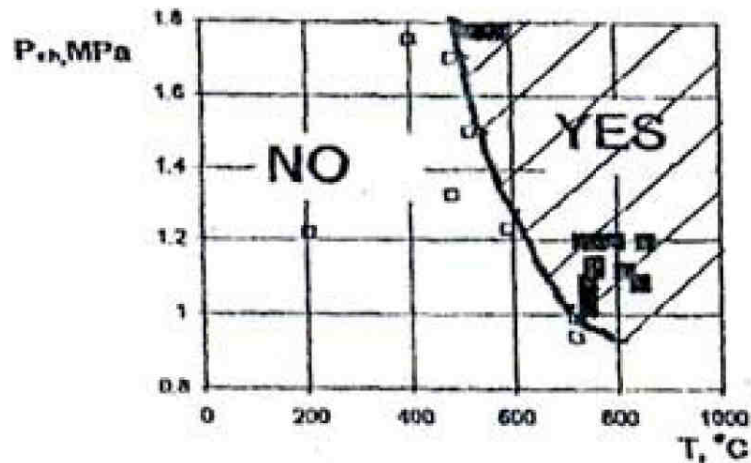
Figure 54 Hydrogen peroxide / kerosene autoignition data found by Ref. 176

Few other instances of investigation on autoignition behavior in staged combustors are available, mainly for larger propellant mass flows compared to the current investigation, such as Sisco et al. [46], who studied ignition of kerosene in decomposed hydrogen peroxide (92-98 wt.%) at large design mass flow rates of ~1.1 kg s^{-1}. However, these data are difficult to scale and therefore difficult to compare to the configuration investigated in this work.

Ref. 173 investigated a variety of different injector designs and found ignition delay to depend strongly on injector design. This points to the fact that the ignition delay times measured were dominated by mixing and evaporation processes rather than chemical ignition delay. Due to simultaneous change of multiple system parameters in the data presented, it is however not possible to isolate the effect of a single parameter change [173].

In the case of autoignition capability of staged combustors using ethanol as fuel, less data is available. However, general ignitability of ethanol-hydrogen peroxide mixtures under ambient pressures has been reported in Ref. 39. References 124, 125, and 126 have published ignition behavior of ethanol in terms of autoignition delay times in air mixtures. Yates et al. [125] published ignition delay times as a function of temperature for a variety of pressures, including 12 bar, which is in the order of the experiments carried out in section 4.3.3.3. Saxena and Williams [126] provide ignition delay times for ethanol as a function of equivalence ratio for 1 bar chamber pressure. According to the data provided [125], ignition delay times for ethanol are considerably increased compared to kerosene and may be expected to be in the order of milliseconds. This compares to ignition delay times of Jet A-1 in air in the order of 5 µs [134].

To guide the thruster design, experimental determination of autoignition thresholds for a given injector and combustion chamber design has been conducted in section 4.3, investigating the autoignition capability dependent on thruster system parameters of chamber pressure and injection temperature according to the discussion above. The experimental data found in the studies conducted showed the ability to autoignite with both kerosene and ethanol. In the former case, exponential dependency of autoignition limits according to Eq. (3.27) was confirmed. The results from the experimental ignition studies can be found in Figure 134 and Figure 135.

3.6. Flow through nozzle and combustion chamber
3.6.1. Isentropic flow equations

This section reviews isentropic flow correlations as found in various text books such as Ref. 4. These correlations are later used as the basis for the combustion chamber thermal simulation. The main purpose of the final thermal analysis is a thorough understanding of the thermal budget of the thrust chamber and the entire thruster to aid the design of a fully operational thruster able for steady state operation with appropriate cooling technique. All analysis presented hereafter is therefore based on the final DM thruster geometry described in section 4.5.
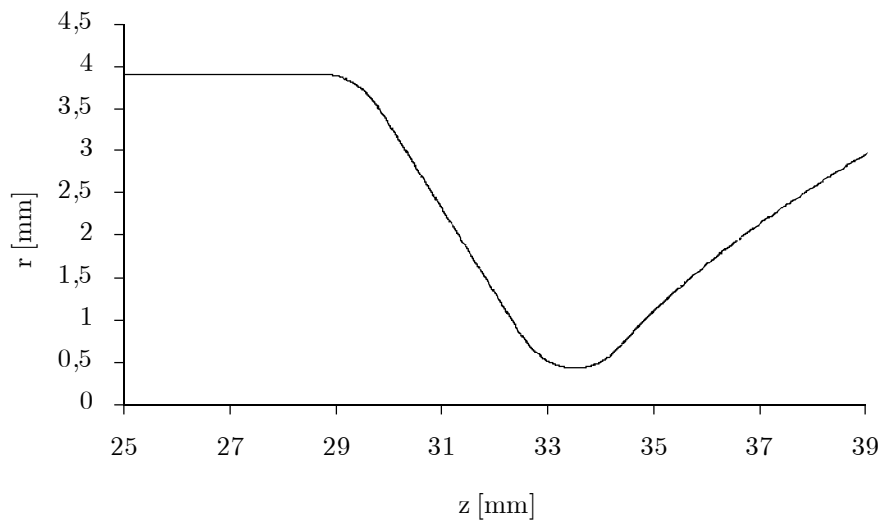
Figure 55 Nozzle inner wall contour, throat section

Figure 55 shows the chamber wall contour for the nozzle section of the DM thruster. The mass-, momentum, and energy balance for any control volume for stationary, compressible flow for an ideal gas are given by

$$\nabla(\vec{u}\rho) = 0$$
$$(\vec{u} \cdot \nabla)\vec{u} = -\frac{1}{\rho}\nabla p \qquad (3.30)$$
$$(\vec{u} \cdot \nabla)s = 0 \qquad .$$

The constant entropy s in the energy balance determines the problem as isentropic with the isentropic relation

$$p/\rho^\gamma = const . \qquad (3.31)$$

For one dimensional isentropic flow of an ideal gas, the enthalpy can be expressed as the sum of the stagnation enthalpy of the fluid and a velocity dependent term. The stagnation state,

70

denoted the subscript *0*, is defined as the state of the fluid when brought to zero velocity without losses in a reversible and adiabatic process ($dQ = 0$) without work ($dP_S = 0$) done to the fluid directly from the energy equation

$$\dot{m}\left(dh + u\,du\right) = d\dot{Q} - dP_S \tag{3.32}$$

by integration as

$$h_0 = h + \frac{u^2}{2}. \tag{3.33}$$

By the definition of enthalpy

$$h - h_0 = \int_{T_0}^{T_1} c_p\,dT \tag{3.34}$$

and assuming constant specific heat ratio, Eq. (3.33) can be rewritten as

$$\frac{T_0}{T} = 1 + \frac{u^2}{2c_p T}. \tag{3.35}$$

The Mach number is defined using the local speed of sound a:

$$M = \frac{u}{a} = \frac{u}{\sqrt{\gamma RT}}. \tag{3.36}$$

Using the Mach number and $c_p = R\gamma/(\gamma - 1)$, Eq. (3.35) can be rewritten to express the free stream temperature of the flow as a function of local Mach number

$$\frac{T_0}{T} = 1 + \frac{\gamma - 1}{2}M^2. \tag{3.37}$$

Rewriting the first law of thermodynamics with $dw = -p\,dv$ and $dq = T\,ds$ yields

$$T\,ds = de + p\,dv. \tag{3.38}$$

e is used for the internal energy instead of commonly used letters u to avoid confusion with flow velocity. As enthalpy is defined as $h = e + pv$, this becomes

$$T\,ds = dh - v\,dp, \tag{3.39}$$

where v is the volume per unit mass. Using the equations of state for a perfect gas $pv = RT$ and $h = c_p T$ with the assumption of vanishing variations of specific heat capacity c_p with temperature T, this becomes

$$ds = c_p \frac{dT}{T} - R \frac{dp}{p}.$$ (3.40)

Constant specific heat and the assumption of an isentropic process ($ds = 0$) allow integration of Eq. (3.40) to an arbitrarily state chosen to match the stagnation state

$$\frac{p_0}{p} = \left(\frac{T_0}{T} \right)^{c_p/R}$$ (3.41)

with

$$\gamma = \frac{c_P}{c_V} \quad \text{and} \quad R = c_p - c_v.$$ (3.42)

Eq. (3.41) becomes

$$\frac{p_0}{p} = \left(\frac{T_0}{T} \right)^{\frac{\gamma}{\gamma-1}},$$ (3.43)

relating the ratio of pressure and stagnation pressure to the corresponding ratio of temperatures. With the help of Eq. (3.37), an expression relating the pressure at any flow position to the stagnation pressure as a function of Mach number can be derived

$$\frac{p_0}{p} = \left(1 + \frac{\gamma-1}{2} M^2 \right)^{\frac{\gamma}{\gamma-1}}.$$ (3.44)

Using the isentropic relation, the corresponding relation for densities is obtained

$$\frac{\rho_0}{\rho} = \left(1 + \frac{\gamma-1}{2} M^2 \right)^{\frac{1}{\gamma-1}}.$$ (3.45)

Eq. (3.44) and (3.45) combined give the isentropic relationship:

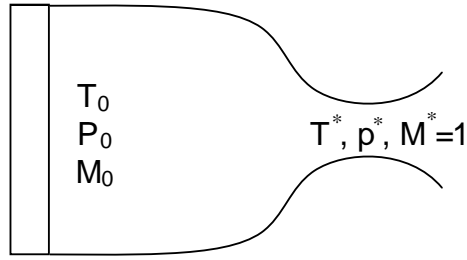$$\frac{p_0}{p} = \left(\frac{\rho_0}{\rho} \right)^{\gamma}.$$ (3.46)

Figure 56 Symbolic view of combustion chamber with nozzle

Figure 56 depicts the combustion chamber with fluid parameters in the combustion chamber assumed to be at zero velocity, and chocked flow conditions at throat. In the case of $M^* = 1$ at throat, the conditions within the thrust chamber are fully determined.

The mass flow, which is constant at any position, is given by

$$\dot{m} = Au\rho. \tag{3.47}$$

With the velocity u, flow cross sectional area A and density ρ. The latter can be determined by the equation of state of an ideal gas and the definition of Mach number. The mass flow can then be expressed as

$$\dot{m} = \frac{Ap}{RT} M\sqrt{\gamma RT}. \tag{3.48}$$

With the use of Eq. (3.37) and (3.44), this can be expressed as a function of stagnation conditions:

$$\frac{\dot{m}}{A} = p_0 M \sqrt{\frac{\gamma}{RT_0}} \left(1 + \frac{\gamma-1}{2} M^2\right)^{\frac{-(\gamma+1)}{2(\gamma-1)}}. \tag{3.49}$$

The assumption of sonic velocity at throat ($M^* = 1$) determines the pressure and temperature. In this case, Eq. (3.49) reduces to

$$\frac{\dot{m}}{A^*} = \frac{p_0}{\sqrt{RT_0}} \sqrt{\frac{\gamma(\gamma+1)}{2}} \left(\frac{2}{\gamma+1}\right)^{\frac{\gamma}{\gamma-1}}. \tag{3.50}$$

The quotient of Eq. (3.49) and (3.50) allows the numerical determination of Mach number as function of area aspect ratio A/A^*:

$$\frac{A}{A^*} = \frac{1}{M} \left[\frac{2}{\gamma+1} \left(1 + \frac{\gamma-1}{2} M^2\right)\right]^{\frac{\gamma+1}{2(\gamma-1)}}. \tag{3.51}$$

The quadratic nature of Eq. (3.51) results in two solutions for the Mach number for each area aspect ratio, with one being sub- and the other one being supersonic. In the throat region, both solutions become $M = 1$.

The differential momentum equation for non-viscous flow in the absence of a gravity term is given by

$$\frac{1}{u}\frac{du}{dz} + \frac{p}{\rho u^2}\frac{1}{p}\frac{dp}{dz} = 0 \qquad (3.52)$$

Substituting the quotient of pressure and density by the equation of state of an ideal gas, and incorporating the definition of sonic velocity in Eq. (3.36), this becomes:

$$\frac{1}{u}\frac{du}{dz} + \frac{\gamma}{M^2}\frac{1}{p}\frac{dp}{dz} = 0 \qquad (3.53)$$

The relation of isentropy in Eq. (3.46)

$$\frac{p}{\rho^\gamma} = const. \qquad (3.54)$$

in its differential form becomes

$$\frac{1}{\rho}\frac{d\rho}{dz} - \frac{1}{\gamma}\frac{1}{p}\frac{dp}{dz} = 0 \qquad (3.55)$$

Substituting Eq. (3.55) into Eq. (3.53) yields:

$$\frac{1}{\rho}\frac{d\rho}{dz} = -M^2\frac{1}{u}\frac{du}{dz} \qquad (3.56)$$

Differentiation of the mass balance in Eq. (3.47) gives:

$$d\dot{m} = 0 = \frac{1}{\rho}\frac{d\rho}{dz} + \frac{1}{u}\frac{du}{dz} + \frac{1}{A}\frac{dA}{dz} \qquad (3.57)$$

This allows elimination of density in Eq. (3.56), yielding

$$\frac{1}{A}\frac{dA}{dz} = \left(M^2 - 1\right)\frac{1}{u}\frac{du}{dz} \qquad (3.58)$$

Eq. (3.58) relates the acceleration of a gas to the change in flow cross sectional area, as a function of Mach number. One can see that acceleration can only occur for:

$$M < 1: \quad \frac{\mathrm{d}u}{\mathrm{d}z} > 0 \quad for \quad \frac{\mathrm{d}A}{\mathrm{d}z} > 0$$

$$M > 1: \quad \frac{\mathrm{d}u}{\mathrm{d}z} > 0 \quad for \quad \frac{\mathrm{d}A}{\mathrm{d}z} < 0$$

(3.59)

Thus, acceleration of a gas above sonic velocity can only occur in a converging-diverging configuration with sonic velocity at the smallest flow cross section, denoted throat. Therefore, comparison of stream position to throat position allows identification of the proper solution of Eq. (3.51). This solution is shown in Figure 57 for the given geometry along with the area aspect ratio.
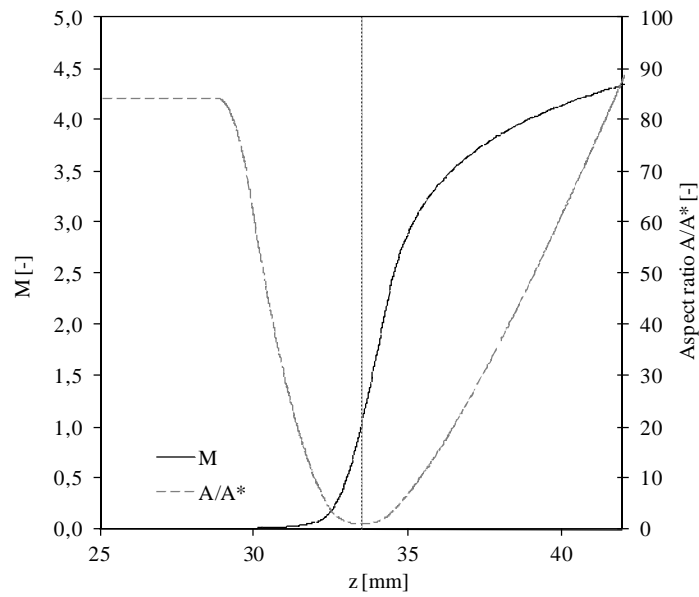
Figure 57 Area aspect ratio and Mach number for nozzle section

The distribution of pressure through the nozzle, determined by Eq. (3.44) is shown in Figure 58.
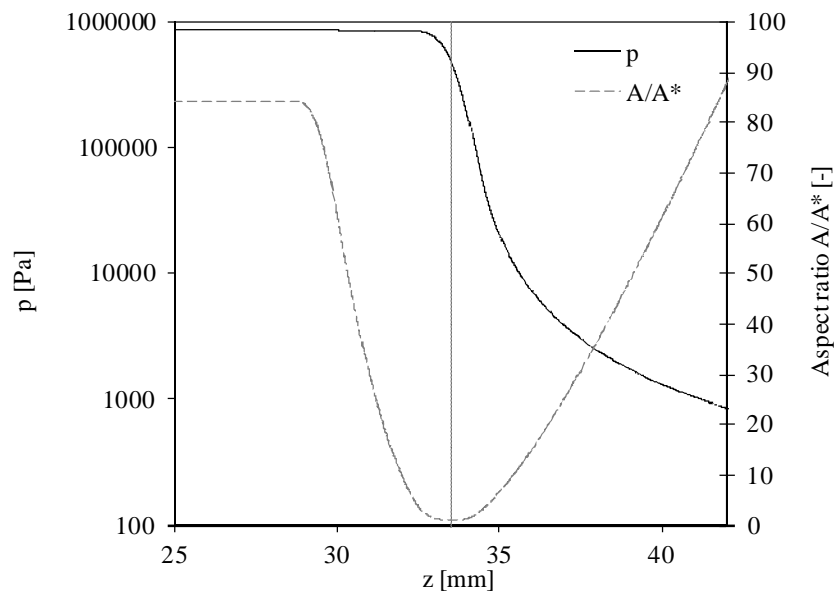
Figure 58 Area aspect ratio and pressure in nozzle section

3.6.2. Non-adiabatic flow through combustion chamber

The swirl flow with large swirl number in the cylindrical combustion chamber introduces high velocity flow near the combustion chamber wall with reduced temperature boundary layer thickness and therefore non-negligible heat transfer from the hot gas to the wall structure. To account for the effect of decreasing enthalpy due to heat losses of the combustion gases while flowing towards the nozzle in the absence of work done to the fluid, the enthalpy change can be expressed as, neglecting the change in kinetic energy:

$$\mathrm{d}\dot{H} = \mathrm{d}\dot{Q} = -h_g\left(T - T_W\right)2r_{CC}\mathrm{d}z\,,\tag{3.60}$$

where H refers to the enthalpy, h_g refers to the convective heat transfer coefficient and the product $2r_{CC}\mathrm{d}z$ refers to the surface area increment, given by $\mathrm{d}z = u_{ax}\mathrm{d}t$.

Integrating the momentum equation of a frictionless flow in a constant area duct with axial velocity u_{ax} and density ρ

$$\mathrm{d}p = -\rho u_{ax}\mathrm{d}u_{ax}\tag{3.61}$$

and introducing the Mach number, yields:

$$\frac{p}{p_1} = \frac{1 + \gamma M_1^2}{1 + \gamma M^2}\,,\tag{3.62}$$

where the subscript 1 refers to the initial condition. With Eq. (3.44), this relation can be expressed by the stagnation conditions:

$$\frac{p_0}{p_{01}} = \frac{1 + \gamma M_1^2}{1 + \gamma M^2}\left(\frac{1 + \dfrac{\gamma - 1}{2}M^2}{1 + \dfrac{\gamma - 1}{2}M_1^2}\right)^{\frac{\gamma}{\gamma - 1}}.\tag{3.63}$$

As opposed to isentropic flow, the stagnation condition p_0 is not a constant reference condition, but changes along the flow direction. p_{01} refers to the stagnation pressure at the initial point, that is the most upstream section of the combustion chamber. Using the equation of state of a perfect gas and the continuity condition $\rho u_{ax} = \rho_1 u_{ax1}$, the change in temperature from the initial state can be expressed by

$$\frac{T}{T_1} = \frac{p}{p_1}\frac{\rho_1}{\rho} = \frac{p}{p_1}\frac{u_{ax}}{u_{ax1}}.\tag{3.64}$$

This temperature ratio can be expressed in terms of Mach number as

$$\frac{T}{T_1} = \left(\frac{p}{p_1} \frac{M}{M_1} \right)^2 \tag{3.65}$$

The ratio of pressure to initial pressure is given in Eq. (3.62). Thus, the temperature ratio becomes:

$$\frac{T}{T_1} = \left(\frac{1 + \gamma M_1^2}{1 + \gamma M^2} \frac{M}{M_1} \right)^2 \tag{3.66}$$

which can be related to the stagnation conditions by using Eq. (3.37):

$$\frac{T_0}{T_{01}} = \left(\frac{1 + \gamma M_1^2}{1 + \gamma M^2} \frac{M}{M_1} \right)^2 \left(\frac{1 + \frac{\gamma - 1}{2} M^2}{1 + \frac{\gamma - 1}{2} M_1^2} \right) \tag{3.67}$$

The local Mach number is thus a function of initial Mach number and local and initial stagnation temperatures T_{01} and T_0. The change in stagnation temperature is assumed to be solely due to convective heat loss to the chamber wall, which becomes, for the assumption of constant specific heat and small flow velocities $M <\!<1$, implying $T_0 \sim T$, if the length increment Δs is equal to the distance from the most upstream flow point:

$$\Delta \dot{H} = -h_g \left(T_0 - T_W \right) 2 r_{CC} \Delta s = \dot{m} \int_{T_{01}}^{T_0} c_p \mathrm{d}T = \dot{m} c_p \left(T_0 - T_{01} \right) . \tag{3.68}$$

For each stream position, equations (3.67) and (3.68) can be solved to derive the corresponding stagnation temperature and Mach number. Stagnation pressure change is then calculated by Eq. (3.63)

3.6.3. Swirl flow
3.6.3.1. Swirl number evaluation

Two different swirl injector designs have been used in the experimental investigations: a vane type swirl injector employed in the ignition studies in section 4.3 and the tangential injection type utilized in the thruster tests in section 4.4 and 4.5. The change in injector design was primarily driven by simplifying and therefore reducing the cost in the manufacturing process. The design for the two types of injectors are depicted in Figure 59.
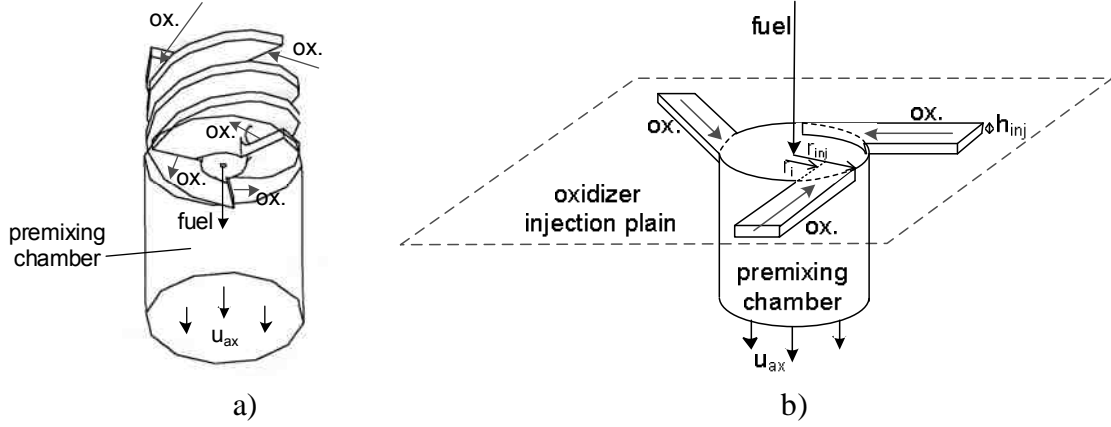
Figure 59 Injection schematics of ignition chamber vane type swirl injector (a) and DM swirl injector (b), both with premixing chamber indicated

Inaccuracies in manufacturing of the tangential injection channels led to significantly injection velocity changes for the two tangential injectors employed in the EBB and DM thruster tests. The resulting deviating geometrical parameters of the injection channels have been determined by visual inspections during assembly, with significantly reduced injection channel width and therefore reduced channel cross section found for the injector employed in the DM thruster.

Various simplified expressions based on geometrical configuration only and thus on homogeneous flow throughout the injector, can be found in literature. These include expressions for vane type injectors with negligible vane thickness published by Huang and Yang [148], geometrical expressions for tangential injectors [195, 196] and expressions accounting for axial injected fuel [197, 198]. However, the general expression of swirl number developed by Chigier and Beér [199] defines the Swirl number more accurately by the ratio of axial flux of the tangential momentum to the product of axial momentum and a characteristic radius [198, 194]:

$$G_\Phi = \int_{r_i}^{r_{inj}} 2\pi\rho u_{ax} u_{tan} r^2 \mathrm{d}r$$

$$G_z = \int_0^{r_{inj}} 2\pi r \rho \left(u_{ax}\right)^2 \mathrm{d}r \quad .$$

(3.69)

The Swirl number is then given by

$$S = \frac{G_\Phi}{r_{inj} G_z}$$

(3.70)

with axial and tangential velocities, for negligible influence of the injected fuel on mixture density:

$$u_{ax} = \frac{\dot{m}_{Ox}\left(1 + \dfrac{1}{O/F}\right)}{\rho r_{inj}^2 \pi}$$

(3.71)

$$u_{tan} = \frac{\dot{m}_{Ox}}{3\rho h_{inj}\left(r_{inj} - r_i\right)}.$$

The swirl number then becomes:

$$S = \frac{2\pi O/F\left(r_i^2 + r_i r_{inj} + r_{inj}^2\right)}{9 h_{inj} r_{inj}\left(1 + O/F\right)}.$$

(3.72)

The swirl number calculated by Eq. (3.72) for the different injectors and fuels at stoichiometric mixture ratio are given in Table 12.

In case of the blade type injector employed in the ignition chamber, h_{inj} equals the blade distance $h_{blade} = 0.4$ mm.

Table 12 Swirl numbers for injectors employed

Injector	Kerosene	Ethanol
Ignition chamber	2.63	2.67
EBB	3.28	3.07
DM	4.93	-

3.6.3.2. Swirl flow types

Most scholars [207] distinguish between three types of swirl flow structures, based on the radial distribution of the angular momentum, as indicated in Figure 60. Concentrated vortex type flows, with angular momentum concentrated near the center of the flow, solid body rotation flows, with linear dependency of tangential velocity on radial position, and wall jet type flow with angular momentum concentrated at large radial positions.
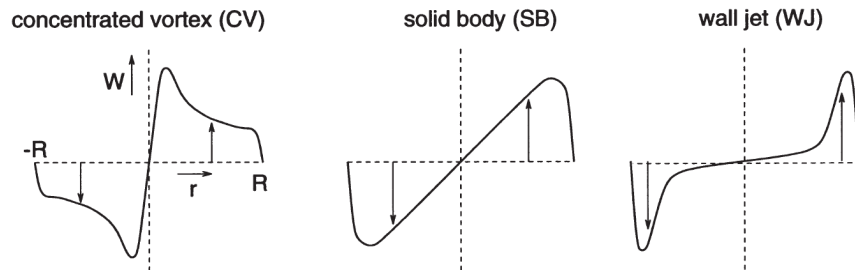
Figure 60 Different swirl flow types, Ref. 207

Two types of vortices are commonly distinguished [162, 204, 205]: forced (rotational vortex: e.g.: solid body rotation) and free vortex (irrotational) structures. While in the former case the tangential velocity shows linear dependency on the radial distance from the vortex center, in the latter case, tangential velocity varies indirect proportional with radial distance from the

vortex center and angular momentum remains uniform for all radii. Thus, vorticity W is zero in an ideal free vortex, except for the singularity at the center.
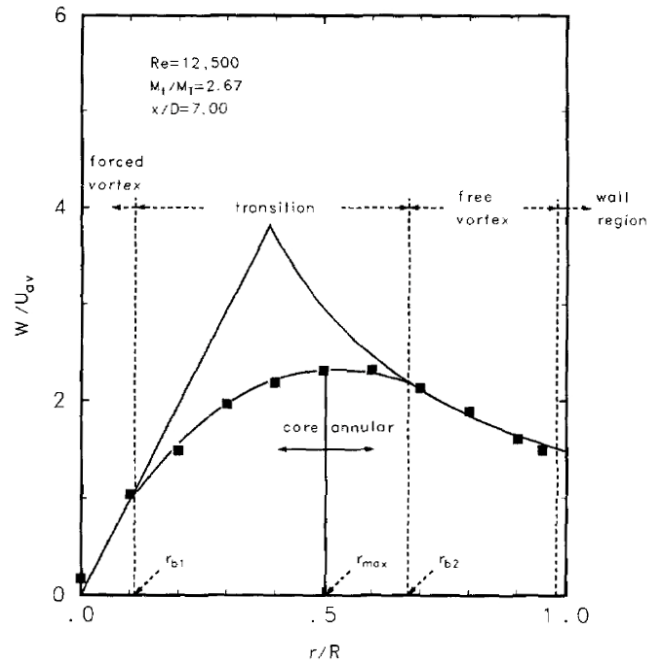

Figure 61 Tangential velocity distribution in vortex after tangential injection, Ref. 205

Ref. 205 investigated the type of swirl occurring in tubes after tangential injection similar to the injector geometry used in this work for large Reynolds number, reporting Rankine type vortex flows for radial injected gas, that is a combination of forced (solid body vortex) and free vortex structures. They found a rather narrow zone of forced vortex with linear velocity distribution and a rather large transitional zone with maximum tangential velocity at $r \sim 5$ and decreasing velocity for larger radius $\sim 1/r$ as in the case of free vortex flow [204]. Their findings are presented in Figure 61.
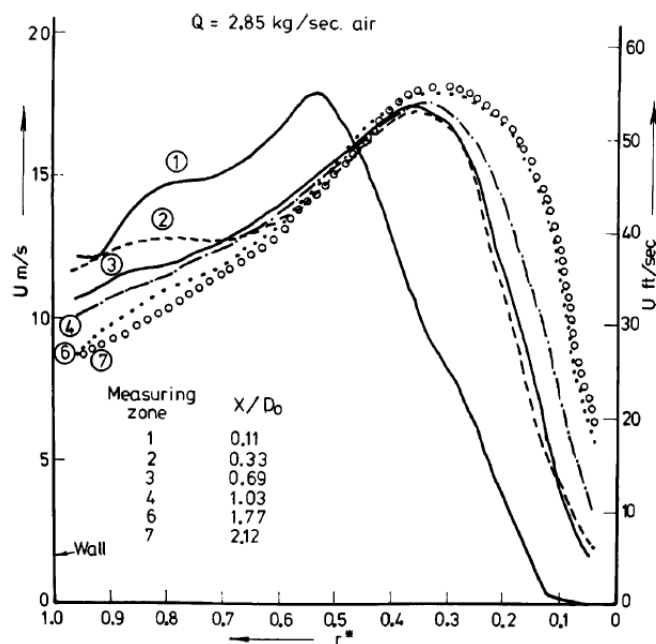
Figure 62 Tangential velocity distribution in vortex after tangential injection at different downstream positions x normalized by the combustion chamber diameter D_0, Ref. 162.

Syred [162] investigated vortex structures in a configuration featuring gas injection utilizing two tangential injection channels similar to the configuration investigated in this work. He reported Rankine vortex structures. In this case, the section of forced vortex decreased for increased distance from the injector as shown in Figure 62. However, the geometrical dimensions of the test setup investigated by Syred exceed the dimensions in this work by far.

The combustion chamber design features a swirl injector with tangential gaseous oxidizer injector together with axial liquid fuel injection. Both are mixed in a dedicated mixing and evaporation chamber with radius r_{inj} significantly smaller than the combustion chamber. Due to the high oxidizer fuel mixture ratio, the fuel is evaporated or partially evaporated and accelerated by the swirl of the gaseous oxidizer before the mixture is injected into the combustion chamber over a backward facing step, inducing large axial vortices.
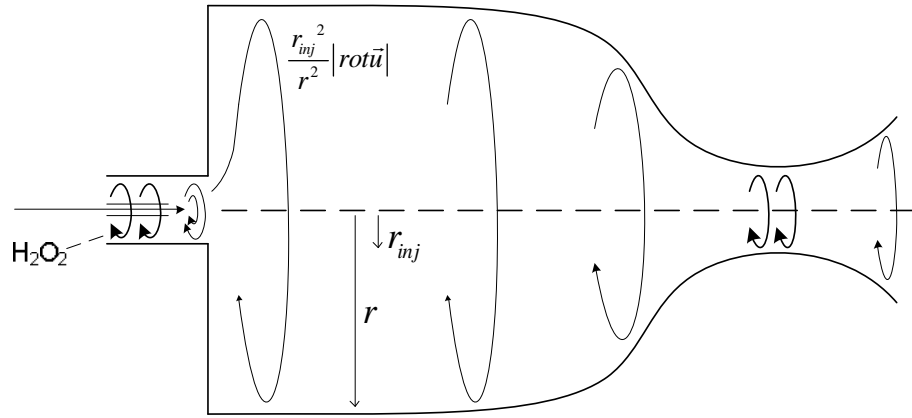
Figure 63 Swirl flow in combustion chamber

Neglecting any induced vortices in axial direction, one can derive from Helmholtz's first theorem on the consistency of vortex flow for inviscous fluids:

$$A\left|\text{rot}\vec{u}\right| = \text{const.} \tag{3.73}$$

that tangential velocities of the radial swirl are reduced from the injector premixing chamber to the combustion chamber by a factor

$$\sim \frac{r_{inj}^2}{r_{CC}^2}. \tag{3.74}$$

Neglecting any influences from combustion, temperature increase, changing chemical properties and friction, the swirl flow would then lead again to larger tangential velocities with converging flow cross sectional area at the nozzle. As the axial velocity determines $M = 1$ at the throat in the absence of any swirl, the vector sum of axial and tangential velocity becomes unity upstream of the geometric throat, leading to a shift in effective throat area from the geometric throat area further upstream, as in the case of friction induced boundary layers. Thus, $M_t > 1$ at the geometric throat occurs, potentially influencing the convective heat

transfer in this section. This vortex behavior is depicted in Figure 63 with size of arrows indicating large or small tangential velocities.

3.6.3.3. Swirl decay

It is now of interest to estimate whether the swirl induced by the injector passes through the combustion chamber or is degraded by viscous friction or other effects upstream of the converging nozzle section.

The vorticity of a stream-threat is given by:
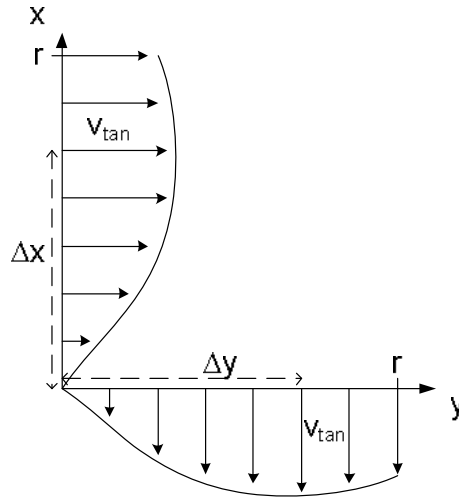
$$\vec{W} = \frac{1}{2}\vec{\nabla}\times\vec{u}.$$
(3.75)

Figure 64 Derivation of vorticity of a stream-threat

Assuming a forced vortex with linear dependency of tangential velocity on radius $\vec{u}\big|_{\text{tan}} = r\omega\hat{e}_{\varphi}$ with angular velocity ω, and evaluating the curl operator in the cylindrical coordinate system, the vorticity of a stream-threat becomes

$$W\hat{e}_z = \frac{1}{2r}\frac{\partial r^2\omega}{\partial r}\hat{e}_z = \omega\hat{e}_z.$$
(3.76)

The circulation of a stream-threat encompassing area A_S is defined as

$$\Gamma = 2\int_{A_S} W\mathrm{d}A_S.$$
(3.77)

The time dependent transport theorem for the circulation of a closed stream line l for viscous flow is given by, for a homogeneous fluid $(\rho = \text{const.}, \mu = \text{const.})$ [226]

$$\frac{d\Gamma}{dt} = -2\upsilon \int_l \text{rot}\,\omega \, dl \,, \tag{3.78}$$

which can be transformed into an integral over the encompassed area using the Stokes theorem. The evolution of circulation becomes

$$\frac{d\Gamma}{dt} = -2\upsilon \int_{A_S} \Delta\omega \, dA_S \,. \tag{3.79}$$

If one is only interested in the decay of the vortex stream line in axial direction, the integral on the right hand side can be solved since angular velocity ω is independent from radius r, and the evolution of angular velocity in the absence of vortex stretching $\vec{\omega}(\nabla \vec{u}) \rightarrow 0$ becomes

$$\frac{d\omega}{dt} = -\upsilon\Delta\omega. \tag{3.80}$$

The solution of Eq. (3.80) is a product of a time-depending exponential decay term and a non-decaying alternating term. The decay of angular velocity is then described by

$$\omega_{(t)} \propto e^{-\frac{\upsilon^{1/3}}{\omega_{t=0}}t} \,. \tag{3.81}$$

However, while the derivation of Eq. (3.81) only incorporates viscous effects of the free stream flow, other effects are known to additionally decreased swirl motion, such as friction wall effects. Exponential form of decay of a swirl flow in a confined space with wall stress has been found in Ref. 206, 207, 208 and 210, where the coefficients of this relation have been fitted to experimental data, usually in the form of [207]:

$$S = S_0 e^{-\frac{\beta}{d_{CC}}x} \,. \tag{3.82}$$

With β relating to the wall friction coefficient of a fully developed pipe flow [203] and therefore relate swirl decay to Reynolds number. Steenberg and Voskamp [207] for example derived the correlation, for small swirl numbers

$$\beta = (1.49 \pm 0.09)\,f \,, \tag{3.83}$$

with f being the friction coefficient for a fully developed flow through a pipe [201]. Various authors have confirmed the order of magnitude of swirl decay factor $\beta = 0.01–0.05$ [202, 203, 209]. Steenberg and Voskamp [207] presented a review on swirl

decay rate values presented by various authors, shown in Figure 65. Note that λ refers to the coefficient of friction f, not the thermal conductivity. The numbers indicated in the plot refer to literature sources reviewed in Ref. 207. Squared markers refer to initial swirl number $S > 0.8$ and are most applicable to the case investigated in this work. These values indicate swirl decay rates increased for increasing swirl numbers to ~0.02-0.1, giving maximum $\beta \approx 0.149$ for small Reynolds numbers.
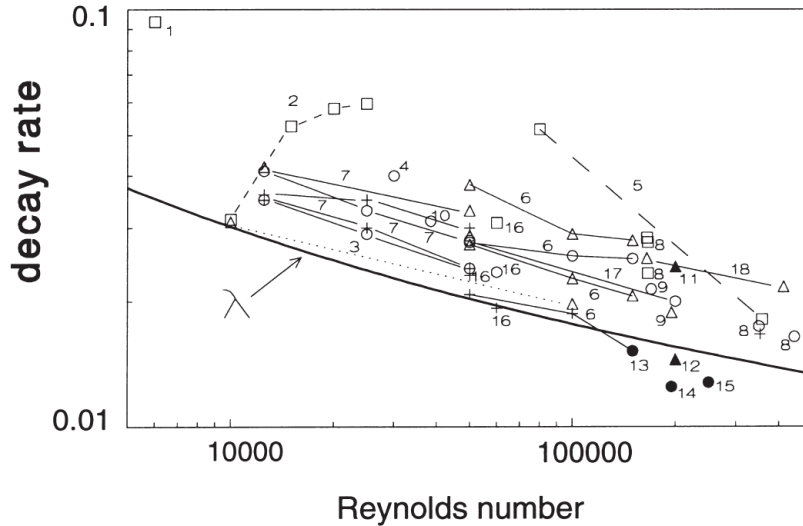
Figure 65 Literature survey on swirl decay rates, from Ref. 207

This shows that viscous effects only do not contribute significantly to the vortex decay for swirling flow in the absence of combustion. This is confirmed by various authors who reported swirl decay in the absence [210, 211, 212, 213] and in the presence [214] of combustion. Ref. 202 for example reported turbulent swirl decay to below 20 % of the initial value at a length of 50 times the vortex diameter. Syred [162] reported sustained swirl flow throughout the entire burner length. Ref. 157 investigated swirl decay as a function of initial swirl number, as shown in Figure 66 for an axial location at 6 times the diameter of the chamber downstream of the injector, which would become, in the case of the DM thruster (section 4.5) approximately 4.7 cm downstream of the injector plane and thus considerably downstream of the converging chamber section.

Although the above mentioned literature does not investigate swirl decay in the presence of combustion, it can be concluded that significant swirl flow will be present throughout the combustion chamber and therefore in the nozzle, necessitating an adaption of the isentropic flow description presented in sections 3.6.1 and 3.6.2.
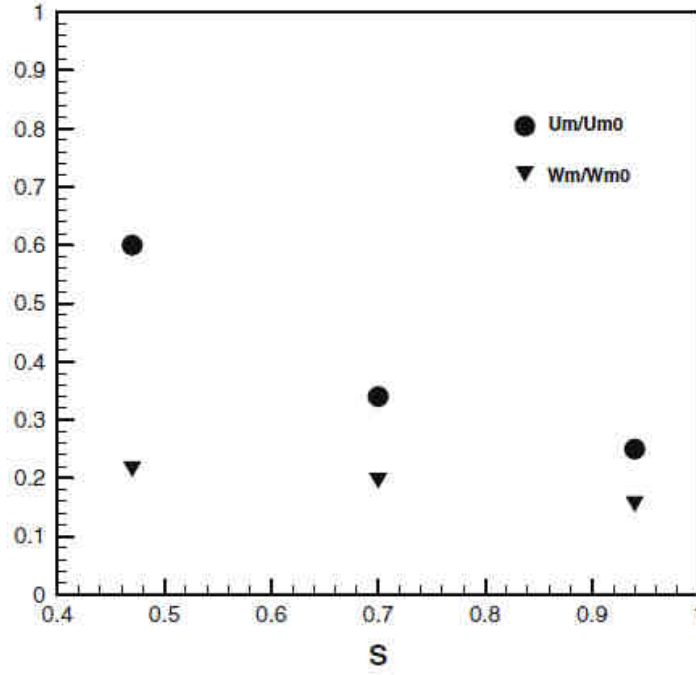
Figure 66 Swirl decay at $x = 6 \, d_{CC}$ as a function of initial swirl number, from Ref. 157

3.6.3.4.   Swirl flow through nozzle

Based on the discussion above, a decreased, but potentially sustained swirl flow at the entrance of the converging nozzle is expected. In this case, a tangential velocity component is present, which is added to the axial velocity originating from exhaust acceleration in the deLaval nozzle. This additional velocity component thus causes Mach number greater unity at the throat. In this case, flow patterns change, decreasing the mass flow passing through the throat, similar to the impact of boundary layers. The swirl distribution with tangential velocity being a function of radius causes the lines of constant Mach numbers to bend, therefore transforming the one-dimensional problem into a two dimensional problem. However, approximations to such complex flow fields are available and presented hereafter. The decrease of mass flow through the nozzle as a function of swirl intensity S is shown in Figure 67. The swirl intensity for the throat can be defined by the area average of tangential velocity at throat, normalized to the critical speed [215].

$$S = \frac{1}{A^*} \int_{A^*} \frac{u_{\tan}}{a^*} \, \mathrm{d}A^* . \tag{3.84}$$
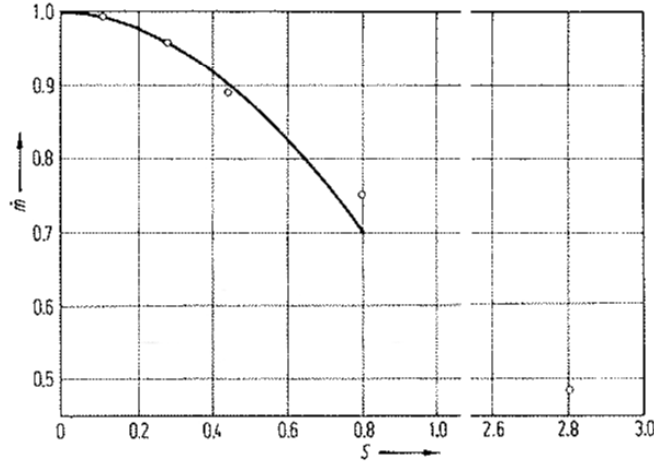
Figure 67 Mass flow decrease as a function of swirl intensity, from Ref. 215

Van Holten et al. [216] proposed analytical expressions deriving the Mach number in a nozzle in the presence of a swirl velocity component. Their work bases on a deLaval tube with an inner body, thus reducing the two-dimensional velocity distribution to a one-dimensional problem in the case of a narrow flow tube. Their expressions however can be interpreted to describe the Mach number at a vortex line close to the chamber wall, which is the region of interest for heat transfer analysis. The Mach number at throat can be expressed as

$$M_t^2 = \frac{u_{tan}^2 + u_{ax}^2}{\left(a*\right)^2}.$$ (3.85)

Taking into account, that at the throat, $u_{ax} = a*$ and by relating the critical velocity to stagnation conditions

$$\left(a*\right)^2 = a_0^2 \left(1 + \frac{\gamma - 1}{2} M_t^2\right)^{-1},$$ (3.86)

the Mach number at throat can be expressed as

$$M_t^2 = \frac{1 + \dfrac{u_{tan}^2}{a_0^2}}{\left(1 - \dfrac{\gamma - 1}{2}\dfrac{u_{tan}^2}{a_0^2}\right)}.$$ (3.87)

With the isentropic relation for density in Eq. (3.45), and the critical velocity $u_{ax} = a*$, the mass flow at the throat can be related to stagnation conditions according to

$$\dot{m} = \rho_t u_{ax} A_t = \rho_0 a_0 A^* \left(1 + \frac{\gamma - 1}{2} M_t^2\right)^{-\frac{\gamma + 1}{2(\gamma - 1)}}.$$ (3.88)

The mass flow at any station of the nozzle is given by

$$\dot{m} = A \rho u_{ax} .$$ (3.89)

With $u = \sqrt{u_{tan}^2 + u_{ax}^2}$, $M = u/a$ and Eq. (3.45), the axial velocity can be expressed by

$$u_{ax} = \sqrt{\frac{M^2 a_0^2}{1 + \frac{\gamma-1}{2}M^2} - u_{tan}^2}$$ (3.90)

,

where the tangential velocity near the wall is determined by the tangential injection velocity and the ratio of areas as a function of radius r:

$$u_{tan} = \frac{r_{inj}^2}{r^2}\left(1 + \frac{1}{OF}\right)^{-1} u_{tan}^{inj} .$$ (3.91)

However, since a decay of the vortex is observed, it is useful to define a decay parameter η_S accounting for the decay of tangential velocity from the injector to the nozzle section. Substituting into Eq. (3.89) and equating with Eq. (3.88), since the mass flow is constant at any stream position, gives an expression relating the Mach number to area aspect ratio:

$$\frac{\sqrt{\frac{M^2 a_0^2}{1 + \frac{\gamma-1}{2}M^2} - \eta_S u_{tan}^2}}{\left(1 + \frac{\gamma-1}{2}M^2\right)^{\frac{1}{(\gamma-1)}}} = a_0 \frac{A^*}{A}\left(1 + \frac{\gamma-1}{2}M_t^2\right)^{-\frac{\gamma+1}{2(\gamma-1)}}$$ (3.92)

.

For $u_{tan} = 0$, the Mach number at throat becomes $M_t = M^* = 1$ and the expression above becomes equal to Eq. (3.51).

3.6.4. Evaluation of thermodynamic combustion properties

Chemical analysis of decomposition and combustion processes are performed using NASA Chemical Equilibrium and Applications (CEA) code [92], which is widely used in literature as a benchmark code for chemical analysis in propulsion system design [68, 217, 218]. CEA is an algorithm minimizing the Gibbs free energy, which bases on a thermodynamic system in equilibrium at any position. However, it is not obvious that the assumption of equilibrium composition adequately depicts the situation in the combustion chamber since chemical reaction equilibrium does not occur instantaneous, especially in the case of accelerated flow through the nozzle to supersonic speed. In addition to the equilibrium reaction mode it is therefore possible to evaluate the system with frozen reaction, that is infinite slow reacting species after a certain flow position, e.g. combustor or throat. In this case, no further changes in chemical species distribution occur downstream of the specified position. As the real case will be located in between these two assumptions, the methods of equilibrium and frozen reactions constitute the two limits for chemical properties used for evaluation.

Since flow velocities are small upstream of the throat, an often found approximation to the real case is the assumption of frozen flow downstream of the throat and equilibrium condition upstream [68]. The large area contraction ratio from combustion chamber to throat and the therefore small flow velocities within the cylindrical combustion chamber incline to this approach.

CEA code allows both Infinite Area combustion Chamber (IAC) and Finite Area combustion Chamber (FAC) analysis for the region upstream of the nozzle. The former assumes adiabatic, infinite combustion chamber cross section and therefore vanishing flow velocity, whereas the latter allows calculation for a specified combustion to throat area aspect ratio [219].

A typical chemical analysis utilizing CEA code is given in appendix X.4. The analysis depicted corresponds to the long duration bipropellant firing test performed within the investigation of the DM thruster presented in section 4.5.3.1. The analysis was performed using experimentally determined input parameters such as oxidizer to fuel mass flow ratio, injection temperatures and combustion chamber pressure. These input parameters where determined by averaging of the experimentally recorded, near stationary data as explained in 4.5.3. All calculated parameters such as combustion gas temperature, characteristic velocity, chamber pressure as well as the thruster performance related parameters such as specific impulse are given at different flow stations of the analysis, corresponding to the combustion chamber, at throat and at the specified nozzle exit area. In the sample analysis shown in appendix X.4, the expansion ratio was chosen to match the nozzle expansion ratio of the DM thruster. In addition to the calculated parameters shown in the sample output file, additional combustion properties such as thermodynamic transport properties can be calculated.
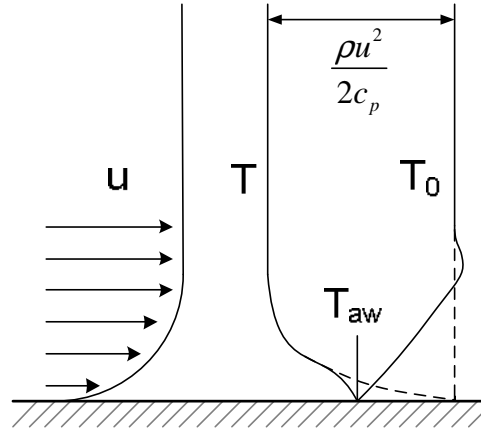
3.6.5. Adiabatic wall temperature

Figure 68 Adiabatic wall temperature and stagnation temperature, dashed line indicates solution in absence of heat conduction

In the case of high speed flow as encountered in a rocket nozzle, viscous effects in the turbulent boundary layer, in which the velocity decays from free stream velocity to zero, cause significant heat conduction from low speed flow to regions with larger flow velocities. This is intuitive, since the static temperature is higher in the slow velocity flow near the wall than in the high speed free stream. The heat conduction within the fluid causes a decrease in stagnation temperature in the proximity of the wall. Therefore, the temperature of the fluid closest to the wall differs from the stagnation temperature of the free stream, although no-slip condition dictates zero velocity. A depiction of static and stagnation temperature distribution in the proximity of an adiabatic wall is shown in Figure 68. The velocity profile is indicated to estimate the boundary layer. The dashed line indicates temperature increase to the free stream stagnation temperature in the absence of heat conduction in the fluid.

The magnitude of the adiabatic wall temperature can be related to the free stream gas temperature by the recovery factor [4]

$$\tilde{r} = \frac{T_{aw} - T}{T_0 - T},$$
(3.93)

where temperature T relates to the free stream temperature. With the help of the recovery factor, the ratio of adiabatic wall to stagnation temperature becomes a function of Mach number only:

$$\frac{T_{aw}}{T_0} = \frac{1 + \tilde{r}\frac{\gamma - 1}{2}M^2}{1 + \frac{\gamma - 1}{2}M^2}.$$
(3.94)

Ref. 228 suggests a recovery factor of $\tilde{r} = 0.89$, whereas Ref. 4 found $\tilde{r} = 0.91$ as a good approximation for compressible turbulent flow below $M = 4$. The free stream temperature and the adiabatic wall temperature across the nozzle region of the given geometry are shown in Figure 69 for $\tilde{r} = 0.89$, again for the DM thruster configuration.
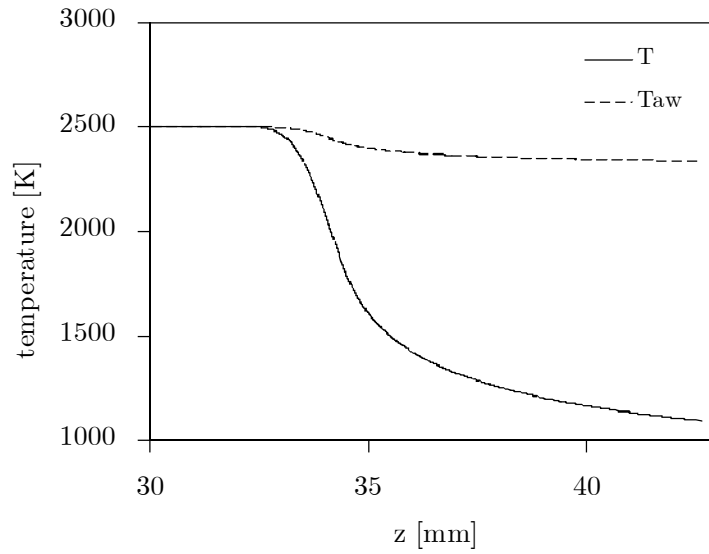
Figure 69 Free stream temperature and adiabatic wall temperature in nozzle region

3.7. Hot side heat transfer

3.7.1. Convective heat transfer in the nozzle

The total heat transferred into the combustion chamber structure is defined as

$$\dot{Q} = \int \dot{q} \, dA \qquad (3.95)$$

In a rotation symmetric combustion chamber, the heat flow per area $\dot{q}$ is in most regions downstream of the injector, amongst others, a function of combustion chamber contraction ratio, with significant increase for the throat. The leading process dominating the heat flow in the vicinity of the throat is the convective heat transfer process from the accelerated gaseous flow of combustion gases to the structure walls.

A variety of authors have investigated the convective heat transfer within rocket nozzles [4, 220, 221, 222, 223, 224], with the work of Bartz et al. [225, 228] identified as the most widely used and cited. In the following sections, two expressions of alternate manageability, describing the convective heat transfer in nozzles are presented.

3.7.1.1. Improved Nusselt correlation

Bartz [225] developed a widely used correlation estimating the hot side convective heat transfer coefficient based on Reynolds analogy, relating the heat transfer to the turbulent momentum. Bartz argued, since c_p and Pr do not vary appreciably with temperature, they can be evaluated at stagnation temperature. Density ρ and viscosity however are evaluated at the arithmetic mean of local static temperature and wall temperature and can be expressed as functions of local Mach number and stagnation values according to the isentropic flow relations. With the definitions of Reynolds-, Prandtl and Nusselt number, the heat transfer in an axisymmetric nozzle can then be expressed by the product of values evaluated at stagnation conditions, the area aspect ratio and a correction parameter σ, accounting for all property changes due to high speed flow. Note that only the latter term is not a function of combustion chamber condition only. This leads to the typical notation of the heat transfer coefficient as a product of parameters evaluated at stagnation conditions and the flow correction parameter σ. To account for the effect of radius curvature of the nozzle r_{curv}, Bartz introduced a factor proportional to the throat radius $\sim (2r_t/r_{curv})^{0.1}$, motivated by nozzle similarity considerations. The skin friction parameter was substituted by the skin friction factor for pipe flow. The correlation for convective heat transfer coefficient for a nozzle according to Bartz thus becomes [4, 225]

$$h_g = \left[\frac{0.026}{D_H^{0.2}} \left(\frac{\mu^{0.2} c_p}{\text{Pr}^{0.6}} \right)_0 \left(\frac{p_c}{c*} \right)^{0.8} \left(\frac{2r_t}{r_{curv}} \right)^{0.1} \right] \left(\frac{A_t}{A} \right)^{0.9} \sigma \qquad (3.96)$$

The factor σ, which accounts for all properties variation caused by gas expansion through the nozzle, is given by

$$\sigma = \left[\frac{1}{2} \frac{T_w}{T_0} \left(1 + \frac{\gamma-1}{2} M^2 \right) + \frac{1}{2} \right]^{\bar{\omega}/5 - 0.8} \left[1 + \frac{\gamma-1}{2} M^2 \right]^{-\bar{\omega}/5} \qquad (3.97)$$

M and T are functions of the stream position. Since Eq. (3.97) depends on the wall temperature T_w, which is again dependent on the convective heat transfer, an iterative solving approach is necessary. This is accomplished by choosing a starting wall temperature T_w, at which Eq. (3.96) and (3.97) are evaluated. After solving the thermal model with this boundary condition, T_w is taken from the solution, and Eq. (3.96) and (3.97) are again evaluated to calculate the new boundary condition for the thermal model. These steps are repeated until a convergence value, for the temperature distribution solution of successive iterations, is reached. The solid domain model is discussed in detail in section 3.9.1. The resulting converged solutions for the convective heat transfer coefficients given Eq. (3.96) is shown in Figure 70 for the converging-diverging nozzle section for a transient solution of $t = 30$ s. The vertical line indicates the throat position.
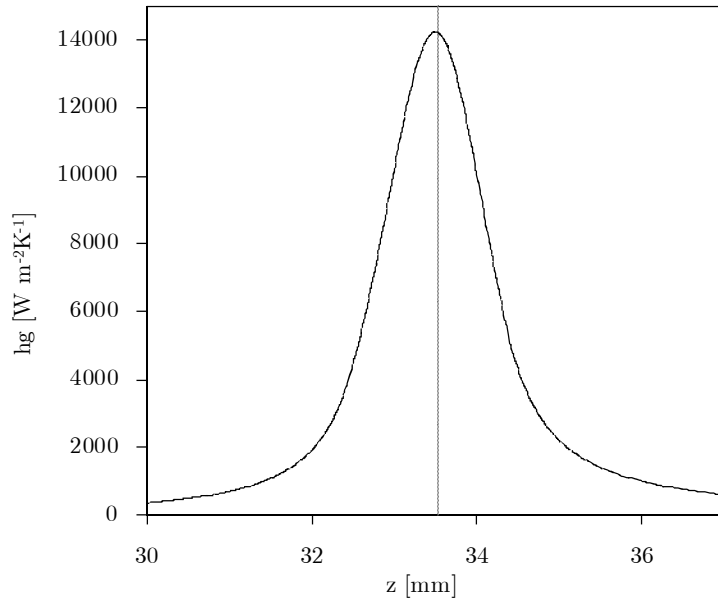
Figure 70 Analytical correlation for the convective heat transfer in nozzle region according to Bartz [225], converged solution

3.7.1.2. Turbulent boundary layer model

In this section, a model for turbulent boundary layer growth is presented and adapted to the given geometry. The derivation is based on the model developed Elliott, Bartz, and Silver [228]. The general validity of this model has been shown by comparison to experimentally determined heat transfer coefficients in experimental rocket thrust chambers [228, 229].

The driving idea of the following model is the assumption, that flux deficiencies occurring in boundary layers can be treated by flow geometry changes for assumed potential flow. A flux defect $(U - u)/\rho$ in the boundary layer necessarily implicates an increased flux in the free stream to obey conservation of mass. Assuming potential flow, this increase can accordingly be described by assuming narrower flow geometry, caused by fictional wall displacement. In the following, the subscript r will refer to the real flow, whereas remaining parameters refer to the potential flow. Capital letters refer to potential or, in the real flow, to free stream flow, whereas non capital letters refer to properties within the boundary layer which are a function of radial distance from the wall in y-direction.

The displacement thickness is defined as the displacement of the wall, making a flow region unavailable for the free stream which causes equal mass flux defect as does the velocity profile within the boundary layer with thickness δ_r [4]:

$$U \delta^* = \int_0^{\delta_r} (U - u_r)\, \mathrm{d}y .$$

(3.98)

92

Under the assumption, that boundary layers are small compared to the free stream flow area, the displacement thickness can be derived by equating the mass flow in the boundary layer with the fictional mass flow that would occur in the displacement region for potential flow velocity U. Solving for the displacement thickness, this gives:

$$\delta^* = \int_0^{\delta_r} \left(1 - \frac{\rho_r u_r}{\rho U}\right) \mathrm{d}y \,. \tag{3.99}$$

With the help of the momentum fluxes of boundary flow and displacement flow, a momentum thickness can be defined as the thickness in the potential flow that leads to a momentum flux equal to the momentum flux defect of the boundary layer compared to the free stream potential flow:

$$\theta = \int_0^{\delta_r} \frac{\rho_r u_r}{\rho U} \left(1 - \frac{u_r}{U}\right) \mathrm{d}y \,. \tag{3.100}$$

In the same manner, an energy thickness can be defined as the thickness in the potential flow which corresponds to the defect in enthalpy flow in the boundary layer compared to the potential flow as:

$$\Phi = \int_0^{\delta_r} \frac{\rho_r u_r}{\rho U} \left(1 - \frac{t_{0,r} - T_w}{T_0 - T_w}\right) \mathrm{d}y \,. \tag{3.101}$$

Assuming that forces acting on the fluid are only caused by pressure gradients and the friction at the wall, the momentum equation is given by [228]:

$$\frac{\mathrm{d}\theta}{\mathrm{d}z} = \frac{C_f}{2}\left[1 + \left(\frac{\mathrm{d}r}{\mathrm{d}z}\right)^2\right]^{1/2} - \theta\left[\frac{2 - M^2 + \frac{\delta^*}{\theta}}{M\left(1 + \frac{\gamma-1}{2}M^2\right)}\frac{\mathrm{d}M}{\mathrm{d}z} + \frac{1}{r}\frac{\mathrm{d}r}{\mathrm{d}z}\right] \,. \tag{3.102}$$

The energy equation is derived assuming adiabatic wall condition with the help of the Stanton number S_t [228]

$$\frac{\mathrm{d}\Phi}{\mathrm{d}z} = S_t\left(\frac{T_{aw} - T_w}{T_0 - T_w}\right)\left[1 + \left(\frac{\mathrm{d}r}{\mathrm{d}z}\right)^2\right]^{1/2} - \Phi\left[\frac{2 - M^2}{M\left(1 + \frac{\gamma-1}{2}M^2\right)}\frac{\mathrm{d}M}{\mathrm{d}z} + \frac{1}{r}\frac{\mathrm{d}r}{\mathrm{d}z} - \frac{1}{T_0 - T_w}\frac{\mathrm{d}T_w}{\mathrm{d}z}\right] \,. \tag{3.103}$$

As the distributions of parameters within the boundary layers remain unknown, standard distributions for turbulent boundary layers found in literature are employed:

$$\frac{u_r}{U} = \left(\frac{y}{\delta_r}\right)^{1/7} \qquad for \quad y < \delta_r$$

$$\frac{u_r}{U} = 1 \qquad for \quad y > \delta_r \tag{3.104}$$

$$\frac{t_{0,r} - T_w}{T_0 - T_w} = \left(\frac{y}{\Delta_r}\right)^{1/7} \qquad for \quad y < \delta_r$$

$$\frac{t_{0,r} - T_w}{T_0 - T_w} = 1 \qquad for \quad y > \delta_r \tag{3.105}$$

,

where Δ_r is the temperature thickness of the real flow. The dimension y is orientated in inwards radial direction normal to the wall, originating at the position of the wall. The proportion of densities in Eq. (3.99) to (3.101) can be determined by the distributions given above and the equation of state of an ideal gas. The assumed distributions within the boundary layer allow the definition of a shape factor:

$$\zeta = \left(\frac{\Delta_r}{\delta_r}\right)^{1/7} , \tag{3.106}$$

which is larger than unity for temperature thickness larger than velocity thickness δ_r. With the help of this shape parameter, the ratio of velocity to momentum thickness (Eq. (3.99) and (3.100)) can be expressed in the case of both $\delta_r < \Delta_r$ and $\delta_r > \Delta_r$ by (a detailed derivation of the expressions can be found in Ref. 228):

$$\frac{\delta^*}{\theta} = \frac{\frac{T_w}{T}\frac{\zeta^7}{7} - I_2 - I_3}{I_1} \qquad for \quad \delta_r < \Delta_r$$

$$\zeta = \left[\frac{\Phi I_1}{\theta\left(I_2' + I_3'/\zeta\right)}\right]^{1/8} \tag{3.107}$$

and

$$\frac{\delta^*}{\theta} = \frac{\frac{T_w}{T}\frac{1}{7} - I_6 - I_7}{I_4 + I_5} \qquad for \quad \delta_r > \Delta_r$$

$$\zeta = \left[\frac{\Phi\left(I_4 + I_5\right)}{\theta I_1'}\right]^{1/8} \tag{3.108}$$

.

The integrals $I_1 ... I_5$ in Eq. (3.107) and (3.108) are found in appendix X.1.

The Stanton number can be expressed by [228]:

$$S_t = \frac{\dfrac{C_f}{2}\left(\dfrac{\Phi}{\theta}\right)^n}{1 - 5\left(\dfrac{C_f}{2}\right)^{1/2}\left[1 - \mathrm{Pr} + \ln\left(\dfrac{6}{5\mathrm{Pr}+1}\right)\right]} \qquad (3.109)$$

The exponent n was chosen to account for a minor correction to fit experimental data and was found to be $n = 0.1$ [228].

Coles [230] showed the possibility of fitting experimental determined wall friction coefficients

$$\bar{C}_f = \frac{\rho \mu_s}{\rho_{aw}\mu_{aw}}\bar{C}_{f_a}$$

as a function of

$$\bar{C}_f\overline{\mathrm{Re}_\theta} = \frac{\rho\mu}{\rho_{aw}\mu_{aw}}\bar{C}_{f_a}\overline{\mathrm{Re}_\theta}\,,$$

where the subscript aw indicate evaluation at the adiabatic wall and s refers to the sublayer structure within the boundary. An expression on the temperature of the sublayer is given in Eq. (3.116). The bar indicates the solution for low-speed [230]. C_{f_a} refers to the adiabatic wall friction coefficient. Using the correlations found by Coles, the wall friction parameter can be calculated based on experimental data from Coles [230] for the low speed adiabatic skin-friction coefficient $\bar{C}_f$ as a function of the product of the wall friction coefficient with the Reynolds number based on the momentum thickness $\bar{C}_f\overline{\mathrm{Re}_\theta}$. The product $\bar{C}_f\overline{\mathrm{Re}_\theta}$ is calculated by

$$\bar{C}_f\overline{\mathrm{Re}_\theta} = \left(\frac{T_{aw}}{T}\right)^{1-\bar{\omega}}C_{f_a}\mathrm{Re}_\Phi \qquad (3.110)$$

with the Reynolds number based on energy thickness being calculated by

$$\mathrm{Re}_\Phi = \frac{\rho U \Phi}{\mu_0}\left(1 + \frac{\gamma-1}{2}M^2\right)^{\bar{\omega}} \qquad (3.111)$$

with $\bar{\omega} = 0.8$ being the exponent of temperature dependence of viscosity, defined by

$$\frac{\mu}{\mu_0} = \left(\frac{T}{T_0}\right)^{\bar{\omega}} \qquad (3.112)$$

.

Coles proposes differing correlations for limits of large and small $\overline{C}_f \overline{\text{Re}}_\theta$, with interpolation of experimentally fitted data points in the intersection region. Thus, the expressions for the turbulent wall friction coefficient become:

$$\left(\frac{2}{\overline{C}_f}\right)^{1/2} = 2.44 \ln\left[\frac{\overline{C}_f \overline{\text{Re}}_\theta}{\overline{C}_f\left(3.781 - 25.104\left(2/\overline{C}_f\right)^{-1/2}\right)}\right] + 7.68 \qquad \text{for } \overline{C}_f \overline{\text{Re}}_\theta > 64.8. \quad (3.113)$$

$$\overline{C}_f = \frac{0.009896}{\left(\overline{C}_f \overline{\text{Re}}_\theta\right)^{0.562}} \qquad \text{for } \overline{C}_f \overline{\text{Re}}_\theta < 2.51. \quad (3.114)$$

The experimentally derived data points for $2.51 < \overline{C}_f \overline{\text{Re}}_\theta < 64.8$ are given in Table 13.

Table 13 Tabulated wall friction coefficients, Refs. 228, 230

$\overline{C}_f \overline{\text{Re}}_\theta$	$\overline{C}_f$	$\overline{C}_f \overline{\text{Re}}_\theta$	$\overline{C}_f$
2.51	0.00590	16.36	0.00290
3.10	0.00524	23.2	0.00269
3.97	0.00464	29.6	0.00255
4.88	0.00426	35.9	0.00246
5.73	0.00398	41.8	0.00238
7.41	0.00363	53.9	0.00227
8.94	0.00340	64.8	0.00219
12.75	0.00308		

The wall friction parameter is plotted in Figure 71.
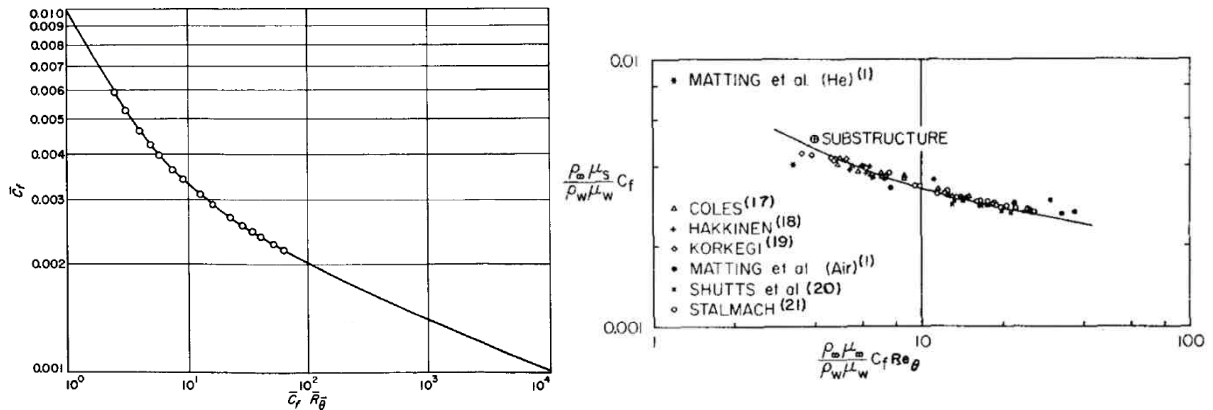
Figure 71 Plotted C_f values determined by experiments from Ref. 230 (left) and experimental values jointly with values determined from correlations from Ref. 228 (right)

Based on the correlations for the low speed friction coefficient, the adiabatic wall friction coefficient C_{f_a}, that is the wall friction coefficient evaluated at the wall temperature, can be determined by [229]

$$C_{f_a} = \frac{\bar{C}_f}{\left(\dfrac{T_{aw}}{T}\right)\left(\dfrac{T_s}{T_{aw}}\right)^{\bar{\omega}}} \tag{3.115}$$

with the sublayer temperature determined accordingly to Coles [230] by

$$\frac{T_s}{T_{aw}} = 1 + 17.2\left(\frac{T_0}{T_{aw}} - 1\right)\left(\frac{\bar{C}_f}{2}\right)^{1/2} - 305\left(\frac{T_0}{T_{aw}} - \frac{T}{T_{aw}}\right)\frac{\bar{C}_f}{2} \tag{3.116}$$

To determine C_f from C_{f_a}, Ref. 228 suggests, for the approximation of an adiabatic nozzle wall:

$$\frac{C_f}{C_{f_a}} = 1 \tag{3.117}$$

An alternative way to calculate the wall friction coefficient C_f is to derive it directly from the low-speed solution of $\bar{C}_f$ employing a film-temperature correction. This approximation serves the model of a severely cooled nozzle wall:

$$\frac{C_f}{\bar{C}_f} = \left(\frac{1}{2}\left(\frac{T_w}{T} + 1\right)\right)^{(\bar{\omega}-3)/4} \tag{3.118}$$

Radiation cooling is best approximated by the adiabatic wall model, therefore Eq. (3.117) is employed to determine the wall friction coefficient.

Solving the system of differential equations comprised by Eq. (3.102) and (3.103) yields the leading boundary layer thickness parameters as a function of stream position. The solution for the given nozzle configuration is shown in Figure 72 along with the value for wall friction parameter. The behavior of minimum thickness at the throat and the general trend of energy thickness larger than momentum thickness for all stream positions agree to the findings in Ref. 228.

Ref. 228 gives a discussion regarding appropriate choice for initial values for momentum and energy thickness. In Figure 72, initial conditions have been chosen to achieve vanishing gradients

$$\left.\frac{\mathrm{d}\Phi}{\mathrm{d}z}\right|_0 = \left.\frac{\mathrm{d}\theta}{\mathrm{d}z}\right|_0 = 0 \tag{3.119}$$
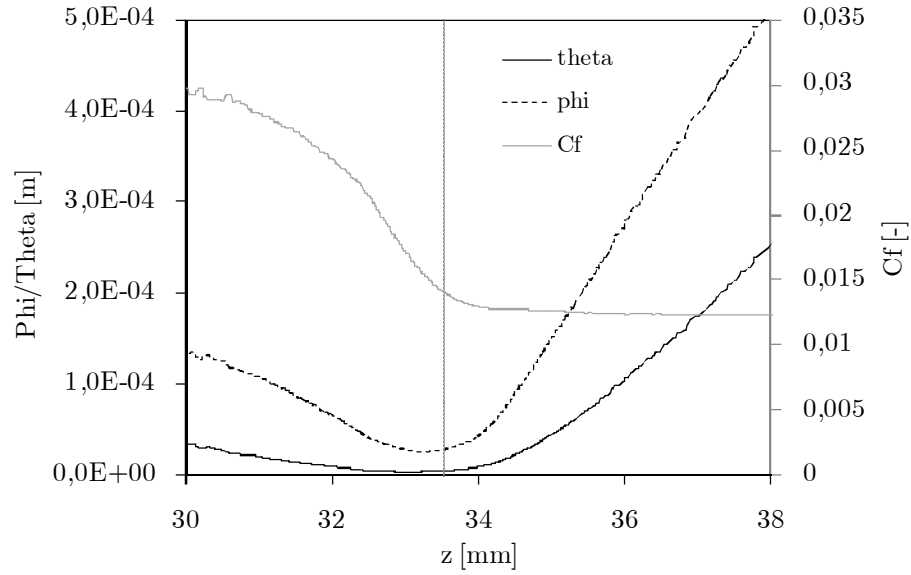
Figure 72 Momentum (theta) and energy (phi) thickness and wall friction coefficient as a function of stream position in the nozzle region

Rapid boundary layer growth for the diverging nozzle section shown in the result in Figure 72 agrees with simulation results based on different models [227]. The solution of the model above allows the determination of the convective heat transfer with the definition of the Stanton number:

$$h_g = c_p \rho U S_t \tag{3.120}$$

and the convective heat flux, incorporating temperature recovery, by:

$$\dot{q}_w = h_g \left(T_{aw} - T_w \right). \tag{3.121}$$

The convective heat transfer coefficient is shown in Figure 73 in combination with the area aspect ratio for the nozzle section.

As heat transfer coefficient is dependent on the wall temperature T_w, which is again, among other parameters, a function of heat transfer, iteratively solving of the system is required, with the FEM solution of temperature at the walls from the previous iteration acting as T_w for the successive iteration.

An analysis of the increase of convective heat transfer based on the turbulent boundary model as a function of combustion chamber pressure can be found in Ref. 89.
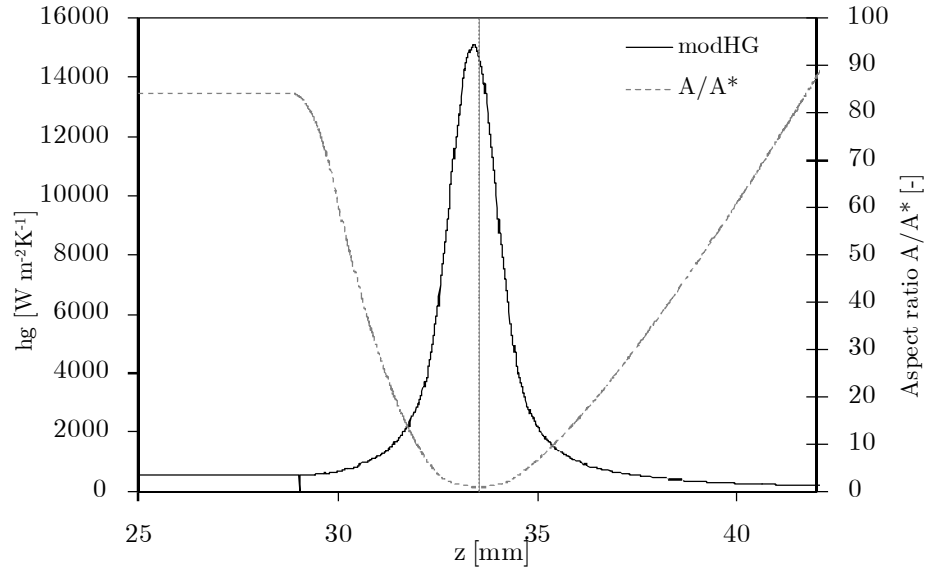
Figure 73 Turbulent boundary layer convective heat transfer coefficient and area aspect ratio in throat region, converged transient solution $t = 30$ s.

Back et al. [70] came to the conclusion that the turbulent boundary layer model outlined in this section showed better accordance to their experimental results than the correlations presented in section 0.

Smith [229] investigated the accordance of the turbulent boundary layer model presented by Bartz with experimental results, using a solid rocket motor with two different throat radii of r_t ≈ 2.47 mm and r_t ≈ 1.7 mm, and chamber pressure levels of p_{CC} ≈ 15bar, p_{CC} ≈ 28 bar and p_{CC} ≈ 51 bar. He reported overestimation of the turbulent boundary model. It can therefore be concluded that the convective heat transfer presented in this section allows for calculating a worst case scenario in terms of thermal load to the combustion chamber.

3.7.2. Convective heat transfer in the cylindrical combustion chamber section

The convective heat transfer in the cylindrical combustion chamber section is dominant in the zone of reattachment of the swirling flow downstream of the backward facing step, where combustion of the propellant mixture occurs and highest stagnation temperatures are found. The swirling flow in combination with the backward facing step causes not only the proximity of the combustion zones to the wall but also increases the total velocity $u^2 = u_{ax}^2 + u_{tan}^2$, and therefore the convective heat transfer coefficient.

Ref. 231 investigated heat fluxes through cylindrical combustion chamber walls of an LOX/gaseous methane combustion engine at flow rates of 7.5 g s^{-1} with a combustion chamber diameter of 2.54 cm. They measured an increase of chamber heat flux by a factor of two for their swirl injector configuration compared to shear coaxial injectors. For a chamber

pressure of 20 bar, they measured a heat flux density in the swirl combustion case of ~ 6.5 MW m^{-2}.

Locally increased Nusselt numbers in swirl configurations in combination with a backward facing step have been investigated by various scholars, including Ref. 232. Their findings are presented in Figure 74 for a swirl air flow downstream of a sudden expansion, showing Nusselt numbers of 250 (for Re = 7600), after a backward facing step, decaying with distance to value of Nu ≈ 70. The swirl number for their test setup has been calculated to $S ≈ 1.37$, based on the description of the experimental setup [232], assuming negligible vane thickness.
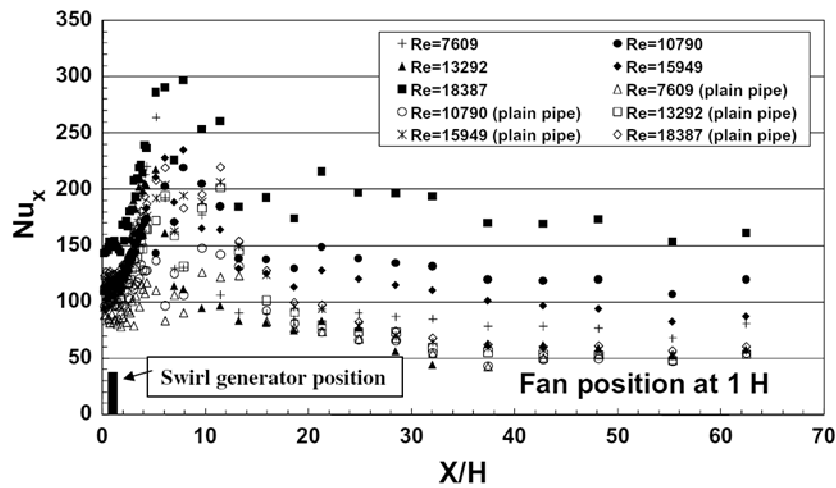
Figure 74 Increase in Nusselt number due to reattaching swirl flow, Ref. 232

An investigation of increase in Nusselt number as a function of swirl number at high Reynolds numbers can be found in Ref 208. The dependency of the Nusselt number in such configurations on Reynolds number has been investigated by various scholars [233, 234].

Studies for low Reynolds numbers have been conducted by Saha et al. [235] for liquid flow using twisted tape inserts to generate swirling flow fields. Again, significantly increased Nusselt numbers compared to non-swirling flows have been reported.

Hedlund et al. [236] investigated the effect of swirl flow on heat transfer in the absence of a sudden flow expansion. They derived a correlation describing the local increase of Nusselt number from experimental data. They derived a correlation from experimental data for air streams at Reynolds numbers of Re > 2000

$$Nu_D = 0.63 \left(\frac{T}{T_w} \right)^{5.7} \mathrm{Re}_D^{\frac{0.56 T_w}{T}} \tag{3.122}$$

.

Hedlund and Ligrani [237] developed an alternative correlation based on experimental data in a similar test configuration of swirl flow without sudden flow expansion, presented in Figure 75.
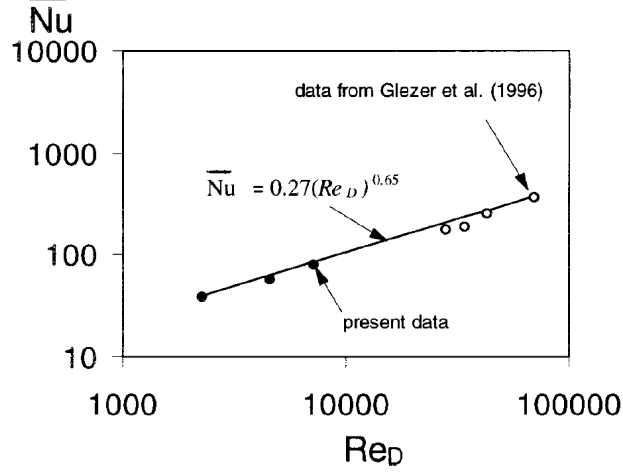
Figure 75 Increase in Nusselt number due to reattaching swirl flow, Ref. 237

Their correlation, valid for $2000 < \mathrm{Re_{eD}} < 80000$ becomes

$$Nu = 0.27 \, \mathrm{Re}_D^{0.65} .$$
(3.123)

Applying their correlation to the DM thruster configuration, with Reynolds number evaluated using the total azimuthal velocity and the vortex ring diameter, therefore incorporating the geometry change due to the rearward facing step [165]

$$\mathrm{Re} = \frac{\rho u D_H}{\mu} ,$$
(3.124)

applied to the DM combustion chamber, for density and flow velocity corresponding to the location of full combustion, yields Nu = 47.5 and therefore a convective heat transfer coefficient at this position of

$$h_g = \frac{Nu_D \lambda}{D_H} \approx 3650 \quad \mathrm{Wm^{-2}K^{-1}} .$$
(3.125)

Density and velocity are however parameters of temperature and therefore vary as functions of axial position within the combustion chamber due to non-adiabatic flow. Reynolds and Nusselt numbers and the convective heat transfer coefficient in Eq. (3.125) are thus calculated dependent on axial position, according to section 3.6.2.

3.7.3. Radiation

Heat transfer by radiation refers to energy loss of a gas, liquid or solid by emitted electromagnetic radiation at the expense of lowering the internal energy of the body. It generally refers to the integral energy transfer over the entire spectrum with its maximum in the thermal infrared region. In the context of propulsion systems, radiation effects become significant in two areas: Radiation emitted by the combustion gases, which is absorbed by the chamber walls and therefore increases the total heat transfer to the thruster structure. The second significant radiation process occurs at the outer chamber wall, emitting radiation to the ambient space and spacecraft, which is therefore an important feature for thrust chamber cooling.

Various authors address the radiative heat transfer contributions within the combustion chamber as a contribution to the overall heat transfer from the hot gas to the chamber structure. Most authors stress the complexity of this matter, influenced by the molecules radiative and absorptive spectral properties, as well as contributions from possible presence of liquid and solid particles such as soot from excess fuel [4, 238]. The complexity of these processes together with the effort to solve complex geometrical integrals lead to rough order of magnitude estimations found in propulsion textbooks, such as in Sutton and Biblarz [3], referring to a contribution of radiative heat transfer to the overall heat transfer in the order of 5% to 35%. However, there is considerable literature available on detailed numerical models incorporating spectral details such as narrow and wide band models [239]. The most commonly used numerical model is the weighted-sum-of-grey-gas model, in which the emissivity of the real gas is assumed to be the sum of weighted emissivities of multiple grey gases, which are then independent from the radiation frequencies [240, 241]. Various authors have expanded and generalized this model to fit to a variety of different problems, including soot contributions [242, 243]. Benchmark evaluations of numerical models concerning their overall ability to model the resulting radiative heat flux are available in literature [244, 245]. In addition to literature concerning with radiative heat transfer only, Viskanta [246] gives an overview of combined convective and radiative heat transfer, including a section on turbulent combustion flow.

However, as indications are that the contribution of radiative heat transfer to the overall heat transfer is in the order of less than 10 % with decreasing importance for decreasing chamber geometries [3, 247], a preliminary estimation based on engineering models is conducted to avoid unnecessary efforts spent for detailed numerical modeling in the case of small radiative contributions.

3.7.3.1. Gas radiation within combustion chamber

An approach following the synopsis on mixture gas radiation by Vortmeyer and Kabelac [248] is presented in this section. In this approach, the actual geometry is replaced by equivalent geometries to ease the calculation of occurring integrals by utilizing symmetry effects. A calculation for non-luminous flames is presented in this section, where the leading radiative sources are triatomic combustion product gases H_2O and CO_2, as opposed to soot particle radiation in luminous flames [250].

The decrease of incident intensity I along a line-of-sight path dl through a gas is given by the radiation transport equation [239]:

$$dI_\lambda = -\alpha_\lambda I_\lambda dl .$$
(3.126)

where α is the linear absorption coefficient. Integrating over the wavelengths λ yields the total intensity change

$$dI = -\alpha I dl .$$
(3.127)

Assuming constant temperature,

$$I = I_0 e^{-\alpha l} ,$$
(3.128)

the total intensity absorbed over length l can be written as

$$I_0 - I = I_0 \left(1 - e^{-\alpha l}\right).$$
(3.129)

If assuming a hemisphere with surface element ΔA located at its centre as shown in Figure 76, all beams of intensity emitted by this surface element have equal traverse paths to the hemisphere's surface. In this case, Eq. (3.129) can be expressed in terms of the radius r of the hemisphere

$$I_0 - I = I_0 \left(1 - e^{-\alpha r}\right).$$
(3.130)
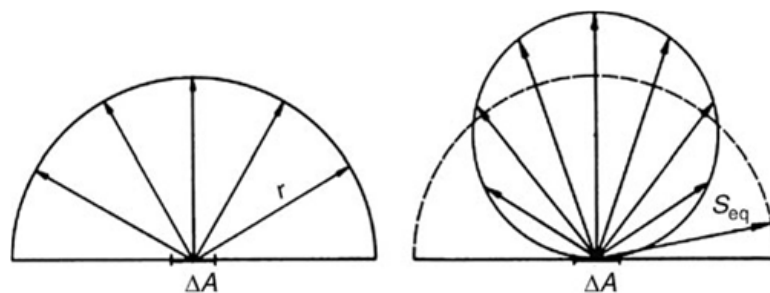
Figure 76 Hemispheric gas space geometry and equivalent layer thickness for sphere, from Ref. 248

To account for geometries other than hemispheres, the concept of equivalent layer thickness s_{eq} is introduced. The main idea is to reduce any geometry to an equivalent hemisphere with radius s_{eq}. This radius is defined as the radius of a hemisphere absorbing the same amount of radiation as the actual geometry. This is shown for a sphere on the right hand side of Figure 76. Eq. (3.130) thus becomes:

$$I_0 - I = I_0 \left(1 - e^{-\alpha s_{eq}}\right).$$
(3.131)

The main disadvantage of this simple concept is the dependency of s_{eq} on the optical density of the absorbing gas, which is the product of mean length l and absorption α. Values for s_{eq} can be found in Ref. 248 for a typical optical density. Ref. 239 gives values for both vanishing optical density and finite values for the optical thickness. Ref. 248 gives an expression for geometries differing from the example geometries:

$$s_{eq} = 0.9 \frac{4V}{A},$$
(3.132)

where V and A are the gas volume and surface respectively. A detailed synopsis of determining the effective gas emissivity ε_g for the narrow band emitters H_2O and CO_2 and the geometry dependent absorption A_v and deriving the radiative heat flux absorbed by the chamber walls can be found in appendix X.3.

The net flow rate density of thermal radiation energy between a gas volume and the surrounding wall at the wall surface is given by [248]

$$\dot{q}_{rad} = \sigma_{SB} \frac{\varepsilon_w}{1 - (1 - \varepsilon_w)(1 - A_V)} \left(\varepsilon_g T_g^4 - A_V T_w^4\right).$$
(3.133)

This allows the calculation of the mean radiation flux at the surface of the equivalent cylinder, which will be approximated as equal to the mean radiation flux of the combustion gas to the surface of the combustion chamber, by Eq. (8.7).

For $\varepsilon_w = 0.16$, which corresponds to Pt-20%Rh, the chamber wall material of the DM thruster, at the reference temperature of $T = 1300$ K (Figure 78), the radiative power density and the total radiative power to the combustion chamber inner surface, originating from hot combustion product gases Q_{rad}, become

$$\dot{q}_{rad} = 31.37 \, \text{kW m}^{-2}$$
$$Q_{rad} = 26.07 \, \text{W} .$$
(3.134)

In comparison to an average value of $\dot{q}_{conv} \approx 1.5 - 5.0 \, \text{MW m}^{-2}$ (section 3.9.2) originating from the convective heat transfer calculated by the heat transfer model for non-adiabatic conditions

incorporating swirl flow, the radiative contribution to the total heat transfer from the combustion gases to the chamber structure amounts to 0.6-2.1 %. This result is below the lower boundary of radiative heat transfer contribution in combustion chambers from Sutton and Biblarz [3] and corresponds well to the miniaturized geometry employed in this investigation, leading to small values for the equivalent layer thickness

$$s_{eq} = 0.62128 \cdot 10^{-2} \text{ m}.$$

(3.135)

3.7.3.2. Radiation from luminous flame

The second main contribution to the radiation emitted during the combustion of fossil fuels besides the radiation from the hot tri-atomic exhaust gases H_2O and CO_2, is the radiation emitted by suspended particular matter such as soot particles [238]. Ref. 251 showed in a numerical analysis of total combustion chamber heat flux, incorporating a weighted-sum-of-gray-gases model accounting for H_2O and CO_2 radiation, the importance for radiation originating from soot particles in LOX-kerosene combustion chambers. Soot particles are mainly carbon particles originating from the gas phase combustion of hydrocarbons with typical mean diameters in the order of 10-100 nm [238], causing visible flames and thermal emission. Whereas no quantitative theory able to predict soot formation and therefore soot concentration is known [238], reference concentration values can be found in literature focused on numerical investigation of combustion processes [251, 261, 262, 263, 264]. Ref. 251 calculated maximum soot mass fractions within the combustion zone of $6 \cdot 10^{-3}$ at $p_{CC} \approx 20$ bar chamber pressure. However, their discussion on dependency of soot formation on chamber pressure suggests the following dependency, given in soot volume fraction f_v [251]:

$$f_v \propto p^n \quad (1 \leq n \leq 2)$$

(3.136)

Thus, their mass fraction can be assumed to constitute an upper limit to the given application, since chamber pressure is significantly larger than the chamber pressures investigated in this work. Ref. 238 gives emissivity values for soot loaded combustion volumes based on soot mass loading B_r and equivalent layer thickness s_{eq}, as shown in Figure 77 for oil flames.

Based on the results from References 251 and 238 together with the results for equivalent layer thickness discussed in section 0, soot emissivity values of $\varepsilon_r < 0.02$ are expected. Based on this upper limit, an upper limit for the heat transfer including soot radiation is estimated, according to Eq. (3.133) [238, 248]:

$$\dot{q}_{rad} < 71.76 \text{ kW m}^{-2}$$
$$Q_{rad} < 60.0 \text{ W}.$$

(3.137)

In comparison to an average value of $\dot{q}_{conv} \approx 1.5 - 5.0 \text{ MW m}^{-2}$ (section 3.9.2) originating from the convective heat transfer, the radiative contribution to the total heat transfer from the

combustion gases to the chamber structure amounts to approximately 1.4-4.8 %. This result corresponds to the findings of the contribution of radiative heat transfer in combustion chambers from Sutton and Biblarz [3] and, especially for combustion chambers featuring small geometries [247]. The increased radiative contribution for larger chamber geometries due to larger equivalent layer thickness makes the small contribution for the miniaturized chamber geometry investigated consistent with the findings from other authors [245].

Therefore, contribution of internal chamber radiation from combustion gases and soot particles is neglected in the simulation and is treated as underestimating error when discussing the simulation results.
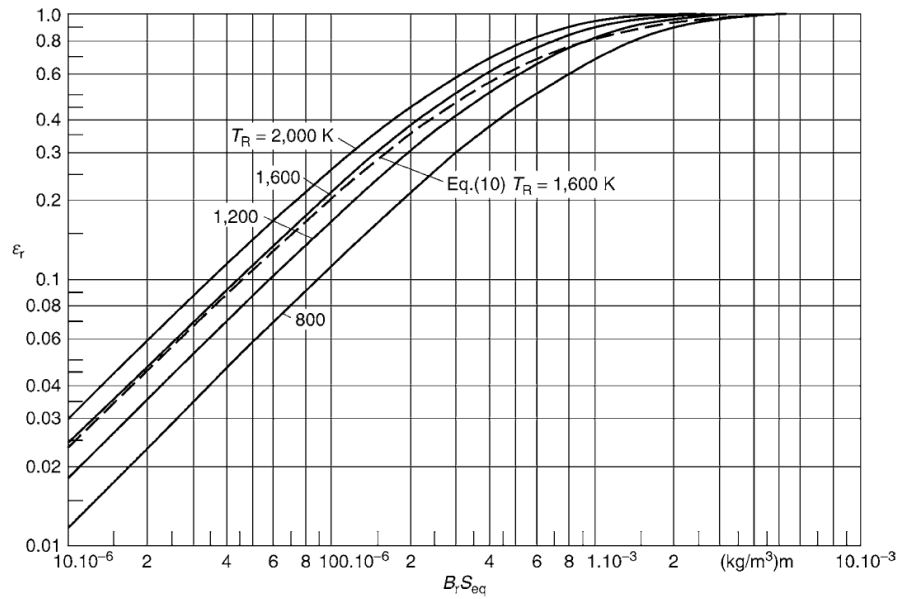
Figure 77 Soot emissivity as function of soot mass loading B_r and equivalent layer thickness s_{eq}

106

3.8. Combustion chamber and nozzle cooling
3.8.1. Different cooling approaches

A variety of text books discuss the topic of cooling approaches for thrust chambers and their applicabilities [3, 4, 115]. Sutton and Biblarz [3] for example give a classification of cooling techniques according to the maximum heat flux density in the combustion chamber walls. Cooling techniques of thrust chambers can generally be divided into transitional capacitive cooling, where a large heat sink allows, in combination with high thermal conductivity, for capacitive cooling, and steady state cooling techniques. Since the former either require large thermal masses and therefore inevitable large chamber masses or limitations to the firing duration, this approach is not applicable to the given thruster concept, although it was used in the experimental ignition chamber described in section 4.3.

Steady state cooling techniques encompass regenerative cooling, where a low temperature propellant is fed along the throat and combustion chamber outer wall for active cooling purposes [252]. This approach is an attractive cooling technique since heat lost by the combustion gases is used to increase the enthalpy of the injected propellants, considerably decreasing energy losses. This approach, usually employed in high thrust, high mass flow engines, was investigated for miniaturized bipropellant engines [253, 254], but was later dismissed due to the high complexity in manufacturing. Other steady state cooling approaches include ablative cooling, transpiration cooling or film cooling techniques. Ablative cooling utilizes melting and vaporization of thrust chamber wall materials to dissipate heat [115]. In the film cooling approach, a certain amount of propellant is fed along the chamber walls, creating locally zones of reduced combustion temperature and therefore reduced heat flux to the chamber walls [3]. Whereas this additional propellant is injected through holes around the main injector in case of film cooling, propellant is introduced into the combustion chamber via partially porous combustion chamber walls in case of transpiration cooling. However, these techniques necessarily decrease the overall combustion performance, since the additional injected propellant is not completely combusted, whereas ablative cooling limits the lifetime especially regarding throat erosion [3, 4]. The latter is considered especially problematic for combustion chamber pressure built-up in an autoignition configuration. A cooling approach for low heat flux combustion chambers, most commonly used for low thrust, small engines, is the radiative cooling of the combustion chamber [255]. This approach features highest combustion chamber wall temperatures of all cooling techniques discussed above, and therefore poses stringent requirements for the high temperature behavior of the chamber material, necessitating the utilization of usually costly materials. However, the high wall temperatures found for radiative cooling lead to a decreased heat loss of the combustion gases compared to other cooling approaches and therefore high performance.

3.8.2. Radiative cooling approach

Thermal radiation of the thruster is investigated as cooling method of the bipropellant engine. Compared to other cooling approaches like regenerative cooling or film cooling, this strategy features simplicity and avoids decreased performance caused by the cooling technique, as this is the case for film cooling. The main drawback of radiative cooling of the thrust chamber is the high structural temperature, usually necessitating exotic high temperature materials. However, the high wall temperatures for purely radiation cooled chambers also imply smaller heat loss of the propellant gas to the structure and have therefore a positive impact on thruster performance. Ref 256 reports an increase in specific impulse of up to 20 s for high temperature iridium coated rhenium chambers (up to 2200 °C) compared to traditional niobium chamber materials. The high wall temperatures found for radiative cooled chambers are explained by the dependency of radiated energy on the fourth power of temperature in the Stefan-Boltzmann law

$$P_{rad} = \varepsilon_{surf} \sigma_{SB} A T^4 .$$
(3.138)

Besides the strong dependence on temperature, the total radiated power is dependent on the radiating surface area and the material surface dependent parameter of emissivity. The emissivity is a material parameter of the thrust chamber and its surface properties. The proper choice of material is therefore a trade-off between thermal transport properties, the ability to withstand stresses at high temperatures, radiative properties, machinability and cost.

A variety of scholars have investigated different materials and alloys for high temperature rocket chamber walls [257, 258, 260]. Decker [89] conducted a thorough structural analysis of candidate materials Iridium and Platinum-Rhodium alloy. The choice of material was based, besides acceptable emissivity, on the ability to withstand the pressure exerted by the combustion gases at high temperatures over various thermal cycles. Machinability at moderate expenses as well as relatively moderate material costs have been included as additional requirements complying with the requirement of low cost propulsion.

The inert nature of platinum and platinum based alloys, as well as its availability and machinability and the ability of laser welding with high temperature steel alloys such as Nimonic 90 led to the choice of Pt-20%Rh as proper combustion chamber material, despite its low emissivity values, as discussed in section 4.5.

Ref. 259 gives maximum experimental operation temperatures for thruster conditions for the materials employed as 1100 °C for Nimonic 90 and 1650 °C for platinum-rhodium alloys. Both materials feature long space heritage and fail-safe operation in radiation cooled onboard thrusters at these temperature levels.

Emissivity values of platinum and platinum based alloys are given Figure 78. Temperature dependent values for combustion chamber materials Platinum (polished) and Pt-10%Rh are

based on the literature indicated, whereas properties for Pt-10%Rh and Pt-20%Rh have been calculated using Maxwell's theory.
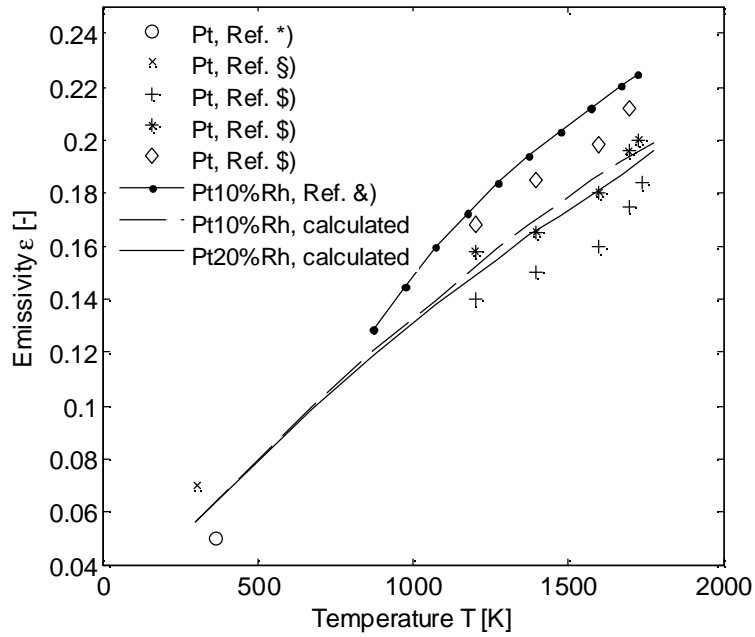
Footnotes: *) Ref. 265, §) Ref.102, $) Ref. 266, &) Ref. 267

Figure 78 Total surface emissivity as function of temperature for Pt (polished), Pt-10%Rh and Pt-20%Rh

Besides the dependency on the surface material property ε, the total radiative power emitted by the thrust chamber is a function to the fourth power of temperature and the total radiative surface area. The temperature at the radiative surface is dependent on the heat conduction within the chamber wall, as depicted in Figure 79. Due to the cylindrical nature of the combustion chamber, an increase in wall thickness leads to an increase in the radiative surface area A, which has a positive impact on the radiative cooling. However, the heat conduction, which introduces an inverse proportion to the chamber wall thickness, then leads to a decrease of temperature at the radiative surface, which has a negative impact on the total radiated power. The contributions to the thermal budget within the chamber wall are depicted in Figure 79.
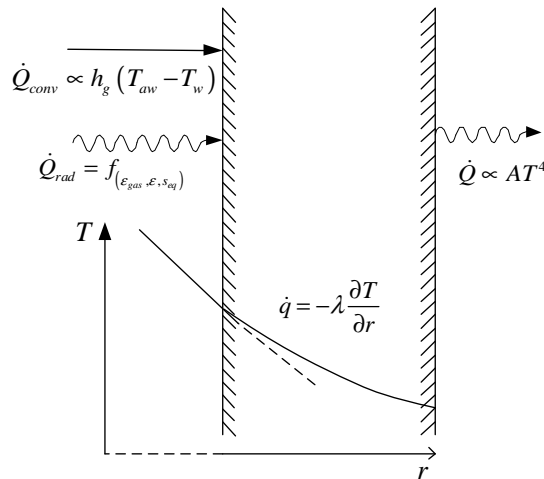
Figure 79 Radiative chamber cooling

The proper design of chamber wall thickness in the context of cooling capabilities is therefore a trade-off between the heat transport resistance within the wall and increasing the radiative surface. This is especially of great importance in the vicinity of peak heat flux from the hot gas to the chamber caused by the nature of the hot gas convective heat transfer coefficient at the throat region of the nozzle. However, high material densities cause a significant increase in thruster structural mass which violates the requirement of miniaturization. A tradeoff between thermal stress and mass has led to the final design of the DM thruster throat configuration.

3.9. Thruster simulation results
3.9.1. Description of simulation

The simulation of the thruster system has been performed using the finite element solver Ansys Multiphysics. The FEM geometry comprises of the solid model of the DM thruster described in section 4.5, with a simplified injector compartment geometry. The complex swirl injector was not modeled, as focus of the simulation was laid on the evaluation of the critical combustion chamber wall temperatures located further downstream. A catalyst of $L_M = 10$ mm length has been modeled in accordance with the experimental thruster. However, the decomposition chamber flange was not modeled, since no interest was laid on the thermal behavior of this upstream section of the thruster. The FEM mesh of the solid domain used for simulation purposes, featuring adaptive mesh size, is shown in Figure 80.
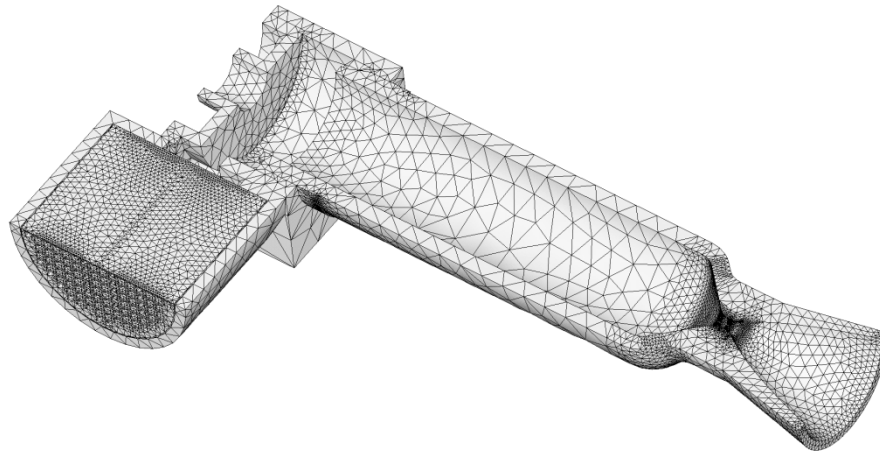
Figure 80 FEM mesh of DM thruster geometry with catalyst.

The thermal fields within the solid domain of the thruster were modeled according to Eq. (2.27). Hot gas side boundary conditions within the combustion chamber were modeled according to the correlations for convective heat transfer coefficients for the cylindrical combustion chamber section developed in section 3.7.2. The results presented hereafter base on the hot gas convective heat transfer in the nozzle section determined by the turbulent boundary layer model described in section 3.7.1.2, although the simulation would also allow to use different formulations such as Eq. (3.96). However, literature indicated the solution of

the turbulent boundary model to fit the experimental data more precisely [70]. Stagnation combustion parameters were determined using NASA CEA [92] as discussed in section 0.

Temperature boundary conditions within the decomposition chamber were modeled according to the stationary solution depicted in section 2.3.5. Temperature boundary conditions for the surfaces in contact with decomposed hydrogen peroxide were modeled using the exhaust decomposition temperature found by the model in section 2.3.5 and a heat transfer coefficient for laminar flow α, based on Nusselt correlation. Linear interpolation from catalyst exhaust temperature to combustion stagnation temperature was employed downstream of the injector location for a distance d_{comb}. The interpolation length was chosen in accordance to the findings from section 3.4.2. The model was solved for non-adiabatic flow within the cylindrical combustion chamber section (section 3.6.2) with convective heat transfer coefficients in accordance with section 3.7.2. Flow within the combustion chamber was modeled incorporating swirl flow according to section 3.6.3.4. Thermal boundaries on the thruster's outer surface were modeled by radiation exchange with surrounding vacuum, as discussed in section 0, with material parameters for Pt-20%Rh and Nimonic chosen in accordance to the materials employed in the DM thruster. In addition to the radiation boundary, a free convective heat transfer at the outer surface of the thruster was modeled to resemble ambient test conditions as found in the experimental investigation. It should however be noted that this does not comply with the final application of the thruster in space but allows for an adequate comparison to the experimental results from section 4.5.3.1. No radiation from luminous flame or combustion product gases within the combustion chamber was modeled. To resemble the test conditions of the DM thruster, flow separation with significantly reduced heat transfer was modeled according to the separation criteria in Eq. (4.16) as discussed in section 4.5.3.2.

3.9.2. Results

Figure 81 shows the converged solution of hot side wall temperature for a time of $t = 30$ s after bipropellant ignition. The data points shown are the solutions for all nodes of the three dimensional calculation grid sorted by axial distance z. Note that inhomogeneities caused by the injector head lead to non uniform temperature distribution for different angular positions, indicated by scattering of the temperature solution for the region near the injector. This result shows, in accordance to the DM experimental results presented in section 4.5.3, a peak wall temperature for the nearly stationary case near the zone of reattachment of the swirling combustion flow downstream of the backward-facing step. This is traced back to the high swirl number imposed by the injector and may be avoided in future thruster designs by lowering the tangential injection velocities within the injector. This can be easily achieved by larger injection cross sectional areas, as in the case of the EBB injector geometry. Due to the high heat losses in this region of peak heat transfer, gas temperature is considerably reduced at downstream positions. The peak in convective heat transfer coefficient in the vicinity of the throat, indicated by the vertical dotted line, is translated into high wall temperatures at the hot

side wall of the thrust chamber. However, significantly increased wall thickness near the throat leads to lower surface temperatures near the throat compared to the cylindrical chamber section, as shown in Figure 83.
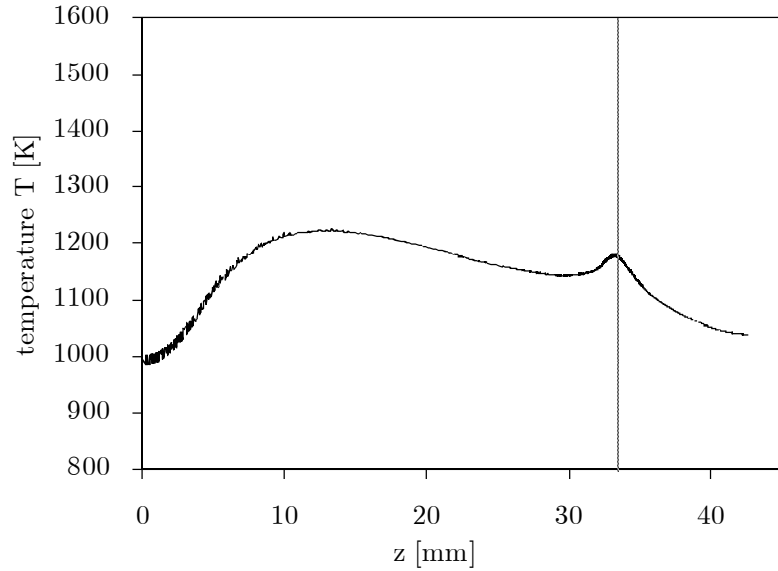
Figure 81 Combustion chamber hot gas side wall temperature for converged solution for $t = 30$ s.

Figure 82 shows the convective heat flux density to the combustion chamber wall as a function of axial position z in the region near the throat. Due to temperature decreased in the cylindrical section, heat flux decreases with increased axial distance from the injector plate until the converging chamber geometry causes acceleration of the exhaust gases and therefore significantly increased heat flux densities peaking in the vicinity of the geometrical throat, indicated by the vertical dotted line. The area aspect ratio is shown to visualize the chamber geometry.
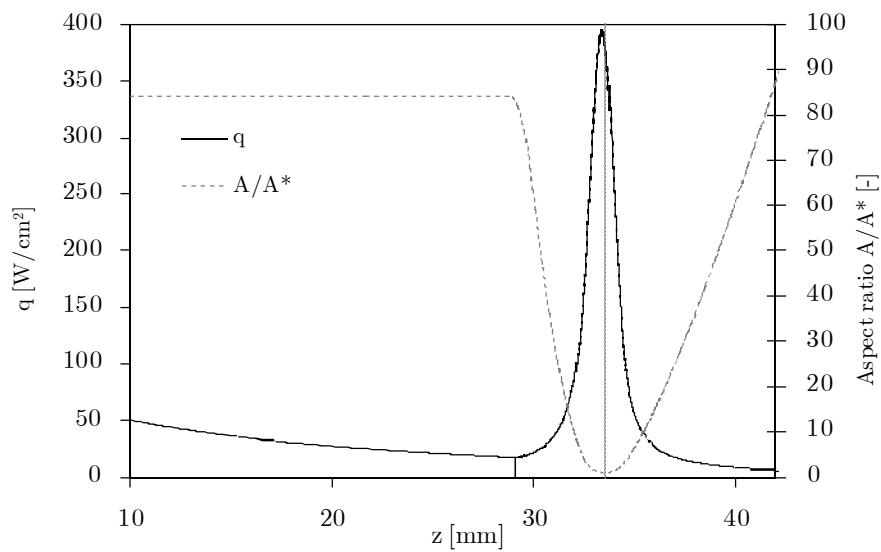
Figure 82 Heat flux to structure near throat, for converged solution for $t = 30$ s.
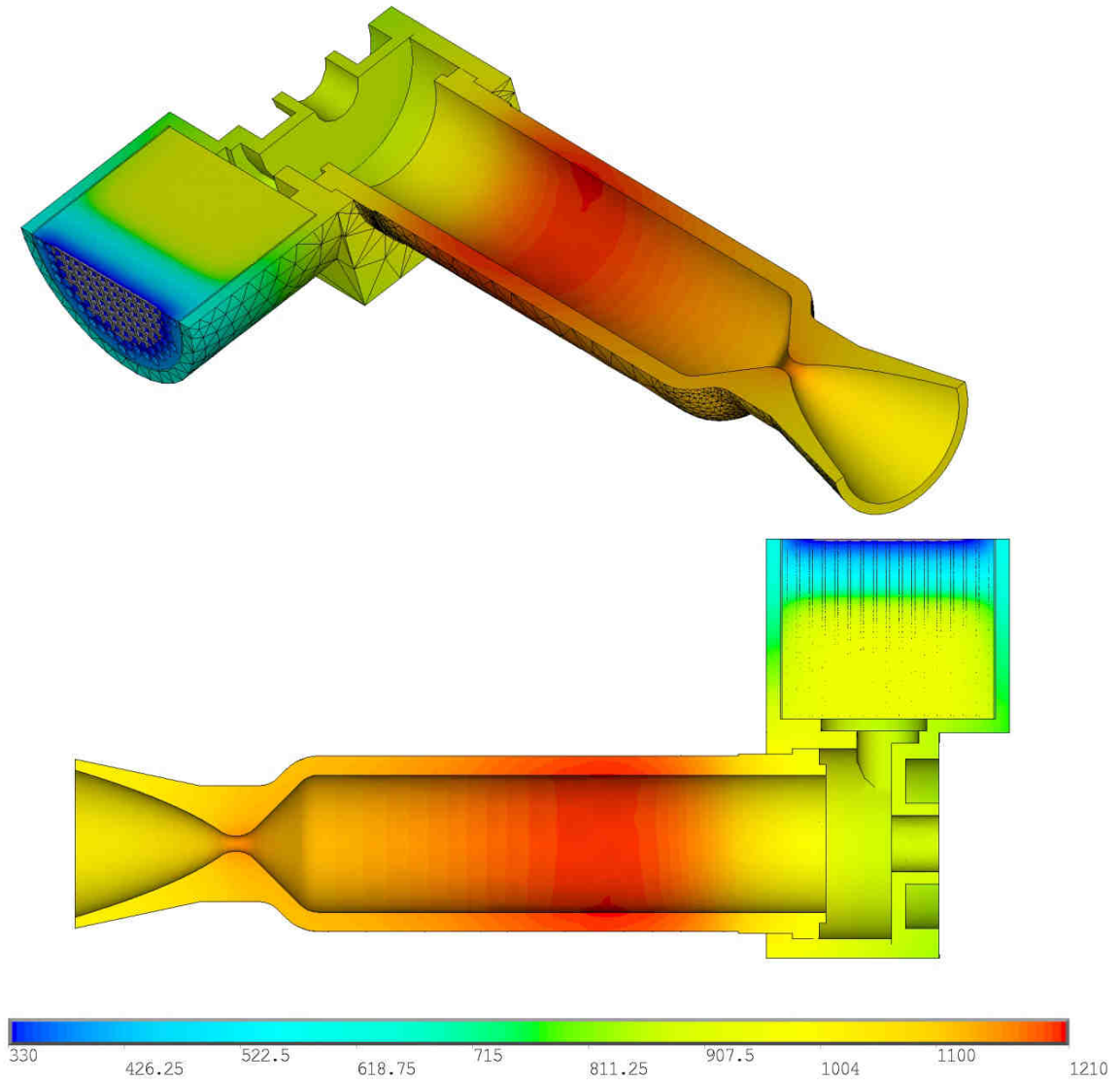
Figure 83 Converged solution of thruster hot gas side structural temperature for non-adiabatic conditions in cylindrical section, temperatures in Kelvin

The solution of the thermal simulation for the hot gas side of the thrust chamber is shown in Figure 83 for the near stationary case of $t = 30$ s, resembling the experimental DM thruster long duration test presented in section 4.5.3.1. The corresponding surface temperature distribution on the thruster outer surface is shown in Figure 84. Comparison to the experimental data in Figure 168 for the corresponding bipropellant firing time, shows an underestimation of maximum temperature in the cylindrical chamber section of $\Delta T \approx 180$ K, whereas the difference from experimental data to the simulation in the vicinity of the throat results in a relatively good accordance of $\Delta T \approx 30$ K. While the uncertainty in absolute values in the experimental data prevents a precise evaluation of the simulation results, this shows while Eq. (3.125) is able to predict the order of magnitude of the heat losses in the cylindrical combustion chamber section, an underestimation of the overall heat transfer coefficient in this region is anticipated.
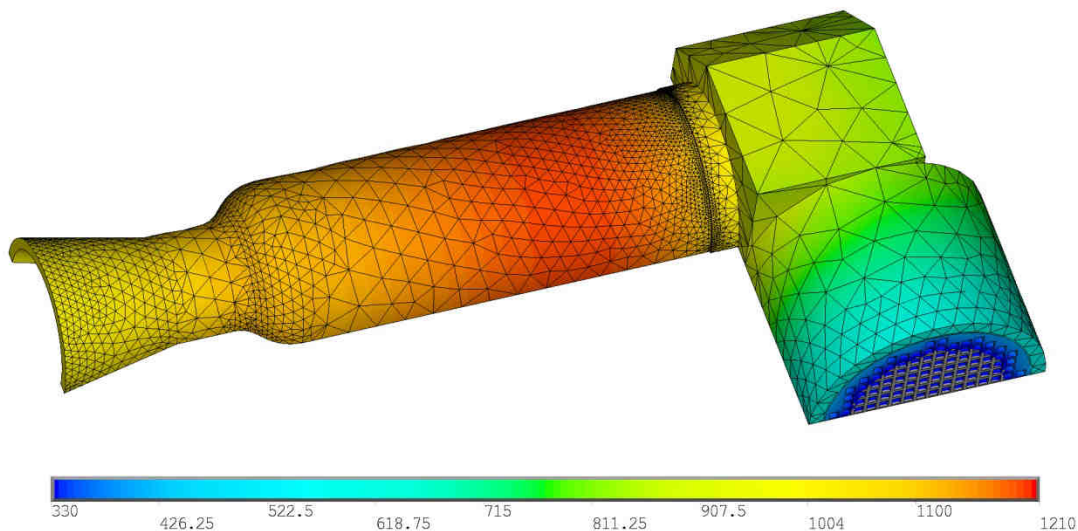
Figure 84 Converged solution of thruster structural temperature for non-adiabatic conditions in cylindrical section, temperatures in Kelvin

The experimental efforts undertaken in section 4.5 allowed determining the transient surface temperature evolution at three different axial locations on the outer surface of the combustion chamber. Although, as discussed in the experimental section, the absolute temperature values determined are potentially afflicted with errors, the data presented in Figure 168 allows for a relative comparison to the transient temperature evolution of the simulation. The modeled temperature evolution is shown in Figure 85. It should be noted that a uniform combustion chamber initial structural temperature of $T = 573$ K (corresponding to the highest structural temperature appearing in the experimental data) was used for the simulation, whereas the structural temperature of the DM chamber at time of transient into bipropellant mode showed a difference of $\Delta T \approx 100$ K over the axial distance of the three thermocouples.
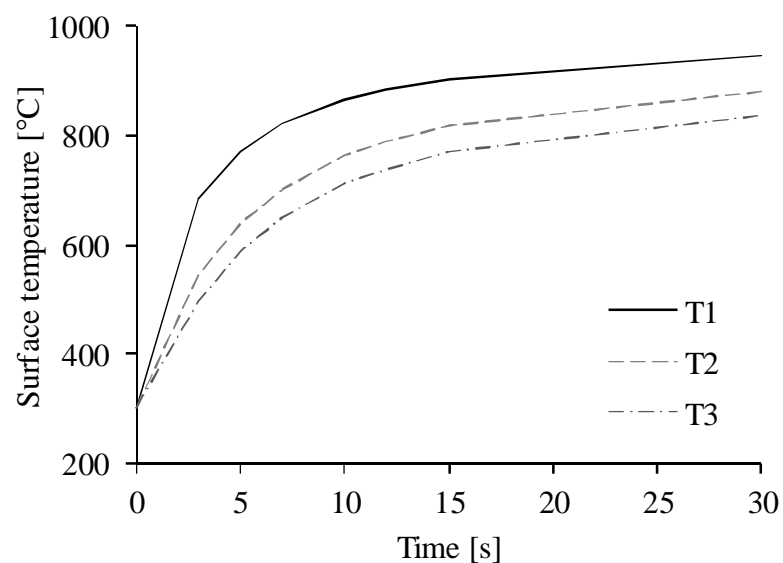
Figure 85 Transient solution for surface temperature of combustion chamber.

While good accordance in the transient behavior according to the temperature gradient is obtained, comparison of Figure 85 to the corresponding experimental data presented in Figure 168 shows a general underestimation of surface wall temperature by the simulation. This

114

underestimation is even further increased since the temperature measurements in Figure 168 are anticipated to be afflicted with a negative error due to thermocouple placement as discussed in section 4.5. However, the simulation does not incorporate any internal radiation from soot and combustion product gases, as discussed in section 0. As discussed in these sections, neglecting the radiative heat exchange is anticipated to introduce an error concerning the overall heat transfer rate of ~ 2-7 %, possibly explaining the underestimations in surface wall temperatures found in the simulation. In addition, the uncertainty introduced by convective heat loss due to free convection in the experimental setup remains widely unknowns since tests have been conducted in an uncontrolled environment in an outside test facility.

The transient temperatures shown in Figure 85 however show temperatures to level off at temperatures below maximum system temperatures proven in long term space propulsion operation [259] of the materials employed and thus indicate radiative cooling to be a valid cooling technique for the thruster, including margins large enough to allow for steady state thruster operation even in the case of underestimation of the heat transfer in the cylindrical thrust chamber section.

4. Experimental investigation

4.1. Propellant feed system

4.1.1. Oxidizer feed system

The oxidizer feed system comprises of a gaseous pressurization section and a storage and feed section of the liquid propellant, housed in a safety compartment to prevent uncontrolled distribution of the hydrogen peroxide in case of a high pressure leakage.

Figure 86 shows a schematics of the oxidizer feed system. The main features of the feed system are the hydrogen peroxide high pressure tank ($p_{tank,max}$= 40 bar) with a storage capacity of 300 ml and a pressurization gas tank (BV1) to simulate blow down operation. The feed system is equipped with two high pressure safety relieve valves, one on the incoming gas side upstream of the gas storage tank (SV1) and one directly mounted to the hydrogen peroxide tank (SV3). The latter is intended to relieve pressure in case of rapid decomposition of the stored oxidizer. The gaseous pressurization section is equipped with a manual valve (MV3) between the storage tank and the N_2 cylinder, an analogue and a digital pressure gauge (P1 and p_{tank}) of the pressurization gas as well as a gas filter element (F). The liquid hydrogen peroxide mass flow downstream of the H_2O_2 tank is monitored by a Bronkhorst Coriflow M54C5I-AAD-22-K-C (FL1). The measurement technique employed bases on the deformation of tubing due to Coriolis force and allows mass flow measurements to be independent from density and thus independent from hydrogen peroxide concentration. Hydrogen peroxide injection is controlled by a pneumatic feedline valve (AV1) which is actuated by a magnetic solenoid valve (S), avoiding any preheating of the injected fluid. The feedline pressure downstream of the oxidizer feedline valve is monitored by a digital pressure gauge (p_{feed}). The H_2O_2 tank is filled via I1 and is additionally equipped with a manual drainage valve (MV6) allowing for disposal of remaining hydrogen peroxide. Before testing, the hydrogen peroxide feedlines are filled by opening valve MV7, preventing any void volumes within the propellant lines at start-up. Stainless steel tubing of 1/4 and 1/8 inch are used in the assembly. Analogue pressure gauge P2 allows for adjusting the pneumatic valve actuator pressure. A dedicated thermocouple attached to the feedsystem close to the utilized test chamber is monitoring ambient temperature conditions.

All components are manufactured of stainless steel complying with the compatibility requirements of hydrogen peroxide. The maximum system operation pressure is 40 bar.
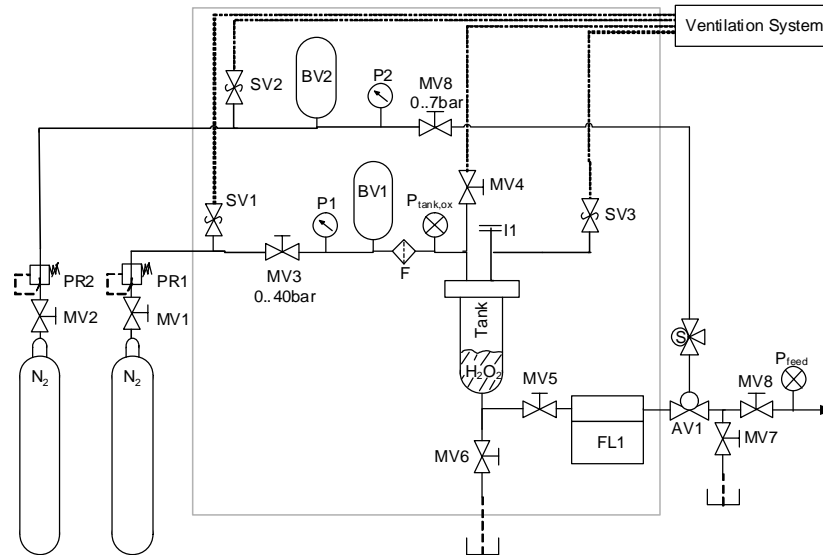
Figure 86 Oxidizer feed system schematics

Figure 87 shows an image of the oxidizer feed system. The high pressure oxidizer tank and the pressurization gas buffer volume are visible through the opened glass window. The pneumatic oxidizer feedline valve is visible on the right bottom of the safety compartment, whereas the magnetic actuator valve is not shown in the picture. The manual control panel featuring the manual valve controls and the manual pressure gauges for oxidizer tank pressure and valve actuator pressure is located at the bottom of the oxidizer safety compartment below the access window.
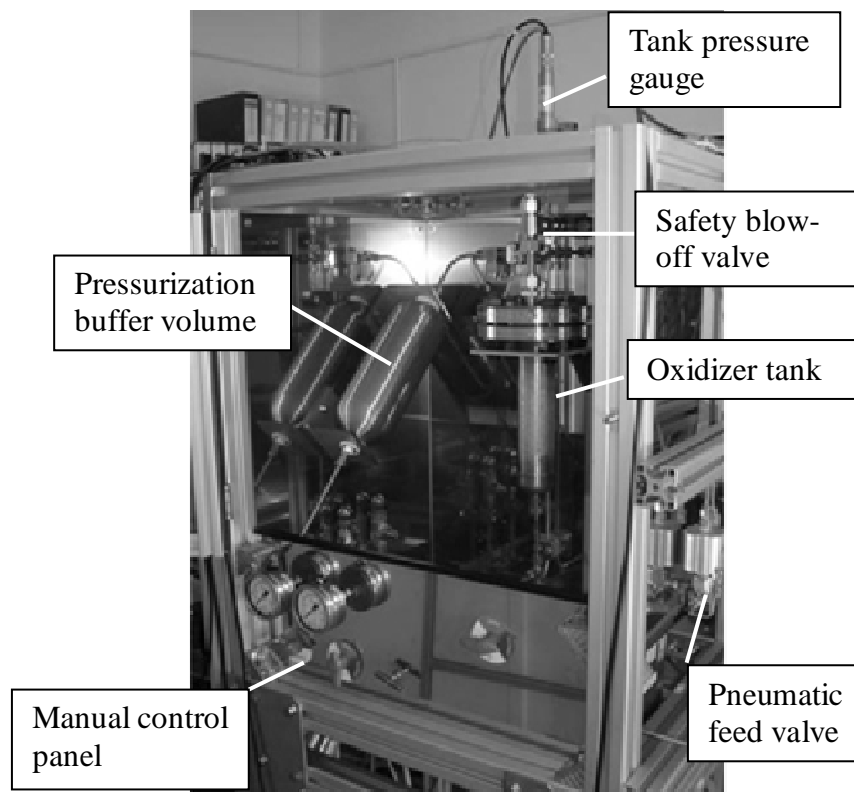
Figure 87 Oxidizer feed system compartment

4.1.2. Fuel feed system

The fuel feed system comprises of the same main components as the oxidizer feed system described above, except the safety compartment and the different type of mass flow meter employed. The schematics of the fuel feed system is shown in Figure 88. A Bronkhorst Liqui-Flow L1-FAD-22-0 (FL2) is used to monitor the fuel mass flow. A different design is used for the fuel tank (200 ml capacity) compared to the oxidizer tank. The main feature of this tank is the exit pipe entering the tank through the top flange, extracting the fuel from above the bottom of the tank to avoid debris entering the feedline. The fuel is fed into the tank through the manual drainage valve (MV10) from the bottom with the use of a syringe. Blow-down feed modus is achieved using the stored gas in buffer volume BV2 with closed manual valve (MV12). The feed system is equipped with a safety relived valve (SV4) in case of system pressure surpassing the safety requirements. The fuel flow is controlled by a magnetic solenoid valve AV2 (Parker 009-0172-900, < 5 ms response time). All components are manufactured of stainless steel complying with the compatibility requirements of hydrogen peroxide. The maximum design system pressure is 40 bar. The tubing consists of 1/8 inch feedlines in the liquid section and ¼ inch tubing for the gaseous pressurization section.

The same fuel panel has been used for both ethanol and kerosene testing, with thorough cleaning procedure including the emptying of the panel using a vacuum pump, a series of flushings with demineralized water followed by flushing with the respective fuel in between. A change in fuel necessarily involved calibration of the mass flow meter as discussed hereafter.

The fuel panel, shown in Figure 89 has been mounted on the backside of the oxidizer safety compartment.
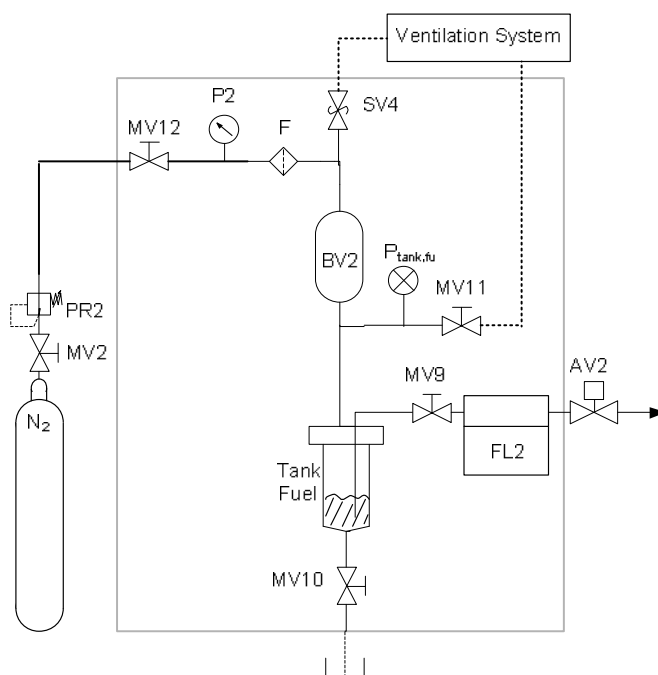
Figure 88 Fuel feed system schematic
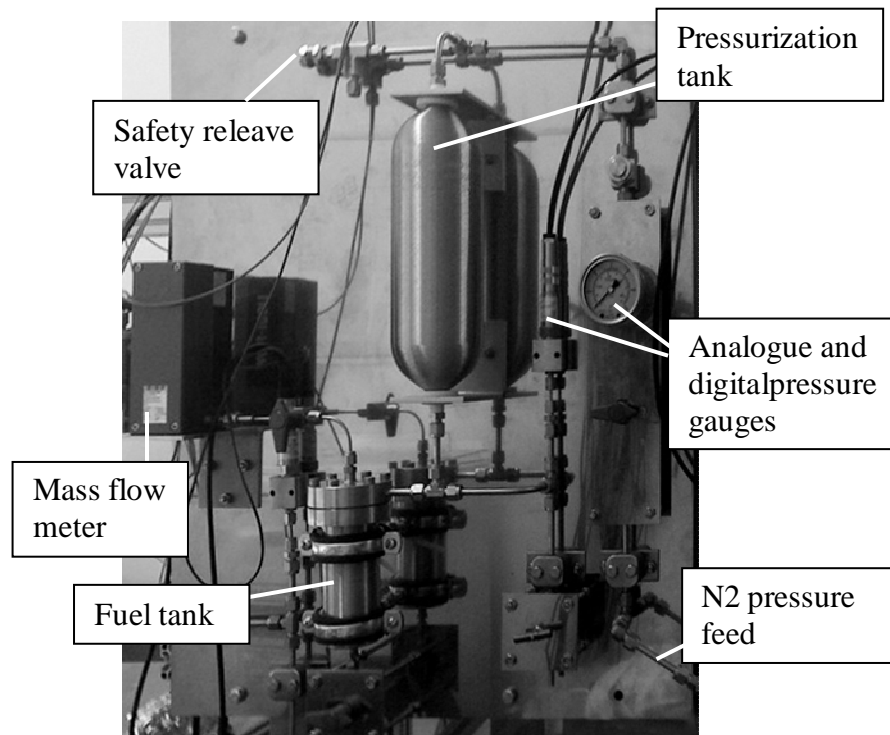
Figure 89 Fuel feed system

4.1.3. Data acquisition

Data acquisition and automated system operation such as valve control, has been conducted using a dedicated LabVIEW software in combination with a DAQ input/output device (NI-cDAQ 9172) housing 16 thermocouple input channels, 8 shrouded PNC input channels (pressures, mass flows and thrust) and the output controls for the feedline valve commands (8 channels). Experimental data has been recorded at 10 samples and 100 samples per second, depending on experimental configuration.

4.1.4. Calibration and error estimation
4.1.4.1.   Mass flow

To calibrate the mass flow measurements, a standard procedure featuring 100 s valve opening duration at various pressure levels has been conducted. The fluid was collected downstream of the flow meter and its gravimetrically determined weight was used for calibration in conjunction with the recorded integrated voltage signal. Calibration was conducted for a wide range of different pressure levels to confirm the anticipated linear behavior, each test point has been repeated three times. The fuel line was calibrated directly, whereas the oxidizer line was calibrated using demineralized water. In the latter case, the result was manipulated accordingly to the ratio of densities of water and hydrogen peroxide at the concentration employed. This procedure was validated by a final calibration test using hydrogen peroxide, confirming the conducted calibration before. This calibration procedure has been conducted before test series were started, after periods without using the propellant feed system or any

changes applied to the given propellant feed system, such as change in propellant. The calibration procedure was completed by a series of additional calibration runs with implemented signal to mass flow conversion, determining the error achieved by the implemented calibration at various mass flow levels, again covering the entire calibration range. The calibration was deemed successful for errors smaller than 1.1%.
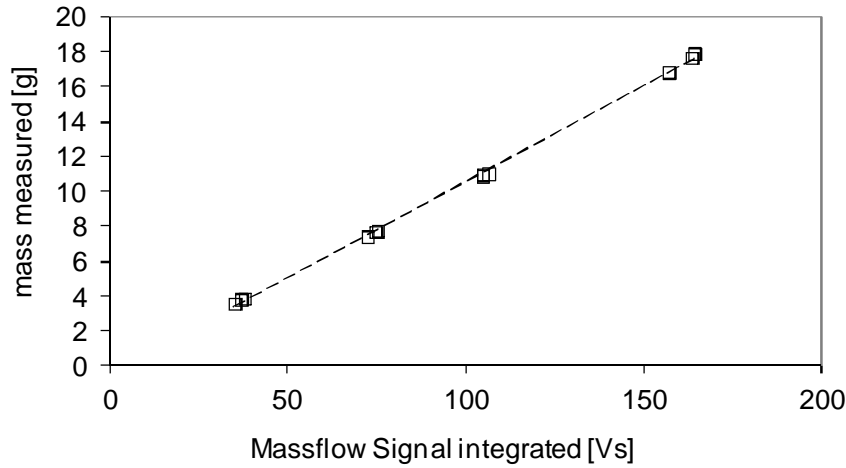
Figure 90 Typical mass flow calibration procedure for the kerosene propellant feed system

Figure 90 shows a typical resulting calibration curve for the mass flow measurement of the fuel feed system for kerosene. The resulting signal to mass flow conversion in this case gives

$$\dot{m} = 0.1097\frac{\text{g}}{\text{Vs}}U - 0.402\frac{\text{g}}{\text{s}},$$

(4.1)

where U is the sensor signal in V, whereas the mass flow is measured in g s^{-1}.

4.1.4.2. Pressures

The piezo-resistive pressure gauges (Keller PA-23SY, error guaranteed by manufacturer: < 0.5 % (<1.5 % for p < 2 bar)) were calibrated by pressurization of the closed feedline system at various pressure levels. After equilibrium was reached and any dynamical effects such as leakage flow were excluded, all measured pressure signals were recorded. This procedure was repeated three times, before the next pressure level was investigated the same way. After this procedure was completed, covering the entire system pressure range in pressure level intervals of 5 bar, mean values for each pressure level were calculated. The individual pressure determinations where then compared to the mean values, showing negligible deviations in the targeted system pressure test range of p = 10 bar, as shown in Figure 91 for a sample of three pressure gauges in the oxidizer feed system. For the gauges investigated, maximum errors are well below 0.5 % for the pressure range of interest (p > 5 bar), complying with the manufacturer's calibration.
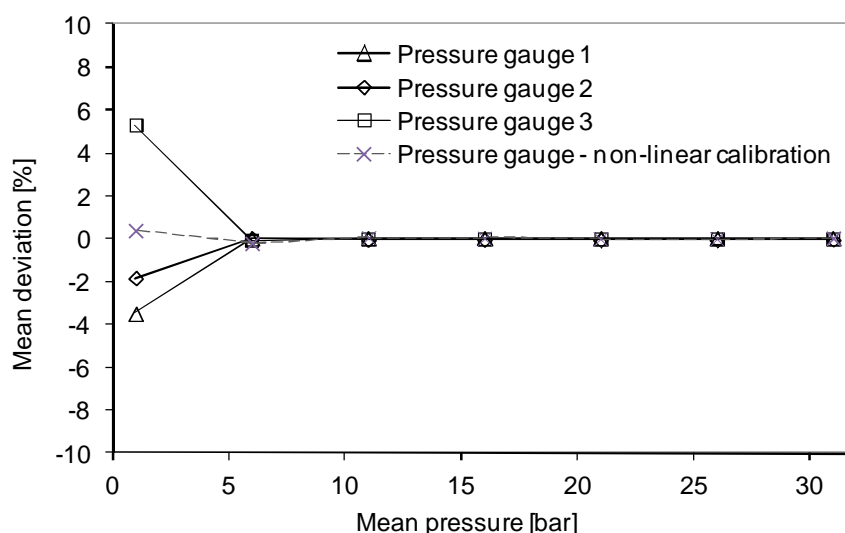
Figure 91 Sample pressure gauge calibration procedure for oxidizer feed system

While only negligible deviations were found for the standard pressure gauges for $p > 5$ bar, significant nonlinearities where recorded for one high temperature pressure gauge (Keller 25 X HTC) additionally employed in the combustion experiments. Calibration of this instrument was performed using the calibration procedure described above, with the mean value determined by a series of standard pressure gauges only, not including the high temperature sensor. The simultaneously measured signals employing the high temperature sensor where then used to determine a non-linear calibration curve for this particular pressure gauge. This way, maximum deviations from the mean value over all pressure gauges of 0.4 % where achieved for this sensor for $p > 5$ bar.

4.1.4.3.   Temperatures

The thermocouples (type K, Electronic Sensor IKT025/25 (0.25 mm diameter) and IKT05/25 (0.5 mm diameter)) used for temperature measurements have been calibrated in a dedicated calibration oven. The deviations of four thermocouples over the envisioned range of temperature measurements from the calibrated values are shown in Figure 92 for a sample of six thermocouples. The maximum error found was below 2 % of the calibrated measurements.
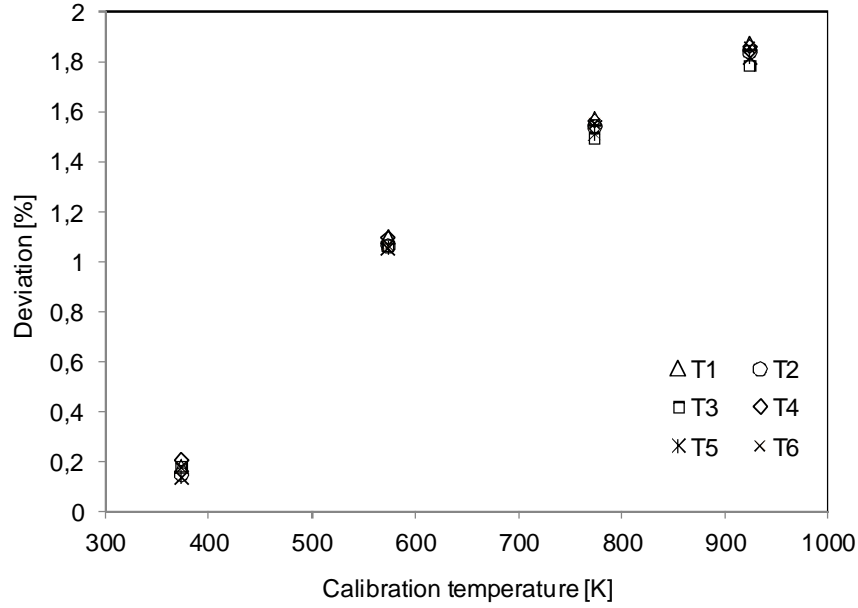
Figure 92 Sample thermocouple (type K) deviation

4.1.4.4. Reduced effective throat area

The evolution of boundary layers in the throat region of the miniaturized nozzle may lead to a reduction of the effective throat area. Any reduction of effective throat area leads to an overestimation of the characteristic velocity defined by

$$c^* = \frac{p_{CC} A^*}{\dot{m}_p}.$$

(4.2)

For isentropic flow, the chamber pressure is inverse proportional to the product of Mach number at throat and throat area, which is, in the absence of boundary layers, a function of free stream velocity u:

$$p \propto \frac{\dot{m}_p}{A^* M} \propto \frac{\dot{m}_p}{A^* u}.$$

(4.3)

This becomes, for non homogeneous velocity within the boundary layer

$$p \propto \frac{\dot{m}_p}{A^* \frac{1}{A^*} \int_{A^*} u_{(r)} dA} = \frac{\dot{m}_p}{A^* \bar{u}} = \frac{\dot{m}_p}{\left(A^* - \Delta A^*\right) u}.$$

(4.4)

Since the chamber pressure is indirect proportional to the product of throat area and mean velocity $\bar{u}$, the expression has been manipulated in Eq. (4.4) by using the free stream velocity u in conjunction with a reduced effective throat area.

Based on theoretical investigation of the turbulent boundary layer evolution near the throat conducted in section 3.7.1.2, the maximum boundary layer thickness can be estimated. Assuming a shape profiles within the boundary layer according to Eq. (3.104), the maximum error expected in terms of effective throat area can be approximated by

$$\Delta A^* = \pi \left[2 \int_{r_t - \delta_r}^{r_t} \left(\frac{r_t - r}{\delta_r} \right)^{\frac{1}{7}} r dr \right]^2 \tag{4.5}$$

.

Eq. (4.5) gives, for a worst case of $\delta_r < 10^{-5} m$, a maximum error for reduced effective throat are of 5% for the DM thruster and 6% for the EBB thruster. Note that this contribution applies to negative uncertainty only.

4.1.4.5.   Error estimation and propagation

The instruments full scale ranges and maximum instrument uncertainties of measurements anticipated from the calibration are summarized in Table 14 for the different measurements. Note that thrust measurement has not been discussed yet, but is discussed in detail in section 4.5.2.

Table 14 Measurement uncertainties

Quantity	Sensor type	Range	Measurement accuracy
H_2O_2 mass flow	Coriflow M54C5I-AAD-22-K-C	0.139 -2.8 g s^{-1}	± 1.1 %
Kerosene mass flow	Liquiflow L1-FAD-22-0	0.02 – 1.0 g s^{-1}	± 1.1 %
Ethanol mass flow	Liquiflow L1-FAD-22-0	0.02 – 1.0 g s^{-1}	± 1.1 %
Temperatures	Type K	0 -500 K	± 0.5 %
		500 – 600 K	± 1.1 %
		600 – 800 K	± 1.5 %
		800 – 1273 K	< 4 %
Pressures	PA-23	0 – 1 bar	± 6 %
		1 – 2 bar	± 1.5 % from FS
		2 – 50 bar	± 0.6 % from FS
Throat uncertainty			- 6 % (EBB)
			- 5 % (DM)
Thrust	DMS	0 – 2.5 N	0.04 N (absolute)

The propagation of uncertainties for a parameter $f(x_i)$ dependent on the measurements x_i afflicted with uncertainty Δx_i is calculated according to

$$\Delta X = \sqrt{\sum_i \left(\frac{\partial f}{\partial x_i} \Delta x_i \right)^2} \tag{4.6}$$

.

Selected uncertainties for dependent parameters frequently employed in the following are listed in Table 15.

Table 15 Propagated uncertainties for selected measurements

Parameter	Uncertainty
Characteristic velocity (bipropellant) :	$\Delta c^* = \left\{ \begin{array}{l} + \sqrt{\left(\dfrac{\partial c^*}{\partial p_{CC}} \cdot \Delta p_{CC}\right)^2 + \left(\dfrac{\partial c^*}{\partial \dot{m}_{ox}} \cdot \Delta \dot{m}_{ox}\right)^2 + \left(\dfrac{\partial c^*}{\partial \dot{m}_{fu}} \cdot \Delta \dot{m}_{fu}\right)^2} \\ - \sqrt{\left(\dfrac{\partial c^*}{\partial p_{CC}} \cdot \Delta p_{CC}\right)^2 + \left(\dfrac{\partial c^*}{\partial \dot{m}_{ox}} \cdot \Delta \dot{m}_{ox}\right)^2 + \left(\dfrac{\partial c^*}{\partial \dot{m}_{fu}} \cdot \Delta \dot{m}_{fu}\right)^2 + \left(\dfrac{\partial c^*}{\partial A^*} \cdot \Delta A^*\right)^2} \end{array} \right.$
Characteristic velocity (catalyst tests):	$\Delta c^* = \sqrt{\left(\dfrac{\partial c^*}{\partial p_C} \cdot \Delta p_c\right)^2 + \left(\dfrac{\partial c^*}{\partial \dot{m}_p} \cdot \Delta \dot{m}_p\right)^2}$
Mixture ratio:	$\Delta O/F = \sqrt{\left(\dfrac{1}{\dot{m}_{fu}} \Delta \dot{m}_{ox}\right)^2 + \left(\dfrac{\dot{m}_{ox}}{\dot{m}_{fu}^2} \Delta \dot{m}_{fu}\right)^2}$
Specific impulse:	$\Delta I_{sp} = \sqrt{\left(\dfrac{1}{(\dot{m}_{ox} + \dot{m}_{fu}) g_0} \Delta T\right)^2 + \left(-\dfrac{1}{(\dot{m}_{ox} + \dot{m}_{fu})^2 g_0} \Delta \dot{m}_{ox}\right)^2 + \left(-\dfrac{1}{(\dot{m}_{ox} + \dot{m}_{fu})^2 g_0} \Delta \dot{m}_{fu}\right)^2}$

Standard deviations calculated by averaging of experimentally recorded time-dependent parameters are added to the propagated instrument uncertainty of the measurement parameter.

4.2. Decomposition chamber

4.2.1. Description of experimental setup
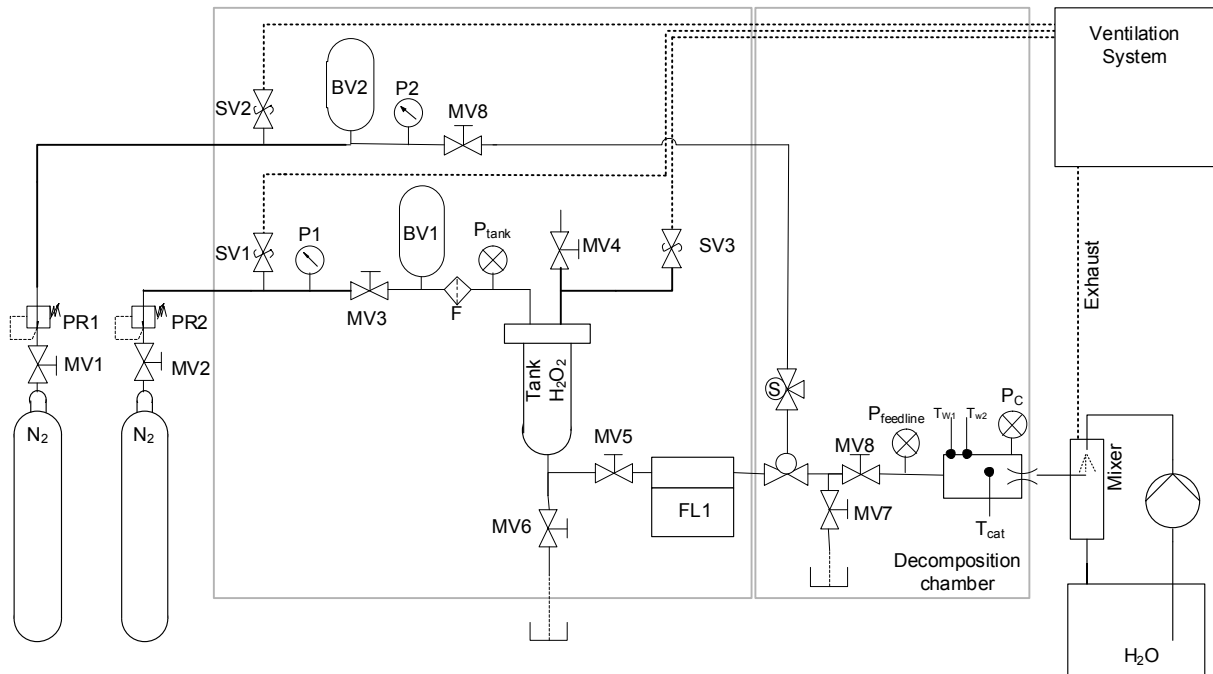
Figure 93 Schematics of catalyst test facility

A schematics of the catalyst test facility and the fluidic feed system is shown in Figure 93. The test apparatus uses the oxidizer feed system described in section 4.1.1 in conjunction with the dedicated catalyst test compartment attached to the feed system, as shown in Figure 94. The tests have been performed in a pressurized blow-down modus (MV3 closed) do simulate onboard conditions. A Buffer volume was used to counteract feed pressure decay. The decomposed, high temperature exhaust downstream of the decomposition chamber was treated in an exhaust ventilation system. A description of the feed systems main features is given in section 4.1.1. In addition to the diagnostics of the decomposition chamber described hereafter, mass flow and pressure measurements incorporated in the feed system and described in section 4.1, are recorded.
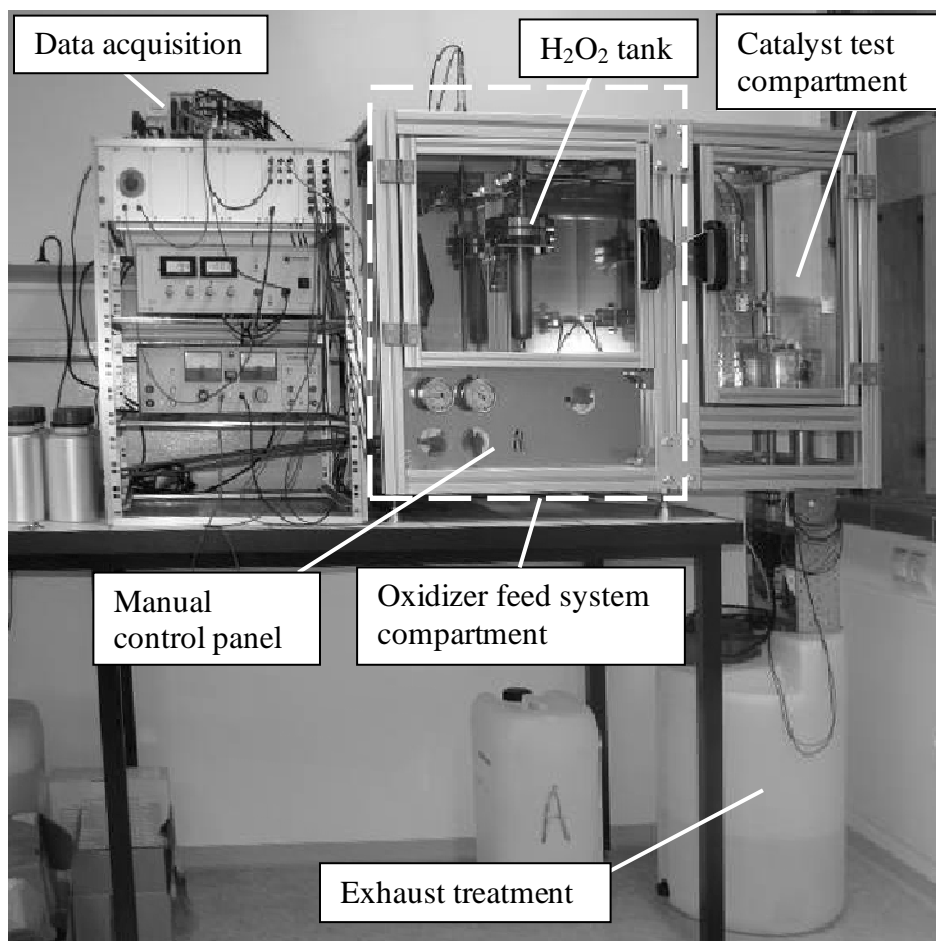
Figure 94 Oxidizer feed system in catalyst test configuration with data acquisition
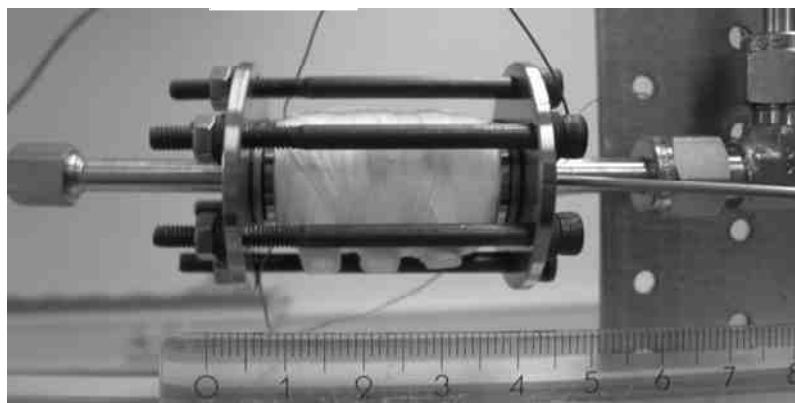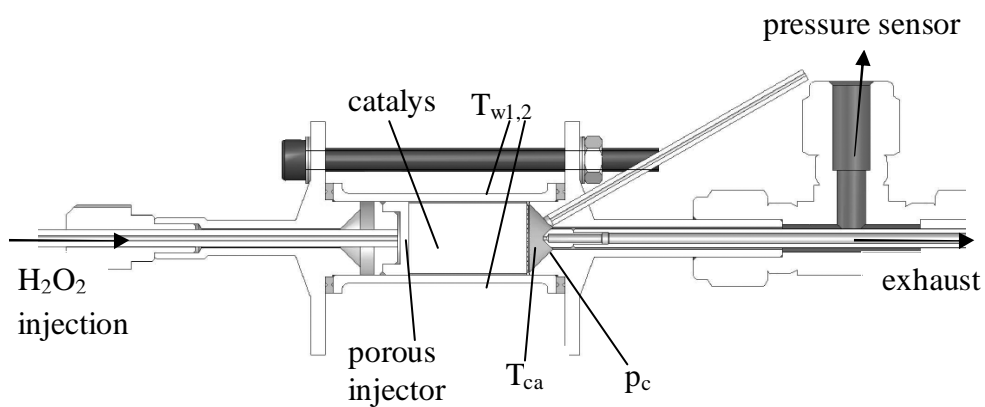
Figure 95 Schematics and picture of decomposition chamber

The catalyst chamber used to investigate catalysts is shown in Figure 95. The exhaust temperature just downstream of the catalysts exit face, the decomposition chamber pressure and the decomposition chamber wall temperatures were monitored at the stations indicated in Figure 95 at the top. The main exhaust temperature thermocouple was inserted into the exhaust stream for 15 mm, avoiding any influence from the cold structure. The thermal insulation of the chamber tube was necessary to avoid temperature gradients at the position of wall temperature measurements.

Ambient conditions have been monitored and tests have been conducted for $T_w = 25 \pm 2.5$ °C (with $T_w = \max(T_{W1}, T_{W2}, T_{cat})$) only, and ambient temperatures of $T_{amb} = 25 \pm 5$ °C. Liquid hydrogen peroxide temperatures before testing have been $T_w = 20 \pm 2.5$ °C.

To account for test to test variations, a total of four repetitive tests have been recorded for each catalyst. In between tests, the decomposition chamber and catalyst were brought back to ambient conditions, to meet the requirement of $T_w = 25 \pm 2.5$ °C. To investigate stationary performance, test sequences of $t_{on} = 200$ s have been conducted. Recorded data before and after the period of valve opening were used to perform zero adjustment of the mass flow measurement. The leading parameters chosen for catalyst examination such as decomposition temperature and chamber pressure have been determined in the stationary case at three time points at $t = 150$ s, $t = 175$ s and $t = 200$ s with averaging intervals of 2 s.

Catalyst to catalyst variation within one configuration has been faced by investigation of four catalysts for any given catalyst configuration in test campaign 1. In test campaign 2, the number of catalysts tested for each configuration is indicated separately.

The examination on catalyst configuration level at stationary conditions has been conducted using the three average values for each of the four tests per catalyst and corresponding standard deviation to calculate one mean value for each configuration with corresponding standard deviation according to error propagation calculation. The error bars shown in the graphs in the result section represent the 95 % confidence level (2σ) for a given catalyst configuration.

4.2.2. Decomposition chamber injector design

After studying various alternative injector designs, including spray injectors [36, 106] and showerhead injectors [93], an injector design featuring a porous element was chosen. This design features, experimentally validated, good wetting behavior of the entire surface at design pressure, the avoidance of void volumes and direct H_2O_2 application by contact to the catalyst surface, therefore decoupling the flow of different channels from each other at the upstream catalyst face. The homogeneous distribution of hydrogen peroxide over the entire injector face allows additionally for a simple integration into the decomposition chamber, as opposed to the necessary exact agreement of injector and catalyst orientation for a shower head injector design. Furthermore, as opposed to the latter design, the porous injector design

is unaffected by catalyst channel geometry and density and significantly reduces manufacturing costs for testings of multiple catalyst configurations. However, substitution of the filter injector design by a dedicated shower head design remains possible for the final catalyst selected, without major impact on the overall decomposition chamber design.

A design featuring a stainless steel porous disc welded to the injector dome volume featuring axial injection was chosen, as shown in Figure 95.

However, during the catalyst tests, a blocking phenomenon of the porous injector was observed, eventually leading to total blocking of the oxidizer flow. As this effect has been noticed during the catalyst test campaign, it was decided to abstain from a change in injector design to guarantee comparability of all test results. Instead, potential blocking of the injector was monitored before and after each catalyst tested by a standardized and therefore reproducible flow measurement procedure with water. For each of these injector flow tests, the oxidizer tank was filled with 150 ml de-mineralized water after all feedlines was evacuated from remaining fluids. The feedsystem pressure was then set to 11 bar and a test sequence with 100 s valve opening time was initiated. The fluid was collected downstream of the injector to gravimetrically determine the throughput in addition to the data recorded by the mass flow meter. This procedure was repeated twice. Once decay in injector discharge coefficient was observed, a new injector was employed.
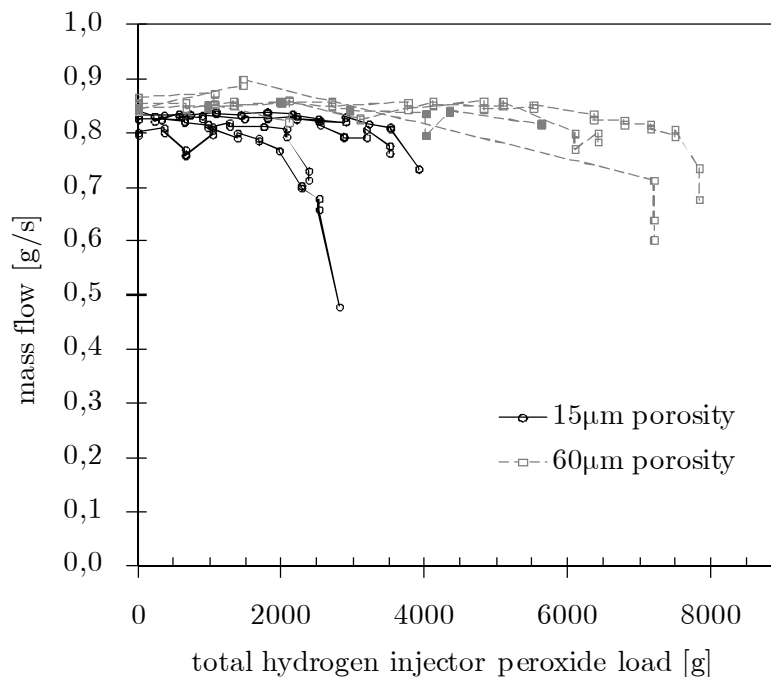
Figure 96 Injector flow was a function of total accumulated hydrogen peroxide mass

Figure 96 shows the resulting flow rate values for a sample of eight injectors featuring two different filter element porosities as a function of total oxidizer throughput. The dependency of blocking is apparently affected by the porosity. By increasing the injector porosity, total accumulated hydrogen peroxide mass throughput could be increased to up to 7 kg without blocking phenomena occurring. Even further increase in open porosity to 90 μm was chosen

for the injector of the DM thruster presented in section 4.5, but has been tested only for accumulated hydrogen peroxide mass flows of approximately 1.85 kg, with no blocking phenomena noticeable so far.

The blocking phenomenon has been observed visually in the form of white crystalline structures found within the porous stainless steel pores, as shown in Figure 97. Two samples, one located at the upstream face of the porous element facing the injector dome, and one located on the opposite face which was in contact with the catalyst, were studied by EDX analysis as shown in Figure 98. The Stannate observed in the upstream sample points to the blocking of the injector originated in residue from the hydrogen peroxide, since Sn is used as a stabilizer in the hydrogen peroxide utilized (appendix X.3). The alumina however could be originating from both the hydrogen peroxide and the catalyst washcoating. The fact that Al dominates the spectra from the downstream sample, which was in direct contact with the catalyst, may point to the latter cause. It is therefore not clear whether the blocking effect is caused by hydrogen peroxide stabilizers or degradation of the catalyst. It is proposed that this phenomenon could be studied by investigation with differently stabilized hydrogen peroxide or different catalyst washcoatings. However, since any such changes would have directly impacted the comparability of the test campaigns presented hereafter, no such investigation has been conducted and is left for further investigation. It should be noted however that successful attempts to clean a blocked injector using diluted sodium Hydroxid Solution (Merck Extran MA01) in an ultrasound bath led to total hydrogen peroxide throughput of 14 kg for a 60 μm porosity injector element.

It is therefore recommended to substitute the porous filter element in a final step by a shower head injector design adapted to the final selected catalyst geometry to avoid blocking by increased area of the flow orifices. However, since all thrusters investigated in this thesis provided easy accessibility to the decomposition chamber and therefore to the filter injector, no such substitution was necessary within this work since injectors could eventually be replaced if injector failure was noticed.
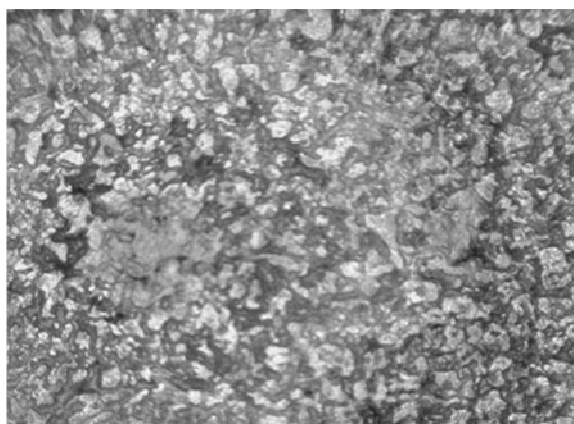
Figure 97 Visual inspection (6× magnified) of blocked porous injector, upstream side facing the injector dome

upstream side, facing injector dome   downstream side, attached to catalyst
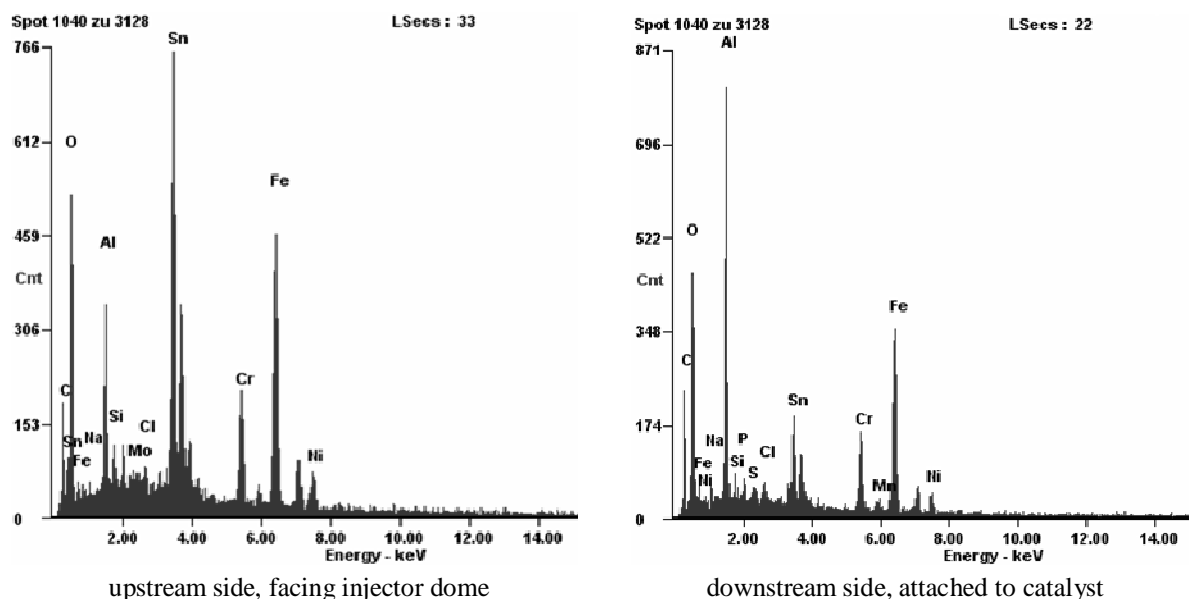
Figure 98 EDX analysis of blocked porous injector

4.2.3. Catalyst and oxidizer selection

Preliminary comparison of different catalyst types can be conducted according to the catalyst bed loading (CBL), which is defined as the ratio of mass flow rate and the total cross sectional area of the catalyst. In this work, an approach utilizing small catalyst bed loading of $CBL = 2.5$ kg m^{-2} s^{-1} has been chosen to guarantee long catalyst lifetime and high efficiencies. This bed loading compares to other catalytic hydrogen peroxide decomposition efforts with typical bed loadings ranging from $CBL \approx$ 10-420 kg m^{-2} s^{-1} [32, 268, 78, 269, 270, 271, 272, 273, 274].

The catalyst configurations investigated in this work feature alternate supporting structure type, including Monoliths, Foams and Pellets, differing procedures to apply the wash coating layer and alternate active surfaces as listed in Table 16 and Table 17.

The catalysts have been manufactured by CTI (catalyst structure) and surface treated by LACCO (washcoating procedure and application of active phase) [67, 275].

In the first test campaign, all catalysts tested were monolith type with a design length of $L_M = 20$ mm and a design diameter of $d_M = 12.2$ mm. The catalyst variations tested in this phase were focusing on comparison between the carrier materials Cordierite and Silicium carbide (SiC), the active phases MnO$_x$ and Platinum, different channel densities and channel geometries (squared and triangular channel shape). In addition, two wash coating procedures referred to as wash coating A and B are examined. For each variation, four catalysts were tested, which led to a total number of 88 catalysts for this test campaign. The catalyst variations tested in this campaign are given in Table 16. All monolith catalysts have an outer diameter of $d_M = 12.2\pm0.1$ mm. The length of catalysts investigated is indicated in Table 16. The design channel densities are 400 and 600 channels per square inch (cpsi) with the actually

achieved values given in Table 16. The intrinsic channel density given refers to the channel density based on the surface cross section of the catalyst, without the outer skirt. A design content of 10 wt.-% washcoat was aimed at. The weight percentage of active material achieved after the washcoat procedure in terms of total catalyst weight is given as an arithmetic mean of all catalyst of the configuration. In addition, the standard deviation for the weight percentage is given to account for catalyst to catalyst variation.

Table 16 Test Matrix of 20mm length monolithic catalysts

Configuration	Catalyst Carrier Material	Catalyst Type, L_M [mm]	Channel Geometry	Intrinsic Channel Density [cpsi]	Washcoating Procedure	Active Phase, wt% active phase [%], Standard deviation
#1	Cordierite	Monolith, 20	square	370	A	Pt, 1.95, 0.13
#2	Cordierite	Monolith, 20	square	370	B	Pt, 1.40, 0.08
#3	Cordierite	Monolith, 20	square	370	A	MnO_x, 2.08, 0.37
#4	Cordierite	Monolith, 20	square	370	B	MnO_x, 2.53, 0.15
#5	SiC	Monolith, 20	square	438	A	Pt, 3.38, 0.33
#6	SiC	Monolith, 20	square	438	B	Pt, 0.58, 0.13
#7	SiC	Monolith, 20	square	438	A	MnO_x, 2.18, 0.24
#8	SiC	Monolith, 20	square	438	B	MnO_x, 3.50, 0.35
#9	Cordierite	Monolith, 20	square	635	A	Pt, 2.98, 0.17
#10	Cordierite	Monolith, 20	square	635	A	MnO_x, 5.73, 1.25
#11	Cordierite	Monolith, 20	square	635	B	Pt, 3.58, 0.25
#12	Cordierite	Monolith, 20	square	635	B	MnO_x, 5.00, 0.22
#13	SiC	Monolith, 20	square	668	B	Pt, 3.70, 0.83
#14	SiC	Monolith, 20	square	668	B	MnO_x, 5.58, 0.73
#15	Cordierite	Monolith, 20	triangular	420	B	Pt, 3.90, 0.36
#16	Cordierite	Monolith, 20	triangular	420	B	MnO_x, 5.25, 0.26
#17	SiC	Monolith, 20	triangular	400	B	Pt, 2.95, 0.66
#18	SiC	Monolith, 20	triangular	400	B	MnO_x, 3.43, 1.24
#19	Cordierite	Monolith, 20	triangular	540	B	Pt, 4.83, 1.16
#20	Cordierite	Monolith, 20	triangular	540	B	MnO_x, 5.33, 0.13
#21	SiC	Monolith, 20	triangular	620	B	Pt, 1.98, 0.30
#22	SiC	Monolith, 20	triangular	620	B	MnO_x, 4.50, 0.36

In a second test campaign, emphasis on the investigation of the impact of the type of catalyst support structure was taken, including Foams and Pellets. The objective of this test campaign was a qualitative performance comparison of alternative catalyst types implemented in the same decomposition chamber with the same injection system as honeycomb catalysts. In addition, different catalyst lengths have been investigated in this test campaign. Therefore, monoliths with decreased length, different lengths of foam type carriers and pellets have been investigated. Less than four catalysts have been examined in this test campaign for certain catalyst types as indicated in Table 17 and for all pellet types. All monolith catalysts featured diameters of $d_M = 12.2 \pm 0.1$ mm, whereas foam type catalysts had outer diameters of $d_M = 10.2 \pm 0.4$ mm. The foam catalysts have been coated in insulating ceramics to account for the small diameter. The pellets of 1 to 1.4 mm diameter were investigated in a container with outer diameter of $d_M = 12.2$ mm. All pellet type catalysts have been treated with the same washcoating procedure. There is thus no use in designating names to these washcoating procedures.

Table 17 Additional Test Matrix: Evaluation of different catalyst types

Conf.	Number of catalysts	Catalyst Carrier Material	Catalyst Type, L_M [mm]	Geometry	Intrinsic channel density [cpsi] / pore density [ppi][a]	Washcoating Procedure	Active Phase, wt% active phase [%], Standard deviation
#23	2	Cordierite	Monolith, 10	squared	304	SOL A	MnO_x, 8.53, 1.95
#24	2	Cordierite	Monolith, 10	squared	304	SOL A	Pt, 4.45, 4.03
#25	5	Cordierite	Monolith, 20	squared	304	SOL A	MnO_x, 7.72, 2.34
#26	3	Cordierite	Monolith, 20	squared	304	SOL A	Pt, 1.58, 0.96
#27	3	Mullite	Foam, 20	N.A.	45 ppi [d]	SOL C	MnO_x, 3.80, 0.65
#28	4	Mullite	Foam, 20	N.A.	45 ppi [d]	SOL C	Pt, 2.16, 1.01
#29	4	Mullite	Foam, 10	N.A.	45 ppi [d]	SOL C	MnO_x, 4.45, 1.66
#30	1	γ–Al_2O_3 (CTI)	Pellets, 8 [b]	Tetralobe pellets	1.02±0.02, 4.24±0.5, 224	N.A.	MnO_x, 21.8
#31	1	γ–Al_2O_3 (CTI)	Pellets, 8 [b]	Tetralobe pellets	1.02±0.02, 4.24±0.5, 224	N.A.	Pt, 20.9, -
#32	1	γ–Al_2O_3 (CTI)	Pellets, 8 [b]	Tetralobe pellets	1.0-1.4, milled [c], 218	N.A.	MnO_x, 23.1, -
#33	1	γ–Al_2O_3 (CTI)	Pellets, 8 [b]	Tetralobe pellets	1.0-1.4, milled [c], 218	N.A.	Pt, 13.2, -
#34	1	CeO_2 (CTI)	Pellets, 8 [b]	Tetralobe pellets	1.17±0.04, 3.79±0.82, 139	N.A.	MnO_x, 22.6, -
#35	1	CeO_2 (CTI)	Pellets, 8 [b]	Tetralobe pellets	1.17±0.04, 3.79±0.82, 139	N.A.	Pt, 18.7, -
#36	1	CeO_2 (CTI)	Pellets, 8 [b]	Tetralobe pellets	1.0-1.4, milled [c], 133	N.A.	MnO_x, 23.2, -
#37	1	Ceria (CTI)	Pellets, 8 [b]	Tetralobe pellets	1.0-1.4, milled [c], 133	N.A.	Pt, 16.3, -
#38	1	γ–Al_2O_3 (Sigma Aldrich)	Pellets, 8 [b]	Bimodal gamma alumina	1.0-1.4, milled [c], 256	N.A.	MnO_x, 30.8, -
#39	1	γ–Al_2O_3 (Sigma Aldrich)	Pellets, 8 [b]	Bimodal gamma alumina	1.0-1.4, milled [c], 256	N.A.	Pt, 14.7, -

Annotations:

[a] For pellets: pellet diameter [mm], pellet length [mm], surface area per g [$m^2 g^{-1}$]

[b] Pellets have been investigated in 8mm high stacked configuration

[c] Pellets have been milled and sieved to achieve comparable outer diameter

[d] Porosity chosen so that internal surface area matches internal surface area of 304 cpsi monolith type catalysts

This leads to a total number of 39 configurations and a total number of 121 catalysts investigated within both test campaigns. Selected catalysts of test campaign 1 are displayed in Figure 99, whereas catalyst samples of campaign 2 are shown in Figure 100.

Conf. #6: SiC-Pt 438 cpsi   Conf. #13: SiC-Pt 668 cpsi   Conf. #15: Cordierite-Pt 420 cpsi   Conf. #19: Cordierite-Pt 540 cpsi
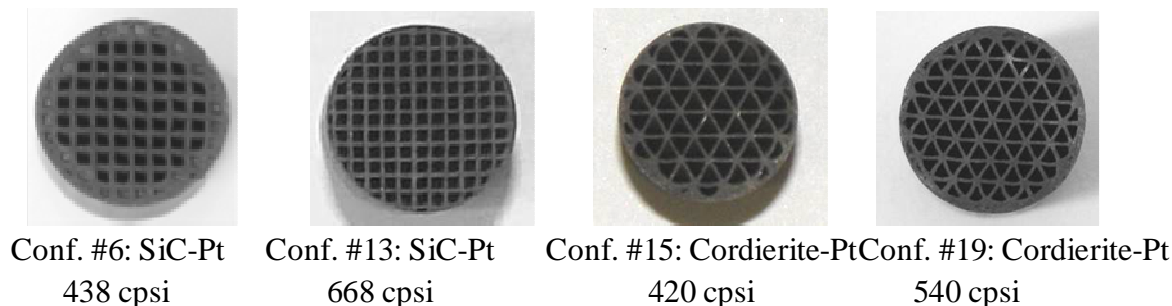
Figure 99 Catalyst samples of test campaign 1 before testing: front face view

Figure 100 Catalyst of test campaign 2: from left to right: 304 cpsi monoliths of 10mm length (#23), foam of 20mm length (#28) and detail of pellets #30 and of milled pellets of conf. #38

For the tests discussed, hydrogen peroxide from three different batches was used, which resulted in different initial hydrogen peroxide concentration. Hydrogen peroxide concentration showed deviation from nominal 87.5 wt %. Batch 1 had a concentration of 86.7 wt.%, whereas Batch 2 and Batch 3 had a concentration of 87.7 wt.%. The exact specifications for each batch can be found in appendix X.3. This leads to theoretical maximum achievable temperatures different than the theoretical temperature for nominal concentration of 87.5 wt.%. The theoretical achievable decomposition temperatures for Batch 1 and Batch 2/Batch 3 are 670.7 °C and 695.23 °C respectively. These theoretical values have been calculated using NASA Chemical Equilibrium and Applications code [92]. To account for different initial hydrogen peroxide concentration and thus different decomposition temperatures theoretically achievable, experimentally determined decomposition temperatures are not compared against each other directly but with the help of temperature efficiency as outlined hereafter.

4.2.4. Decomposition results

To account for test to test variation of recorded data on a catalyst test level, each catalyst test was repeated four times in a standardized test procedure. Typical time traces for decomposition exhaust temperatures and decomposition chamber pressures are shown in Figure 101 and Figure 102 for one selected catalyst from configuration #15. All analysis results presented hereafter, such as stationary performance values and transition times, base on the results retrieved for each catalyst by these successive tests at nominal mass flow of 0.3 g s^{-1}.
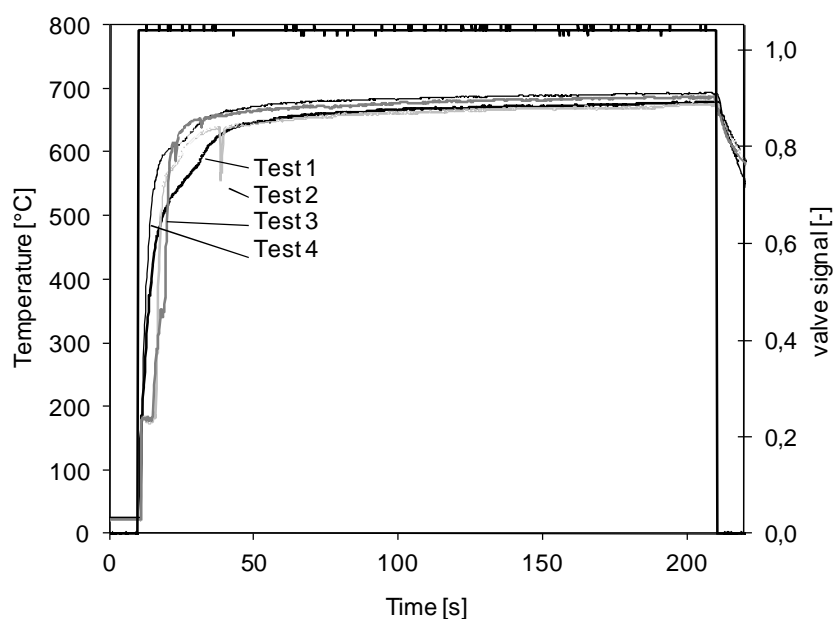
Figure 101 Time traces of decomposition product temperature for one catalyst of configuration #15

System pressures have been determined at the hydrogen peroxide tank, the feedline upstream of the injector and in the decomposition chamber downstream of the catalyst. Typical recorded pressure signals at these stations are shown in conjunction with the recorded mass flow in Figure 102.
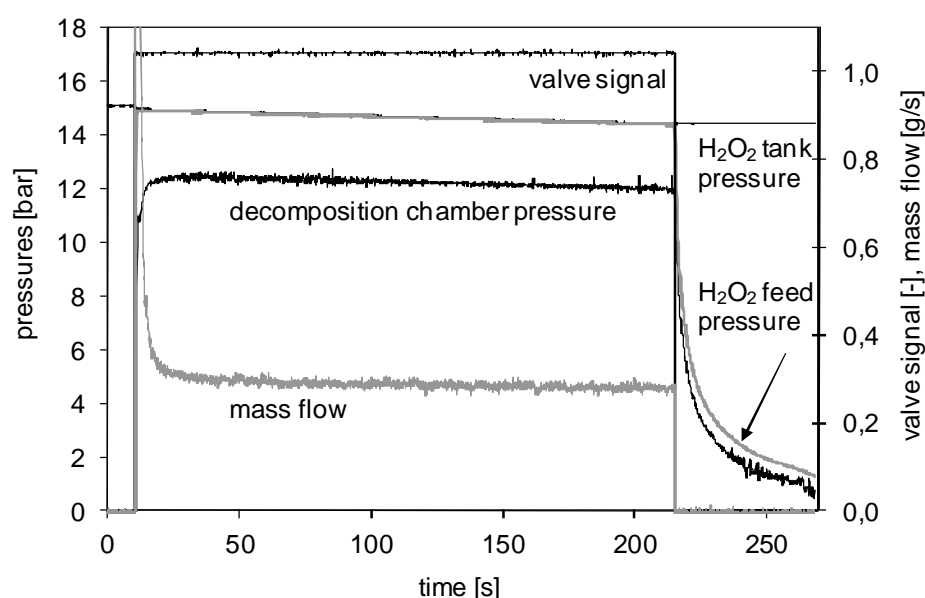
Figure 102 Pressure and mass flow signal in for a typical single catalyst test of a configuration #15 catalyst

Figure 103 shows the initial decomposition chamber pressures relative to ambient pressure of four successive tests with catalyst GC-143 after the hydrogen peroxide feed valve has been opened at $t \approx 10$ s. The pressure rise times from first increase in pressure signal to 90 % of the stationary chamber pressure are determined as 350 ms, 410 ms, 490 ms and 570 ms for the catalyst shown.
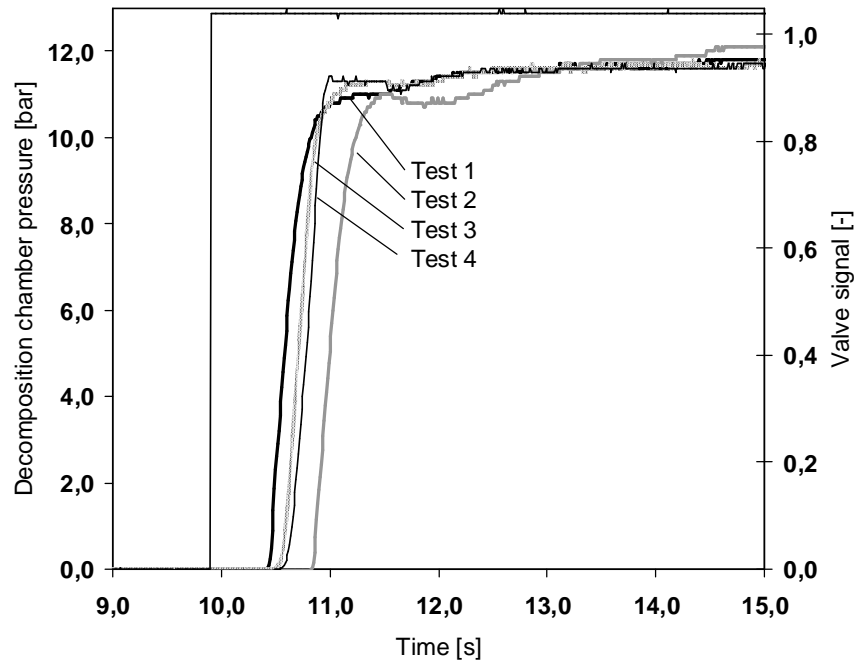
Figure 103 Initial chamber pressure build-up for a sample catalyst of configuration #15

4.2.4.1. Transient results
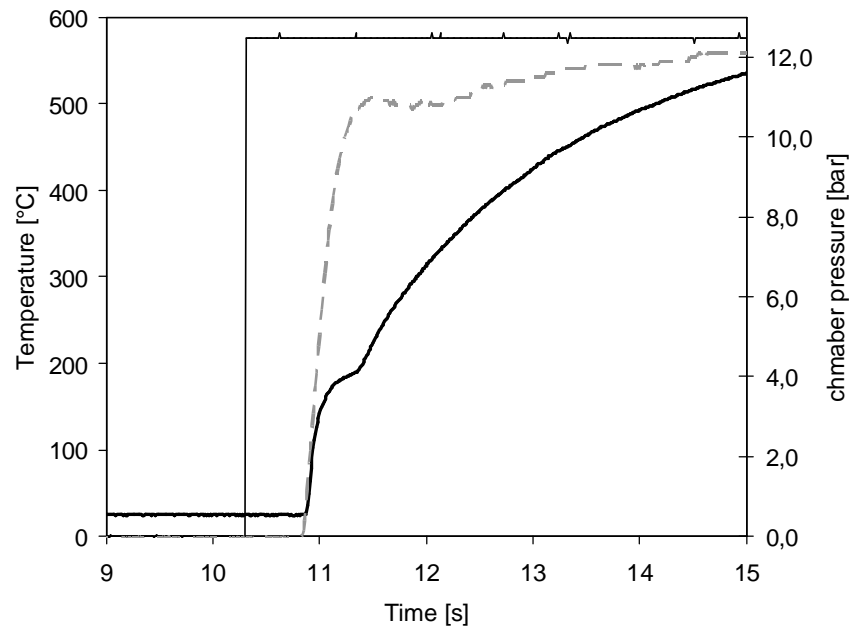
Figure 104: Transient single test detail of a single test of configuration #15, temperature (solid black line) and pressure (dashed gray line) with valve signal indicated (fine black line)

The temperature signal has been chosen as leading parameter to investigate the transient behavior for catalysts in an autoigniting bipropellant system. Figure 104 shows a close capture of the transient behavior for a single test of a catalyst from configuration #15. One can see that the time elapsed to reach 90 % of decomposition chamber pressure is in the order

hundreds of milliseconds after first increase in chamber pressure is noticed, whereas temperature transition times are in the order of several seconds. Since the rise in temperature is much slower than the rise in chamber pressure signal, surpassing the temperature threshold for autoignition has been identified as the limiting parameter in transitional thruster behavior. This temperature requirement is different from the commonly used investigation based on chamber pressure rise, which relates to thrust generation in monopropellant systems.

For the test shown in Figure 104, the transition time for the temperature is determined to $t_{500} = 3.85$ s after valve opening at $t = 10.31$ s.

Figure 104 however shows an initial delay of 0.57 s before first temperature rising occurs, caused by filling of internal volumes of the feedline and the injector before injection of hydrogen peroxide into the decomposition chamber occurs. This 0.57 s can therefore be subtracted from the values shown in the examination above to retrieve the actual transition time. In this case, the transition time results in a true transition time of $t_{500} = 3.28$ s. However, this correction is not applied in the analysis of transition times presented hereafter in Figure 105 and Figure 106 which therefore show the data of time elapsed until 500 °C are reached after valve opening including the filling of internal volumes.
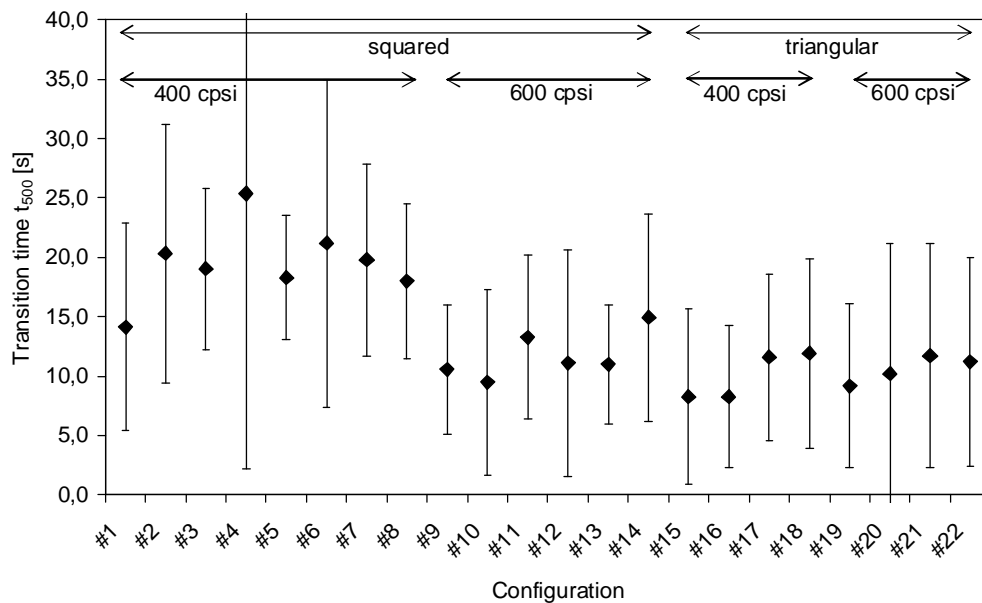
Figure 105 Time from first H_2O_2 injection until $T_{cat} = 500$ °C is reached, for catalyst configurations
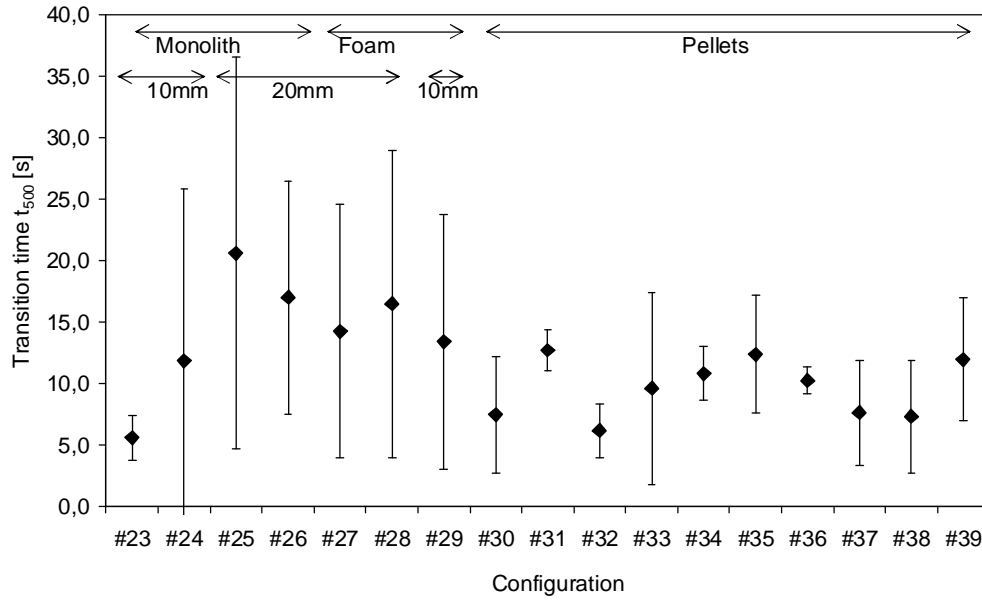
Figure 106 Time from first H_2O_2 injection until T_{cat} = 500 °C is reached, for catalyst configurations

For squared channel geometries, Figure 105 shows a general trend of decreased transition times for higher channel density, which is explained by increasing the active surface per volume of catalyst. However, this trend is not reproduced for triangular channel geometries. Comparing triangular to squared channel geometries, again the larger ratio of active surface to internal volume for triangular channels explains the better performance. A general trend of shorter transition times for catalyst based on Cordierite carrier material can be identified compared to catalysts based on SiC. This trend can be seen for the case of configuration #15 and #16 (Cordierite) compared to configuration #17 and #18 (SiC). Comparison of #23-#24 to #25-#26 shows a general trend of decreased transition times for shorter catalysts, hence smaller thermal masses. The findings of increased performance for shorter catalysts compare well to the findings in Ref. 37. Figure 106 shows best transition times being achieved by short catalyst configuration (L_M = 10 mm) # 23 and Pellets #32. This coincides with the findings in Ref. 65, identifying thermal mass as the limiting parameter for transition performance due to heat losses to the catalyst structure. Therefore, reduction of the thermal mass by shortening catalysts (L_M = 10 mm) or utilizing pellets in a 10 mm container can increase the transitional performance. Total dry mass of pellets tested was smaller compared to monolithic catalysts, thus explaining the general trend of better transitional performance for pellets.

4.2.4.2. Stationary conditions

Two types of efficiencies are defined, relating to different types of experimental measurements. Both are based on the characteristic velocity, defined by

$$c^* = \frac{P_c \cdot A^*}{\dot{m}} = \frac{\sqrt{\gamma \cdot R \cdot T_{cat}}}{\gamma \cdot \sqrt{\left[2/\left(\gamma+1\right)\right]^{(\gamma+1)/(\gamma-1)}}} \qquad (4.7)$$

Method 1 (related to temperature): $\qquad \eta_{c^*} = \dfrac{c^*}{c_{th}^*} = \sqrt{\dfrac{T_{cat}}{T_{dec}}}$ $\qquad$ (4.8)

Method 2 (related to pressure and mass flow): $\quad \eta_{c^*} = \dfrac{c^*}{c_{th}^*} = \dfrac{p_c \cdot A^*}{\dot{m} \cdot c_{th}^*}$. $\qquad$ (4.9)

The quasi static behavior of time traces during the test sequence is shown in Figure 101 for four repetitive tests. Quasi-static values are averaged over ± 2 s at $t = 150$ s, $t = 175$ s and $t = 200$ s, thus generating three values for the efficiency for each method per test per catalyst. Each data point presented in Figure 107 and Figure 108 represents the mean over four catalysts per configuration, which were tested four times each. The error bars are based on 95 % confidence intervals (2σ) and incorporating error propagation analysis.
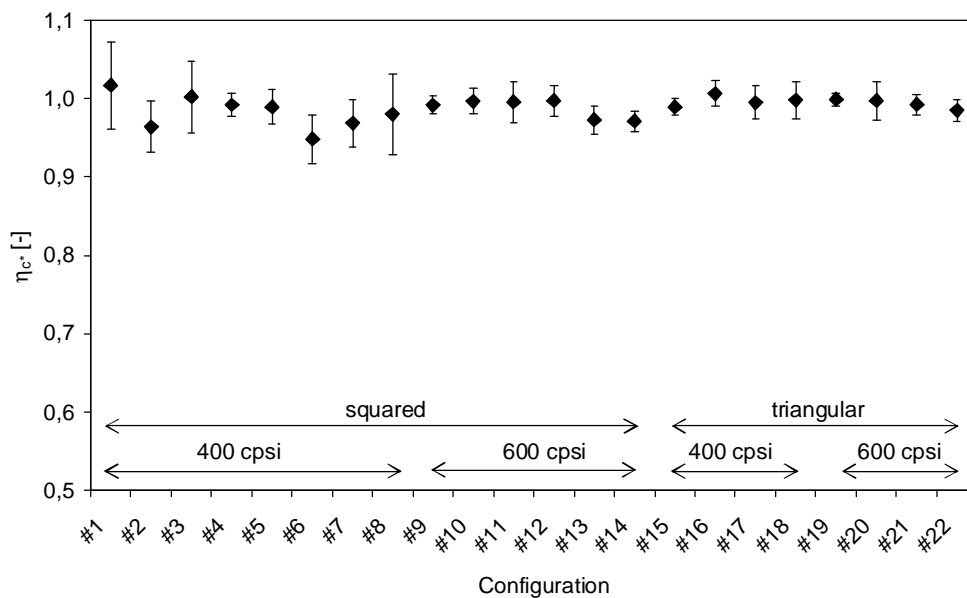
Figure 107 Mean Efficiencies (Method 1, related to temperature) for different catalyst configurations

Figure 107 shows the results for test campaign 1. Regarding temperature, all configurations tested showed performance values above 95 %. Values larger than unity are explained by radial inhomogeneities in temperature profile over catalyst exit surface versus temperature determination at the centre line of catalyst. The radial inhomogeneity with a local excess in temperature for the central exhaust stream and significantly decreased temperatures for outer channels has been experimentally measured in Ref. 65 and has also been found by other researchers [276]. This effect is explained by thermal conduction within the catalyst structure and preheating of injected hydrogen peroxide before decomposition occurs, as well as non uniform mass flow injection as discussed in section 2.3.6.5. These effects may be amplified by locally preheating within the injector element, leading to a local increase of the resulting exhaust temperature in the vicinity of the catalysts central axis. The caloric mean over the entire exhaust stream however remains below the ideal decomposition temperature, as no heat other than from the decomposition process itself is introduced to the system. Therefore, the analysis of central exhaust temperature can only partially be employed to guide the

classification of catalysts. A combination of method 1 and method 2 is therefore employed to evaluate the stationary catalyst performance.
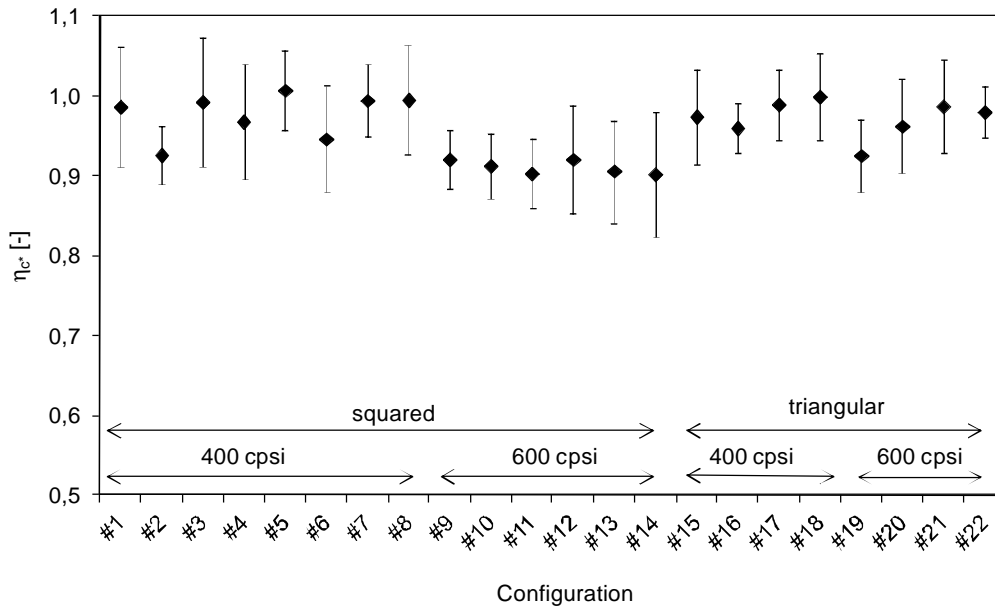
Figure 108 Mean Efficiencies (Method 2, related to pressure) for catalyst configurations

As the presence of a radial temperature distribution renders an evaluation of catalyst performance solely based on temperature impossible, efficiencies have been additionally determined based on pressure measurements according to Eq. (4.9). These results are presented in Figure 108. For squared channels, decreasing stationary performance for higher channel density is observed. However, this finding is not reproduced in case of triangular channel shapes.

Second set of assessment:

In the second test campaign, emphasis was taken on investigating different types of catalysts when employed in the same system. Therefore, monoliths, foams and pellets have been investigated using the same test setup and procedure as in test campaign 1. However, only two monoliths were tested for each configuration instead of four. Pellet configurations have been investigated by four successive tests of the same pellets filled into a dedicated pellet container only. Figure 109 and Figure 110 display the stationary results based on temperature related method 1 and pressure related method 2 respectively.
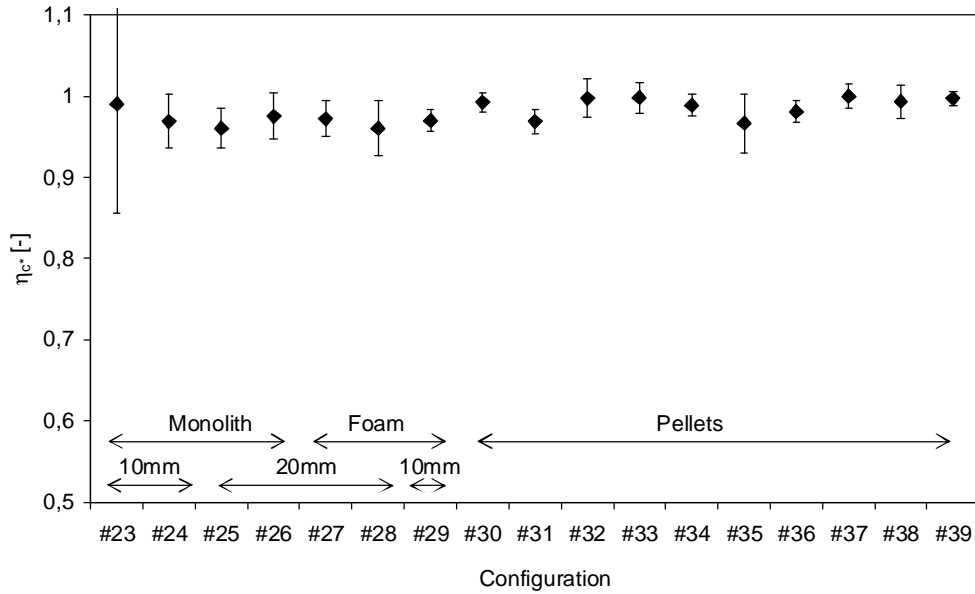
Figure 109 Mean Efficiencies (Method 1, related to temperature) for different catalyst configurations

Large chamber pressure oscillation has been observed for configuration #23, explaining the large standard deviations in Figure 109 and Figure 110. For #27, reduced mass flow rates compared to other configurations have been observed for equal remaining test parameters such as feedline pressure. This is assumed to be caused by systems influence such as a partially blocked orifice and leads to a significant increase in efficiency based on method 2 in Figure 110 surpassing unity. Therefore, this result is excluded from further analysis.
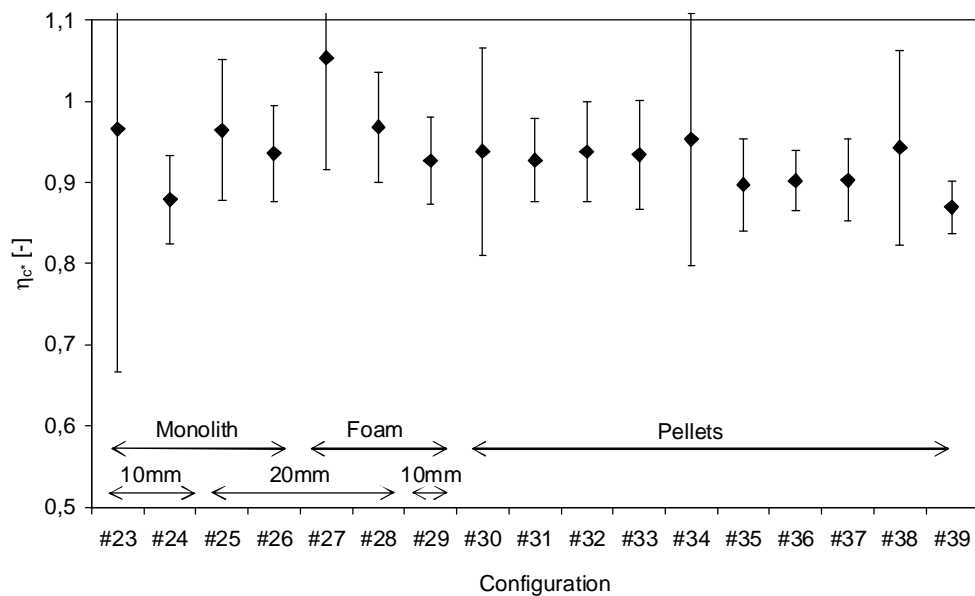
Figure 110 Mean Efficiencies (Method 2, related to pressure) for catalyst configurations

Crushing of pellets has been noticed by observing significant amounts of debris after disassembling the test apparatus for #30, #31 and #32 after accumulated hydrogen peroxide loads of 360 g per configuration, whereas no damage was observed for remaining pellet configurations. Figure 111 shows the partially crushed pellets of configuration #30 after four successive tests with total accumulated hydrogen peroxide load of 360 g.

Figure 111 Close capture of pellets (left) and debris (right) of configuration #30 after accumulated hydrogen peroxide load of 360 g

4.2.5. Discussion of catalyst test results

Although the tests campaigns were performed to assess different catalyst configurations on a system level, the results allow for a certain interpretation on the basis of single catalyst parameters, such as carrier material.

Since the existence of a radial temperature distribution of the catalyst exhaust stream make a determination of the efficiency based on temperature measurement ambiguous, the following discussion of the results is additionally based on assessment of efficiency based on pressure determination (method 2) and the assessment of transition times.

The sensitivity of the results presented above regarding stationary performance (method 2) and transition times show, that the test setup used for the assessment effort is not capable of guiding a distinct selection and de-selection process. A wide range of catalysts show satisfying performance, but spread of the results is in many cases larger than the difference of results between different configurations. However, the results allow for a discussion of the general trends found in this particular effort. These trends are discussed hereafter.

Since the investigation of pellets was not exhaustive, no analysis differentiating within the pellets will be performed. Instead, results from pellets should be regarded in a cohesive manner, comparing the results achieved for a variety of pellets to the results of different catalyst types on a system level. It should be noted that this investigation does not incorporate an assessment of the behavior of the different catalyst types for hydrogen peroxide total loads beyond 400 g per catalyst. This behavior might differ significantly for different types of catalysts and would have to be taken into account for a final assessment of the best catalyst configuration.

Test campaign 1
With the exception of Configuration #7 and #8, washcoating A yields shorter transition times and higher efficiencies than the equivalent configuration with washcoating B (Comparing: #1 to #2, #3 to #4. #5 to #6).

Comparing #1-#4 to #5-#8 shows increased transition times for SiC. A slight trend towards higher efficiencies can be identified for the SiC based catalysts. This trend is reproduced for 400 cpsi triangular channels (Comparison of #15-#16 to #17-#18) and 600 cpsi triangular

channels (Comparing #19-#20 to #21-#22). However, this trend is not reproduced for 600 cpsi catalysts (#11-#12 compared to #13-#14) where inconsistent results are found for the two pairs of comparable configurations. It should be noted that for configurations #1-#14 and #19-#22 the change of carrier material from Cordierite to SiC comes with a slight increase of the intrinsic channel density as shown in Table 16 caused during the manufacturing process by different rates of honeycomb shrinking.

Although the impact of active material can be assessed by comparison of 11 catalyst configuration pairs only differing in active material over a variety of different parameters such as carrier materials, channel density and geometry, no clear trend can be identified. Concerning both transition times and stationary performance, almost equal number of cases are identified which point either to an improved performance for Pt or which would identify MnO_x as improved active material. Therefore, no clear conclusion concerning the result of the assessment of these active materials can be drawn.

Comparing #1-#8 to #9 - #14 shows decreased transition times for increasing channel densities for squared channels. However, a decrease in stationary performance is observed for increasing channel density. For triangular channel geometries, no such trend can be identified. Comparison of 400 cpsi squared configurations shows a decrease in transition times for all triangular configurations compared to their squared channel pendants (comparison of: #2 to #15, #4 to #16, #6 to #17 and #8 to #18). Comparing the same configuration also shows an increase in efficiency for triangular geometries except for the comparison of #4 to #16, where no change in efficiency can be identified. Comparing the 600 cpsi configurations (#11 to #19, #12 to #20, #13 to #21 and #14 to #22) reproduces the trend of increased stationary efficiencies for the triangular channel geometries for all configurations. A decreasing transition time for triangular channel geometries compared to squared geometries is found for three out of four compared configurations, with the exception being the comparison of #13 to #21.

Test campaign 2
Comparing 10 mm length configurations #23-#24 to their 20 mm length pendant #25-#26 shows significantly improved transitional performance for the shorter catalysts in both cases, corresponding to the smaller thermal mass. Comparing the stationary efficiencies shows no improvement for the MnO_x configuration and a decrease for 10 mm length Pt catalysts compared to the equivalent 20 mm length configuration. It should be noted that in the case of #23, significant chamber pressure oscillations led to large standard deviation in the recorded data.

Due to the simultaneous change of various parameters such as the wash coating procedure, the carrier material and catalyst mass and volume, identification of the impact of the change of a single parameter on the catalyst performance is impossible in the evaluation of different catalyst types. Instead, the results are discussed on a qualitative basis comparing the overall catalyst configurations on system level. Although differing in carrier material, $L_M = 20$ mm length monoliths (configuration #26) can be set in relation to corresponding foams of equal length (#28). This shows a reduction in transition time for the foams. However, this reduction

is not observed for L_M =10 mm length configurations (#23 and #29). Comparing transition times of foams and monoliths to the pellets investigated is not possible due to the significant reduction of catalyst volume and mass for the pellets. Since this is associated with a significant decrease of thermal mass for the pellet type catalysts, any impact of the transition time will be outweighed by this change in thermal mass.

Comparing the stationary performance in Figure 110 between L_M = 20 mm monoliths and foams shows similar performance except for the unusual large value greater than unity for #27. Since this is an unphysical result, it has to be discarded from the analysis as it has probably been caused by an influence not related to the catalyst performance. Therefore, no clear trend regarding the stationary performance of monoliths versus foams can be concluded from the data presented.

Comparing stationary performance values for pellets to the remaining catalyst types shows that although the significantly reduced amount of catalyst mass in the case of pellets, still high performance is achieved for a large variety of different pellets.

4.2.6. System considerations

4.2.6.1.   Early transient stage – influences on temperature measurement

Large temperature gradients and possible recondensation phenomena occurring in the early transient stage of decomposition by hot exhaust gas encountering cold structural chamber elements in the vicinity of the thermocouple may influence the recorded temperature. Therefore, tests dedicated to investigate this phenomenon were conducted for single catalysts of configuration #23, #29 and #38. The standard reference chamber (in L_M = 10 mm configuration) was modified by introducing thermal insulation of the converging chamber section.

To minimize any influences of the cold chamber walls on the temperature measurements in the initial transitional phase, shielding of the walls was conducted, as shown in Figure 112 on the left hand side. This was accomplished by a layer of thermally insulating ceramic paper (C), coated by stainless steel (AISI 304) foil (B) of 0.025 mm thickness . The small thermal mass of the steel foil, considerably reduced compared to the chamber wall, allows rapid temperature increase. This way, decomposition products are retained from cold chamber walls and large temperature gradients near thermocouple (A) are avoided. The downstream flange of the decomposition chamber with the insulated nozzle section and the bended thermocouple is shown in Figure 112 on the right hand side.
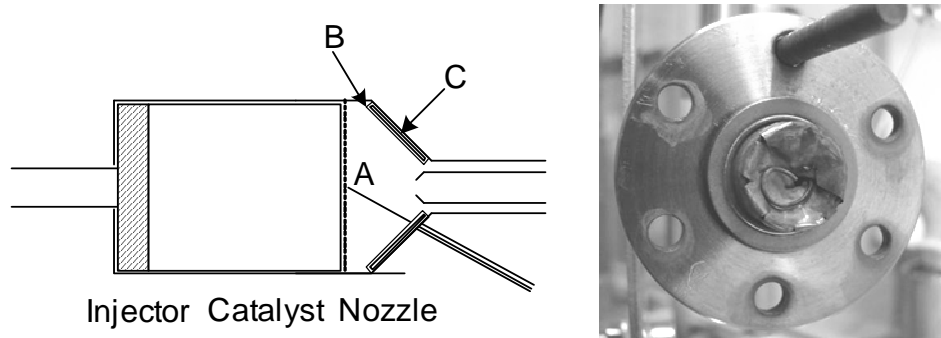
Figure 112 Schematic of shielded transition test setup of convergent chamber section (left) and picture of shielded convergent decomposition chamber section with thermocouple (right)

Figure 113 shows the transition time data for different catalyst types in standard decomposition chamber compared to the transition time data acquired in the shielded decomposition chamber configuration displayed in Figure 112. Shorter transition times are noticed for all configurations investigated, with smallest transition times found for the shielded configuration of C-2/1 with $t_{500} = 1.56$ s.
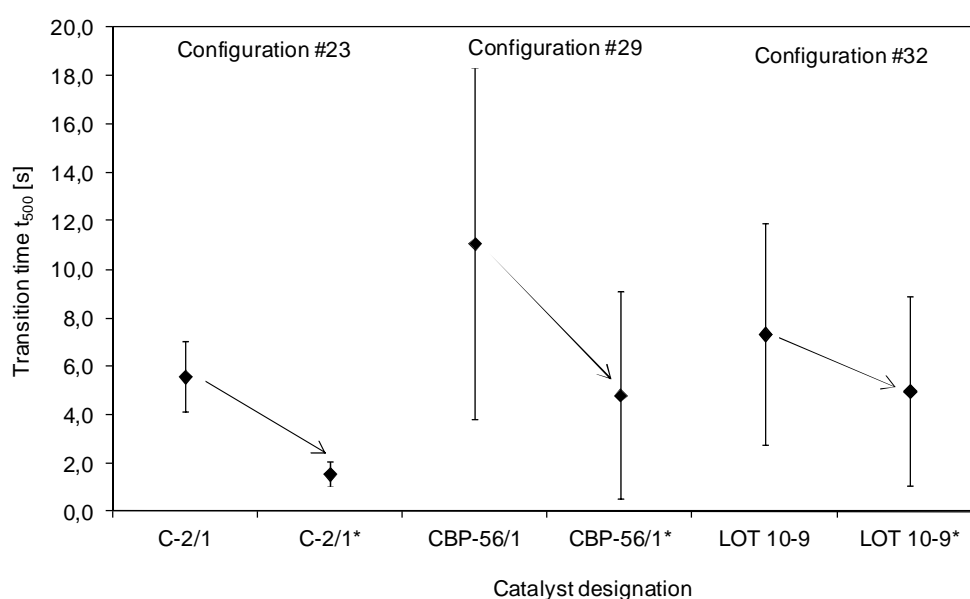
Annotations: *catalyst tested in shielded configuration

Figure 113 Transition times determined in regular and shielded chamber configuration

However, in order to maintain constant test setups for all catalyst configurations, the shielding technique described in this section has not been applied in the investigation in section 4.2.4. While relative comparison of these configurations is still valid, absolute transition times, when proper shielding of the nozzle is guaranteed, are anticipated to be shorter according to the findings in this chapter. The results of this investigation led to a shielded design of the decomposition nozzle in the EBB thruster assembly to avoid excessive heat losses of the oxygen steam mixture before injection into the combustion chamber.

4.2.6.2.   Sensitivity to mass flow

The positive impact of increasing the catalyst bed loading on transitional behavior is shown in Figure 114 for a catalyst of configuration #23 (MnO$_x$-Cordierite) with a channel density of 304 cpsi. As mass flow peaks in the transitional stage of chamber pressure build-up, the stationary mass flow is used as parameter to qualitatively show the decrease of transition time with increasing mass flow. This mass flow has been determined by averaging over 1 s, with according standard deviation (95 % confidence interval) indicated. To achieve large mass flows, a larger orifice of 0.9 mm diameter was employed, explaining the longer transition times for standard mass flow of 0.5 g s^{-1} compared to the results shown in Figure 106.
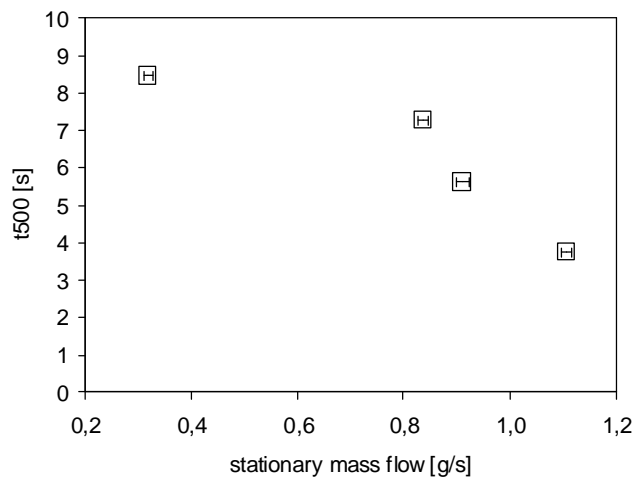
Figure 114 Transition time as a function of stationary mass flow

4.2.6.3.   Total H$_2$O$_2$ load results

Lifetime tests have been conducted using a $L_M = 20$ mm length and a $L_M = 10$ mm length 600 cpsi MnO$_x$ catalysts with triangle channel geometries. Successive tests with valve opening durations between 200 s and 300 s have been conducted. The accumulated total hydrogen peroxide loads decomposed have been 17.8 kg for the $L_M = 20$ mm catalyst and 4.15 kg for the 10 mm length catalyst. This accumulated load refers to the total hydrogen peroxide decomposed before stationary decomposition temperature dropped, determined by gravimetric weighting of the hydrogen peroxide during refueling. After opening the decomposition chamber at the end of the lifetime test, the 10 mm length catalyst was found to be broken in half, with minor debris as shown in Figure 115. However, while mounted into the decomposition chamber, the catalyst had maintained its structural integrity. In the case of the 20 mm length catalyst, the chamber was opened at H$_2$O$_2$ loads of 6.4 kg and 12.1 kg, showing increasing degrees of damage. At the end of the lifetime test, the $L_M = 20$ mm catalyst was found broken into various parts and showed a significant amount of debris.
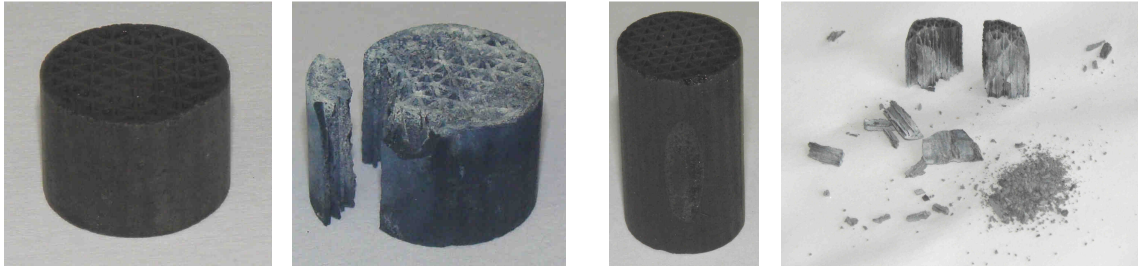
Figure 115 Catalyst before and after lifetime testing (L_M = 10 mm catalyst on the left, L_M = 20 mm catalyst on the right hand side)

Figure 116 shows the maximum decomposition temperature achieved per test by the L_M = 20 mm length catalyst as a function of total hydrogen peroxide mass load over the entire lifetime and the transition times to reach T_{cat} > 500 °C from ambient conditions after valve opening. An increase in mass flow for tests above 4.98 kg total hydrogen peroxide load led to a significant reduction in transition times. The opening of the decomposition chamber during the test series is indicated in the figure by the manipulation performed. Debris removal has been performed in case the catalyst was found broken. With the exception of a performance drop between 9.0 kg and 12 kg total load, the catalyst performed well even after structural damage occurred.
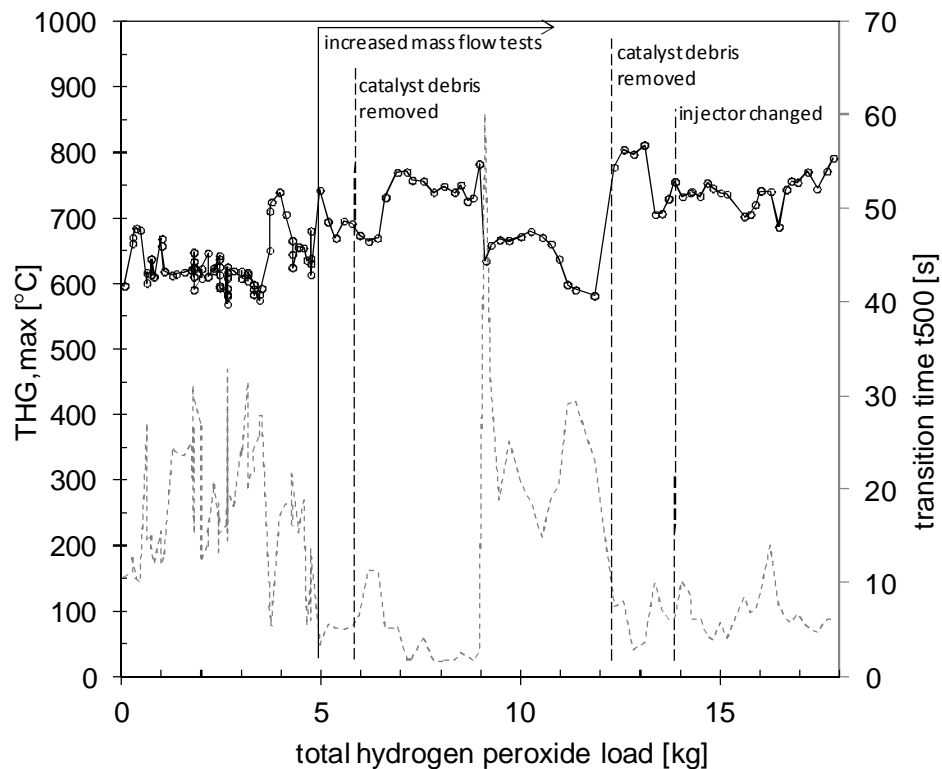
Figure 116 Maximum decomposition temperatures and transition times as a function of total hydrogen peroxide load

4.2.6.4. Overloading experiments

In this section, tests with a variety of mass flows significantly above the design mass flow of $0.3g\ s^{-1}$ have been conducted, to intentionally cause overloading of the catalyst. To investigate overloading of the catalyst, two test modes have been employed. In the first mode, each data point has been retrieved by setting a given feed pressure before starting the test sequence. During the test, this feed pressure was held constant. After the test and cooling down of the chamber, the feed pressure was adjusted to a higher value, before the next test sequence was initiated. This mode has been employed to determine all data retrieved for catalysts C2-1 and C2-2.

In the second test mode, one dedicated overloading test was conducted after the catalysts performance has been verified in four successive incoming tests. During this dedicated overloading test, the feed pressure was increased stepwise during the test sequence, with plateaus of constant pressure of 20 seconds in between pressure increases to allow quasi-stationary retrieval of data. This mode has been employed to conduct investigation of overloading effects at small accumulated hydrogen peroxide loads for a given catalyst. This mode has been employed for catalyst GC94a and GC94b.

Increasing the mass flow by varying the feed pressure leads to an increased decomposition chamber pressure in case of constant nozzle throat diameter. This change in chamber pressure impacts the evaporation regimes and therefore possibly impacts the overall catalyst behavior. To account for this, tests have been conducted with differing throat diameters of 0.4 mm, 0.9 mm and 1.0 mm. This way, the chamber pressure was held in certain boundaries of ± 2 bar from the design chamber pressure of $p_C = 13$ bar.

The total accumulated hydrogen peroxide loads at the end of the test sequences presented in this section are given in Table 18. A comparison of the values for the different catalysts and to lifetime results from identical catalysts shows that aging of the catalyst can be ruled out as influence causing the rapid decrease in performance. Therefore, this decrease is solely attributed to an overloading effect. Table 18 additionally shows the amount of active material per catalyst. Again, deviations in the amount of active material do not constitute any trend in the resulting overloading tests. The weight of the catalysts was determined before and after the overloading tests after storage under controlled conditions. All four catalysts tested lost weight during these tests, although to significantly different amounts. The changes in weight of the catalysts are listed in Table 18. Again, the weight loss is not correlated with the mode of testing. It should be noted that the accumulated H_2O_2 load does not correspond to the H_2O_2 employed for the overloading tests, since it also incorporated the H_2O_2 load from previous investigations. Therefore, relating the mass loss to the H_2O_2 load is not feasible. However, larger H_2O_2 loads have been employed during overloading tests for C2-1 and C2-2 compared to GC94a and GC94b.

As catalysts have shown irregularities in decomposition behavior after overloading in previous investigations, each catalyst was discarded for further analysis after the first overloading effect was detected.

Table 18 Total H2O2 loads at end of overloading investigation and catalyst properties

Catalyst designation	Accumulated H_2O_2 load [g]	Intrinsic channel density [cpsi]	Catalyst length [mm]	Amount of active material [g]	Overall catalyst weight change during overloading tests [%]
C2-1	1766.8	304	10	0.0787	-3.31
C2-2	1043.1	304	10	0.1027	-1.24
GC94a	558.9	635	10	0.0294	-1.02
GC94b	714.7	635	10	0.0353	-0.32

The recorded decomposition exhaust temperatures are shown in Figure 117 as a function of hydrogen peroxide mass flow. It is obvious that at mass flows of approximately 1.0-1.7g s^{-1}, thresholds for the given catalysts are reached. Further increasing the mass flow led to exhaust of incompletely evaporated fluid and thus to an immediate decrease in temperature. At this stage, the residence time within the catalyst caused by large flow velocities appears to be too small for complete decomposition and temperature of the catalyst structure remains low because of the increased cooling effect of the large amount of injected liquid hydrogen peroxide. This leads to the expulsion of only partially decomposed liquid at low temperatures close or even below the evaporation temperature region. As chamber pressure decreases in case of overloading, the evaporation temperatures decrease accordingly.

The deviation of overloading threshold in the experimental data is not related to the type of measurements (ramped (GC94a and GC94b) versus individual (C2-1 and C2-2) tests) or the channel density of the catalyst (304 cpsi for C2-1 and C2-2 versus 635 cpsi for GC94a and GC94b).
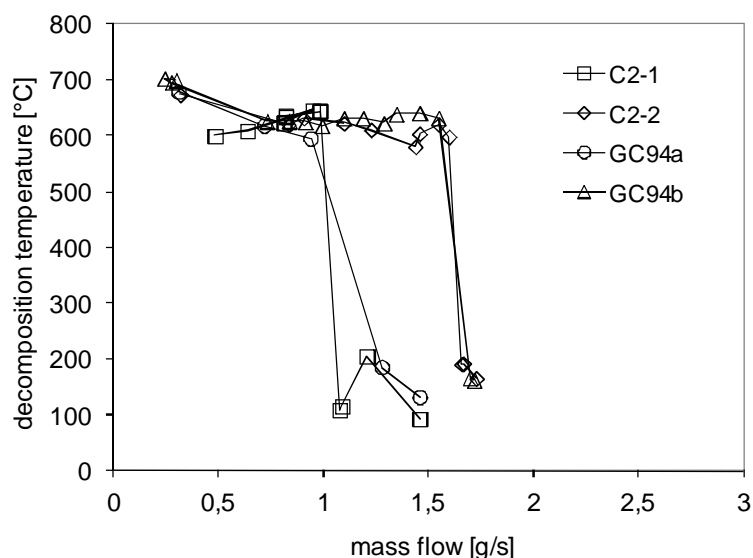
Figure 117 Experimental found overloading effect of catalysts

4.2.6.5. Measurement of radial temperature inhomogeneity

The simulation efforts predicted the existence of a significant temperature gradient of the exhaust gas over the catalyst exit face, introducing a significant error into the performance determination based on a single location temperature measurement.

To verify the existence of such a radial distribution of the exhaust gas temperature exiting the catalyst, a second thermocouple was inserted into the chamber downstream of the catalyst. One thermocouple (Ø 0.25 mm) was positioned at the central line of the catalyst, serving as reference temperature measurement, whereas the additional thermocouple (Ø 0.5 mm) was repositioned in radial direction to determine the exit temperature at distinguished positions. Both thermocouples were bended to increase the total length inserted into the gaseous flow to minimize heat conduction to the decomposition wall, as shown in Figure 118. The repositioning of the 0.25 mm thermocouple was done by bending only, keeping the overall length inserted into the stream constant to avoid modification of the measurement setup. The error introduced by changing the radiative environment between thermocouple tip and decomposition chamber wall when repositioning the thermocouple has been simulated and was found to be well below 0.5 % of the measured temperature differences.

To increase reliability of the measurements, four repetitive tests were performed for each radial position, including four tests with both thermocouples at the central line to guarantee agreement between the results among the thermocouples. In addition, four tests were performed at a mirrored position verifying the assumption of symmetric temperature distribution for one of the tested catalysts.

Radial thermocouple, repositioned (0.5mm diameter)   Central reference thermocouple kept at constant position (0.25mm diameter)
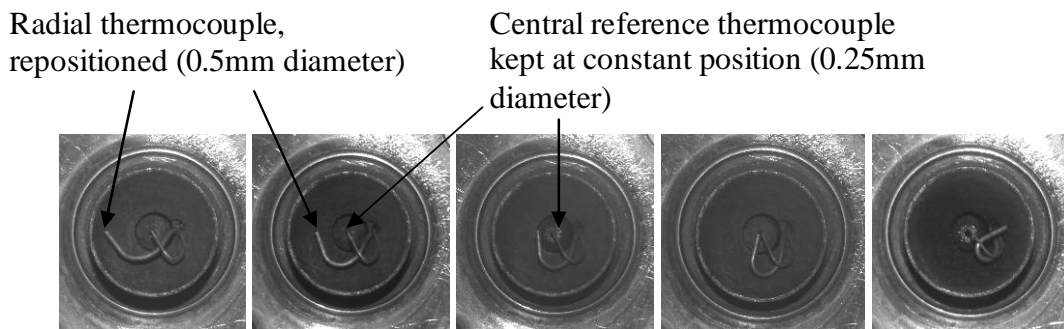
Figure 118: Thermocouple configuration for radial temperature measurements

The resulting distributions measured for catalyst GC-65 (635 cpsi squared channel type with $L_M = 20$ mm length) and GC-007 (400 cpsi squared channel type with $L_M = 20$ mm length) are shown in Figure 119. One can see good agreement with the measured temperatures at the central line of the catalyst. As reference measurements have been taken for each test, a large number of data points can be found at this position for the 0.5 mm thermocouple, compared to the values for the 0.25 mm which was positioned at the central line for four successive tests. All of these central values are well above the ideal decomposition temperature of hydrogen peroxide at the given concentration which amounts to 695.23 °C, pointing to a preheating effect of the undecomposed central fluid stream. The tests investigating the radial distribution show a significant decrease in temperature with radius as thermal losses to the surrounding

decomposition chamber increase. As the area and thus, for uniform mass flow, the cumulative heat capacity of the exhaust flow increases with radius, these regions feature increased weight when determining the overall mixture temperature. The overall mixture temperature thus turns out to be below the ideal decomposition temperature for the given initial concentration and therefore obeys the conservation of energy. These locally increased temperatures of the centrally located gas stream due to radial inhomogeneities explain the temperature excesses above the ideal decomposition temperature measured in this work and by other researchers [276, 277].
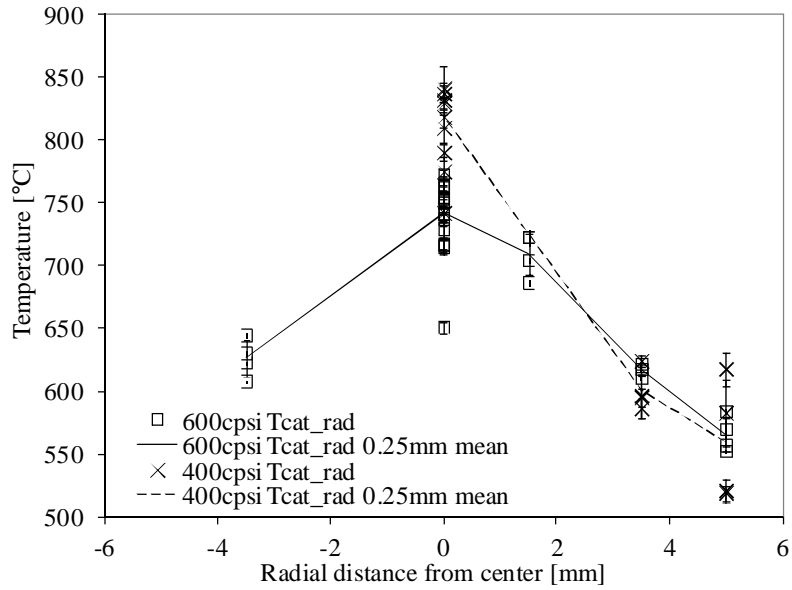
Figure 119 Radial temperature distribution downstream of catalyst
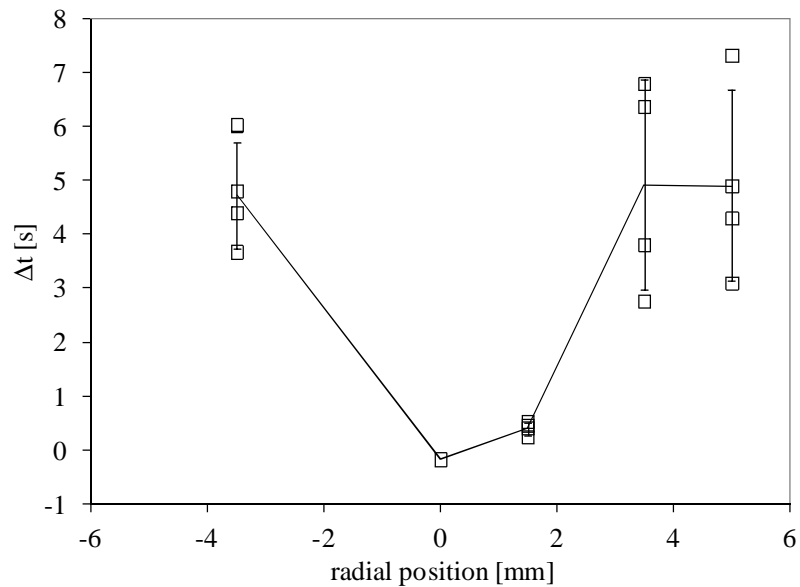
Figure 120 Time delay to reach $T = 500$ °C as function of radial position

Figure 120 shows differences in transition times between the centrally located and radially repositioned thermocouple measurements, Relative values are shown rather than absolute values to avoid test to test scattering of the data. As can be seen from Figure 120 in

comparison to the center location an additional time delay has to be taken into account for channels located off the central catalyst axis. Near the decomposition chamber wall up to $\Delta t = 5$ s, in addition to the time delay of the center thermocouple were necessary to reach $T_{cat} = 500\ °C$.

4.2.6.6.   Impact of decomposition chamber structure on performance
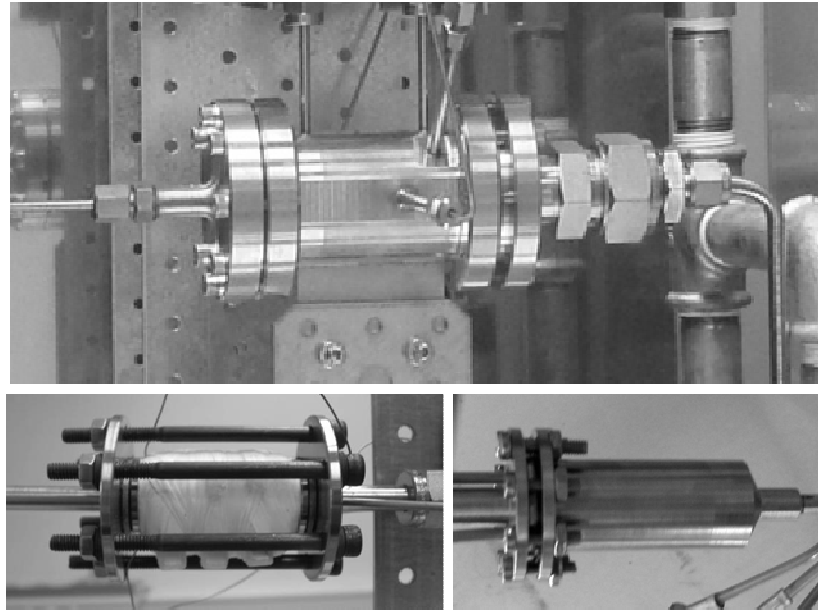
Figure 121 Different chamber designs to investigate impact of structural mass on decomposition, chamber L (top), chamber S (bottom left) and chamber EBB (bottom right)

In addition to the decomposition chamber design shown in Figure 95, alternative chambers differing in structural mass have been employed to qualitatively assess the impact of chamber structural mass on decomposition performance. These are shown in Figure 121.

Three different chamber designs have been used, all manufactured out of stainless steel. The largest chamber (shown in Figure 121 at the top) features two flanges to access the catalyst. The wall thickness of the conical part housing the catalyst is 13.5 mm. The second chamber design is the standard reference chamber, in which all the experimental investigations of catalysts presented above have been conducted. It features two flanges, with a tubal part housing the catalyst in between. The wall thickness of this tube is 1.28 mm (Figure 121, bottom left). The third and smallest design, shown in Figure 121, bottom right, has only one flange upstream of the hydrogen peroxide injector. The downstream section, housing the catalyst, is composed of a 0.8 mm stainless steel cone, with a nozzle design equal to the reference chamber design shown in Figure 95 top. Like the reference chamber, this chamber has been thermally insulated during testing. All chambers were manufactured out of stainless steel, the approximate masses are given in Table 19

Table 19 Approximate decomposition chamber masses

Chamber designation	Approximate mass [g]
Chamber L	~1440
Chamber S	~240
Chamber EBB	~50
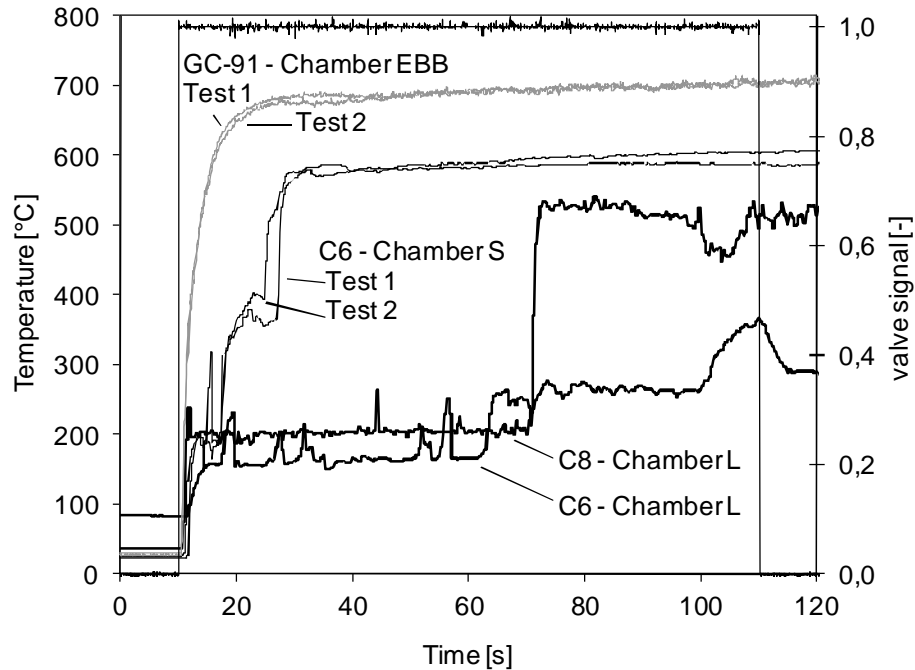
Figure 122 Temperature profiles of exhaust flow for different chamber designs

Figure 122 shows experimental temperature time traces for different chamber designs. All catalysts compared to each other are Cordierite carrier type with MnO_x as active phase. C6 and C8 are 204 cpsi, whereas GC-91 has a channel density of 635 cpsi. Monoliths with both channel densities 204 and 635 cpsi have additionally been tested in the chamber S, yielding minor improvement in performance for larger channel densities in the stationary case. Thus, the increase in channel density can be excluded as single cause for the vast improvement in transitional performance found in the data of chamber EBB compared to chamber S. It can thus be concluded that the major impact responsible for the improvement is due to the reduced thermal mass of the decomposition chambers. For the large chamber for catalyst C6, one can distinguish between the different plateaus of evaporation at chamber pressure of 10 bar. Spikes in the temperature data during the lower plateau however indicate the presence of fluid at higher temperature. Since evaporation occurs in accordance to the binary phase diagram, this data may indicate local exsolution of the mixture. For catalyst C8, the test showed incomplete chamber pressure build-up and chamber pressure remained at 5.5 bar, with correspondingly lower evaporation temperature of the mixture. The presence of partially liquid fluid at the exit of the catalyst however indicated incomplete decomposition throughout large portions of the test period for this chamber design.

4.2.6.7. Preheated catalyst

In this section, catalyst behavior in the case of hydrogen peroxide injection at elevated catalyst temperature is investigated. This scenario is in particular interest for pulsed firing operation of the thruster.

Due to the strong positive impact of increased temperatures on the rate of hydrogen peroxide decomposition, favorable transitional behavior is anticipated. This has been confirmed in various test runs, with a selected test for a catalyst of configuration #5 shown in Figure 123. In this case, reduced non operational time in between test runs resulted in temperatures measured downstream of the catalyst of $T_{cat} = 320$ °C before start of the test. The immediate total decomposition facilitated by the elevated temperatures is apparent from the fast transient of the temperature signal.
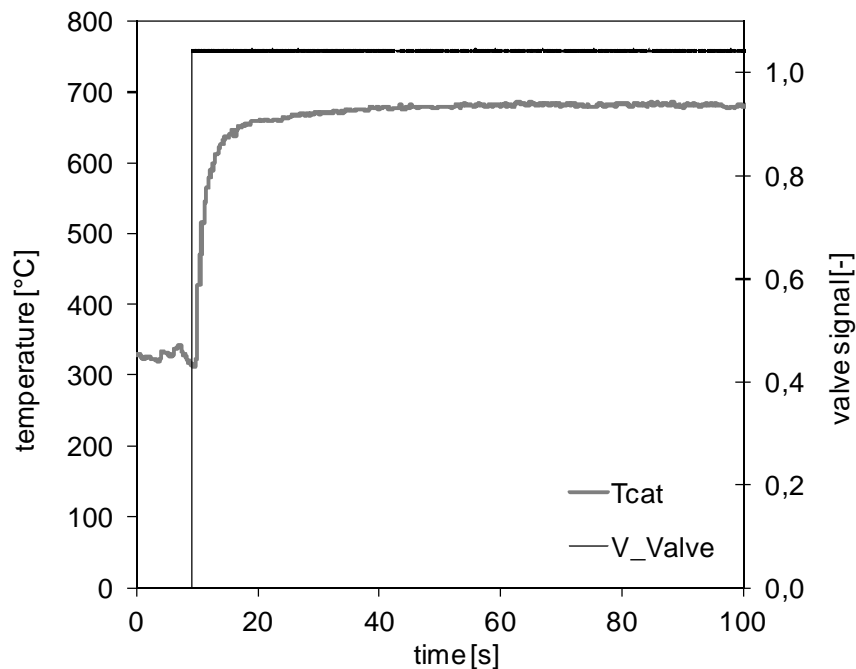
Figure 123 Hot start behavior of catalyst GS-039 in standard configuration, preheated to $T_{cat} = 320$ °C

4.2.7. Catalyst investigation summary and conclusion

In this chapter, two test campaigns investigating a total of 37 different catalyst configurations in a propulsion like test environment have been conducted. Test campaign 1 investigated different channel geometries, active materials, different carrier materials and washcoating procedures. A standardized test procedure regarding transitional start-up behavior and near stationary conditions was implemented. Test-to-test variations and catalyst-to-catalyst variations have been addressed by a total of 16 consecutive tests with 4 different catalysts per configuration.

Transitional test results regarding pressure rise to 90 % of the stationary chamber pressure after hydrogen peroxide injection was found to be in the order of 350 ms to 500 ms. Temperature start-up times for reaching 500 °C after cold start were found as small as 3.28 s. Tests in an advanced measurement setup however showed temperature transition times as small as 1.56 s. Major findings stress the importance of decreasing the length and hence the thermal mass of the catalyst to increase transitional performance. Stationary performance was evaluated by both temperature and characteristic velocity related efficiencies. Trends regarding the type of washcoating procedure, channel density and carrier material could be identified.

Test campaign 2 was used to investigate different types of catalyst, including monoliths and foams at different lengths, and pellet type catalysts. A qualitative comparison of different types of catalysts utilized in the same test reactor allowed the comparison of monoliths, foams and different types of pellets on a qualitative basis.

Selection of the catalysts employed in further ignition, bipropellant and final demonstration tests are based on the findings from the two test campaigns regarding channel geometry and density, material composition. These findings led to the selection of reduced length catalysts with high channel densities to be employed in the thruster tests in sections 4.4.3.6 and 4.5.

Catalyst system features such as sensitivity to increased mass flow including catalyst overloading, radial temperature distribution of the exhaust flow and impact of decomposition chamber mass on decomposition performance have been investigated on an experimental basis, confirming major theoretical predictions from section 2.3.

Lifetime tests of both a $L_M = 20$ mm and a $L_M = 10$ mm length monolith catalyst showed total accumulated hydrogen peroxide loads of 17.8 kg and 4.15 kg for the two configurations respectively. In the case of the $L_M = 20$ mm catalyst, severe structural damage was observed at the end of lifetime while still maintaining high decomposition efficiency.

4.3. Ignition chamber

4.3.1. Description of experimental setup and instrumentation

The capacitively cooled modular combustion chamber presented in this section is designated "ignition chamber" in accordance to its main purpose of investigating the autoignition behavior of decomposed hydrogen peroxide with a liquid fuel. The main features of this ignition chamber are a modular combustion chamber design allowing for a change of combustion volume, a back-pressure device decoupling mass flow and chamber pressure and external preheating of the structure and oxidizer flow to control ignition conditions. These features are discussed in detail hereafter.
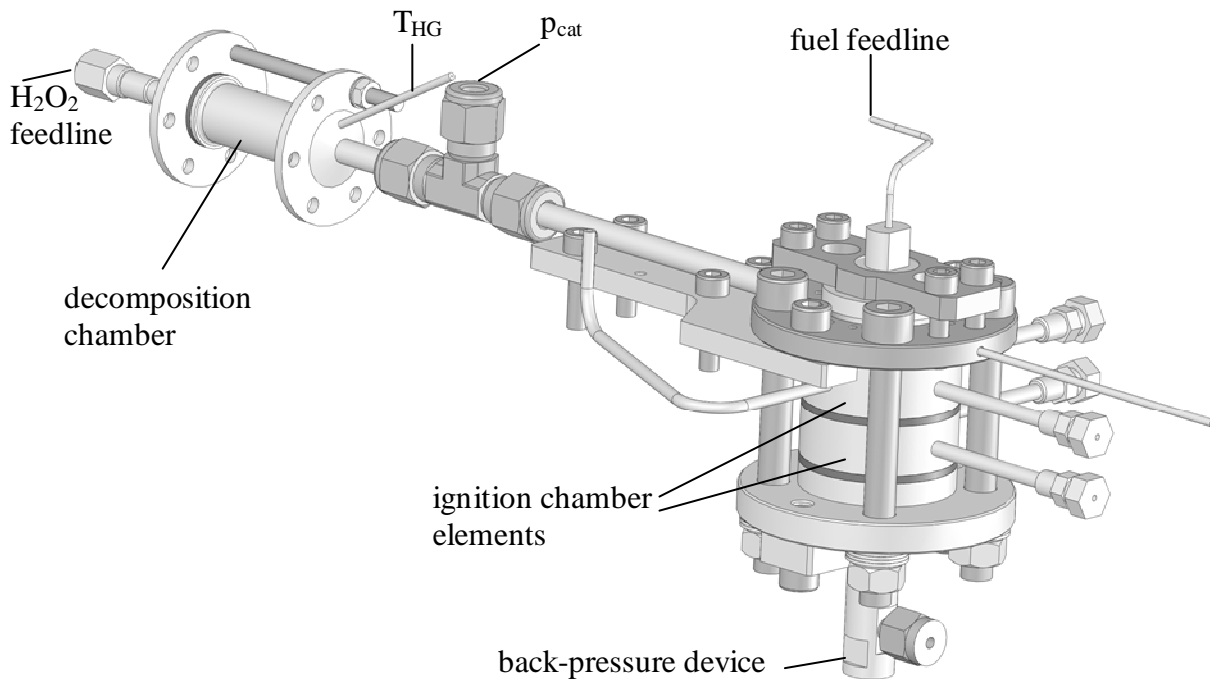
Figure 124 CAD drawing of ignition chamber assembly with decomposition chamber

Figure 124 shows a CAD drawing of the ignition chamber, as assembled on the test stand, which houses the oxidizer and fuel feed system. The connections to the feed systems are indicated using the labels "fuel/H_2O_2 feedline". The hydrogen peroxide is decomposed in a dedicated decomposition chamber equivalent to the one utilized in section 4.2.1. The decomposed hydrogen peroxide is fed into the ignition chamber where it is mixed and combusted with the injected fuel, as shown in Figure 125. The injection system is described hereafter in detail. Figure 125 shows the instrumentation of the ignition chamber. The main temperature parameter T_{inj} is determined directly in the swirl flow of the injected oxidizer and fuel mixture within the premixing chamber as depicted in Figure 125.
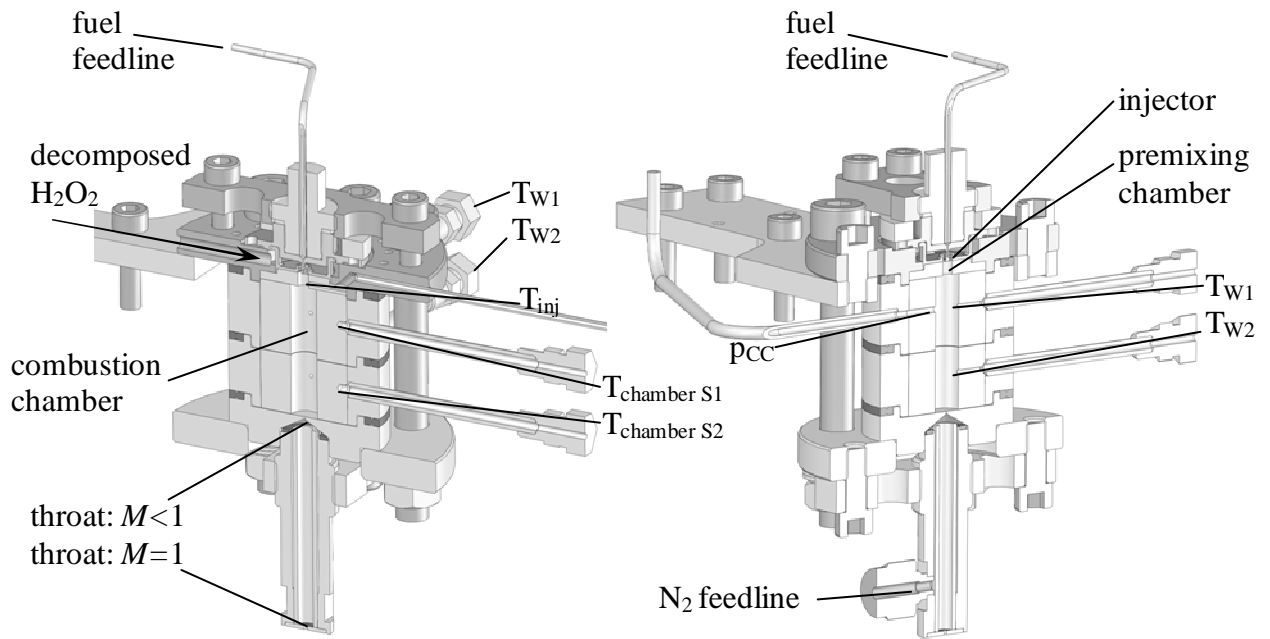
Figure 125 Cut view of ignition chamber (2 elements)

The modular design refers to the combustion chamber volume, which is composed of up to four ignition chamber elements, each equipped with two thermocouples, one measuring the hot combustion gas itself ($T_{W1,2,...}$), and one measuring the elements structural temperature at a radial distance from the hot gas surface of 5 mm ($T_{chamber\ S1,\ S2,...}$). Since thermocouples $T_{W1,2,...}$ are positioned planar to the chamber wall, measured temperatures are a combined temperature of the fluid close to the wall and the structural temperature and are therefore not equal to the gas temperature. These temperatures are thus only valid in relative comparison to each other to determine the position of maximum temperature. A CAD drawing of a single element is shown in Figure 126. The first element is additionally equipped with the direct hot gas combustion chamber pressure instrumentation measuring p_{CC}. Furthermore, thermocouple T_{W1} was inserted into the hot gas stream in monopropellant mode for a length of 10 mm and bended according to the swirl flow motion, to avoid influence of the structural thermal mass on the temperature measurement. This is opposed to all other thermocouples, including the injection temperature thermocouple T_{inj}, which where mounted planar to the combustion chamber surface. With the use of T_{W1}, it was therefore possible to calibrate T_{inj} in stationary monopropellant mode, determining an offset of $\Delta T = -15$ °C for T_{inj} caused by the surrounding thermal mass. Values given for T_{inj} in sections 4.3.3.2 and 4.3.3.3 incorporate this calibration. T_{W1} was later repositioned to a planar surface position for ignition tests to avoid flame holding effects and damage to the thermocouple.
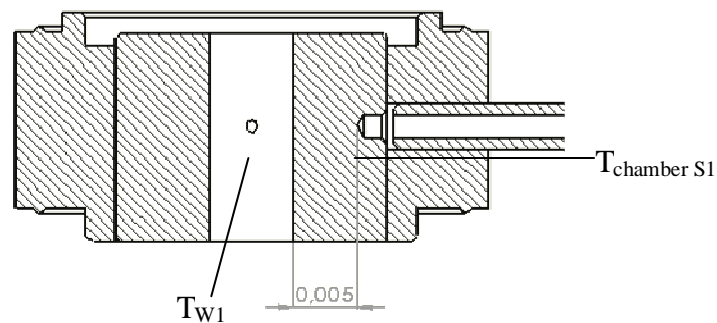
Figure 126 Cut view of single ignition chamber element, distance in meters

All modules, including the injection system and the nozzle, are mounted together between two flanges which are secured by high strength bolts. By changing the number of combustion elements used, the combustion volume, and therefore the characteristic length $L*$ could easily be changed.

The ignition chamber injection system is designed to mix and evaporate an axially injected fuel flow with a gaseous high velocity oxidizer swirl flow in a dedicated premixing chamber as shown in Figure 127. The premixed and evaporated mixture is introduced into the combustion chamber by a backward facing step, inducing large recirculation zones and therefore facilitating further mixing and ignition.
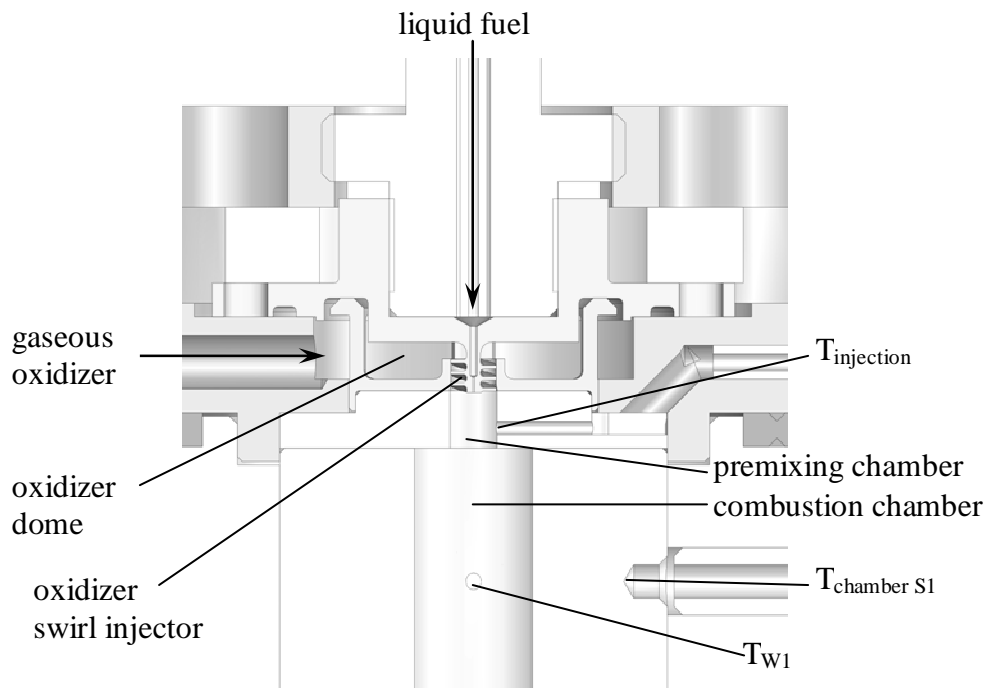
Figure 127 Cut view detail of ignition chamber injector

The swirl flow motion is caused by a vane type injector featuring three blades. The injector utilized was originally designed for a regeneratively cooled combustion chamber [253, 254] and was adapted to the present geometry. A discussion on the injector swirl number can be found in section 3.6.3.1.

The final segment of the combustion chamber features no converging section, but a sub-critical throat, separating the combustion volume from the downstream back-pressure device. This device introduces a cold nitrogen gas flow into the hot combustion gas exhaust stream, therefore increasing the total mass flow through the final throat at the bottom of Figure 125. By manually increasing the nitrogen flow with respect to the propellant mass flow, an increase in pressure upstream of the throat featuring critical conditions is achieved. This increase in pressure translates into an increase in combustion chamber pressure, and therefore allows for a decoupling of propellant flow and combustion chamber pressure without changing the throat diameter. The complex flow design of the nitrogen feed system with considerable pressure losses has been chosen to exclude back flux of the hot exhaust gases into the nitrogen feed system and the gas cylinder. The combustion chamber pressure is then

related to the total propellant mass flow $\dot{m}_p = \dot{m}_{ox} + \dot{m}_{fu}$ and the nitrogen mass flow $\dot{m}_{N2}$ by (derived from Eq. (3.50)):

$$p_{CC} \propto p_{back} = \frac{(\dot{m}_p + \dot{m}_{N2})}{A_t} \sqrt{\frac{2RT_0}{\gamma(\gamma+1)}} \left(\frac{\gamma+1}{2}\right)^{\frac{\gamma}{\gamma-1}} \qquad (4.10)$$

Increasing $\dot{m}_{N2}$ thus causes an increase in chamber pressure p_{CC} for constant propellant flow. To allow for the back pressure device to influence the combustion chamber pressure p_{CC} according to Eq. (4.10), the orifice between combustion chamber and back pressure device has to be subcritical and thus feature a diameter large enough to satisfy:

$$p_{back} > p_{CC} \left(\frac{\gamma+1}{2}\right)^{\frac{\gamma}{\gamma-1}} \qquad (4.11)$$

Therefore, the subcritical throat area is correlated to the total propellant mass flow by Eq. (3.50):

$$A^*_{subcrit} > \frac{\dot{m}_p}{p_{CC}} \sqrt{RT_{CC}} \sqrt{\frac{2}{\gamma(\gamma+1)}} \left(\frac{\gamma+1}{2}\right)^{\frac{\gamma}{\gamma-1}} \qquad (4.12)$$

A picture of the assembled ignition chamber with four elements is shown in Figure 128. Electrical heat system and thermal insulation necessary to achieve test conditions are not shown.
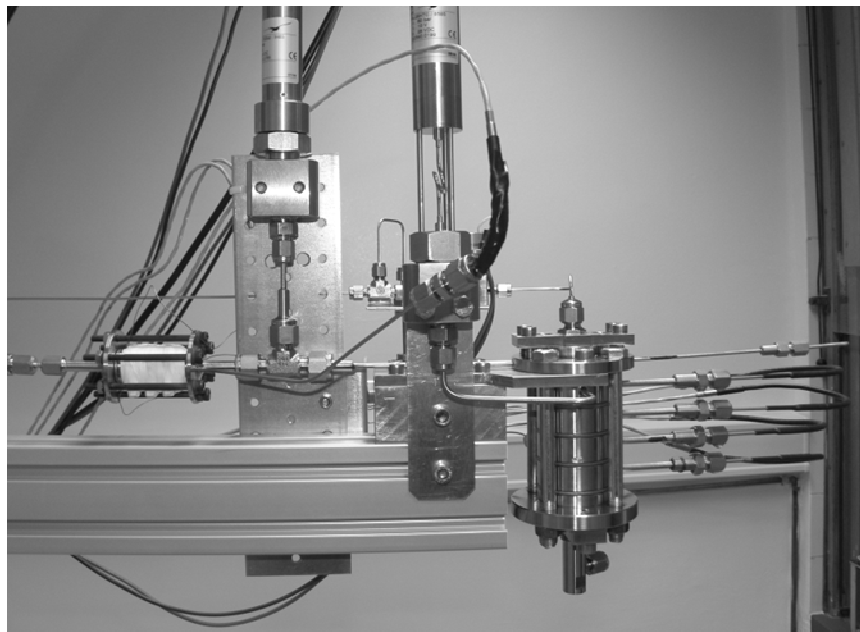
Figure 128 Ignition chamber mounted on test stand

The ignition chambers feed system schematics is shown in Figure 129. The test setup utilizes both oxidizer and fuel feed systems with their main features described in section 4.1. Pressure and mass flow signals recorded are indicated in Figure 129. An additional, manually controlled (MV14) nitrogen line was installed to operate the variable back-pressure device.
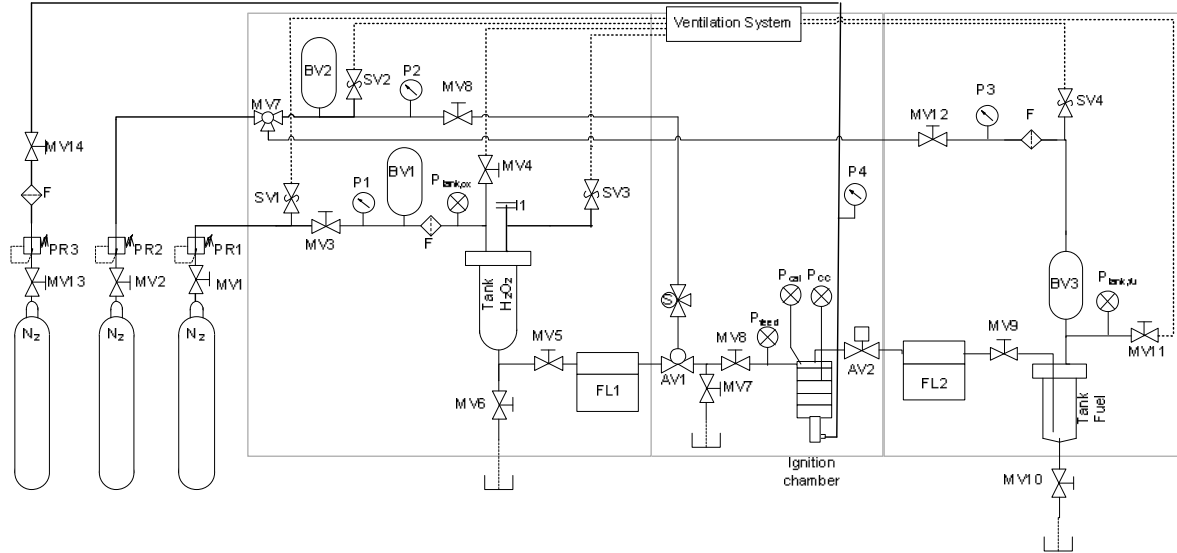
Figure 129 Schematics of ignition chamber test facility

4.3.2. Test procedure and chamber parameters

The test matrix for the ignition chamber consisted of the investigation of ignitability at different pre-ignition chamber pressures and injection temperatures of the mixture gases. While the former parameter is varied with the use of the above described back-pressure device, the latter is varied by both varying monopropellant warm-up times and electrical preheating times. Large temperature losses of the catalyst exhaust gases in the tube element between decomposition chamber and ignition chamber injector in conjunction with the large thermal mass of the ignition chamber yield low injection temperatures in monopropellant mode. Electrical heating of this region including the ignition chamber structure allowed, in conjunction with varying monopropellant mode intervals, fine adjustment of the mixture injection temperature below and above the decomposition temperature.

Figure 130 shows the typical valve and electrical heating settings during a standardized ignition test. Tests started with a variable length monopropellant phase in conjunction with external heating, increasing the structure temperature to achieve the target injection temperature T_{inj}. During this phase, the nitrogen mass flow was manually adjusted to achieve the targeted combustion chamber pre-ignition pressure at the beginning of t_1. The external electrical heating was disabled before fuel injection. The true test parameters T_{inj} and p_{CC} were considerable influenced by the injection of the liquid fuel and were determined after the test from the recorded data at the time of ignition. After the period of fuel injection, in which

either an ignition had occurred or unsuccessful ignition had been confirmed, the system was cooled down in monopropellant mode before the tests was ended by closing the oxidizer feed valve.
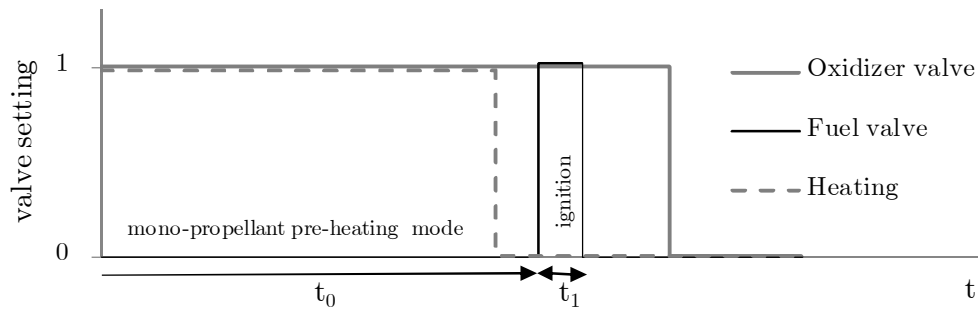
Figure 130 Schematic of ignition test sequence

A summary of the key system parameters of the ignition chamber is given in Table 20.

Table 20 Ignition chamber main parameters

Designation	Value	Dimension	Comment
V_{CC}	1648.71 (2 elements)	mm^3	Combustion chamber volume
	3156.67 (4 elements)	mm^3	
d_t	0.9	mm	Subcritical throat diameter
d_t	0.8	mm	Critical throat diameter
r_{CC}	4	mm	Combustion chamber radius
S	2.63	-	Swirl number, kerosene injection
	2.67	-	Swirl number, ethanol injection
d_{cap}	0.1	mm	Fuel injector capillary diameter
L_{premix}	3.4	mm	Premixing chamber length

4.3.3. Results

Ignition studies for both propellant combinations decomposed H_2O_2/kerosene and decomposed H_2O_2/ethanol have been conducted. This resulted in a total of 87 ignition tests performed with the system described in section 4.3.1. Successful autoignitions with both kerosene and ethanol as fuels could be achieved within this test series.

4.3.3.1.　General results

Recorded system parameters for a sample ignition are shown and discussed hereafter for a successful H_2O_2/kerosene ignition test. Figure 131 shows the recorded temperature signals over the entire test duration. The slow increase in measured temperatures during ignition is caused by the thermocouple position planar to the chamber wall, whose large thermal mass damps any rapid increase in temperature after the first peak, indicating ignition. The slower increase of T_{inj} compared to the thermocouples located at the combustion chamber wall ($T_{W1}...T_{W4}$) indicates the absence of combustion within the premixing chamber, as intended.
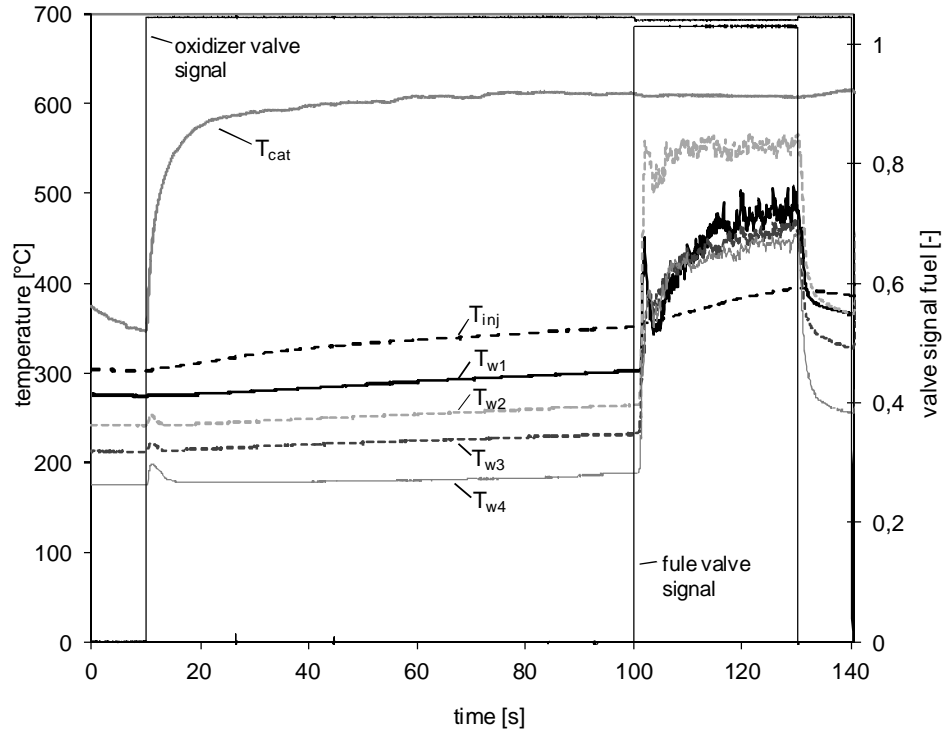
Figure 131 Ignition chamber temperature signals

Pressure and mass flow signals for the same test run are presented in Figure 132 for a detailed time interval covering the period of kerosene injection. The sudden rise in combustion chamber pressure p_{CC} to a stable plateau indicates autoignition and successive stable combustion, as does the reduction to the near stationary behavior of the oxidizer mass flow signal during the bipropellant interval.
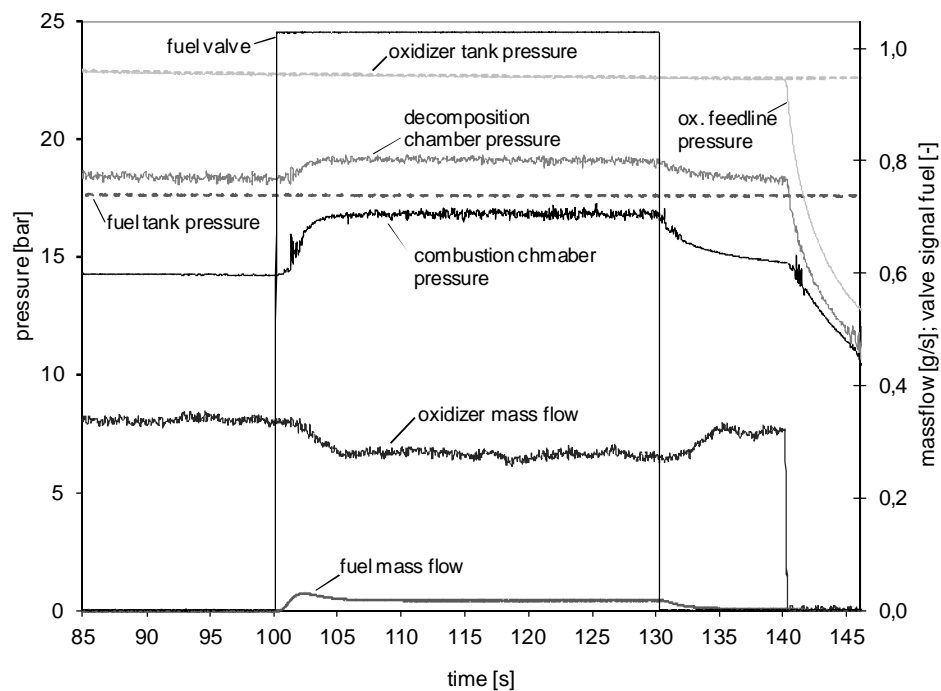
Figure 132 Detail of ignition chamber pressure and mass flow signals

In addition to the successful ignition occurring in Figure 131 and Figure 132, the recorded temperature, pressure and mass flow signals for a test without ignition are shown in Figure 133. The test presented is a failed ignition test for injected ethanol in the 2 element combustion chamber. The temperature decrease due to the evaporation of the injected liquid fuel can easily be seen. The larger heat of vaporization of ethanol compared to kerosene as well as the smaller nominal O/F mixture ratio for this propellant combination magnify the impact of this effect in comparison to H_2O_2/kerosene combustion. Due to the injection of additional propellant, a slight increase in chamber pressure dependent on the increase in total mass flow is observed in Figure 133.
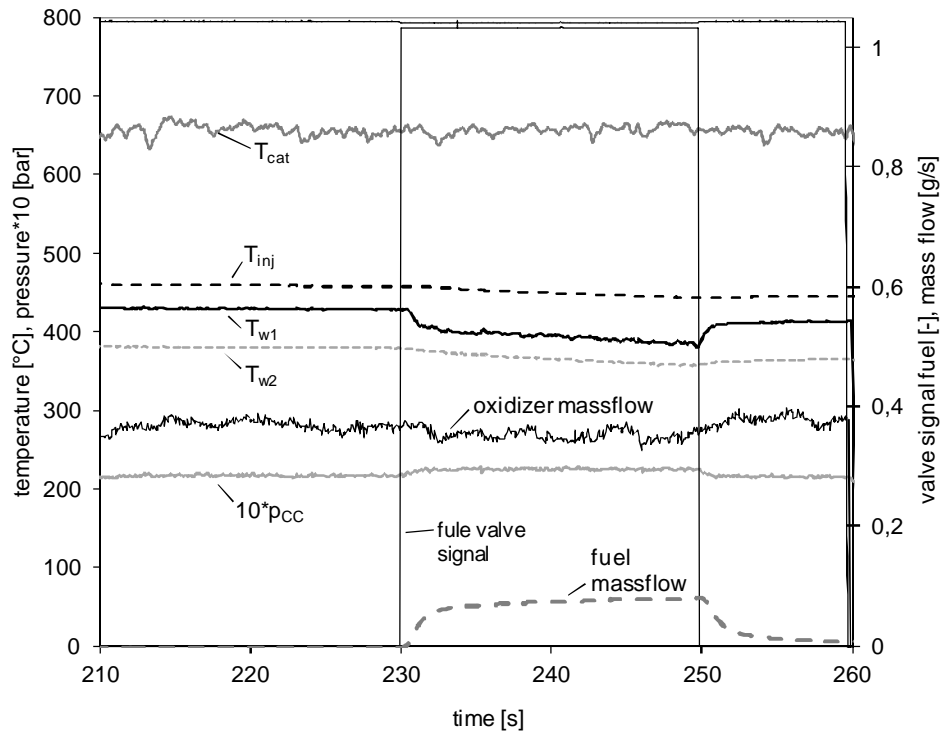
Figure 133 Detail of temperature, chamber pressure and mass flow signals during unsuccessful ignition test

4.3.3.2. Ignition tests: kerosene Jet A-1

65 tests including two different combustion chamber volumes (2 and 4 element configuration) have been conducted using decomposed 87.7 wt.% hydrogen peroxide as oxidizer and kerosene Jet A-1 as fuel. The test series resulted in 26 successful ignitions with stable flame over the entire bipropellant interval. 49 test have been conducted with a combustion chamber volume of $V_{CC} = 3156.67$ mm^3 (4 element configuration) and 16 additional tests have been performed in two element configuration with a combustion chamber inner volume of $V_{CC} = 1648.71$ mm^3.

Adjustment of the combustion chamber pressure p_{CC} independently from the propellant mass flow was achieved utilizing the back pressure device discussed in section 4.3.1. All tests have been performed using the test sequence described in section 4.3.2. Measurement uncertainties

are based on the discussion in section 4.1.4.5 and 4.3.1. Total mass flows $\dot{m}_p = \dot{m}_{ox} + \dot{m}_{fu}$ for the results presented in Figure 134 range from $\dot{m}_p \approx 0.37\,\text{g s}^{-1}$ to $\dot{m}_p \approx 0.44\,\text{g s}^{-1}$. Near stationary oxidizer to fuel mass flow ratio for successful ignitions have been found in the near stationary case to range from $O/F \approx 4.6$ to $O/F \approx 11.5$. No accurate statement regarding the O/F ratio for unsuccessful ignitions could be drawn. Thus extrapolation from successful ignitions with equal remaining feed line settings, was employed.

The identification of successful or not successful ignition behavior has been based on both temperature and pressure data. Instable combustion without stable pressure plateau as in the case of an extinguishing ignition has been classified as unsuccessful ignition in one instance.
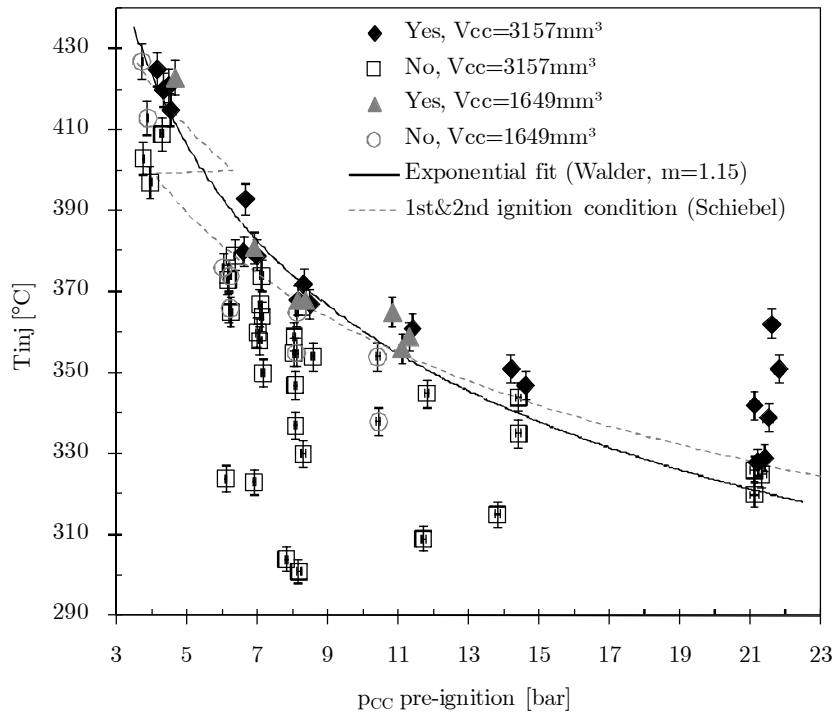
Figure 134 H$_2$O$_2$/kerosene ignition as a function of pre-ignition injection temperature T_{inj} and combustion chamber pressure p_{CC}

Figure 134 shows the ignition thresholds for ignition of kerosene Jet A-1 in decomposed 87.7 wt.% hydrogen peroxide for the swirl injector combustion chamber configuration described in section 4.3.1. The data leads the design process by setting a lower limit for combustion chamber parameters to be achieved by a monopropellant thruster before transition to bipropellant mode is possible.

The data shows no influence of the combustion chamber volume V_{CC} on autoignition behavior for the two volumes investigated. This indicates a potential for further miniaturization, which could be evaluated using the ignition test setup with only one combustion element in a further study and which promises further improvement of the transitional thruster behavior.

The results presented validate the anticipated exponential behavior of the ignition threshold limit, separating successful ignitions from unsuccessful ignitions. The data shows negligible influence of the combustion chamber volume for the range of volumes tested.

The experimental results have been fitted using the simple exponential correlation proposed by Walder [172, 173, 174] for $m' = 1.15$ with fit parameters given in Table 21 for T_0 in Celsius and p in bar.

$$\ln\left(L^* p^{m'}\right) = \frac{K}{T_0} + L'$$

(4.13)

Table 21 Ignition fit parameters for exponential fit

Designation	Value	Dimension
L^*	10000	mm
K	3.61676	K
L'	$3.61676 * 10^3$	-

In addition to this exponential fit, an advanced fit proposed by Schiebl [149, 175] is indicated in Figure 134, which bases on the assumption of parameter L' being dependent on various combustion gas parameters such as initial temperature, specific heat, mixture ratio and isentropic coefficient of expansion and heat loss to the structure. The discontinuity in the fitted data is caused by the usage of a second ignition condition for $T_{inj} > 400\,°C$ [149]. This theory is discussed in detail in Ref. 149. Although the simple correlation proposed by Walder, which assumes adiabatic combustion and therefore no influence of increasing loss terms due to miniaturization, is qualitatively able to fit the experimental results, the improved expressions presented by Schiebl show more accurate results.

4.3.3.3.   Ignition tests: ethanol

22 tests have been conducted using ethanol as fuel, 7 of which led to successful ignition. All tests have been conducted using the two element ignition chamber with a combustion volume of $V_{CC} \approx 1649$ mm³. A considerable increase in temperature threshold values has been observed in comparison to studies utilizing kerosene, necessitating extended preheating intervals to achieve autoignition of ethanol in decomposed 87.7wt% hydrogen peroxide. The necessary increase in pre-ignition combustion chamber pressure to surpass the autoignition pressure threshold necessitated an increase in back-pressure nitrogen mass flow. Figure 135 shows the ignition results as a function of pre-ignition combustion chamber pressure and injection temperature. The error bars are indicated based on the discussion in section 4.1.4.5. The results cover total mass flows $\dot{m}_p = \dot{m}_{ox} + \dot{m}_{fu}$ from $\dot{m}_p \approx 0.313\,\mathrm{g\,s^{-1}}$ to $\dot{m}_p \approx 0.596\,\mathrm{g\,s^{-1}}$.

Oxidizer to fuel mass flow ratios for near stationary combustion have been observed in the range of $O/F \approx 3.0$ to $O/F \approx 5.51$, based on extrapolation from the difference in recorded tank and combustion chamber pressures.
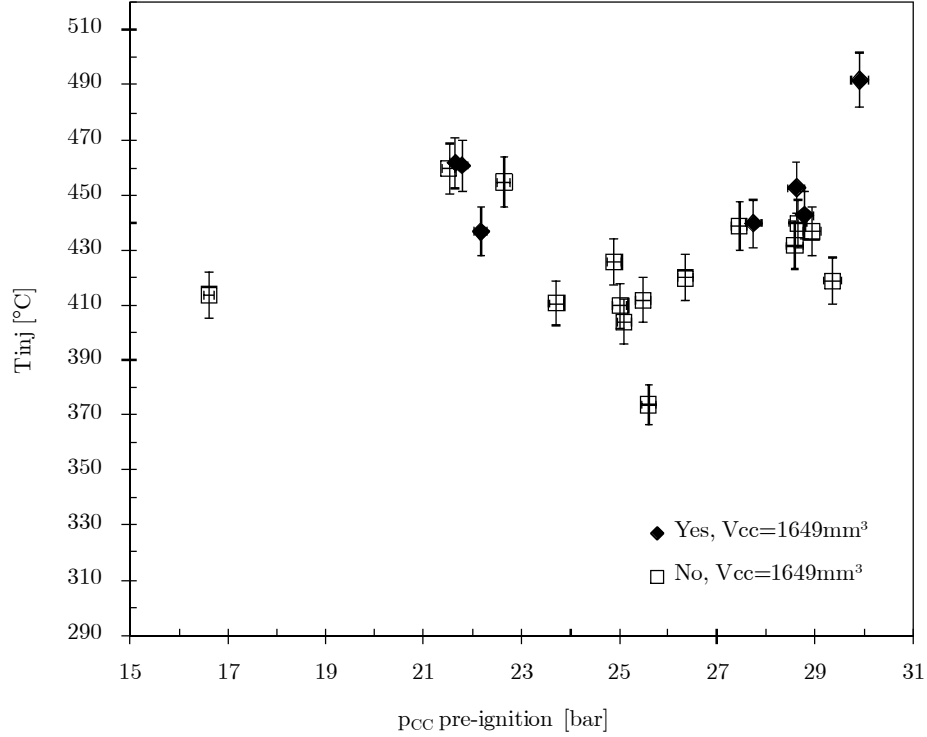
Figure 135 H$_2$O$_2$/ethanol ignition as a function of pre-ignition injection temperature T_{inj} and combustion chamber pressure p_{CC}

Due to the small number of data points for successful ignitions and the small temperature and pressure range covered, derivation of a threshold relation from the data indicating dedicated ignition limits is not feasible. It is however worth noticing that the data indicates reliable ignitions for $p_{CC} > 28$ bar for $T_{inj} > 450$ °C. Although the threshold chamber pressures found are too large for further thruster designs, the results presented in this section showed the ability of using ethanol in an autoigniting thruster with decomposed H$_2$O$_2$. It was concluded that lower chamber pressures needed to be strived for autoignition of ethanol to comply with the requirements of an operating thruster design, even at the cost of substantially increased temperature thresholds for autoignition. This approach is investigated in section 4.4.3.4.

4.3.4. Ignition studies summary and conclusion

The investigation of ignition behavior of decomposed hydrogen peroxide with injected liquid kerosene Jet A-1 conducted in this section allows for the identification of target system parameters such as combustion chamber volume and corresponding temperature and pressure thresholds. These design points dictate any thruster design presented in sections 4.4 and 4.5.

The large number of both successful and unsuccessful autoignition events over a large range of different temperatures and pre-ignition combustion chamber pressures allowed the deduction of a pressure-temperature relation for minimum autoignition conditions for the given combustion configuration. Comparison to parametric models from literature and the theoretical discussion presented in section 0 showed good agreement. Fitting the experimental

data to the simple correlation from Walder [172, 173, 174] allowed for an analytical expression of the minimum autoignition threshold for the given thruster design.

Ignition studies conducted with liquid ethanol showed the ability for autoignition of this propellant combination in miniaturized combustion geometry scales. However, the small number of successful ignition events prohibited any deduction of pressure-temperature relation as it was found possible in the case of kerosene.

4.4. Elegant Bred Board (EBB) thruster
4.4.1. Description of experimental setup

The elegant bread board (EBB) thruster is an actively cooled thruster incorporating the combustion chamber and the decomposition chamber in a single design. It uses both oxidizer and fuel feed systems described in section 4.1. In addition, an external N_2 cooling feed system controlled by manual pressure and valve settings was installed, feeding the coolant flow along the outside of the combustion chamber walls. The coolant flow is distributed to the cooling structure by six 1/8 inch feedlines, symmetrically attached to the combustion chamber outer skirt as shown in the CAD drawing in Figure 136. The thruster assembly and its main features are shown in Figure 136.
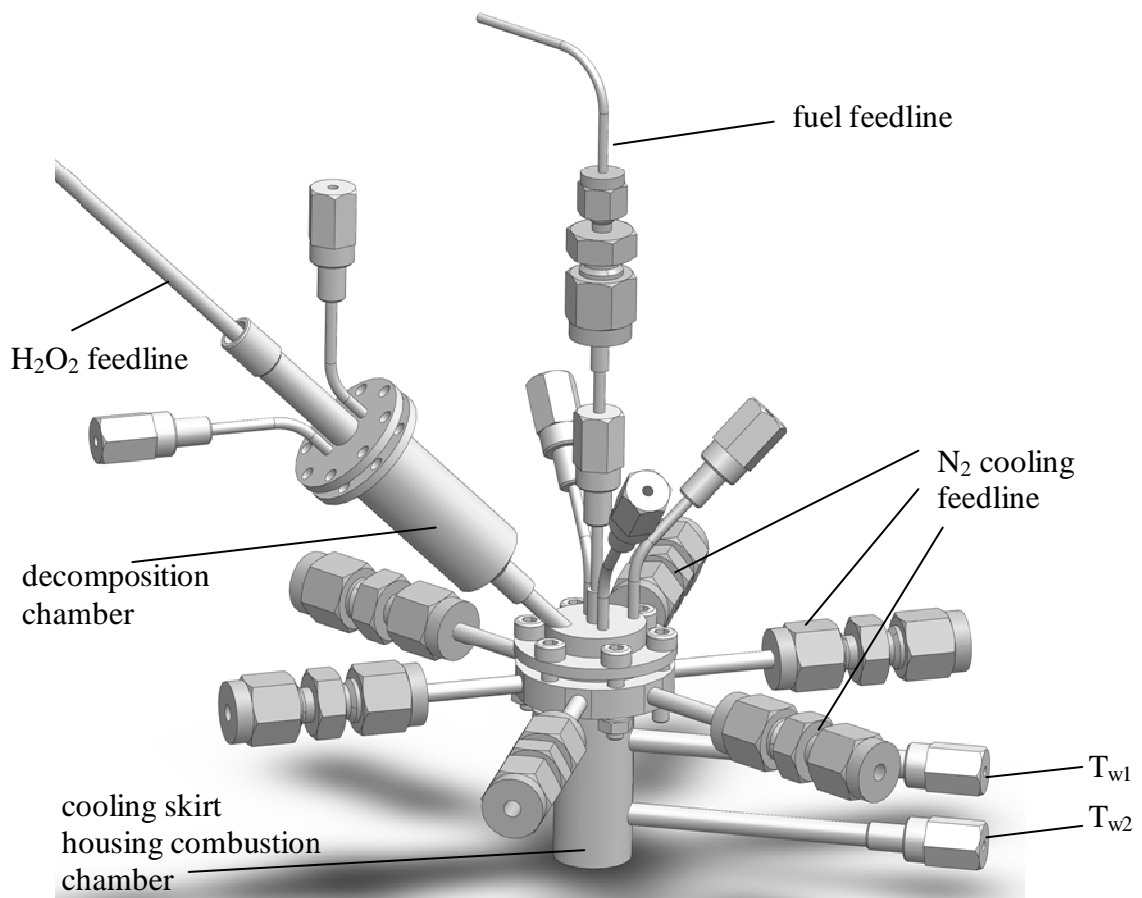
Figure 136 CAD drawing of EBB thruster

Figure 137 shows a cut view of the thruster with main features and positions of diagnostics indicated as they appear in the experimental results. On the left side, the decomposition chamber, able to house a catalysts of $L_M = 20$ mm and $L_M = 10$ mm length, is shown. The converging part of the chamber is insulated by ceramics, separated from the hot gaseous flow by stainless steel foil. The decomposition products are then introduced into the combustion chamber injector dome, which is shown in the detail depiction in Figure 137. The injector is a tangential injection swirl injector causing a swirling flow in the premixing chamber. The liquid fuel is injected axially by a capillary into the swirling oxidizer stream in the premixing chamber. High tangential velocities and large oxidizer to fuel ratios guarantee the mixing and

evaporation of the fuel. The mixture is then expelled via a backward facing step into the combustion chamber, where vortex breakdown is facilitated and combustion occurs.

The combustion chamber features a wall thickness of 0.7 mm and is surrounded by the cooling skirt, with a narrow gap of 0.2 mm in between allowing for the coolant flow. The N_2 coolant is introduced just downstream of the injector and flows axially along the combustion chamber outer wall to the nozzle. As the coolant skirt follows the contour of the combustion chamber at the nozzle while keeping the gap for the coolant flow constant, flow velocities are largely increased in the vicinity of the nozzle, where highest cooling capacity is needed.

The injector top plate, the injector, the combustion chamber and the cooling skirt are secured by a bolted connection, as is the top flange of the decomposition chamber, enabling dismantling of the entire thruster system.
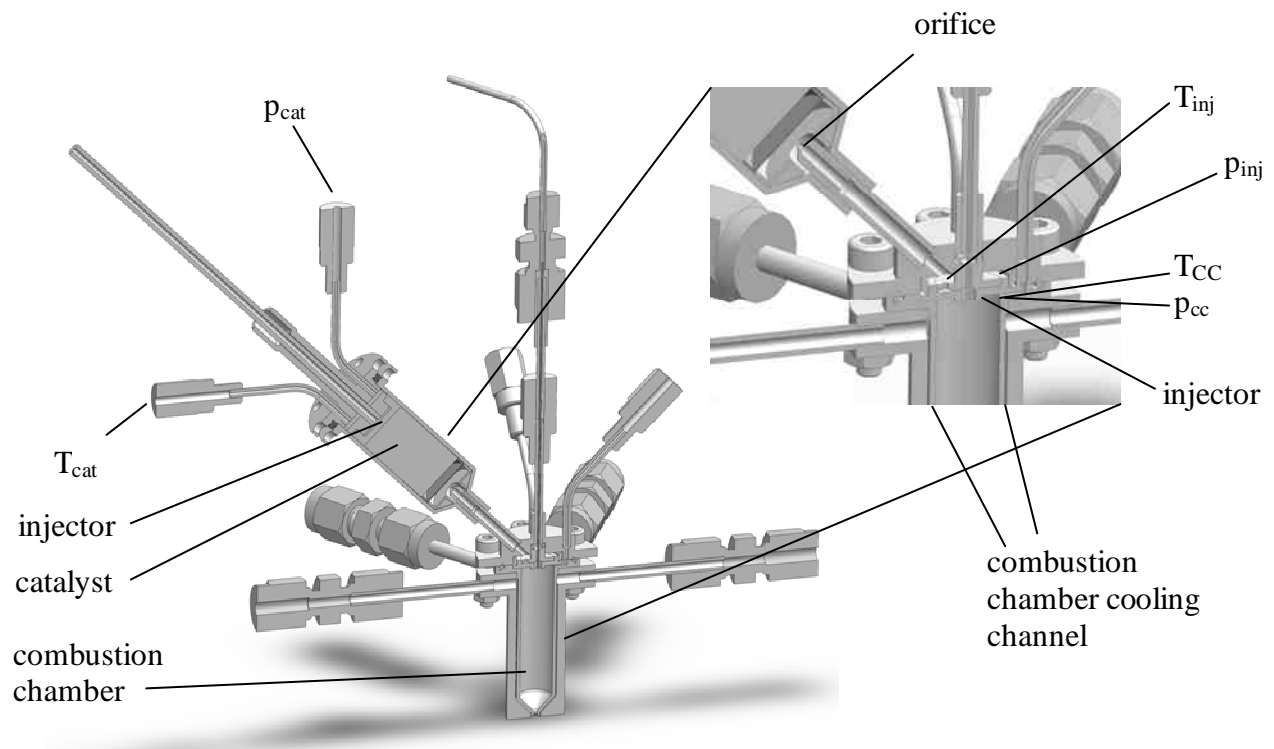
Figure 137 CAD cut view of thruster with combustion chamber injector detail and instrumentation

Figure 137 indicates the positions of diagnostics available in the EBB thruster. The main features are described in this paragraph. The decomposition chamber (designated Chamber EBB in section 4.2.6.6) features temperature diagnostics downstream of the catalyst. Therefore, a thermocouple is introduced into the chamber upstream of the catalyst, bypassing the injector, and then fed through an outermost channel of the catalyst, allowing enough bending of the thermocouple downstream of the catalyst to avoid any influences from its pathway. Decomposition chamber pressure is monitored upstream of the injector.

The main combustion chamber injector dome is equipped with a thermocouple directly inserted into the oxidizer hot gas flow. Pressure is monitored at the same position.

The main combustion chamber features temperature diagnostics directly downstream of the premixing chamber, positioned in a dedicated recess to avoid damage to the type K thermocouple by the combustion gases. The thermocouple is therefore measuring the structural temperature at this position (an upper limit) rather than the actual hot gas temperature in the vicinity of the chamber wall. Combustion chamber pressure is measured at a mirrored position at equal axial position.

Additional temperature structural measurements are introduced through the combustion chamber cooling flow, surrounded by stainless steel tubes, pressing against the combustion chamber to monitor the temperature of the outer combustion chamber surface at downstream positions. Since these measurements are strongly influenced by the cooling gas flow, no absolute temperatures can be determined, but the measured data can give indications on thermal equilibrium achieved.

The injector, which schematically depicted in Figure 59, is designed to induce a swirling oxidizer flow in the premixing chamber region upstream of the combustion chamber. Therefore, the gaseous oxidizer is introduced from the upstream injector dome into three channels which guarantee tangential injection into the premixing chamber. A capillary with inner diameter of $d_{cap} = 0.175$ mm is introduced axially, as shown in Figure 137. As presented in section 3.6.3.1, the swirl number for this particular injector design becomes $S \approx 3.28$ for kerosene and $S \approx 3.07$ for ethanol injection at standard mass flows.

The nozzle with throat diameter of $d_t = 0.7$ mm (which was later increased as described in section 4.4.3.6 to $d_t = 0.8$ mm), is shown in Figure 138. The small nozzle area expansion ratio ($\varepsilon = 5.8$) is fitted to exhaust gas expansion at ambient pressure conditions. The cooling skirt is enclosing the nozzle, with the cooling gap appearing in black in the figure.
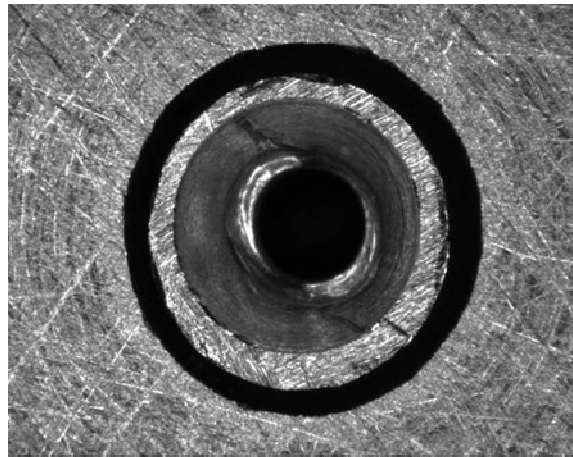
Figure 138 Front view of nozzle and cooling skirt

The leading EBB thruster parameters are summarized in Table 22.

Table 22 EBB thruster main parameters

Designation	Value	Dimension	Comment
V_{CC}	1681.4	mm³	Combustion chamber volume
d_t	0.7 (changed to 0.8)	mm	Throat diameter
r_{CC}	4	mm	Combustion chamber radius
r_{inj}	1.2	mm	Premixing chamber radius
L^*	4369 (d_t=0.7mm)	mm	Characteristic length
	3345 (d_t=0.8mm)	mm	
S	3.28	-	Swirl number, kerosene injection
	3.07	-	Swirl number, ethanol injection
d_{cap}	0.175	mm	Fuel injector capillary diameter
L_{premix}	1.8	mm	Premixing chamber length
ε	5.8	-	Nozzle expansion ratio

The tests described hereafter have been conducted using three catalysts which are listed with their main parameters in Table 23. A 60 µm porosity injector was utilized, as discussed in section 4.2.2.

Table 23 Catalysts employed in EBB thruster tests

Designation	Configuration	Length [mm]	Channel geometry	Channel density [cpsi]
GC-207	Cordierite-Pt-B	20	triangular	540
GC-217	Cordierite-Pt-B	20	triangular	540
GC-222a	Cordierite-Pt-B	10	triangular	540

Figure 139 shows the EBB thruster mounted on the test facility before testing. The EBB thruster feed system schematics is shown in Figure 140. It utilizes both oxidizer and fuel feed systems with features described in section 4.1, as well as a manually controlled (MV14) gaseous nitrogen cooling line.
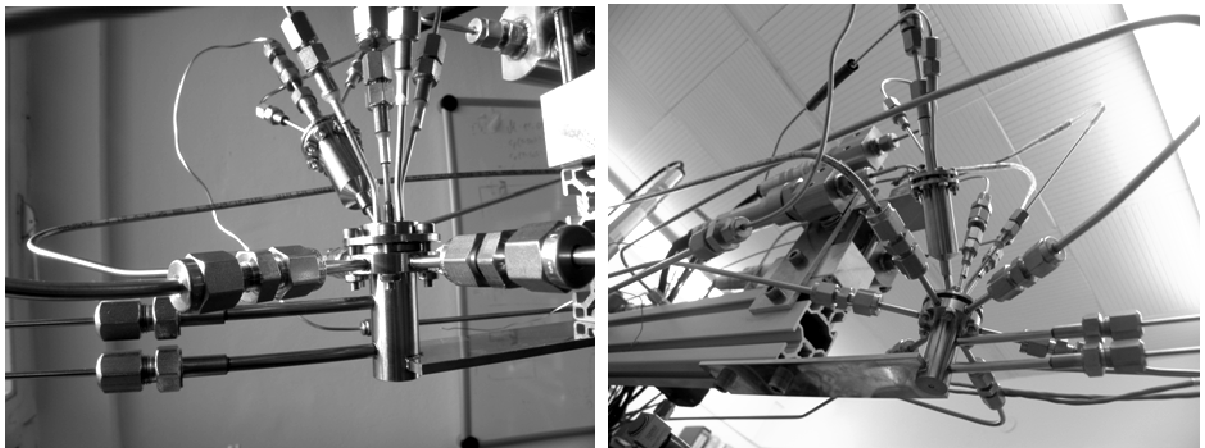
Figure 139 EBB thruster assembly
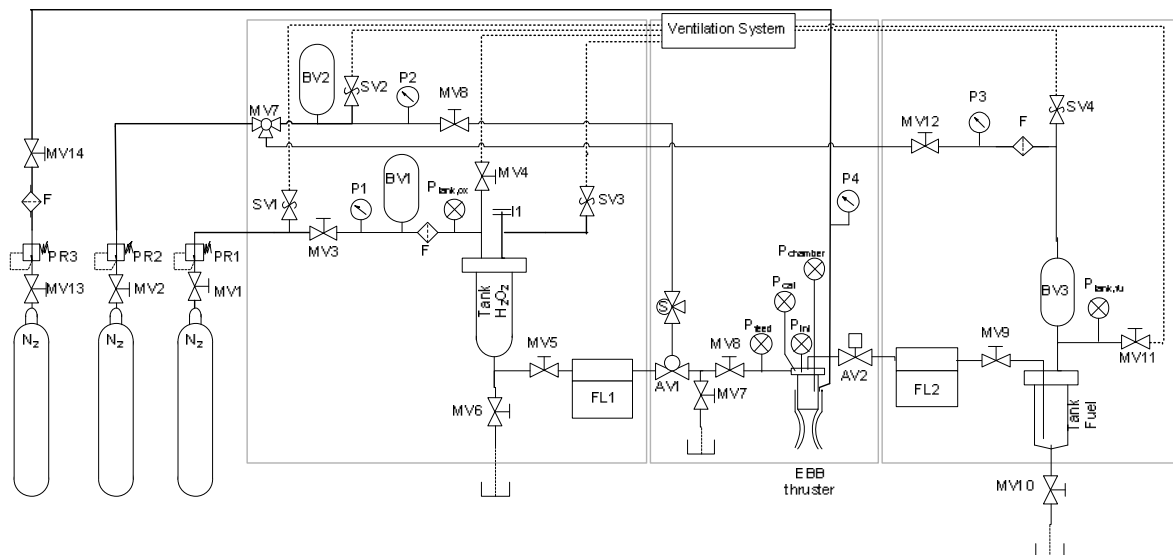
Figure 140 Schematics of EBB thruster test facility

4.4.2. Scope of the EBB test series an thruster parameters

The EBB thruster tests have been conducted to investigate various parameters before the final design of the DM thruster. These include:

- **Verifying the ignition capabilities for a newly employed injector design**

To reduce manufacturing costs, the elaborate swirl injector design used in the ignition chamber (section 4.3) and in previous projects [93] was substituted by a tangential injection design yielding a decrease in complexity and manufacturing cost. In addition, the premixing chamber length was significantly reduced. Ignition capabilities for both kerosene and ethanol are thus investigated.

- **Confirmation of the ability to achieve ignition conditions without external heating**

The system's ability to achieve ignition conditions by preheating using the high temperature exhaust from the catalytic decomposition of hydrogen peroxide only is confirmed.

- **Blow-down configuration tests**

The thruster's capability to be employed in a blow down configuration was studied by studying its ignition capabilities as a function of reduced tank pressure. Since the pre-ignition combustion pressure is manipulated in the EBB ignition studies by manipulating the tank pressure, decreased chamber pressures constitute the ignition performance at decreased tank pressure as found when employed in a blow down configuration.

- **Verifying stable combustion**

After verification of the ability of autoignition, the focus is laid on verification of the ability to sustain a stable combustion within the combustion chamber volume.

- **Investigation of combustion performance as a function of mixture ratio**

Combustion efficiency of the injected propellants is investigated by relating the directly measured chamber pressure during stable combustion to the injected propellant mass flows.

These parameters are compared to ideally achievable combustion efficiencies for the given thruster configuration.

- **Investigation of the thruster behavior in pulsed operation**

The ability of pulsed bipropellant operation is investigated and the thruster dynamical behavior is studied by investigating its capability to perform short duration pulsed firing sequences.

4.4.3. Test results
4.4.3.1. General results and thruster considerations

The tests involving a hot firing period and active cooling by the manually opened N_2 gas stream where conducted similar to the sample test shown in Figure 141 and Figure 142. The figures show the time traces of temperature, pressure and mass flow signals over the entire test period for a test featuring a 10 s hot firing interval. As in the case of the ignition tests, the test sequence is divided into a monopropellant and a bipropellant phase. The former is necessary to preheat the thruster system up to the temperature threshold for bipropellant ignition. In the example shown, the monopropellant mode lasts until 120 s into the test run. Before fuel is injected, the N_2 cooling system is activated manually at $t = 115$ s.
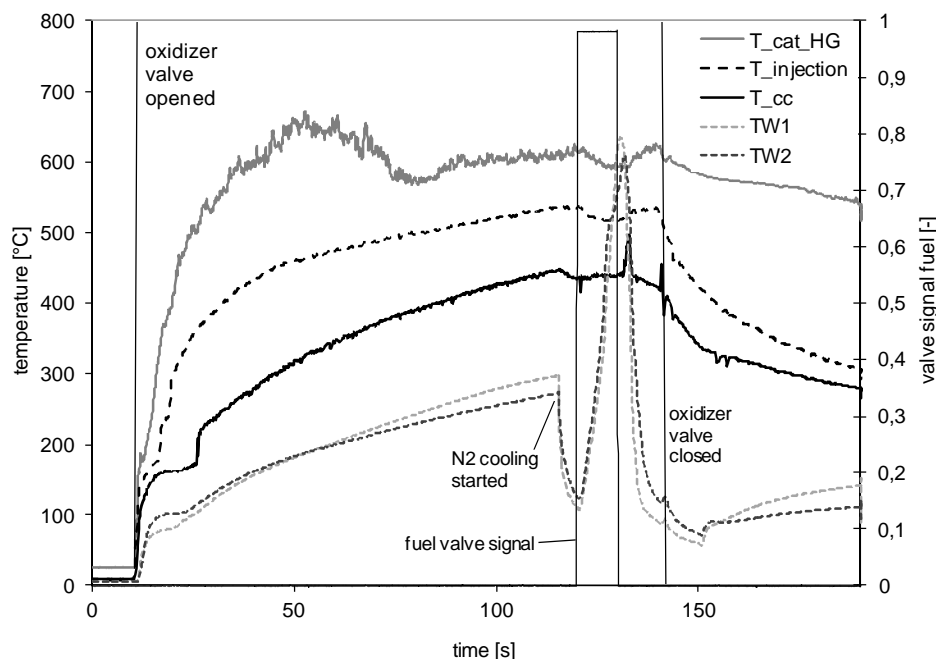
Figure 141 EBB temperature signals during 10s hot firing test (H_2O_2/kerosene)
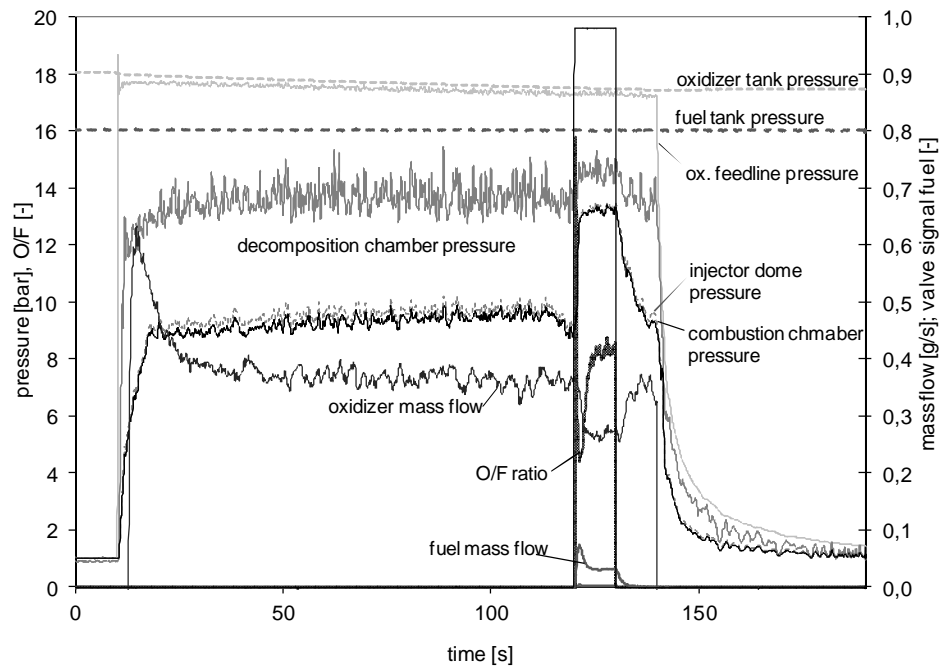
Figure 142 EBB pressure and mass flow signals during 10s hot firing test (H_2O_2/kerosene)

Figure 143 and Figure 144 show details of the bipropellant phase of the test. At temperature and pressure conditions well above the ignition threshold, kerosene Jet A-1 was injected for a duration of 10 s, starting at $t = 120$ s. The combustion chamber pressure signal in Figure 144 shows an increase from approximately $p_{CC} \approx 9$ bar to a stable combustion pressure of $p_{CC} \approx$ 13.2 bar. Stable combustion was achieved 1.2 s after fuel valve opening. After initial rise in the fuel mass flow signal caused by the abrupt start of the fluid flow in the mass flow meter, a reliable mass flow determination is possible in the near stationary case after approximately 5 s into the bipropellant combustion interval. The oxidizer to fuel mass flow ratio at stable ignition is determined to $O/F = 8.25 \pm 0.2$.
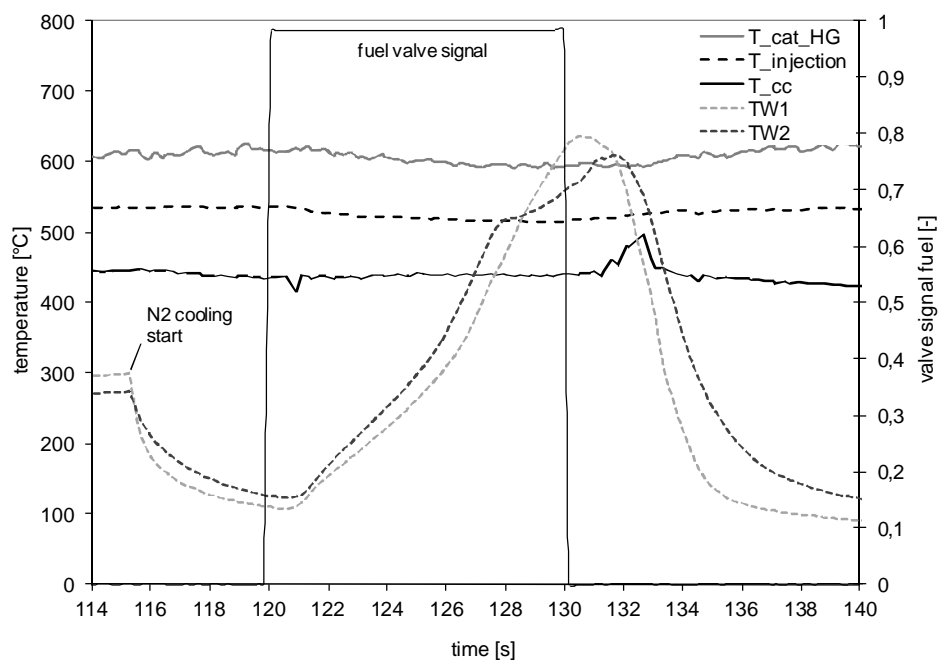
Figure 143 Detail EBB temperature signals during 10 s hot firing test (H_2O_2/kerosene)
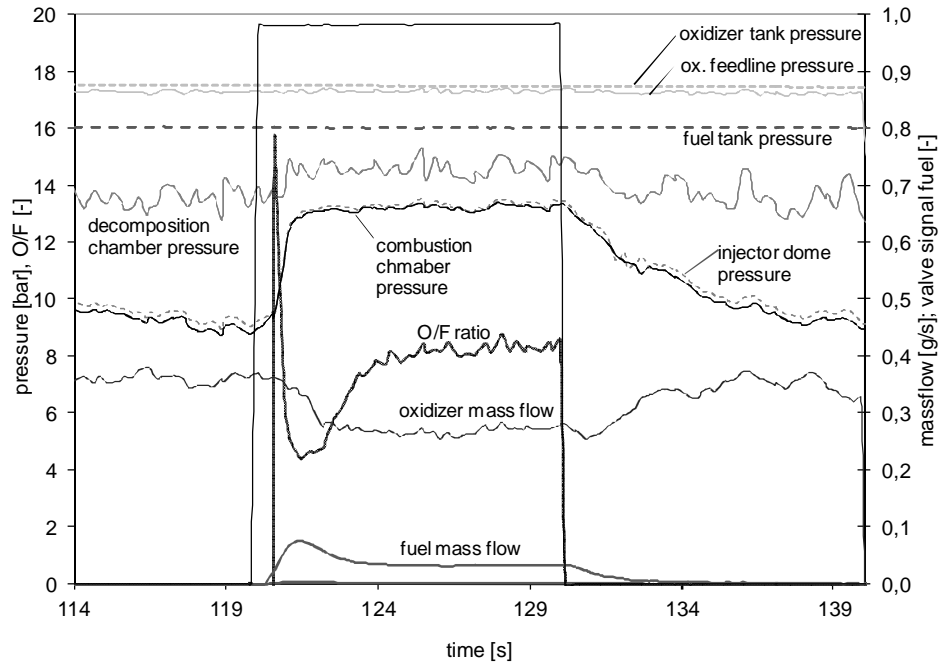
Figure 144 Detail EBB pressure and mass flow signals during 10 s hot firing test (H_2O_2/kerosene)

4.4.3.2. Ignition tests: kerosene Jet A-1

The scope of the EBB ignition studies was to verify the ignition thresholds found using the ignition chamber for the modified chamber setup. This is of special interest, since not only a slight reduced combustion chamber volume has been utilized compared to the ignition chamber, but also since a new injector design is employed in combination with a reduced premixing chamber length. Thus, a test series similar to the ignition tests was conducted for the EBB tests. However, due to the absence of a back pressure device in the EBB tests, no independent variation of mass flow and chamber pressure was possible. The EBB tests thus can only be compared to the ignition results for the standard mass flow of 0.3 g s^{-1} and the corresponding chamber pressure. The results for the remaining mass flow and combustion chamber pressure combinations constitute the case of off-design ignition in a non laboratory thruster.

Figure 145 shows the bipropellant ignition capability of the EBB thruster as a function of combustion chamber temperature T_{CC} and chamber pressure p_{CC}. The chamber pressure was determined directly at the onset of combustion chamber increase indicating ignition and thus incorporates the contributions from the injected fuel to the chamber pressure. The data points cover a variety of *O/F* mixture ratios from *O/F* ≈ 5.3 to *O/F* ≈ 8.1, determined in the near stationary case of achieved combustion. Total propellant mass flow limits of successful ignitions tests at stable combustion lay within $\dot{m}_p$ ≈ 0.18 g s^{-1} for p_{CC} ≈ 4.99 bar (before ignition) and $\dot{m}_p$ ≈ 0.29 g s^{-1} for p_{CC} ≈ 7.7 bar (before ignition).
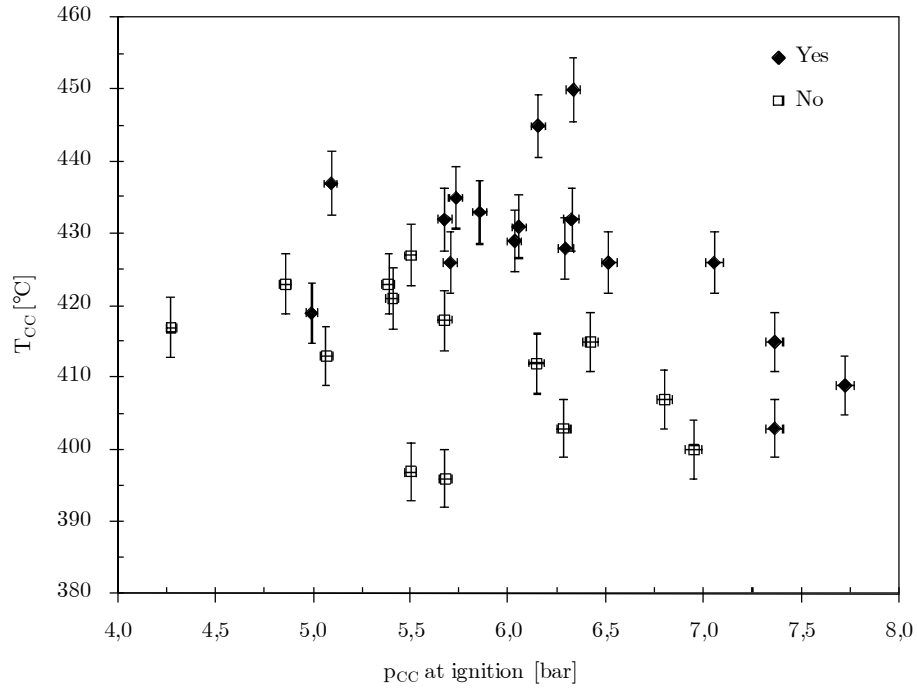
Figure 145 EBB bipropellant ignition capability as a function of pressure and temperature (H_2O_2/kerosene)

Since no stationary input parameters are available for unsuccessful ignition tests, corresponding parameters have been extrapolated from successful ignitions featuring the exact tank pressure settings. If no matching successful test was available, unsuccessful tests have been discarded and are not included in the evaluation. The errors indicated for the individual parameters are based on the discussion in section 4.1.4.5.

Although Figure 145 incorporates results for smaller, and varying, mass flows compared to the constant mass flow ignition chamber results presented in section 4.3.3.2, a general comparison is valid for the EBB data points featuring large mass flows, and thus, large pressures. In this region, a threshold of $p_{CC} > 7.5$ bar for $T_{CC} > 400$ °C is found for the EBB thruster. This compares to the threshold found in the ignition chamber of $T_{inj} > 380$ °C, for equal chamber pressure. The slightly higher temperature threshold is a factor of various parameters changed, with most prominent being the smaller mass flows and the design change of the injector.

In a further test series, the ignition capability of the EBB thruster as a function of off-design mixture ratio was studied. This becomes especially important in the case of different tank pressure decay in the oxidizer and fuel feed system during long duration employment of a thruster in blow down mode and according change in propellant flow rates. Changes in mixture ratio were achieved by varying the fuel mass flow only. Due to the small contribution of the fuel flow to the overall propellant flow, nearly constant combustion chamber pressures could be achieved for all mixture ratios, laying within the boundaries of $p_{CC} \approx 7.06$ bar (at ignition) for $O/F \approx 13.08$ and $p_{CC} \approx 7.36$ bar (at ignition) for $O/F \approx 3.45$.

The moderate increase of temperature ignition threshold for reduced pre-ignition combustion chamber pressure shows the thrusters ability to be employed in a blow down system

configuration. The results shown indicate successful employment in systems guaranteeing pre-ignition pressures as low as $p_{CC} = 5$ bar without drastically affected autoignition performance. The main impact for further reduced chamber pressures results in longer transition times until the autoignition temperature is achieved.

Figure 146 shows good ignition capabilities for a wide range of mixture ratios up to $O/F \approx 13.08$. Successful ignitions at lowest temperatures can be found in the vicinity of the optimum mixture ratio of $O/F \approx 7$. The results from Figure 146 compare well to the narrow O/F results in Figure 145 for combustion chamber pressure at ignition of $p_{CC} > 7$ bar. From this data, an ignition threshold for certain ignition of $T_{CC} > 420$ °C for a pre-ignition combustion chamber pressure of $p_{CC} \approx 7.0$ bar can be concluded. As can be seen from Figure 141, transition times from oxidizer valve opening to reach ignition threshold values in the combustion chamber before approximately $t = 82$ s for the EBB thruster.

The errors for each data point were calculated according to the error propagation calculation for O/F described in section 4.1.4.5.
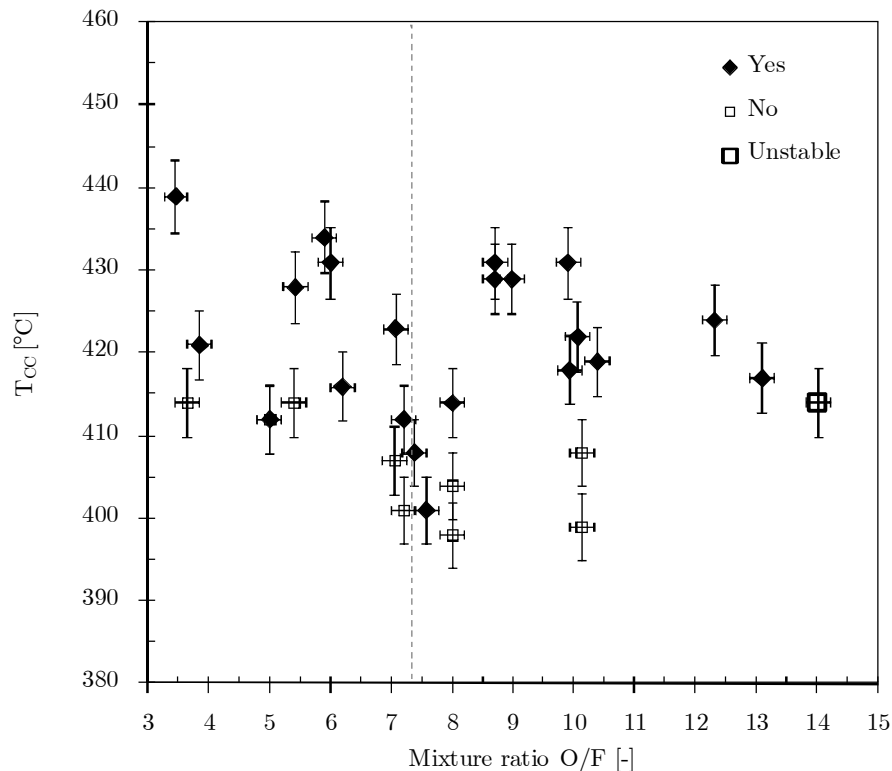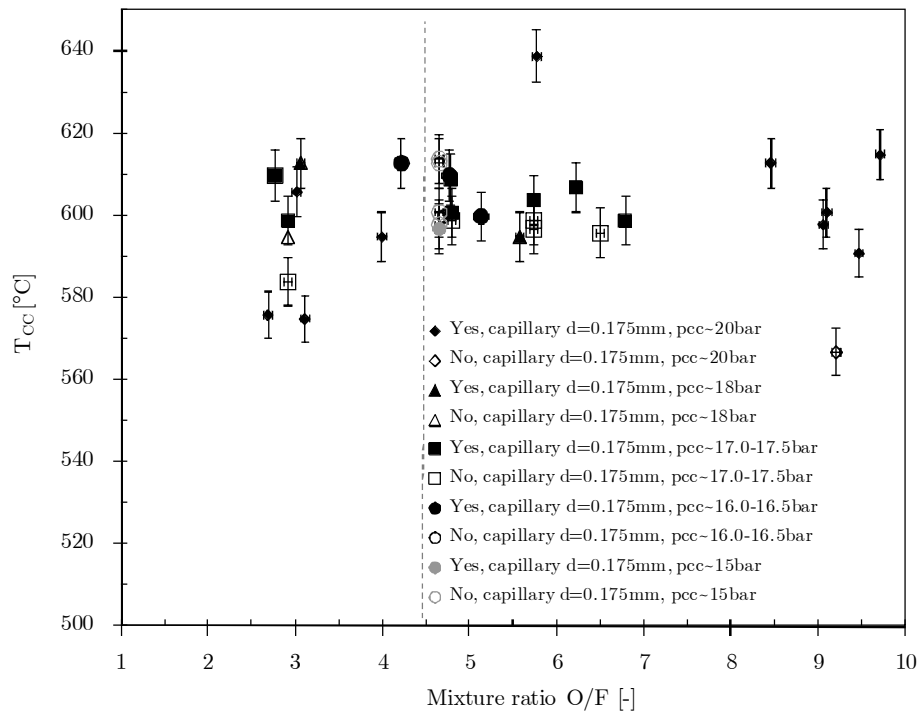

Figure 146 EBB bipropellant ignition capability as a function of mixture ratio (H_2O_2/kerosene), nominal mixture ratio indicated by dotted line

This result shows the thrusters insensitivity of autoignition capability to changes in O/F ratio caused by different pressure decays in a blow down system configuration for mass flow changes by a factor of two. Combined with the relative insensitivity to reduced pre-ignition chamber pressure presented above, these results show the thrusters ability to be employed in a blow down propulsion system.

4.4.3.3.　Combustion tests: kerosene Jet A-1

The scope of this test series was to investigate the steady state combustion performance of the EBB thruster. Therefore, the EBB thruster was operated in bipropellant mode for intervals of 10 s. The behavior of pressure and mass flow signals shown in Figure 144 justifies the determination of near stationary values by averaging over the last four seconds of the bipropellant interval.

The characteristic velocity c^* was used to investigate the combustion performance, defined by Eq. (4.7), using the combustion chamber pressure p_{CC}, the mass flows $\dot{m}_{ox}$ and $\dot{m}_{fu}$ and the throat area of the EBB nozzle with a throat diameter of $d_t = 0.7$ mm. The uncertainties for each data point were calculated according to the error propagation calculation for c^* described in section 4.1.4.5.

The experimentally determined characteristic velocity values as a function of mixture ratio are compared to two types of ideal characteristic velocities:

- "c^* ideal" is the characteristic velocity determined by NASA CEA code [92], based on the experimentally determined input parameters p_{CC}, $\dot{m}_{ox}$ and $\dot{m}_{fu}$ at stationary combustion and T_{inj} before combustion. Again, values are determined by averaging as described above. This ideal parameter thus describes the combustion efficiency achievable for the given combustion chamber injection parameters.

- "c^* total ideal" is the characteristic velocity determined by NASA CEA code [92], based on the experimentally determined input parameters p_{CC}, $\dot{m}_{ox}$ and $\dot{m}_{fu}$ at stationary combustion and the ideal decomposition temperature of hydrogen peroxide at the employed concentration, again determined by NASA CEA code [92]. This parameter describes the combustion efficiency achievable for the entire EBB thruster system, including the decomposition performance. Comparison to this ideal c^* value thus incorporates thermal losses of the catalyst exhaust gases before injection into the combustion chamber.

Figure 147 shows that the behavior of the experimentally determined characteristic velocity values corresponds well to the behavior of ideal characteristic velocity as a function of mixture ratio over a wide range of mixture ratios. Highest performance compared to the ideal values is achieved in the near fuel rich region. The difference in the ideally characteristic velocities achievable for the EBB system is caused by temperature decrease due to thermal losses of the catalyst exhaust before injection into the combustion chamber. Unsymmetrical uncertainties in efficiency are caused by the uncertainty introduced due to the presence of boundary layers affecting the effective throat area, as discussed in section 4.1.4.4.
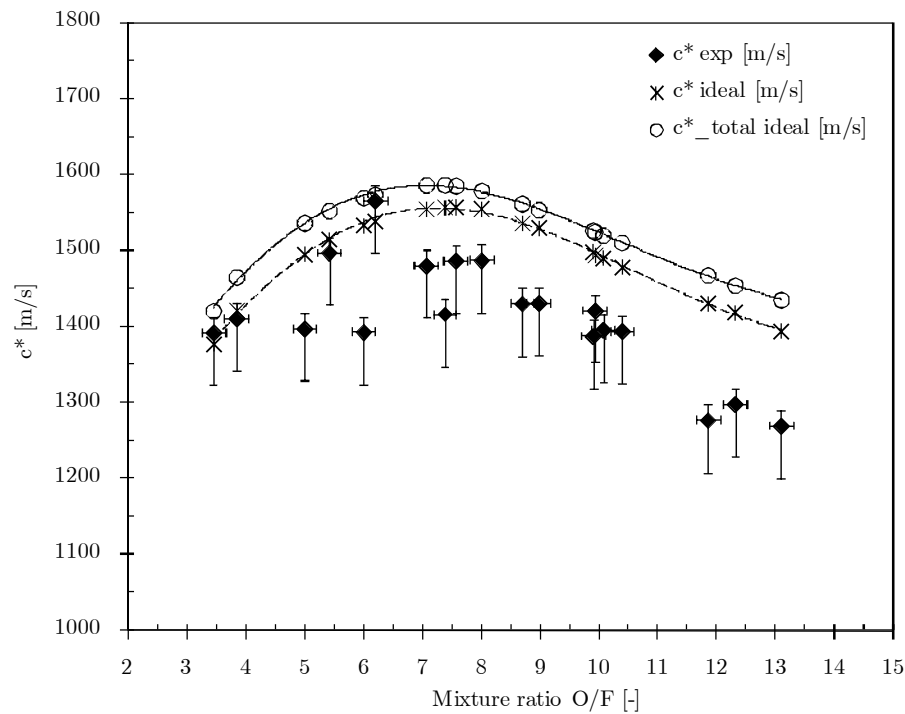
Figure 147 EBB characteristic velocity in bipropellant mode as a function of propellant mixture ratio (H_2O_2/kerosene)
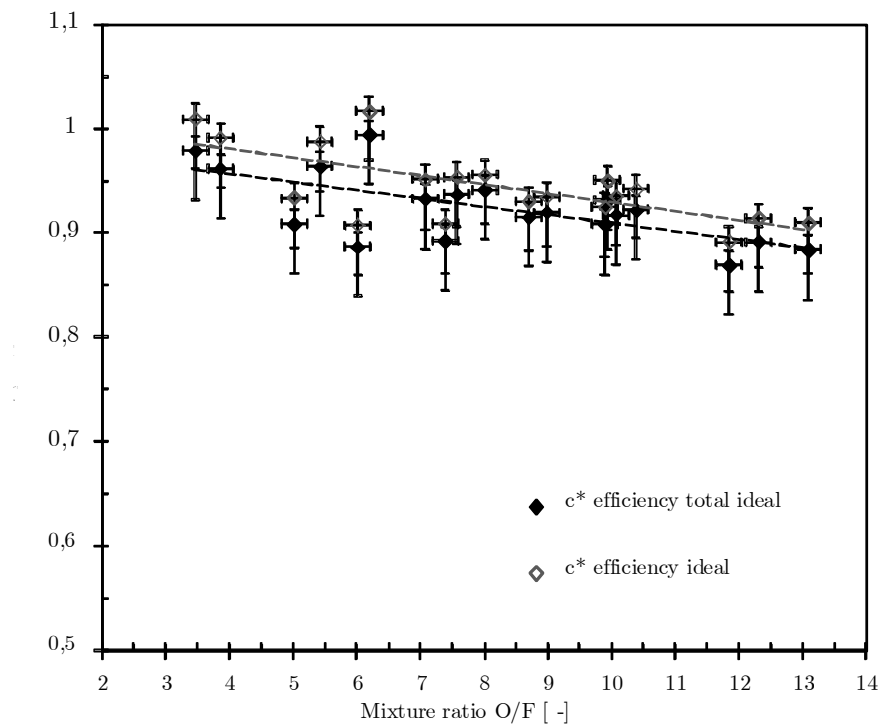
Figure 148 EBB characteristic velocity efficiency in bipropellant mode as a function of propellant mixture ratio (H_2O_2/kerosene)

Figure 148 shows the corresponding efficiency values of the tests presented in Figure 147 with corresponding linear interpolation. While high efficiencies well above 90 % are achieved over the whole range of mixture ratios, highest efficiencies are achieved for small mixture ratios At the nominal operation point near the optimum mixture ratio, efficiency values indicate combustion efficiencies to ~95 %, neglecting the thermal losses before injection (c^*

efficiency ideal). This result shows high stationary combustion efficiency achieved by the EBB thruster in H_2O_2/kerosene bipropellant operation. This efficiency values compare well to values found in literature for combustion chambers orders of magnitude larger in scale, based on the mass flow rates employed [279] and thus shows no decrease in performance measurable with the given test setup due to miniaturization to this scale. The efficiencies presented also compare well to studies utilizing different oxidizers, such as in Ref. 280, investigating kerosene with gaseous oxygen as oxidizer.

4.4.3.4.   Ignition tests: ethanol

In this section, the ignition capability of the EBB thruster for ethanol injected into decomposed hydrogen peroxide as a function of propellant mixture ratio is studied. Due to the large proportion of the fuel to the overall propellant flow, large variations in combustion chamber pressure for different mixture ratios investigated have been encountered. Therefore, different pressure regimes are indicated in Figure 149 in addition to the success of ignition. Only data points corresponding to a similar pressure regime can therefore be compared to each other. As anticipated, higher combustion chamber pressure before ignition enables successful ignition even for temperatures and mixture ratio combinations, where no ignition occurred at smaller chamber pressures.

The same procedures as described in section 4.4.3.2 regarding the display of uncertainties and parameter extrapolation for unsuccessful ignition tests have been employed for the test series presented hereafter.

Figure 149 EBB bipropellant ignition capability as a function of mixture ratio (H_2O_2/ethanol), nominal mixture ratio indicated by dotted line

Figure 150 shows the successful and unsuccessful ignition results as a function of temperature and combustion chamber pressure at time of ignition. Again, the large mass flow variations necessary to achieve the test conditions rendered constant oxidizer to mass flow ratios, as in the case of kerosene as fuel, impossible. The *O/F* ratios are therefore indicated separately and comparison of data points is only valid for similar *O/F* ratios. The wide range of pre-ignition chamber pressure covered led to a wide range of total propellant mass flows, determined for successful tests in the near stationary case, of $\dot{m}_p \approx 0.51\,\mathrm{g\,s^{-1}}$ to $\dot{m}_p \approx 0.68\,\mathrm{g\,s^{-1}}$.
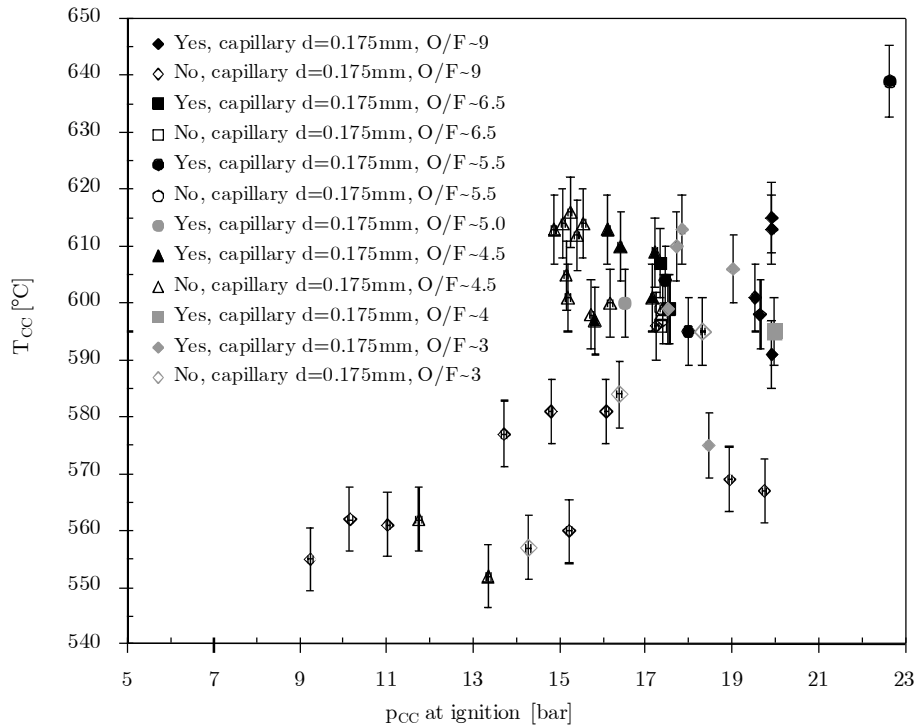
Figure 150 EBB bipropellant ignition capability as a function of pressure and temperature (H_2O_2/ethanol)

A reliable ignition threshold of $T_{CC} > 600\,°C$ for a pre-ignition pressure of $p_{CC} > 17$ bar can be deduced from the data presented in this chapter for all mixture ratios investigated. Pre-ignition chamber pressures could be significantly reduced in comparison to the investigation in section 4.3.3.3. However, comparison of the ethanol ignition behavior to the one of kerosene as fuel still yields both significantly increased temperature and pressure limits, which negatively impacts the design of a thruster system in various ways:

As discussed in section 4.3, increased threshold temperature negatively impacts the system start up time. The close vicinity of the required temperatures to the ideally available decomposition temperature of hydrogen peroxide at the given concentration additionally increases the time necessary to heat up the structure of the thruster.

Secondly, the higher stationary combustion chamber pressure necessary for successful ignition increases the thermal load to the combustion chamber wall by increasing the hot gas side heat transfer coefficient according to the 0.8th power of the combustion chamber pressure ($h_g \sim p_{CC}^{0.8}$).

Moreover, a large combustion chamber pressure necessary for ignition limits the thruster lifetime if utilized in a blow down propulsion configuration and necessitates higher tank pressure levels and therefore larger structural mass.

The high mass flows used to achieve the ignition pressure in this investigation renders direct comparison to the results from the ignition chamber presented in section 4.3.3.3 impossible. In the ignition chamber, the large chamber pressures have been achieved by the utilized back-pressure device rather than by increasing the propellant mass flow as in the case of the EBB thruster. In addition to the different mass flows investigated, the ignition tests have been performed at considerable lower temperatures but larger chamber pressures.

4.4.3.5.   Combustion tests: ethanol

The tests presented in this section investigate the stationary combustion performance of the EBB thruster operated with liquid ethanol as fuel. The investigation bases on the parameter of characteristic velocity and ideally calculated values based on experimental input parameters as described in section 4.4.3.3. However, since the tests showed large deviations in combustion chamber pressure, as explained in section 4.4.3.4, chamber pressure regimes are indicated for the data displayed. Compared to results from kerosene tests, the resulting data shows significantly increased scattering, including outlier values above the indicated ideal values. In addition, uncertainties are increased due to the increased chamber pressure, compared to kerosene combustion. Outlier values above theoretical values are found to lie within measurements uncertainty except for a single instance.
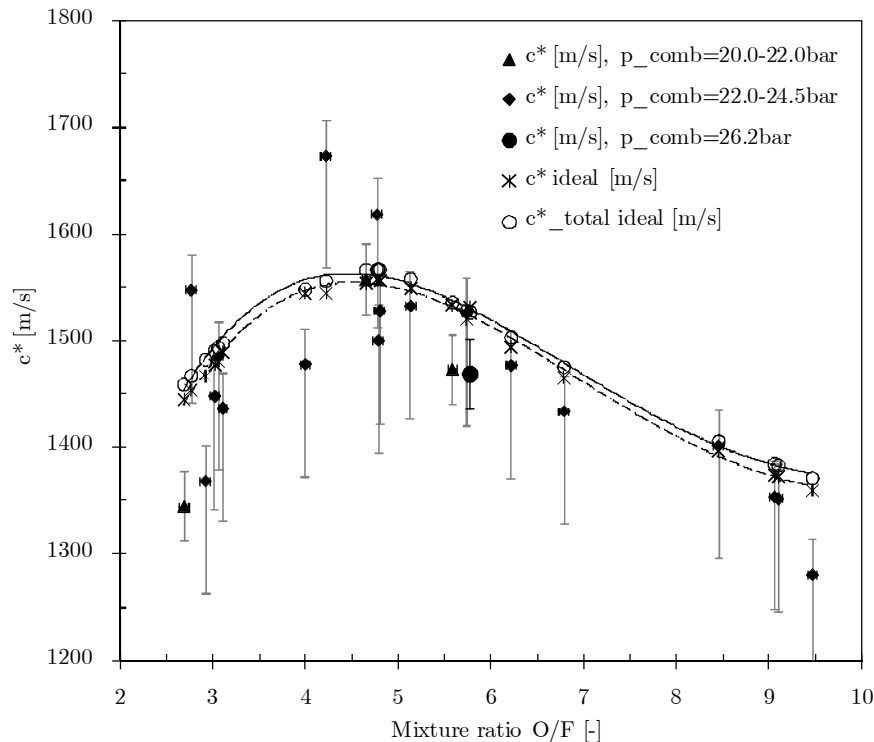
Figure 151 EBB characteristic velocity in bipropellant mode as a function of propellant mixture ratio (H_2O_2/ethanol)

The experimental data is able to reproduce the general behavior of decreasing characteristic velocities for mixture ratios off the nominal mixture. The experimentally found maximum value for the characteristic velocity corresponds well to the optimum *O/F* ratio found by theoretical analysis [92].

4.4.3.6. Optimized EBB thruster operation

After completing the above presented test campaigns, the EBB thruster configuration was changed to optimize the transition times by both increasing the mass flow by increasing the combustion chamber throat area (from $d_t = 0.7$ mm to $d_t = 0.8$ mm) and incorporating the findings from section 4.2.4.1 by implementing a catalyst with length $L_M = 10$ mm. Catalyst GC-222a (600 cpsi triangular, Pt) was selected for the optimized configuration tests.

The ignition capability of the changed EBB design was verified by a series of tests with test parameters aiming at reproducing similar combustion chamber pressures as in section 4.4.3.2. Due to the square dependency of mass flow on throat radius, this resulted in significant increased mass flows of $\dot{m}_{ox} \approx 0.4$ g s^{-1} for $p_{CC} \approx 6.9$ bar as shown in the long duration test firing in Figure 152.
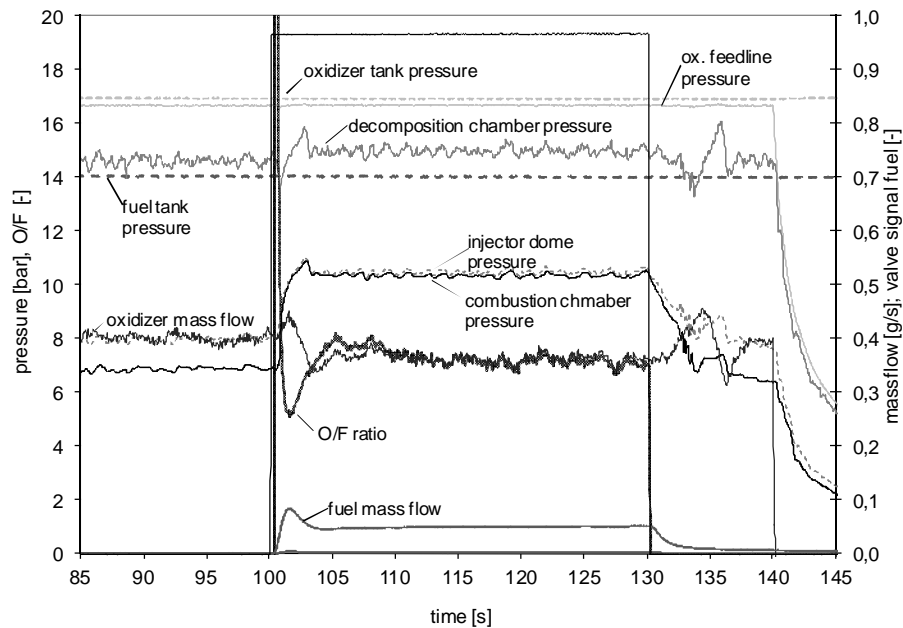
Figure 152 Detail of optimized EBB thruster pressure and mass flow signals during 30 s hot firing test (H$_2$O$_2$/kerosene)

The ignition thresholds obtained for the increased throat diameter configuration are shown together with the data from Figure 145 in Figure 153. In addition to ignitions achieved well above both temperature and pressure thresholds, successfully ignitions have been repeatedly achieved at temperatures below the threshold of the former EBB design. This points to increased injector mixing performance due to larger flow velocities in the tangential injection

channels and shear layer formation. The possibility of achieving autoignition with increased throat diameter led to the final design of the DM thruster.
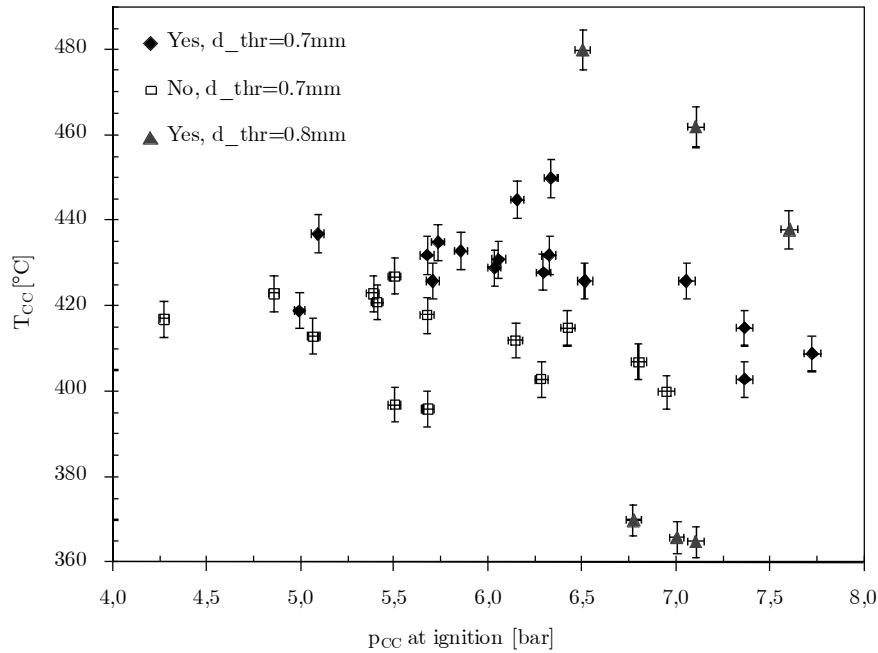
Figure 153 EBB bipropellant ignition capability as a function of pressure and temperature and different chamber throat diameters (H_2O_2/kerosene)

According to the findings from the catalyst simulation presented in section 2.3 and the experimental investigation presented in section 4.2, a catalyst with reduced structural mass had been designed and was investigated in the optimized EBB thruster configuration. The catalyst is a L_M = 10 mm monolith type catalyst with triangular channel geometry with reduced monolith chamber wall thickness. All other catalyst parameters such as carrier material and active material were chosen to resemble the catalyst GC222a described in Table 23.
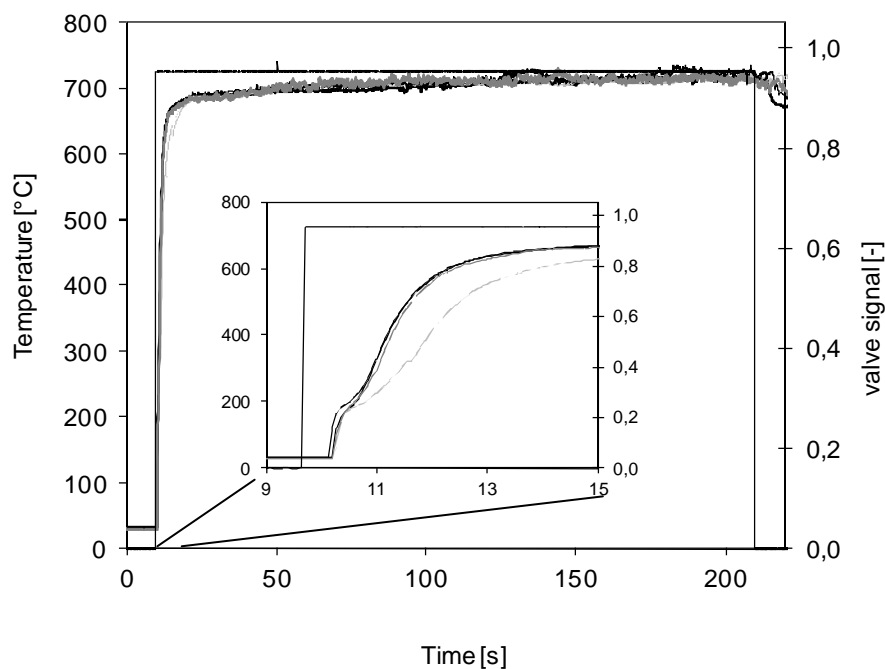
Figure 154 Catalyst with reduced wall thickness in optimized EBB configuration, transitional detail highlighted

Four successive tests of this catalyst are shown in Figure 154 for the standard test procedure of 200 s duration, with a detail of the transitional regime highlighted. The mean transition time for this configuration is found to be $t_{500} = 1.36\pm0.45$ s.

4.4.3.7. Pulsed firing sequences

Pulsed firing tests were conducted in the optimized EBB configuration (catalyst GC222a with length $L_M = 10$ mm, $d_t = 0.8$ mm) with kerosene as fuel. The tests were composed of a series of intervals with different valve settings, as schematically depicted for the first cycles in Figure 155. The initial phase of each test was composed of a warm-up phase in monopropellant mode to achieve autoignition conditions, followed by an interval with both propellant lines closed for a time interval t_0. After this initial phase, pulsed thruster operation was initiated by opening the oxidizer valve. After t_1 seconds in monopropellant mode, the fuel valve was opened, initiating the bipropellant mode of duration t_2, after which the fuel valve was closed again. The oxidizer valve remained open for t_3 seconds to guarantee injector cooling, after which the valve was closed again for an interval t_4. Steps including t_1 to t_4 were repeated for up to 10 cycles.
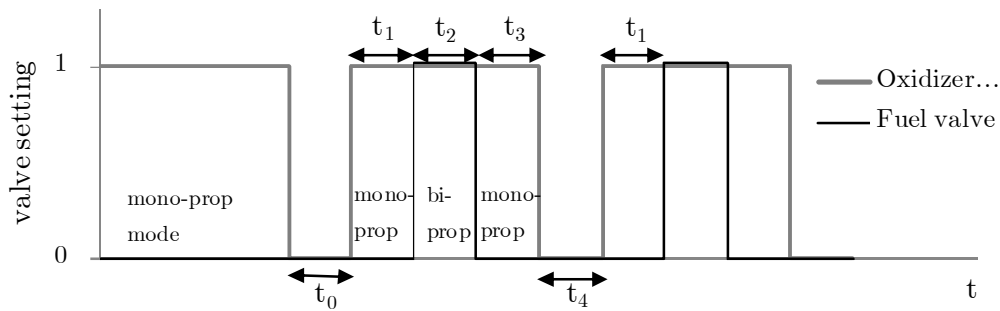
Figure 155 Schematic valve opening commands for pulsed thruster operation (valve open = 1, valve closed = 0)

Figure 156 shows a detail of a pulsing test cycle, with $t_1 = t_2 = t_3 = t_4 = 5$ s at combustion chamber pressure of $p_{CC} \approx 7.0$ bar at the end of the initial warm-up phase (before t_0). Only pressures and no mass flow signals are displayed for clarity purpose. The thruster operation modes are indicated at the bottom for the warm-up phase and the first combustion cycle. A phenomenon shown in the data is the pooling of the catalyst chamber, resulting in an increased pressure peak at the beginning of t_1, after oxidizer valve opening. At this stage, a peak oxidizer mass flow caused by the reduced decomposition chamber back-pressure is entering the decomposition chamber. The high decomposition capability of the preheated catalyst is instantaneously able to decompose this high hydrogen peroxide flux, thus resulting in a high decomposition chamber pressure peak. This pressure peak is continuing downstream through the combustion chamber injector to the combustion chamber. The increased pressure in the decomposition chamber results in a decrease in feed mass flow until nominal flow conditions are achieved. This phenomenon has repeatable occurred and can be seen in Figure 156 during t_1 (denoted "monoprop"). After nominal combustion chamber pressure at $p_{CC} \approx 7.0$ bar is achieved, reliable ignition with the injected kerosene occurs and the combustion chamber pressure signal indicates stable combustion at $p_{CC} \approx 10.7$ bar for the remaining

interval t_2. After closing the fuel valve, combustion chamber decays back to nominal monopropellant chamber pressure, before the oxidizer feedline valve is closed. After t_4, the whole cycle is repeated.
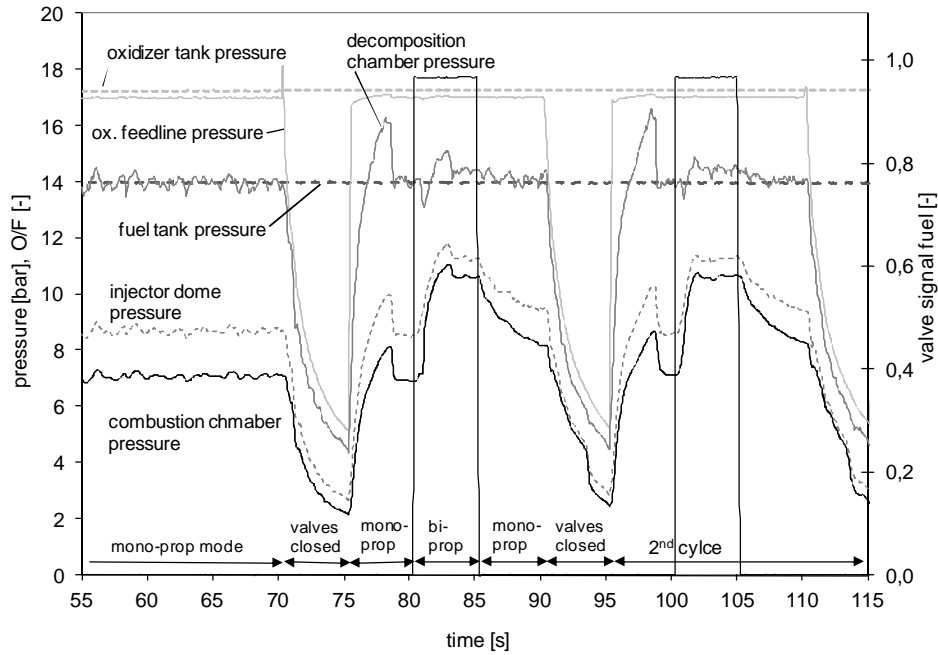
Figure 156 Detail of pressure signals during EBB pulse firing, operation modes indicated at the bottom.

Since the pressure increase in the initial phase during monopropellant mode at the beginning of a combustion cycle can favor ignition behavior, tests with reduced monopropellant operation interval $t_1 = 2$ s were conducted. Figure 157 shows the combustion chamber pressure, oxidizer feedline pressure and fuel valve signals for a series of nine combustion cycles for $t_1 = 2$ s, $t_0 = t_2 = t_3 = 5$ s. Different valve settings of the oxidizer valve can be seen by raise or decay of the oxidizer feedline pressure, with high pressure values indicating open oxidizer feed valve. Instantaneous pressure rise to monopropellant nominal pressure level occurs within the 2 s monopropellant interval, followed by instantaneous transition to bipropellant combustion. The pressure peak of $p_{CC} \approx 11.4$ bar caused by the high initial mass flow after valve opening is now located within the bipropellant mode interval, with a successive decay to nominal bipropellant pressure level of $p_{CC} \approx 10.7$ bar. Mean transition times from oxidizer valve opening to 90 % of the steady state bipropellant combustion chamber pressure are found for the nine cycle test to be $t = 2.77 \pm 0.09$ s, whereas mean pressure rise times elapsed from fuel valve opening are $t = 0.77 \pm 0.09$ s. The small standard deviation values for this pressure rising times shows good reliability of the ignition behavior of the EBB thruster in pulse mode.
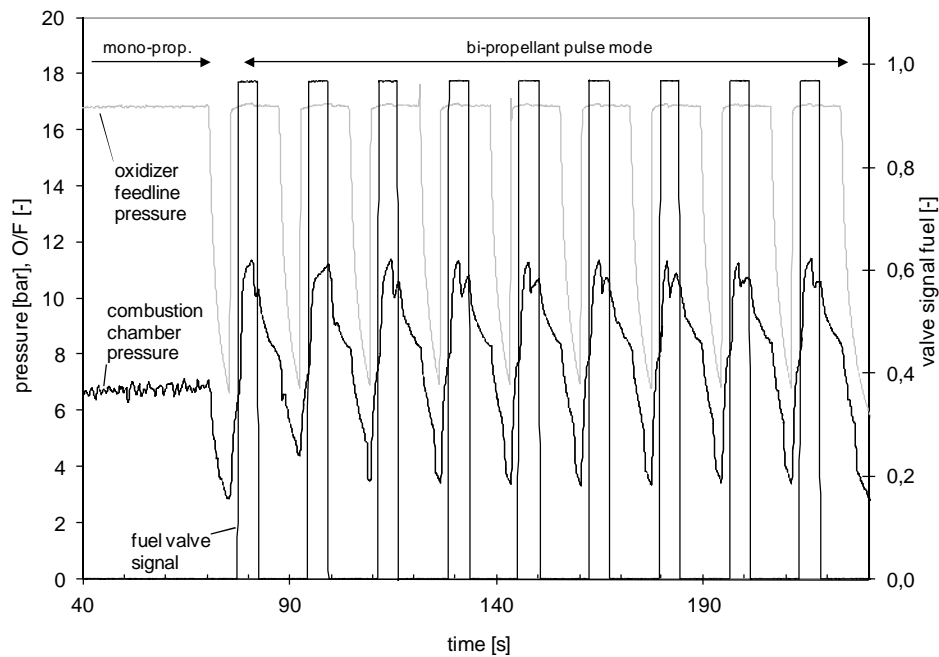
Figure 157 Detail of pressure signal during nine pulse firing cycles, operation modes indicated at the bottom.

4.4.4. EBB thruster summary and conclusion

The experimental investigation conducted with the use of the EBB thruster assisted a variety of purposes, including the validation of proper performance of the simplified tangential injector configuration concerning autoignition capability for both fuels.

Ignition studies have performed for both ethanol and kerosene as fuels as a function of injection temperature and chamber pressure. As opposed to the variation of chamber pressure independent from mass flow as conducted in section 4.3, these investigations have been performed in an environment resembling real operational conditions in this section. Negligible influence of mixture ration on ignition behavior could be shown. The ignition thresholds found are used as guidelines for the final DM thruster design.

The high pre-ignition combustion chamber pressure necessary to achieve successful autoignition of ethanol in decomposed H_2O_2 however render the inclusion of this fuel in the DM phase impossible from a systems point of view. This is mainly due to the significantly increased thermal load on the combustion chamber expected from the increased pressure levels and largely increased transition times due to higher temperature levels necessary for autoignition, compared to kerosene combustion.

Combustion performance was investigated for both fuels based on the characteristic velocity as a function of mixture ratio. The behavior anticipated from theoretical calculations was confirmed for both fuels. Although measurements have been found to be afflicted with certain

errors due to unknown boundary layer thickness at the throat, the results point to high combustion efficiencies achieved.

The EBB thruster was finally used to investigate favorable design changes regarding the transitional operation regime by proving autoignition capability in a configuration with increased throat radius, enabling larger mass flows, and utilizing a reduced length catalyst. In addition, a catalyst with reduced monolith wall thickness was tested in the EBB configuration, yielding improved transitional behavior and confirming theoretical predictions.

Finally, the possibility of pulsed bipropellant operation in a preheated configuration has been confirmed, although a pooling phenomena was observed, creating noticeable pressure increase in the initial phase of the pulses. Ignition delay times as small as 0.77 s after fuel injection (2.77 s after oxidizer injection) were achieved for kerosene in preheated pulse operation.

4.5. Development Model (DM) thruster

4.5.1. Description of experimental setup

The DM thruster combustion chamber is manufactured from Platinum-20%Rhodium, whereas all upstream components are made of Nimonic, a high temperature Ni- based alloy [278]. The thruster consists of three main components: the combustion chamber with nozzle, the injector housing with attached decomposition chamber, and the swirl injector plate. The former two are made of one part, whereas the injector is preassembled and consists of the tangential injection plate and the combustion chamber back plate including the premixing chamber. All these components are laser-welded during assembly, with two welding lines between injector housing and combustion chamber. In addition to these main components, the thruster consists of the fuel injection line with coaxial injector capillary and the removable decomposition chamber flange housing the porous decomposition chamber injector. The main components are shown in exploded view in Figure 158.
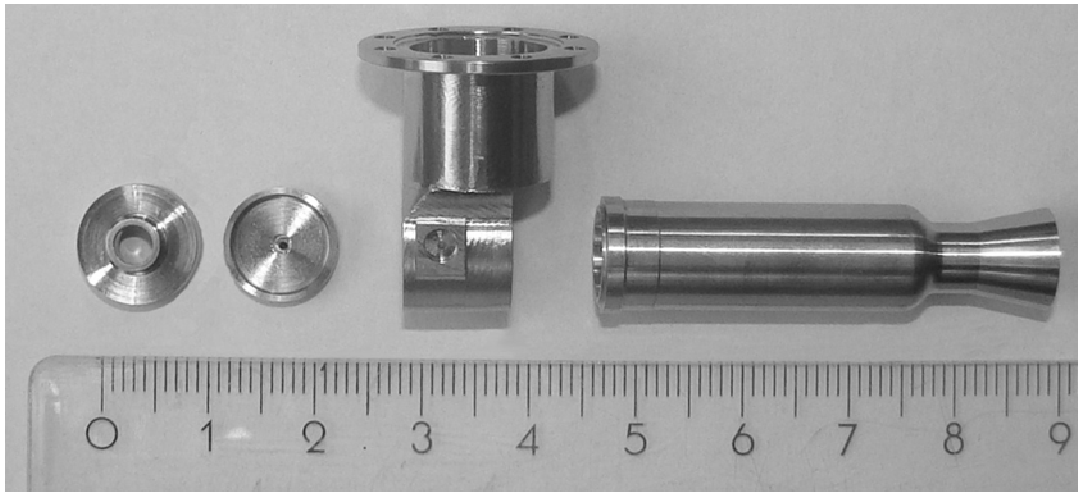
Figure 158 Pre-assembled DM thruster components, scales in cm

In addition to the thruster original components, two stainless steel tubes, each housing the diagnostics for temperature and pressure determination, are laser welded to the sides of the injector housing component. The thruster features a converging-diverging bell-shaped nozzle with a throat to nozzle area expansion ratio of $\varepsilon = 96.5$ which is fitted for reduced ambient pressure testing. However, only ambient pressure tests were conducted within this thesis. The thruster and its main features are shown in Figure 159.
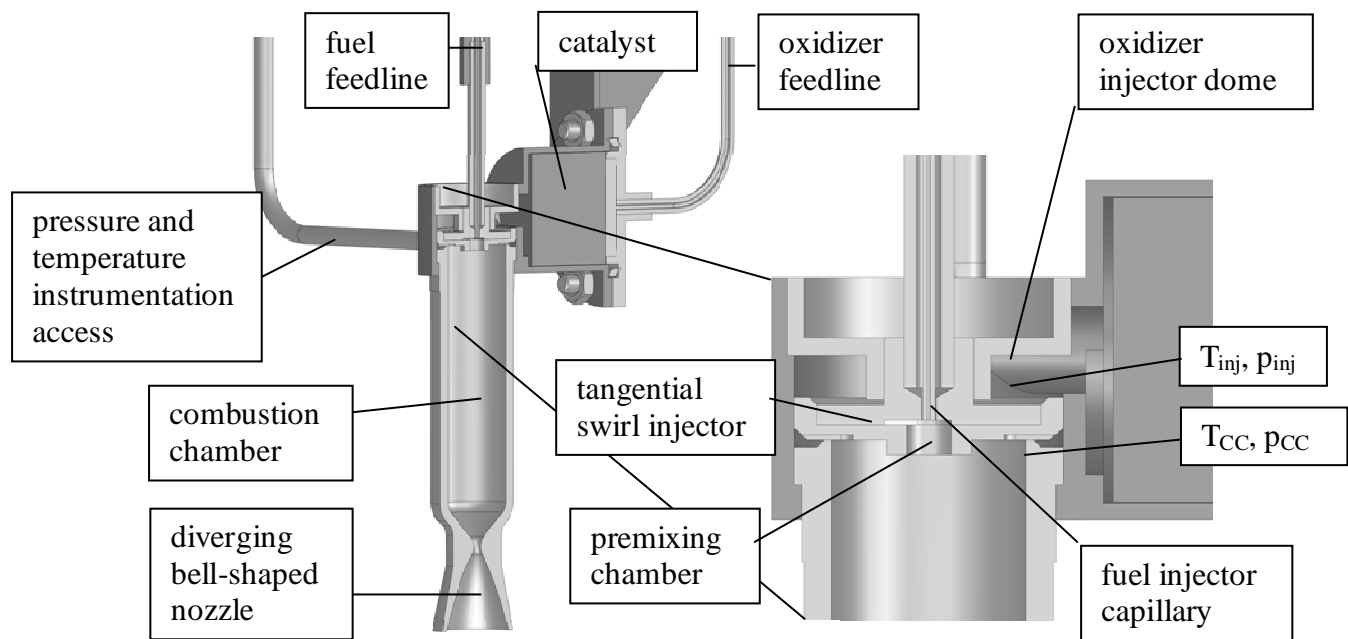
Figure 159 Cut view of the DM thruster

The DM thruster features two instrumentation access points, each equipped with temperature and pressure measurements. One of these access points leads to the injector dome, with the thermocouple inserted 10 mm into the stream of decomposed hydrogen peroxide. The other instrumentation access point leads to the combustion chamber just downstream of the welding line joining the combustion chamber to the injector. The thermocouple tip measuring T_{CC} has been positioned planar to the combustion chamber inner surface to avoid flame holding effects and damage to the thermocouple. It thus measures a combination of structural temperature and fluid temperature as in the case of previous combustion chamber temperature measurements for the EBB thruster. Data from this thermocouple therefore does not constitute a measurement of the combustion temperature but is used to monitor the maximum structural temperature at the welding line.

The thruster is mounted by its decomposition chamber flange below the valve module containing both feedline valves (Parker 009-0172-900, <5 ms response time), onto the test stand via a thrust measurement unit featuring a strain gauge module as shown in Figure 160. Feedlines and instrumentation access are generously bended to prevent any nonlinear influence to the thrust determination. The thrust stand is calibrated with pressurized feedlines and fully instrumented thruster to avoid influence on the measured thrust, as explained in section 4.5.2.
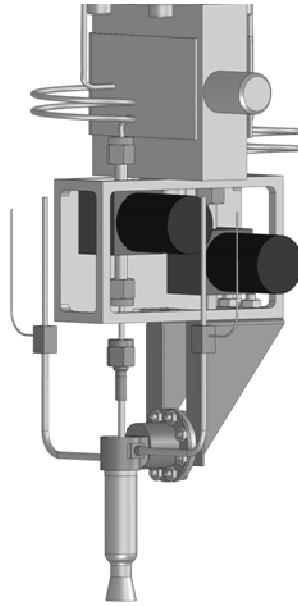
Figure 160 CAD drawing of the DM thruster mounted on thrust stand

Three additional thermocouples are attached at different axial positions of the combustion chamber to the outside chamber wall surface, secured by bended nickel wires ensuring constant contact pressure of the thermocouple tips to the wall for all tests conducted. While relative comparison of the data recorded from these thermocouples is therefore valid, absolute temperatures recorded have to be treated with care, since the temperature measurements are conducted at the hot surfaces facing cold surroundings and are therefore subjected to both convective and radiative errors. However, data from these thermocouples can be used to retrieve the axial position of largest wall temperatures. The DM thruster mounted to the test stand with attached thermocouples is shown in Figure 161. The image on the right hand side shows the thruster attached to the valve compartment and the thrust measurement section above.
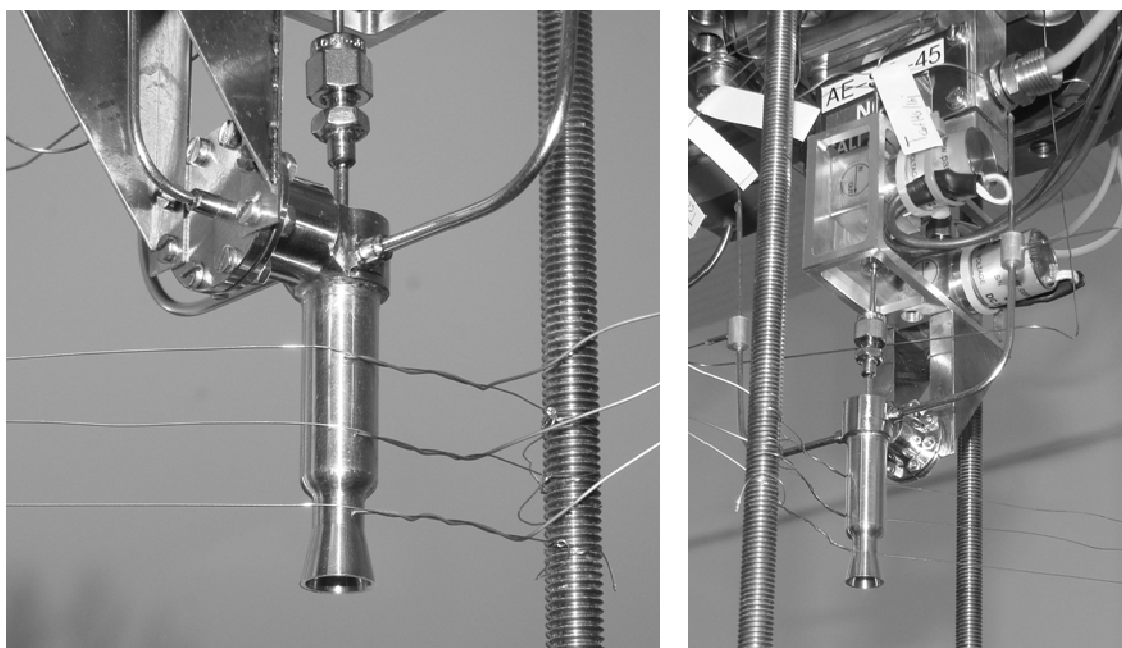
Figure 161 Picture of the DM thruster mounted to test stand

The main thruster parameter of the DM thruster are summarized in Table 24.

Table 24 DM thruster main parameters

Designation	Value	Dimension	Comment
V_{CC}	1426.5	mm^3	Combustion chamber volume
d_t	0.85	mm	Throat diameter
r_{CC}	3.9	mm	Combustion chamber radius
r_{inj}	1.2	mm	Premixing chamber radius
L^*	2242.3	mm	Characteristic length
S	4.93	-	Swirl number, kerosene
d_{cap}	0.15	mm	Fuel injector capillary diameter
L_{premix}	1.4	mm	Premixing chamber length
ε	96.5	-	Nozzle expansion ratio
m	44	g	Total thruster mass

The tangential injector principle of the DM thruster is depicted in Figure 59 on the right hand side. Optical evaluation of the tangential injection channels indicated injection channel width significantly deviating from the EBB injector geometry, leading to an increase of the Swirl number compared to the EBB injector, as discussed in section 3.6.3.1.
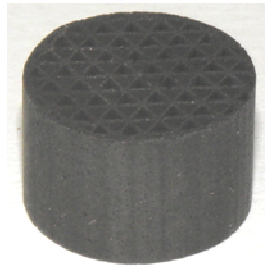
Figure 162 Catalyst GC223b employed in DM test

Based on the findings in section 4.2.2, a decomposition chamber injector featuring a further increased open porosity of 90 µm was employed to improve eventual blocking behavior. The porous plate injector was directly laser welded to the removable decomposition chamber flange. Catalyst GC223b was chosen to be employed in the tests presented hereafter. Main catalyst features are given in Table 25. The catalyst, which is from the same batch as catalyst GC222a which was employed in the EBB pulsed firing tests described in section 4.4.3.7, is shown in Figure 162.

Table 25 DM catalyst GC223b main characteristics

Parameter	Value	Dimension
Length	8.1	mm
Diameter	12.0	mm
Mass	0.8438	g
Active material	Cordierite-Pt	-
Washcoating procedure	B	-
Channel shape	triangular	-
Channel density	540	cpsi
GC-222a	Cordierite-Pt	10

Figure 163 shows the schematics of the DM thruster facility. Both propellant feed systems were used. These components are described in section 4.1. The only modification to the feed system is the change of the main oxidizer feed valve to a magnetic solenoid valve (AV1). In contrast to previously tested systems, the DM thrust stand is equipped with a thrust measurement device (F), recording forces exerted by the DM thruster along the vertical thrust axis.
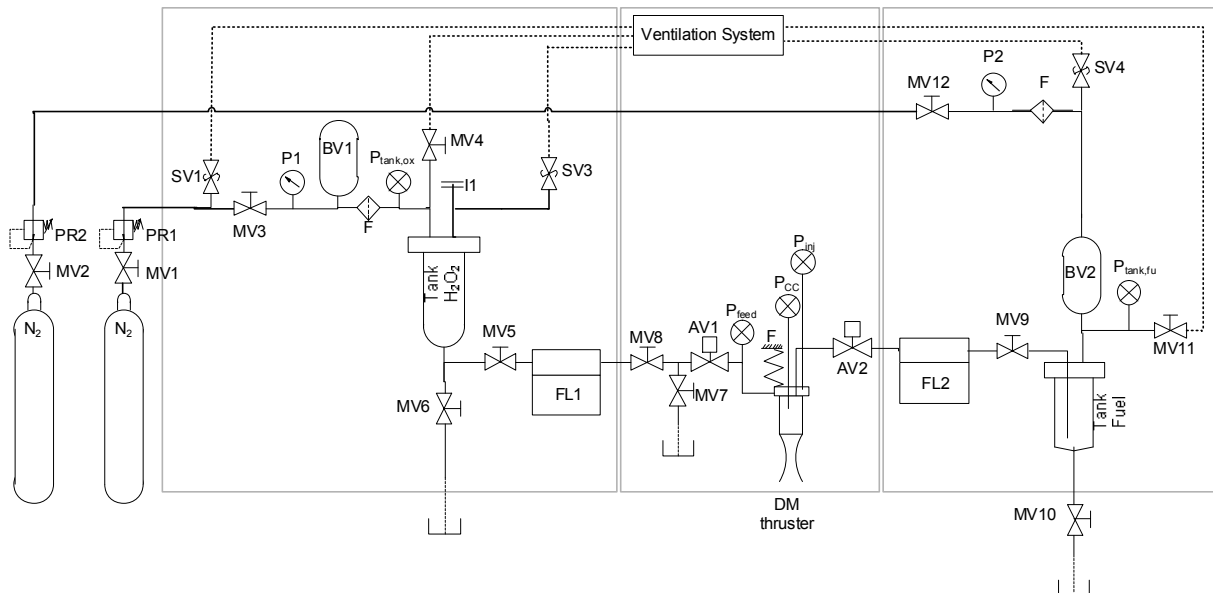
Figure 163 Schematics of DM thruster test facility

4.5.2. Thrust measurement

The thrust measurement is conducted using a strain gauge employed in the thrust measurement unit mounted between the thrust stand and the valve compartment with attached thruster as shown in Figure 160. The strain gauge is operated in a fully compensated Wheatstone bridge, accounting for thermal influences.

The calibration of the thrust stand was performed with the help of a calibrated scale (Sartorius CPA3202S) and a dedicated calibration device able to exert a variable force covering the calibration range, acting between the scales and the nozzle throat. The calibration setup is shown in Figure 164.

The calibration of the strain gauge signal was conducted for the fully assembled thruster with pressurized feedlines and all instrumentation attached. Any influences such as thruster and valve compartment weight, feedline stiffness and forces acting on the thruster due to attached instrumentation are therefore included into the calibration and do not affect the thrust measurement. Linearity of the calibration curve recorded shows these influences only adding an off-set to the measured thrust. No nonlinear influences was detected.

Figure 164 Calibration setup of the DM thrust stand

The calibration curve determined for the DM thruster test stand is shown in Figure 165, with indicated thrust measurement errors based on the resulting linear calibration. The strain gauge signal for zero thrust originates in the elongation of the bendable thrust measurement device due to the weight of the thruster, the negative slope of the calibration curve for increasing thrust originates in compression of the strain gauge in case of applied thrust. The absolute error of the thrust measurements are below 0.04 N, which is therefore used as thrust measurement uncertainty in the error analysis.
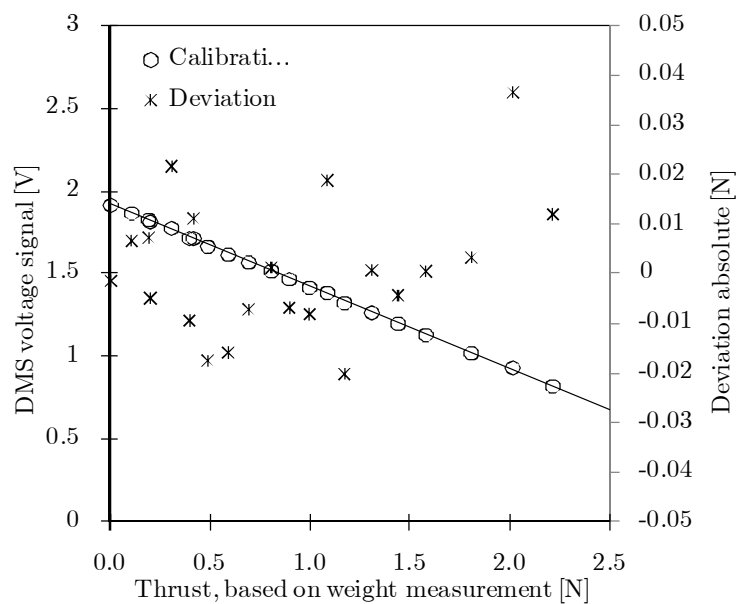
Figure 165 DM thrust stand calibration

To avoid scattering of the figures shown hereafter, the thrust signal is averaged for 100 ms for display purpose, stated values however are based on non-averaged values only.

4.5.3. Test Results
4.5.3.1.   Long duration hot-firing test

The radiative cooling capability of the DM thruster was validated in a test featuring a 25 s duration of bipropellant firing, achieving near stationary temperatures for the bipropellant firing phase. The pressure signals over the entire test period are shown in Figure 166 together with the mass flow signals. The different modes of operation are indicated.
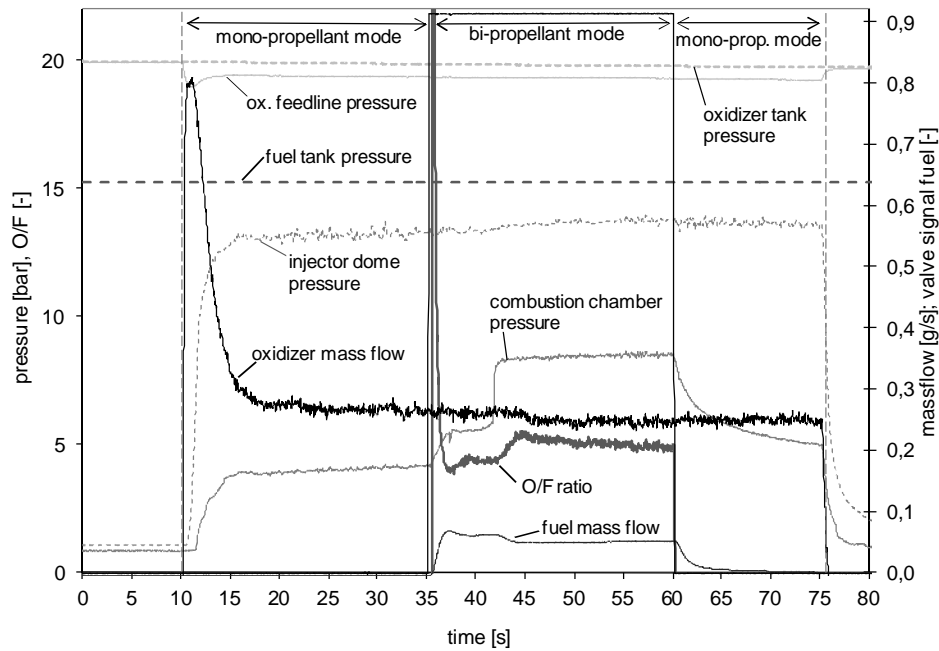
Figure 166 Pressure and mass flow signals in 25s bipropellant mode DM test
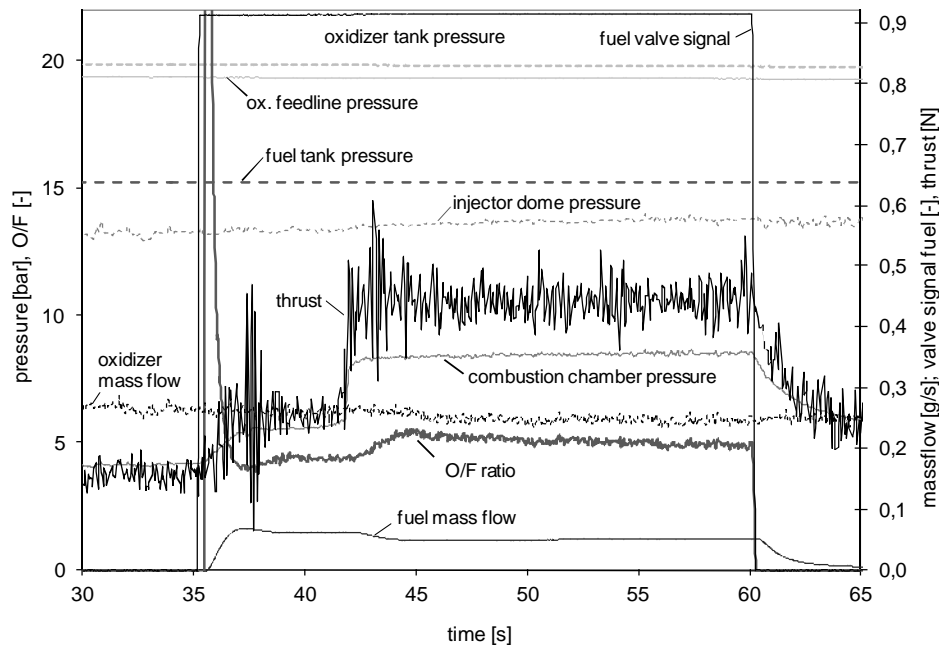
Figure 167 Pressure and thrust signals during bipropellant combustion of DM thruster

A detailed view of the pressure signals during the bipropellant phase of the test is shown in Figure 167. The test features a combustion chamber pressure of $p_{CC} \approx 4.2$ bar, before kerosene is injected, which is small compared to the ignition behavior of the EBB thruster discussed in section 4.4.3.2. This explains the fact that ignition does not occur until approximately 5 s into the bipropellant mode, at a pre-ignition chamber pressure of $p_{CC} \approx 5.7$ bar. Figure 167 additionally shows the signal from the thrust measurement. Although noise in the thrust data is significantly increased compared to other recorded data, the thrust measurement is able to resolve the monopropellant plateau, the intermediate plateau before complete combustion and the bipropellant thrust plateau. The latter is located at approximately $F \approx 450$ mN and therefore well below the targeted 1 N thrust. This is caused by overexpansion and flow separation within the nozzle which is fitted to expansion under vacuum conditions. This is discussed in detail in section 4.5.3.2 hereafter.

The temperature signals during the bipropellant phase of the test are shown in Figure 168. It should be noted, that the results for the external wall temperatures T_{w1}, T_{w2} and T_{w3} are afflicted with potentially large errors due to the way they were mounted to the combustion chamber, as discussed in section 4.5.1. Nevertheless these measurements show the declining slope of wall temperatures near the end of the bipropellant phase, thus validating the radiative cooling concept of the combustion chamber. As relative comparison of these thermocouples remains valid, it is interesting to notice that the point of highest wall temperatures measured is located near the axial middle of the cylindrical part of the combustion chamber (T_{w1}), with reduced temperatures at the convergent section (T_{w2}) and further reduced temperatures measured at the throat position (T_{w3}). This points to both a large heat flux to the combustion chamber in the cylindrical section and non-adiabatic flow.
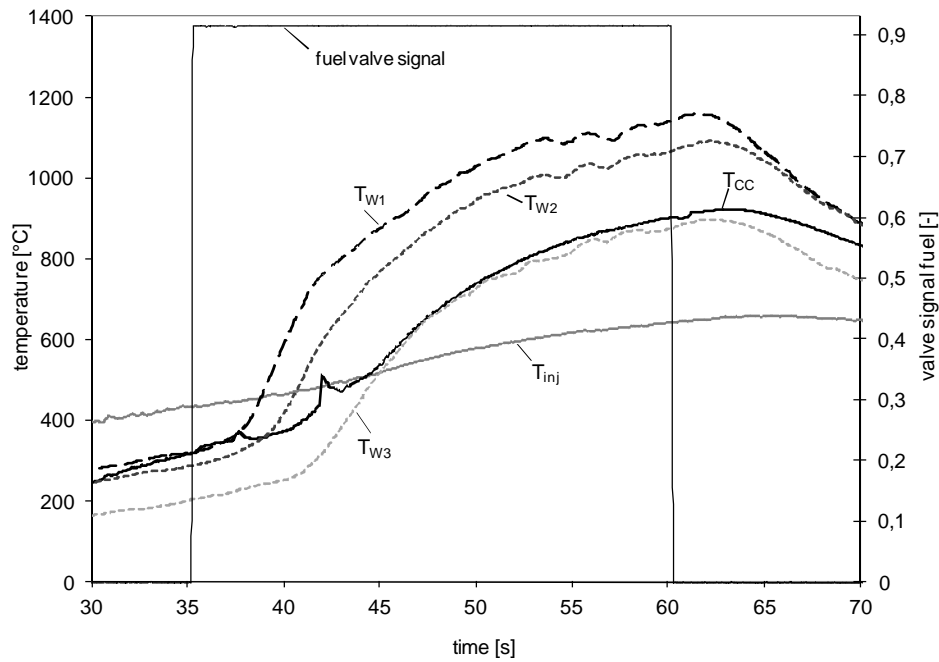
Figure 168 Temperature signals during bipropellant combustion of DM thruster

| $t = 10$ s: oxidizer valve opened | $t = 38$ s: 3 s after fuel valve opening | $t = 42$ s: 7 s after fuel valve opening |

| $t = 60$ s: before end of bi-propellant mode | $t = 67$ s: cooling down in monopropellant mode | $t = 93$ s: 18 s after oxidizer valve closed |
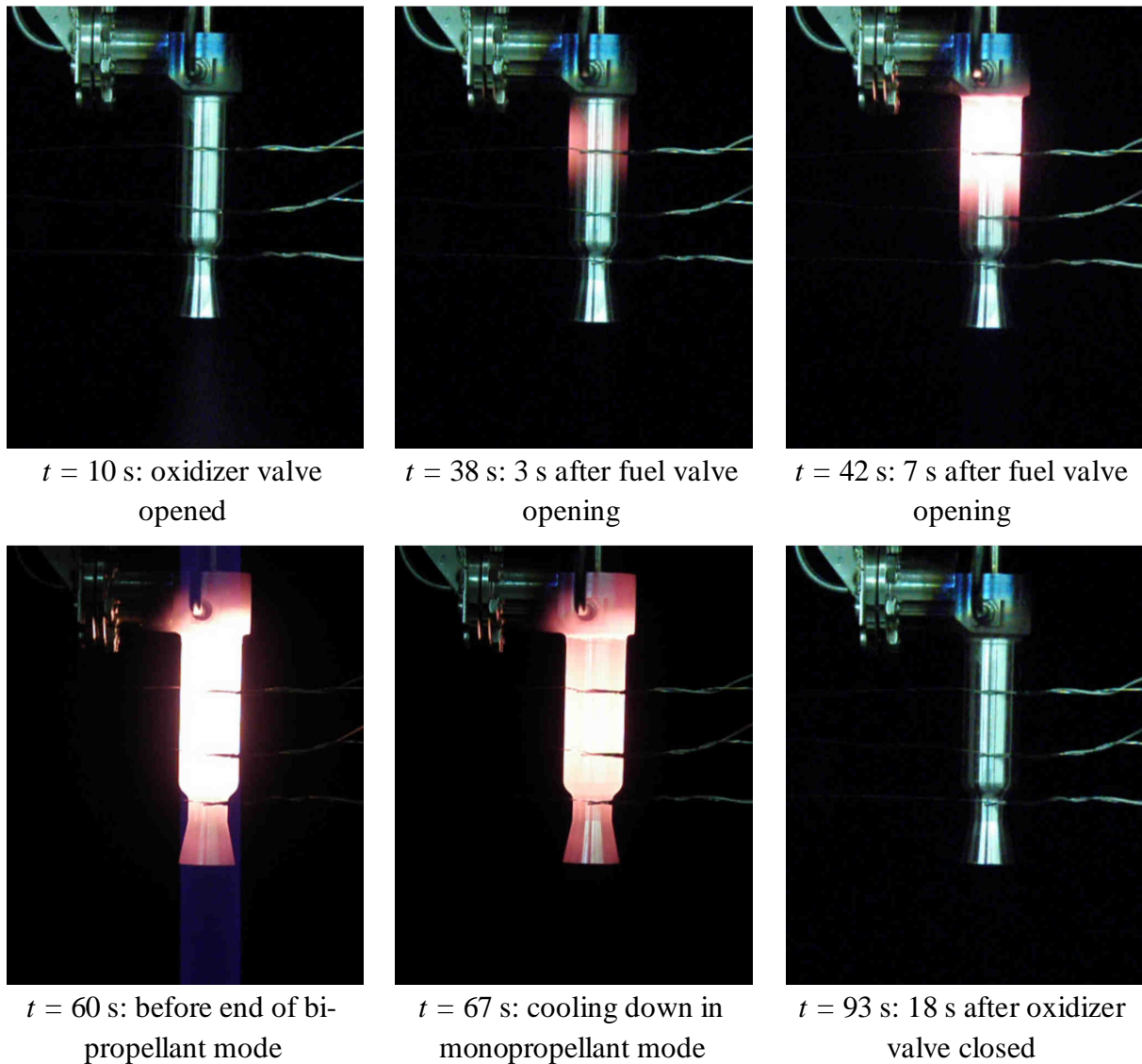
Figure 169 Optical visualization of DM thruster hot firing test

Optical visualizations at indicated times during the test are given in Figure 169. At time $t = 10$ s, the oxidizer valve is opened, and a cold steam plume due to large heat loss from the cold thruster structure is visible. At time $t = 38$ s, 3 s after fuel injection, transitional temperature increase in the cylindrical combustion chamber part points to ignition, the pressure data in Figure 167 however points to incomplete combustion since only marginal pressure increase is observed. At $t = 42$ s, complete combustion is achieved, with largest temperature increase of the combustion chamber outer wall in the upstream half of the cylindrical combustion chamber. At the end of the bipropellant test at $t = 60$ s, near stationary temperatures are observed. The observed shade shown is a visual distortion feature originated from the camera readjusting to the changed lightning conditions. 7 s after fuel valve closing, cooling down of the upstream combustion chamber wall near the injector is observed, with highest temperatures remaining further downstream close to the converging section of the combustion chamber. This effect is both due to radiative cooling by the outer surface and convective cooling from the decomposed hydrogen peroxide, with largest hot gas side convective heat transfer coefficients just downstream of the injector. At $t = 93$ s, 18 s after the end of the final monopropellant mode, the chamber has cooled down.

4.5.3.2. DM thruster performance evaluation

Figure 170 compares the characteristic velocities c^* achieved by the DM thruster as a function of mixture ratio to the ideal values, determined by NASA CEA analysis [92], based on experimental input parameters. The ideal value "c* ideal" refers to the ideally achievable c^* for input parameters determined just upstream of the combustion chamber injector, whereas "c*_total ideal" incorporates the entire tank to combustion chamber configuration. Comparison to the latter value thus incorporates decomposition inefficiencies and thermal losses upstream of the combustion chamber. Input parameters have been determined from recorded experimental data by averaging. A thorough discussion of the significance of these parameters can be found in section 4.4.3.3.

Comparison of the experimentally determined c^* values to the ideal c^* incorporating only the combustion process ("c* ideal") yields efficiencies ranging from 90% to 95%. The uncertainty bars indicated are based on the uncertainty propagation calculations performed in section 4.1.4.5. Unsymmetrical uncertainties in efficiency are caused by the uncertainty introduced due to the presence of boundary layers affecting the effective throat area, as discussed in section 4.1.4.4.
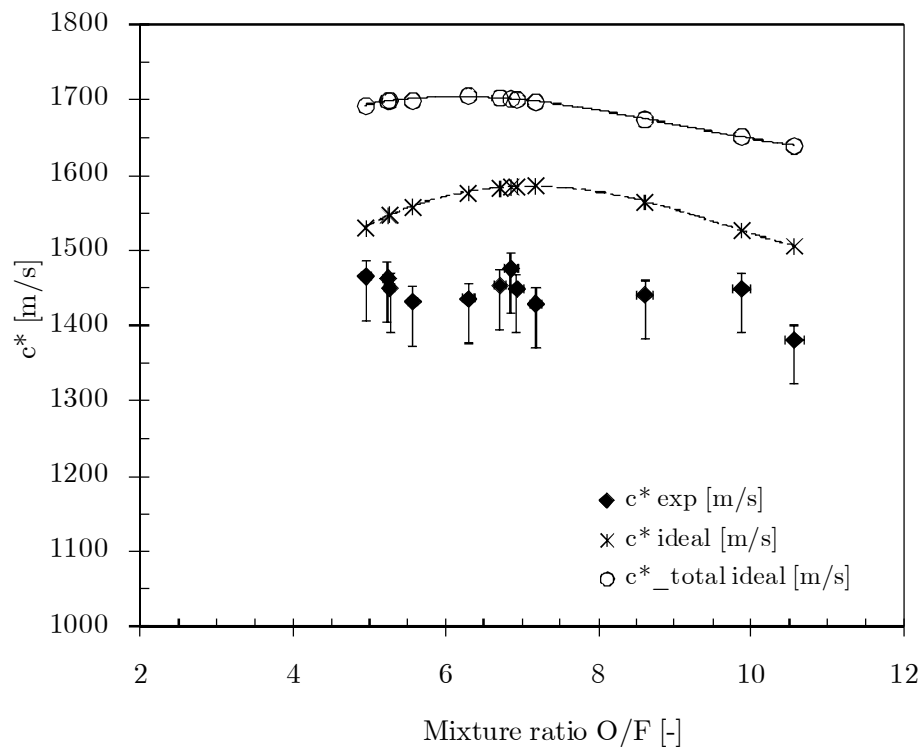
Figure 170 Characteristic velocity of DM thruster as a function of propellant mixture ratio

The thrust of an engine can be expressed as a product of propellant mass flow $\dot{m}_p$, combustion performance related parameter c^* and the thrust coefficient C_F

$$F = \dot{m}_p c^* C_F \,.$$

(4.14)

The thrust coefficient, based on isentropic flow through the nozzle, is given by:

$$C_F = \sqrt{\frac{2\gamma^2}{\gamma-1}\left(\frac{2}{\gamma+1}\right)^{(\gamma+1)/(\gamma-1)}\left[1-\left(\frac{p_e}{p_0}\right)^{(\gamma-1)/\gamma}\right]} + \frac{p_e-p_a}{p_0}\frac{A_e}{A_t} \qquad (4.15)$$

For ambient pressures larger than the nozzle exit pressure $p_a > p_e$, the last term in Eq. (4.15) becomes negative and causes a significant reduction of the thrust coefficient and therefore of the thrust. This behavior is shown in Figure 171. Further increasing the ambient pressure p_a leads to flow separation and shocks occurring within the nozzle, as indicated in Figure 171 by the line denoted "Shock line".
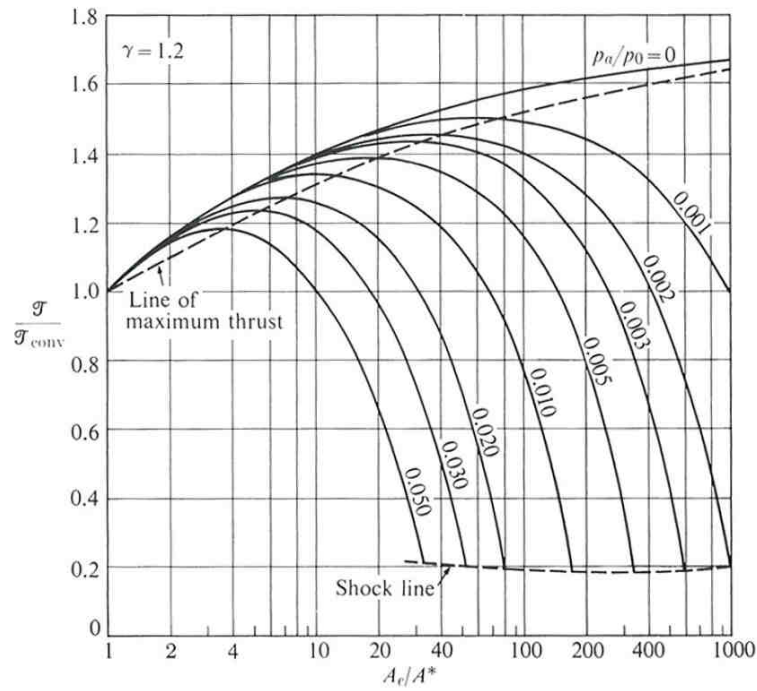
Figure 171 Thrust efficiency as a function of the ratio of ambient pressure to chamber pressure, Ref. 4

The DM thruster features a bell shaped nozzle with expansion ratio of $\varepsilon = 96.5$, which is fitted to reduced ambient chamber pressure tests. Since the DM tests presented here were conducted at atmospheric ambient pressure, the flow in the nozzle is fully overexpanded, with fully separated flow within the nozzle. A variety of analytical expressions estimating the pressure at which flow separation occurs are available [281, 282] including the simple relation known as Summerfield-criterion

$$\frac{P_{sep}}{P_{amb}} = 0.35...0.4 \qquad (4.16)$$

A comparison of experimental results to a large variety of simple flow separation criteria has been published in Ref. 283, showing that Eq. (4.16) is able to predict the point of separation for the expected Mach number in sufficient accuracy. For the given case, the Summerfield-criterion points to an estimated flow separation at approximately $\varepsilon \approx 10$-15. In this case, the

diameter of the supersonic exhaust jet is smaller than the nozzle exit diameter and is surrounded by an annular subsonic flow [3]. The downstream part of the separated, narrow exhaust plume, visible downstream of the nozzle exit area, is shown in Figure 172.
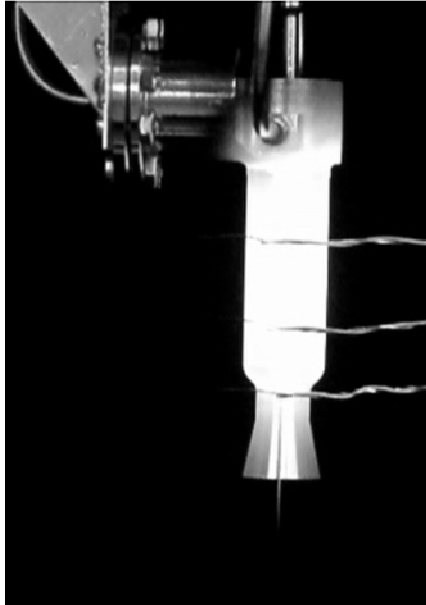
Figure 172 Narrow DM thruster plume with flow separation within the nozzle during ambient pressure test

The flow separation causes a significant reduction of the thrust coefficient C_F, which causes a reduction in resulting thrust, as shown in Figure 171, relating to an adiabatic coefficient of $\gamma = 1.2$ (instead of the more appropriate $\gamma \approx 1.12$) as a function of ambient pressure to chamber pressure ratio and expansion ratio according to Eq. (4.15). The ratio p_a/p_0 for the DM thruster becomes $p_a/p_0 \approx 0.085$. This shows the DM nozzle operating in fully separated mode.

It is therefore useful to define an efficiency based on the thrust coefficient

$$\eta_{C_F} = \frac{C_F^{measured}}{C_F^{ideal\ (CEA)}} \tag{4.17}$$

where the ideal thrust coefficient is based on expansion to vacuum and is calculated using NASA CEA code [92]. The measured thrust coefficient is determined from experimental data by

$$C_F^{measured} = \frac{F^{measured}}{\dot{m}_p c^*} \tag{4.18}$$

With the use of efficiency η_{C_F}, a thrust F_{vac} can be calculated, which is the thrust extrapolated to ambient vacuum conditions:

$$F_{vac} = \dot{m}_p c^* \frac{C_F^{measured}}{\eta_{C_F}} = \frac{F^{measured}}{\eta_{C_F}} \tag{4.19}$$

The thrust F_{vac} is therefore the thrust achieved for an ideal expansion of the combustion gases to a nozzle expansion ratio of $\varepsilon = 96.5$ under vacuum conditions. Figure 173 shows the actually measured thrust at ambient conditions, compared to the thrust extrapolated to vacuum conditions using Eq. (4.19) based on the measured values. In addition to the thrust values, the combustion chamber pressure achieved for stable combustion is shown in Figure 173. The thrust values presented correspond to chamber pressures in the range from $p_{CC} \approx 8.45$ bar to $p_{CC} \approx 10.5$ bar, with increasing thrust values corresponding to increasing combustion chamber pressures.
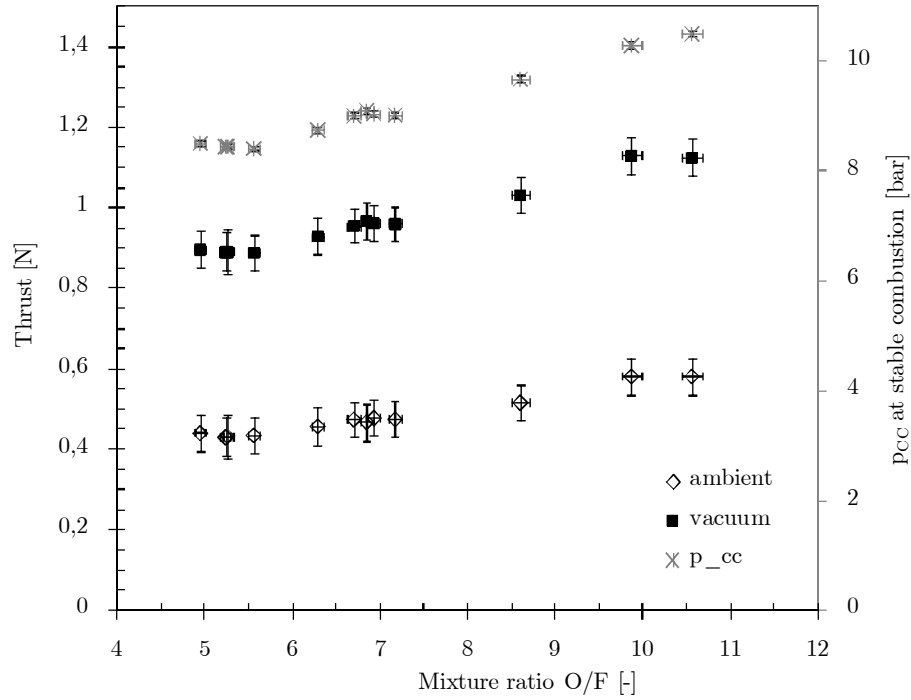
Figure 173 Measured thrust of the DM thruster as a function mixture ratio compared to values extrapolated to vacuum conditions

Since the thrust is mainly influenced by the combustion chamber rather than by the mixture ratio, the thrust is displayed as a function of stable combustion chamber pressure in Figure 174. The data shown incorporates propellant mixture ratios ranging from $O/F \approx 4.95$ to $O/F \approx 10.51$.
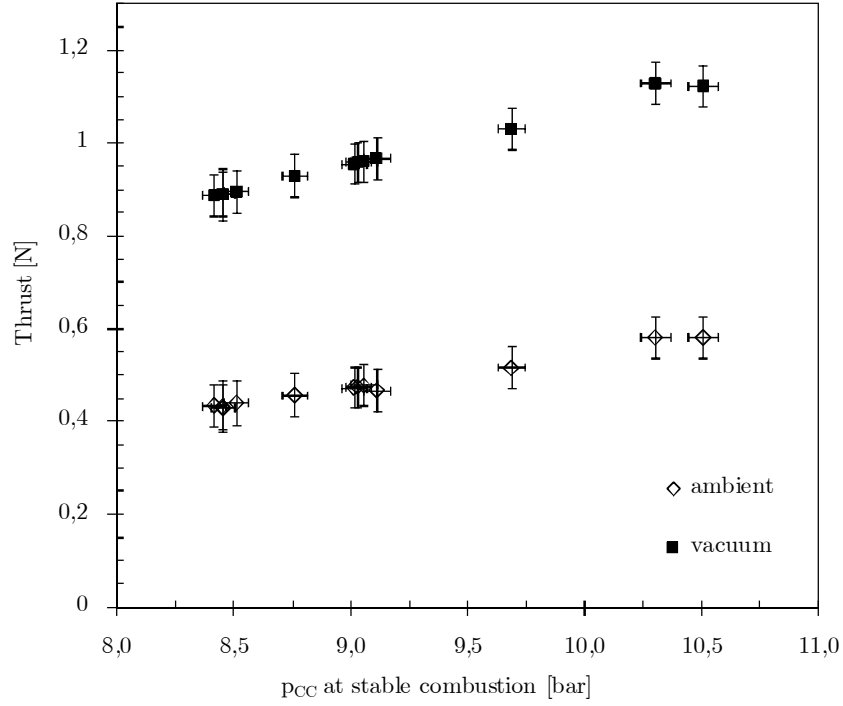
Figure 174 Thrust of the DM thruster as a function of combustion chamber pressure

The specific impulse of the DM thruster is determined by:

$$I_{sp} = \frac{F}{\left(\dot{m}_{ox} + \dot{m}_{fu}\right) g_0} \tag{4.20}$$

with $g_0 \approx 9.807\,\mathrm{m\,s^{-2}}$ being the gravitational acceleration at sea level. The specific impulses achieved for the DM thruster are shown in Figure 175, compared to the specific impulses achieved when based on the thrust extrapolated to vacuum conditions. The uncertainty bars for the specific impulse are again calculated according to error propagation calculation.

The DM thruster tests showed specific impulse values for ambient tests ranging from $I_{sp} \approx 133.3 \pm 19.3$ s to $I_{sp} \approx 138.7 \pm 18.8$ s. Extrapolation for vacuum conditions show specific impulses of $I_{sp} \approx 265.1 \pm 18.5$ s to a maximum of $I_{sp} \approx 282.1 \pm 19.8$ s. As can be seen from Figure 175, the specific impulse is not significantly affected by changes in propellant mixture ratio or combustion chamber pressure.
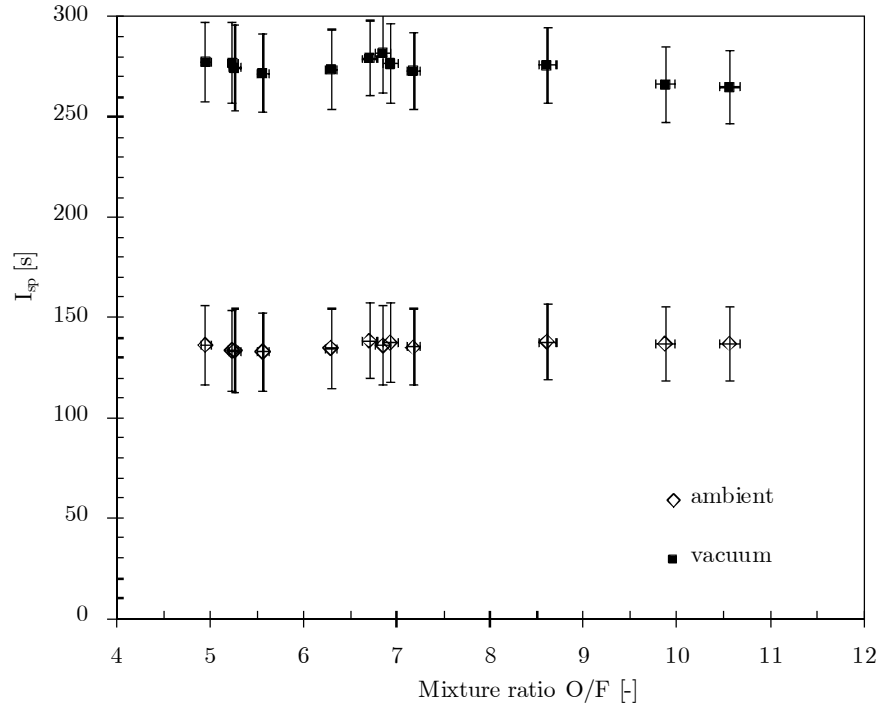
Figure 175 Specific impulse of the DM thruster as a function propellant mixture ratio

4.5.3.3. Pulsing capability and minimal impulse bit

Pulsing capability of the DM thruster was investigated by the same procedure as used in the EBB thruster tests described in section 4.4.3.7, Figure 155. However, fuel and oxidizer were injected at the same time ($t_1 = 0$ s), guaranteeing shortest transition times for thrust build-up. For shut-off, the oxidizer valve was closed $t_3 = 0.5$ s after the fuel valve, to guarantee sufficient cooling of the injector.

In the example shown in Figure 176, pulse duration was set to $t_2 = 5$ s to confirm the system parameters shown reaching stable plateaus. The quasi stationary nature of these combustion plateaus has been verified in various longer duration pulse tests. Successful thrust and chamber pressure built-up to the final combustion pressure level has been proven for pulse firing durations as small as $t_2 = 2$ s. Figure 176 shows a detail of the thrust and chamber pressure signal for three out of five pulses (pulse numbers 3, 4 and 5). Since a hot thruster structure is essential for pulsing capability, a warm-up phase of 40 s was conducted before the pulse sequence was initiated. The time between pulses was set to $t_0 = 10$ s to allow full chamber pressure decay. As opposed to the EBB pulse mode tests, reduced void volumes prevent any decomposition chamber pooling in the DM tests.
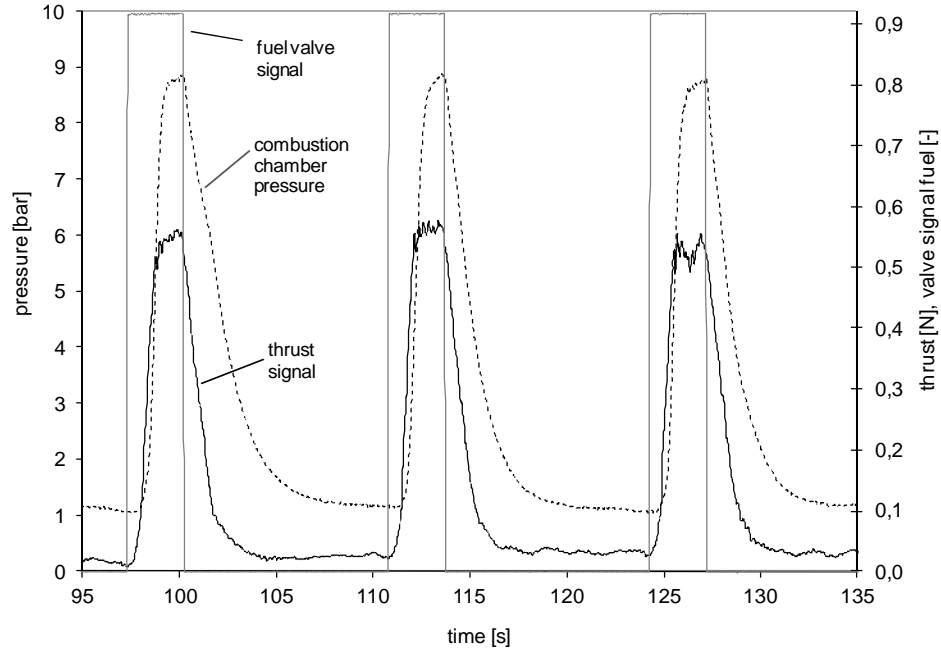
Figure 176 Thrust and combustion chamber pressure signals in 5s duration pulse firing

While certain noise and delay in the combustion chamber pressure build-up was noticed for the first pulse (not shown), initiated at low injection and chamber temperatures, short transition times, stable pressure and thrust plateaus and small thrust noise were achieved for the remaining pulses, where ignition occurred at elevated temperatures of $T_{CC} > 500$ °C caused by preceding pulses. The transient nature of the flow makes any prediction on the performance achieved impossible due to instationary mass flow rate signals. Increase in mass flow in the early transient phase caused by pressure built-up and void fillings however is anticipated to significantly decrease the I_{sp} compared to the stationary combustion presented before.

Mean transition times from propellant valve opening to 90 % of the steady state bipropellant combustion chamber pressure are found for the test presented in Figure 176 to be $t = 1.64 \pm 0.13$ s. This value is significantly reduced to the transitional behavior found for the EBB thruster, presented in section 4.4.3.7, mainly due to a reduction of void volumes and simultaneous propellant injection. The small standard deviation values for the mean pressure rising time shows good repeatability of the ignition behavior of the DM thruster in pulse mode.

Although the DM thruster is not optimized to achieve minimum impulse bits (*MIP*) as small as possible, it can be useful to estimate the *MIP* values achieved in the current configuration. *MIPs* for the pulses shown in Figure 176, averaged over all five pulses, are $MIP \approx 1.43 \pm 0.26$ Ns. Minimum impulse bits achieved with the DM thruster for 2 s pulsing duration, averaged over five pulses, are found to be as small as $MIP \approx 0.96 \pm 0.17$ Ns. It should however be noted that the fully transitional nature of the leading parameters during the 2 s pulse duration points to significantly reduced specific impulse due to high initial mass flows rates.

4.5.4. DM thruster summary and conclusion

The DM thruster has proven ignition capabilities and, compared to previous thruster designs, reduced monopropellant time, before successful bipropellant ignition is possible, to be as small as 25 s. Again, this transition time is only limited by achieving the necessary injection temperature for autoignition and could be considerably reduced in a preheated configuration, as shown in the pulse mode tests.

Various bipropellant combustion firing tests of different durations have been conducted, with the maximum bipropellant interval lasting for 30 s. Near stationary external wall temperatures have been observed and were found, although afflicted with errors, below the maximum operational temperatures of the materials employed. The possibility for radiation cooling of the thruster in steady state operation could be validated. High combustion efficiencies in the order of 90-95 % were achieved in accordance with previous results.

Thrust measurements utilizing a dedicated, calibrated thrust stand have been shown to be able to resolve thrust plateaus of mono- and bipropellant thrust achieved by the DM thruster with sufficient small noise. Although flow separation occurred within the employed nozzle at ambient test conditions, measured thrust levels could be interpolated to vacuum conditions. Interpolated vacuum thrust was found in accordance to the target thrust level of 1 N.

Pulsing capability was investigated at high structure temperatures from previous testing. Pulses of durations as short as 2 s showed successful ignitions. Stable ignition plateaus have been achieved for pulse durations of 5 s at elevated structure temperatures. Transition times elapsed between the opening of the propellant valves and achieving stable combustion chamber pressure were found to be as short as ~1.64 s. However, this is only true for elevated structural temperatures such as in a preheated configuration or in a sequence of pulses in bi- or monopropellant mode.

68 successful ignitions, including pulse firings, have been performed using the DM thruster, with a total of t_{biprop} = 618 s of bipropellant operation and an accumulated total hydrogen peroxide mass flow of 1.85 kg. No damage to the thruster has been observed throughout the entire test period.

5.   Conclusion

The scope of this thesis was the development of a miniaturized high performance chemical bipropellant engine, operated with green propellants at a nominal thrust of 1 N. The thesis comprises of both experimental and theoretical work, with the latter guiding the experimental investigation and the design of a final, fully operational development model thruster.

The thesis was organized as follows: After an introduction to the topic of chemical onboard propulsion, the issue of green propulsion was motivated and discussed with respect to currently used, highly toxic, propellants based on hydrazine and its derivatives. Highly concentrated hydrogen peroxide was introduced as alternative propellant and the reduction of hazards was discussed by comparison based on data available in literature.

The first part of the thesis comprised of the investigation of hydrogen peroxide decomposition on both theoretical and experimental basis. A simulation of hydrogen peroxide decomposition within the catalyst with a focus on the impact of structural catalyst and decomposition chamber mass was presented. This simulation was used to guide the experimental design of both the catalysts and the decomposition chambers utilized and was able to explain decomposition effects such as radial inhomogeneous exhaust temperatures and catalyst behavior in case of mass flow overloading. Reducing length and thermal mass of the monolithic catalysts to improve transitional behavior was suggested on the bases of simulation results. These trends have been confirmed experimentally.

The experimental section included an exhaustive investigation of 39 different catalyst configurations, with a total of 121 catalysts. Two test campaigns were carried out and allowed the investigation of leading catalyst parameters such as catalyst type, catalyst length, channel geometry and density, as well as active material and washcoating on decomposition performance. A focus of both the experimental and theoretical work presented, was laid on the transient behavior of decomposition, which is identified as a key parameter in thruster design. Experimentally found results showed pressure to rise to 90 % of the stationary chamber pressure after hydrogen peroxide injection in the order of 350 ms to 500 ms. Shortest temperature start-up times found for reaching 500 °C after cold start were as small as 1.56 s. Lifetime tests of a 20 mm length monolith catalyst showed total accumulated hydrogen peroxide loads of 17.8 kg before tests were aborted due to structural damage to the catalyst.

The thrusters ability to autoignite with injected liquid fuels kerosene and ethanol was investigated both on theoretical and experimental bases. The experimental investigation utilizing a dedicated modular ignition chamber design allowing the identification of ignition thresholds regarding pre-ignition chamber pressure and temperature for different, miniaturized, combustion chamber volumes. A dedicated back-pressure device allowed for independent variation of combustion chamber pressure from propellant mass flow without changes to the combustion chamber geometry. Within this work, a large number of successful autoignitions where performed, using kerosene as fuel for a wide range of different injection temperatures and chamber pressures. This data allowed the deduction of a parametric model

for autoignition limits in accordance to applicable literature, guiding the design of successive thrusters featuring autoignition capabilities. In addition, the possibility of autoignition of ethanol in the decomposition products of highly concentrated hydrogen peroxide could be shown.

Theoretical investigations led the design of a steady state combustion chamber, featuring a newly designed swirl injector, a dedicated premixing chamber and flame stabilization by a backward facing step. Previously found autoignition limits could be confirmed for this modified setup and an increasing number of successful ignitions for ethanol were collected. Robust ignition behavior for a large range of mixture ratios for both propellant combinations was found for this thruster setup. An active cooling system was implemented to investigate steady state combustion performance. The test setup allowed the determination of combustion performance as a function of propellant mixture ratio for both hydrogen peroxide/kerosene and hydrogen peroxide/ethanol combinations. High combustion efficiencies above 90 % were found for both propellant configurations. The ability of pulsed thruster operation was shown using this thruster. Employment of a catalyst featuring reduced wall thickness and thus reduced thermal mass led to reduced cold start transition times of 1.36 s to achieve decomposition temperatures above 500 °C when employed in this thruster configuration.

The design of the final radiation cooled thruster was guided by a numerical simulation of the thermal loads of the combustion chamber and catalyst. The final thruster, manufactured out of Pt-20%Rh and high temperature steel Nimonic, was successfully tested and used to evaluate predictions from the simulation. The radiative cooling approach was validated in long duration bipropellant firing tests up to 30 s. Combustion efficiencies above 90 % of the ideally calculated values were achieved. Thrust measurements at ambient conditions performed with this thruster showed flow separation in the nozzle due to overexpansion, but allowed for an interpolation to vacuum thrust levels achievable. These thrust levels were interpolated to $F = 0.9$-1.1 N depending on combustion chamber pressure, complying with the envisioned design thrust level. Pulsing capability was investigated at high structural temperatures from previous testing. Pulses of durations as short as 2 s showed successful ignitions resulting in minimum impulse bits achieved in bipropellant mode below 1 N s. This final thruster was operated successfully over an accumulated bipropellant firing duration of 618 s and performed 68 successful transitions from mono- to bipropellant operation mode without damage.

Nomenclature

a	[m s^{-1}]	local speed of sound
$a*$	[m s^{-1}]	critical speed
a_M	[m]	catalyst channel sidewall
A	[m^2]	area
A^*	[m^2]	throat area
A_0	[s^{-1}]	pre-exponential factor
A_c	[m^2]	cross sectional area
A_d	[m^2]	droplet surface
A_e	[m^2]	nozzle exit area
A_{surf}	[m^2]	surface area
A_V	[-]	absorption
$c*$	[m s^{-1}]	characteristic velocity
C_D	[-]	drag coefficient
C_F	[-]	thrust coefficient
c_p	[J kg^{-1} K^{-1}]	specific heat capacity at constant pressure
c_v	[J kg^{-1} K^{-1}]	specific heat capacity at constant volume
CBL	[kg^{-3} s^{-1} m^{-2}]	catalyst bed loading
d_{cap}	[m]	fuel injection capillary inner diameter
d_{CC}	[m]	thrust chamber inner diameter
d_d	[m]	droplet diameter
d_M	[m]	catalyst diameter
d_t	[m]	throat diameter
d_w	[m]	monolith minimum wall thickness
D	[m]	diameter
$\hat{D}$	[m^2 s^{-1}]	mass diffusion coefficient
Da	[m]	Damköhler number
D_H	[m]	hydraulic diameter
e	[J kg^{-1}]	internal energy per unit mass
E_a	[J mol^{-1}]	energy of activation
F	[N]	force
$F^{measured}$	[N]	experimentally measured thrust
F_{vac}	[N]	vacuum thrust
f	[-]	coefficient of friction
f_V	[-]	soot volume fraction

g_0	[m s^{-2}]	standard acceleration of gravity
G_z	[kg m s^{-2}]	axial flux of axial momentum
G_Φ	[kg m^2 s^{-2}]	axial flux of tangential momentum
h	[J kg^{-1}]	enthalpy per unit mass
h_g	[W m^{-2} K^{-1}]	hot side convective heat transfer coefficient
h_{inj}	[m]	injection channel height
h_{step}	[m]	backward facing step height
h^{vap}	[J kg^{-1}]	specific enthalpy of vaporization
H	[J]	enthalpy
I	[W m^{-2}]	radiation intensity
I_0	[W m^{-2}]	initial radiation intensity
I_{sp}	[s]	specific impulse
I_{sp}^V	[s]	specific impulse density
j_{lg}	[kg m^{-2} s^{-1}]	mass flux density
k	[s^{-1}]	rate of reaction
l	[m]	distance
L	[m]	length
L^*	[m]	characteristic chamber length
L_{CC}	[m]	thrust chamber length
L_M	[m]	catalyst length
L_{premix}	[m]	premixing chamber length
L_r	[m]	reattachment length
m	[kg]	mass
$\dot{m}$	[kg s^{-1}]	mass flow
m_0	[kg]	spacecraft dry mass
m_d	[kg]	droplet mass
$\dot{m}_{fu}$	[kg s^{-1}]	fuel mass flow rate
$\dot{m}_{ox}$	[kg s^{-1}]	oxidizer mass flow rate
$\dot{m}_{vap}$	[kg s^{-1}]	evaporation mass flow rate
M	[-]	local Mach number
M^*	[-]	critical Mach number at throat
M_t	[-]	Mach number at throat
M_X	[g mol^{-1}]	molar mass of X
MIP	[N s]	minimum impulse bit
n	[mol]	amount of substance
Nu	[-]	Nusselt number
O/F	[-]	oxidizer/fuel mixture ratio

p	[Pa]	pressure
p^*	[Pa]	critical pressure
p_a	[Pa]	ambient pressure
p_{back}	[Pa]	backpressure
p_c	[Pa]	decomposition chamber pressure
p_{CC}	[Pa]	combustion chamber pressure
p_{feed}	[Pa]	feedline pressure
p_{sep}	[Pa]	flow separation pressure
p_{Tank}	[Pa]	tank pressure
p_{vap}	[Pa]	vapor pressure
P	[W]	power
P_S	[W]	shear power
Pe	[-]	Péclet number
Pr	[-]	Prandtl number
$\dot{q}$	[W m^{-2}]	heat flux density
Δq	[J mol^{-1}]	heat release
Q	[J]	heat
$\dot{Q}$	[W]	heat flux
Q_{Loss}	[W]	energy loss to walls
Q_{Sink}	[W]	energy flux used to increase enthalpy
Q_{Source}	[W]	energy flux released by decomposition
r	[m]	radius
$\tilde{r}$	[-]	temperature recovery factor
r_c	[m]	nozzle curvature radius
r_{cap}	[m]	radius of fuel injection capillary
r_{curv}	[m]	throat curvature radius
r_{CC}	[m]	combustion chamber radius
r_d	[m]	droplet radius
r_i	[m]	radius of swirl injector center body
r_{inj}	[m]	premixing chamber radius
r_t	[m]	throat radius
R	[J K^{-1} kg^{-1}]	specific real gas constant
$\bar{R}$	[J K^{-1} mol^{-1}]	universal gas constant
R_M	[m]	catalyst radius
Re	[-]	Reynolds number
s	[J K^{-1} m^{-3}]	entropy per unit mass

$s_{cladding}$	[m]	decomposition chamber wall thickness
s_{eq}	[m]	equivalent layer thickness
s_{gap}	[m]	gap between catalyst and decomposition chamber
S	[-]	swirl number
S_t	[-]	Stanton number
S_Φ	[W m^{-3}]	energy source per volume
t	[s]	time
t_{500}	[s]	transition time to $T_{cat} > 500$ °C
T	[K]	temperature
T^{boil}	[K]	single species boiling temperature
T_{cat}	[K]	decomposition temperature
T_{CC}	[K]	experimental combustion temperature
T_{dec}	[K]	adiabatic decomposition temperature
T_{dew}	[K]	dew point curve
T_{inj}	[K]	injection temperature
T_w	[K]	wall temperature
T_S	[K]	droplet surface temperature
$\vec{u}$	[m s^{-1}]	flow velocity
u	[m s^{-1}]	flow velocity, z-component
u_d	[m s^{-1}]	droplet velocity
u_e	[m s^{-1}]	nozzle exit velocity
U	[m s^{-1}]	flow velocity, potential flow
v	[m^3 kg^{-1}]	volume per unit mass
V	[m^3]	volume
V_{CC}	[m^3]	thrust chamber volume
w	[m s^{-1}]	tangential velocity component
w	[J kg^{-1}]	work done per unit mass
$\vec{W}$	[s^{-1}]	vorticity
x^{H_2O}	[-]	fraction of H_2O evaporated
$x^{H_2O_2}$	[-]	fraction of H_2O_2 evaporated
$x_{H_2O_2}$	[-]	H_2O_2 mass concentration

Greek symbols:

α	[m^{-1}]	absorption coefficient
α	[W m^{-2} K^{-1}]	convective heat transfer coefficient
β	[-]	swirl decay factor
β_m	[-]	evaporation coefficient
δ^*	[m]	displacement thickness
δ_r	[m]	velocity boundary layer thickness
Δ_r	[m]	temperature thickness of real flow
Δs	[m]	length increment
Δv	[m s^{-1}]	velocity increment
ε	[-]	nozzle area expansion ratio
ε_g	[-]	gas emissivity
ε_r	[-]	soot emissivity
ε_w	[-]	wall emissivity
Φ	[m]	energy thickness
Γ	[m^2 s^{-1}]	circulation
Γ_Φ	[kg m^{-1} s^{-1}]	diffusion constant
γ	[-]	specific heat ratio
η_{c*}	[-]	characteristic velocity efficiency
η_{C_F}	[-]	thrust coefficient efficiency
λ	[W m^{-1} K^{-1}]	thermal conductivity
λ	[m]	wavelength
μ	[N s m^{-2}]	dynamic viscosity
ν	[m^2 s^{-1}]	kinematic viscosity
Θ	[m]	momentum flux thickness
ρ	[kg m^{-3}]	density
σ	[N m^{-1}]	surface tension
σ_{SB}	[W m^{-2} K^{-4}]	Stefan-Boltzmann constant
τ_i	[s]	ignition delay time
τ_{hc}	[s]	mixing time
τ_{sl}	[s]	shear layer residence time
τ_r	[s]	residence time
ω	[rad s^{-1}]	angular velocity
$\bar{\omega}$	[-]	exponent of temperature dependency of viscosity
ζ	[-]	boundary layer shape factor

Subscripts and Abbreviations

0	stagnation condition
amb	ambient
aw	adiabatic wall
ax	axial direction
CC	combustion chamber
$conv$	convective
CS	control surface
CV	control volume
DM	Development model
EBB	Elegant bread board
f	free stream
fu	fuel
g	gas
H_2O	water
H_2O_2	hydrogen peroxide
$init$	initial
inj	injection
l	liquid phase
LC	lethal concentration
LD	lethal dose
LOX	liquid oxygen
N_2	nitrogen
O_2	oxygen
ox	oxidizer
p	propellant
$premix$	premixing chamber
Pt	platinum
r	real flow
rad	radiative
Rh	rhodium
S	sublayer
SiC	silicon carbide
$step$	backward facing step
$subcrit$	subcritical
$surf$	surface
t	throat
th	theoretical
vap	vapor phase
w	wall
$wt.\%$	weight percentage

List of tables

List of figures

References

1   Leyva, I.A.: Spacecraft Sybsystems I – Propulsion, in: Wertz, J.R., Everett, D.F., Puschell, J.J.: Space Mission Engineering: The New SMAD, Microcosm Inc., 2011.

2   Starin, S.R.: Spacecraft Subsystem II – Control Systems, in: Wertz, James, R., Everett, David F., Puschell, Jeffery J.: Space Mission Engineering: The New SMAD, Microcosm Inc., 2011.

3   Sutton, G.P., Biblarz, O.: Rocket Propulsion Elements, 8th Edition, Wiley, Hoboken, New Jersey, 2010.

4   Hill, P., Peterson, C.: Mechanics and Thermodynamics of Propulsion, 2nd Ed. Addison-Wesely Publishing Company, 1992.

5   Caisso, P., Souchier, A., Rothmund, C., Alliot, P., Bonhiomme, C., Zimmer, W., Parsley, R., Neill, T., Forde, S., Starke, R., Wang, W., Takahashi, M., Atsumi, M., Valentian, D.: A liquid propulsion panorama, Acta Astronautica, Vol. 65, 2009, pp. 1723-1737.

6   Scharfe, D.B., Ketsdever, A.D.: A Review of High Thrust, High Delta-V Options for Microsatellite Missions, 45th AIAA/ASME/SAE/ASEE Joint Propulsion Conference & Exhibit, Denver, CO, AIAA 2009-4824, 2009.

7   Mueller, J., Hofer, R., Parker, M., Ziemer, J.: Survey of Propulsion Options for Cubesats, 57th JANNAF Propulsion Meeting, Colorado Springs, CO, JANNAF-1425, 2010.

8   Woschnak, A.: Market Analysis: Low Thrust Bipropellant Thruster based on Green Propellants, ESA Technical Report, 22277/09/NL/RA, TN3, 2009.

9   Haeseler, D., Bombelli, V., Vuillermoz, P., Lo, R., Marée, T., Caramelli, F.: Green propellant propulsion concepts for space transportation and technology development needs, 2nd International Conference on Green Propellants for Space Propulsion, ESA SP-557, Italy, 2004.

10 Seller, J.J., Paul, M., Sweeting, M.: Investigation Into Cost-Effective Propulsion System Options for Small Satellites, Journal of Reducing Space Mission Costs, Vol. 1, No. 1, 1998, pp. 53-72.

11 German, B.J., Branscome, E.C., Frits, A.P., Yiakas, N.C., Mavris, D.: An evaluation of green propellants for an ICBM post-boost propulsion system, AIAA 2000 Missile Sciences Conference, Monterey, CA, 2000.

12   Grayson, G.D.: Propellant Trade Study for a Crew Space Vehicle, 41th AIAA/ASME/SAE/ASEE Joint Propulsion Conference & Exhibit, Tucson, AZ, AIAA 2005-4313, 2005.

13 Scharlemann, C., Winborg, N., Roberts, G., Kappenstein, C., Musker, A., Russor, A., Haidn, O., Walzer, E., Muszynski, M., Delbianco, N., Wolejsza Z.: General Assessment of Green Propellants, Test Readiness Report, Grasp D2.1, 2009.

14 Scharlemann, C.: Green Propellants: Global Assessment of Suitability and Applicability, European Conference for Aerospace Sciences (EUCASS), Versailles, France, 2009.

15 Caramelli, F.: Green propulsion activities overview, Space Propulsion 2008 – Green Propulsion Workshop, Crete, May 2008.

16 Bombelli, V., Ford, M., Marée, T.: Road Map for Demonstration of the Use of Reduced-Hazard Mono-Propellants for Spacecrafts, 2nd International Conference on Green Propellants for Space Propulsion, ESA SP-557, Italy, 2004.

17 Frota, O., Mellor, B., Ford, M.: Proposed Selection Criteria for Next Generation Liquid Propellants, 2nd International Conference on Green Propellants for Space Propulsion, ESA SP-557, Italy, 2004.

18 Wernimont, E.J.: Monopropellant Hydrogen Peroxide Rocket Systems: Optimum for Small Scale, AIAA/ASME/SAE/ASEE Joint Propulsion Conference and Exhibit, Sacramento, CA, AIAA-2006-5235

19 Bombelli, V., Simon, D., Marée, T.: Economic Benefits of the Use of Non-Toxic Mono-Propellants for Spacecraft Applications, 39th Joint Propulsion Conference, Huntsville, AL, AIAA 2003-4783, 2003.

20 Morgan, O.M. ,Meinhardt, D.S.: Monopropellant Selection Criteria – Hydrazine and Other Options, 35th AIAA Joint Propulsion Conference and Exhibit, Los Angeles, CA, AIAA-99-2595, 1999.

21   European Centre for Ecotoxicology and Toxicology of Chemicals: Hydrogen Peroxide OEL Criteria Document SR 10, Brussels, 1996.

22   Chemical Evaluation and Research Institute (CERI): Hazard Assessment Report, Hydrazine, Japan, 2007.

23   European Commission/ European Chemicals Bureau: IUCLID Dataset Hydrazine, 2000

24   Ponzo, J.: Small Envelope, High Flux 90% Hydrogen Peroxide Catalyst Bed, 39th AIAA/ASME/SAE/ASEE Joint Propulsion Conference and Exhibit, Huntsville, AL, AIAA 2003-4622, 2003.

25   Chemical and Material Science Department/Rocketdyne: Hydrogen Peroxide Handbook, Technical Report AFRPL-TR-67-144, 1967.

26   Wiswell, R.L.: X-15 propulsion system, 33rd AIAA/ASME/SAE/ASEE Joint Propulsion Conference and Exhibit, Seattle, WA, AIAA 1997-2682, 1997.

27   Cervone A., Torre L., d'Agostino L., Musker A., Roberts G., Bramanti C., Saccoccia G.: Development of Hydrogen Peroxide Monopropellant Rockets, 42nd AIAA/ASME/SAE/ASEE Joint Propulsion Conference and Exhibit, Sacramento, CA, 2006.

28   Sisco, J.C.: Autoignition of Kerosene by Decomposed Hydrogen Peroxide in a Dump Combustor Configuration, Master Thesis, Purdue University, 2003.

29   Davis, N.S., Keefe, J.H.: Concentrated Hydrogen Peroxide as a Propellant, Industrial & Engineering Chemistry, Vol. 48, Iss. 4, 1956, pp. 745-748.

30   McCormick, J.: Hydrogen Peroxide Rocket Manual, FMC Corporation, 1965.

31   An, S., Jo, S., Wee, J., Yoon, H., Kwon, S.: Preliminary flight test of hydrogen peroxide retro-propulsive module, Acta Astronautica, Vol. 67, 2010, pp. 605-612.

32   Cervone A., Torre L., d'Agostino L., Musker A., Roberts G., Bramanti C., Saccoccia G.: Development of Hydrogen Peroxide Monopropellant Rockets, 42nd AIAA/ASME/SAE/ASEE Joint Propulsion Conference and Exhibit, Sacramento, CA, 2006

33   Scharlemann, C.: Experimental verification of green propellant candidates – an overview of GRASP activities, 4th European Conference for Aerospace Sciences (EUCASS), Saint Petersburg, Russia, 2011.

34   Haag, G.S., Sweeting, M.N., Richardson, G.: Low Cost Propulsion Development for Small Satellites at The Surrey Space Centre, 13th Annual AIAA/USU Conference on Small Satellites, Logan, UT, 1999.

35   Lim, H., An, S., Kwon, S., Rang, S.: Hydrogen Peroxide Gas Generator with Dual Catalytic Beds for Nonpreheating Startup, Journal of Propulsion and Power, Vol. 23, No. 5, 2007, 1147-1150.

36   An, S., Brahmi, R., Kappenstein, C., Kwon, S.: Transient Behavior of H_2O_2 Thruster: Effect of Injector Type and Ullage Volume, Journal of Propulsion and Power, Vol. 25, No. 6, 2009, pp. 1357-1360.

37   Barley, S., Palmer, P.L., Coxhill, I.: Evaluating the Miniaturization of a Monopropellant Thruster, 42nd AIAA/ASME/SAE/ASEE Joint Propulsion Conference and Exhibit, Sacramento, CA, AIAA 2006-4549, 2006.

38   Ventura, M.: Long Term Storability of Hydrogen Peroxide, 41st AIAA/ASME/SAE/ASEE Joint Propulsion Conference and Exhibi , Tucson, AZ, AIAA-2005-4551, 2005.

39   Shanley, E.S., Greenspan, F.P.: Highly concentrated Hydrogen Peroxide Physical and Chemical Properties, Industrial and Engineering Chemistry, Vol. 39, Iss. 12, 1947, pp. 1536-1543.

40   Whitehead, J.C., Dittman, M.D., Ledebuhr, A.G.: Progress Toward Hydrogen Peroxide Micropropulsion, 13th Annual AIAA/USU Conference on Small Satellites, Logan, UT, 1999.

41   Wernimont, E., Ventura, M., Garboden G., Mullens, P.: Past and Present Uses of Rocket Grade Hydrogen Peroxide, 2nd International Hydrogen Peroxide Propulsion Conference, Purdue University, IN, 1999.

42   Musker, A.J., Rusek, J.J., KAppenstein, C., Roberts, G.T.: Hydrogen Peroxide – From Bridesmaid to Bride, 3rd ESA International Conference on Green Propellants for Space Propulsion, Poitiers, F, Spt., 2006.

43 Ventura, M., Wernimont, E., Heister, S., Yuan, S.: Rocket Grade Hydrogen Peroxide (RGHP) for use in Propulsion and Power Devices – Historical Discussion of Hazards, 43th AIAA/ASME/SAE/ASEE Joint Propulsion Conference and Exhibit, Cincinnati, OH, 2007.

44 Whitehead, J.C.: Hydrogen Peroxide Storage in Small Sealed Tanks, 2nd International Hydrogen Peroxide Propulsion Conference, West Lafayett, IN, 1999.

45 Campolo, M., Andreoli, M., Soldati, A.: Computing flow, combustion, heat transfer and thrust in a micro-rocket via hierarchical problem decomposition, Microfluid Nanofluid, Vol. 7, No. 1, pp. 57-73, 2009.

46 Sisco, J.C., Austin, B.L., Mok, J.S., Anderson, W.E.: Autoignition of Kerosene by decomposed Hydrogen Peroxide in a dump combustor configuration, 39th AIAA/ASME/SAE/ASEE Joint Propulsion Conference and Exhibit, Huntsville, Alabama, 2003.

47 Sisco, J.C., Austin, B.L., Mok, J.S., Anderson, W.E.: Ignition studies of hydrogen peroxide and kerosene fuel, 41st Aerospace Sciences Meeting and Exhibit, Reno, Nevada, AIAA 2003-831, 2003.

48 Sisco, J.C., Austin, B.L., Mok, J.S., Anderson, W.E.: Autoignition of Kerosene by Decomposed Hydrogen Peroxide in a Dump-Combustor Configuration, Journal of Propulsion and Power, Vol. 21, No. 3, 2005, pp. 450-459.

49 Wernimont, E. J., Durant, D.: Development of a 250lbfv Kerosene – 90% Hydrogen Peroxide Thruster, 40th AIAA/ASME/SAE/ASEE Joint Propulsion Conference & Exhibit, Fort Lauderdale, FL, AIAA 2004-4148, 2004.

50 Lederbuhr, A.G., Antelman, D.R., Dobie, D.W., Gorman, T.S., Jones, M.S., Kordas, J.F., McMahon, D.H., Ng, L.C., Nielsen, D.P., Ormsby, A.E., Pittenger, L.C., Robinson, J.A., Skulina, K.M., Taylor, W.G., Urone, D.A., Wilson, B.A.: Recent Development in Hydrogen Peroxide Pumped Propulsion, 2nd Missile Defense Conference and Exhibit, Washington, DC, 2004.

51 Musker, A.J., Roberts, G.T., Ford, S., Reakes, E., Westbury, T.: Auto-Ignition of Fuels Using Highly Stabilised Hydrogen Peroxide, 41st AIAA/ASME/SAE/ASEE Joint Propulsion Conference & Exhibit, Tucson, AZ, AIAA 2005-4454, 2005.

52 Cong, Y., Zhang, T., Li, T., Sun, J., Wang, X., Ma, L., Liang, D., Lin, L.: Propulsive Performance of a Hypergolic H_2O_2/Kerosene Bipropellant, Journal of Propulsion and Power, Vol. 20, Iss. 1, 2004, pp. 83-86.

53 Baker, A.M., Curiel, A., Schaffner, J., Sweeting, M.: "You can get there from here": Advanced low cost propulsion concepts for small satellites beyond LEO, Acta Astroonautica, Vol. 57, 2005, pp. 288-301.

54 Hitt, D.L., Zakrazwski, C.M., Thomas, M.A.: MEMS-based satellite micropropulsion via catalyzed hydrogen peroxide decomposition, Smart Materials and Structures, Vol. 10, 2001, pp. 1163-1175.

55 Zhou X., Hitt D.L.: Modeling of Catalyzed Hydrogen Peroxide Decomposition in Slender Microchannels with Arrhenius Kinetics, 40th AIAA/ASME/SAE/ASEE Joint Propulsion Conference and Exhibit, Florida, 2004.

56 Takahashi, K., Ikuta, T., Dan, Y., Nagayama, K., Kishida, M.: Catalytic Porous Microchannel for Hydrogen Peroxide MEMS Thruster, Proceedings of the 23rd Sensor Symposium, Kagawa, 2006, pp. 513-516.

57 London, A.P., Ayón, A.A., Epstein, A.H., Spearing, S.M., Harrison, T., Peles, Y., Kerrebrock, J.L.: Microfabrication of a high pressure bipropellant rocket engine, Sensors and Actuators A, Vol. 92, 2001, pp. 351-357.

58 Alexeenko, A., A., Fedosov, D.A., Gimeshein, S.F., Levin, D.A., Collins, R.J.: Transient Heat Transfer and Gas Flow in a MEMS-Based Thrsuter, Journal of Microelectromechanical Systems, Vol. 15, Iss. 1, 2006, pp. 181-194.

59 Alexeenko, A.A., Levin, D.A., Fedosov, D.A., Gimeshein, S.F., Collins, R.J.: Performance Analysis of Microthrusters Based on Coupled Thermal-Fluid Modeling and Simulation, Journal of Propulsion and Power, Vol. 21, Iss. 1, 2005, pp. 95-101.

60 Janson, S.W., Helvajian, H., Hansen, W.W., Lodmell, J.: Microthrusters for Nanosatellites, 2nd International Conference on Integrated Micro Nanotechnology for Space Applications, Pasadena, CA, 1999.

61   Cheah, K.H., Chin, J.K.: Performance improvement on MEMS micropropulsion system through a novel two-depth micronozzle design, Acta Astronautica, Vol. 69, 2011, pp. 59-70.

62   Wernimont, E.J.: Hydrogen Peroxide Catalyst Beds: Lighter and Better Than Liquid Injectors, 41st AIAA/ASMA/SAE/ASEE Joint Propulsion Conference & exhibit, Tucson, AZ, 10-13 July 2005, AIAA-2005-4455.

63   Schiebl, M., Krejci D., Woschnak A., Winter F., Lang M., Scharlemann C.: Modeling and Experimental Verification of Auto-Ignition Processes for a Green Bi-Propellant Thruster, 61st International Astronautical Congress, CZ, 2010.

64   Woschnak, A., Krejci, D., Schiebl, M., Scharlemann, C.: Development of a Green Bi-Propellant Hydrogen Peroxide Thruster for Attitude Control on Satellites, 4th European Conference for Aerospace Sciences (EUCASS), Saint Petersburg, Russia, 2011.

65   Krejci, D., Woschnak, A., Scharlemann, C., Ponweiser, K.: Hydrogen Peroxide Decomposition for Micro Propulsion: Simulation and Experimental Verification, 47th AIAA/ASME/SAE/ASEE Joint Propulsion Conference and Exhibit, San Diego, CA, 2011.

66   Sadov, V.: HP-Based Green Rocket Propellants, International conference on Green Propellants for Space Propulsion, Noordwijk, Netherlands, 2001

67   Amariei, D., Amrousse, R., Batonneau, Y., Brahmi, R., Kappenstein, C., Cartoixa, B.: Monolithic catalysts for the decomposition of energetic compounds, Studies in Surface Sciences and Catalysis, Vol. 175, 2010, pp. 35-42.

68   Bouajila, W., Riccius, J.: Suggestion for a unified performance assessment criterion of spacecraft propellants, European Conference for Aerospace Sciences (EUCASS), Saint Petersburg, Russia, 2011.

69   Satterfield, C.N., Ceccotti, P.J., Feldbrugge, A.H.R.: Ignition Limits of Hydrogen Peroxide Vapor, Industrial and Engineering Chemistry, Vol. 47, Iss. 5, 1955, pp. 1040-1043.

70   Back, L.H., Maisser, P.F., Gier, H.L.: Convective heat transfer in a convergent-divergent nozzle, International Journal of Heat and Mass Transfer, Vol. 7, 1964, pp. 549-568.

71   Foley, W.T., Giguère, P.A.: Hydrogen Peroxide and its Analogues II. Phase Equilibria in the System D_2O-Hydrogen Peroxide-Water, Canadian Journal of Chemistry, Vol 29, Iss. 2, 1951, pp. 123-132.

72   Foley, W.T., Giguère, P.A.: Hydrogen Peroxide and its Analogues IV. Some Thermal Properties of Hydrogen Peroxide, Canadian Journal of Chemistry, Vol 29, Iss. 10, 1951, pp. 895-903.

73   Giguère, P.A., Secco, E. A.: Hydrogen Peroxide and its Analogues V. Phase Equilibria in the System D_2O-D_2O_2, Canadian Journal of Chemistry, Vol 32, Iss. 5, 1954, pp. 550-556.

74   Wernimont, E.J., Ventura, M.C., Grubelich, M.C., Vaughn, M.R., Escapule, W.R.: Low Temperature Operation of Hydrogen Peroxide Gas Generators: Verification Testing & Possible Applications, 7th International Energy Conversion Engineering Conference, Denver, CO, AIAA2009-4617, 2009.

75   Schumb, W. C., Satterfield, C. N., Wentworth, R. L.: Hydrogen Peroxide, Part two, Armed Services Technical Information Agency, AD 22243, 1953.

76   Scatchard, G., Kavanagh, G.M., Ticknor, L.B.: Vapor-Liquid Equilibrium. VIII. Hydrogen Peroxide- Water Mixtures, Journal of the American Chemical Society, Vol. 74, Is. 15, 1052, pp. 3715-3720.

77   An, S., Brahmi, R., Kappenstein, C., Jeongsub, L., Kwon, S.: Pulse Response Times of Hydrogen Peroxide Monopropellant Thrusters, 45th AIAA/ASME/SAE/ASEE Joint Propulsion Conference and Exhibit, Denver, Colorado, AIAA 2009-5230, 2009.

78   Torre, L., Pasini, A., Romeo, L., d'Agostino, L.: Firing Performance of Advanced Hydrogen Peroxide Catalytic Beds in a Monopropellant Thruster Prototype, 44th AIAA/ASME/SAE/ASEE Joint Propulsion Conference and Exhibit, Hartford, CT, AIAA 2008-4937, 2008.

79   Humble, R.W., Henry, G.N., Larson, W. J.: Space propulsion analysis and design, McGraw-Hill, 1995.

80   Richardson, J.T., Remue, D., Hung, J.-K.: Properties of ceramic foam catalyst supports: mass and heat transfer, Applied Catalysis A: General, Vol. 250, pp. 319-329, 2003.

81   Hegedus, L.L.: Effects of channel geometry on the performance of catalytic monoliths, Div. Petr. Chem., American Chemical Society, 1973.

82   Eloirdi, R., Rossignol, S., Kappenstein, C., Duprez, D., Pillet, N.: Design and Use of a Batch Reactor for Catalytic Decomposition of Propellants, Journal of Propulsion and Power, Vol. 19, No. 2, 2003, pp. 213-219.

83   Pirault-Roy L., Kappenstein C., Guérin M., Eloirdi R., Pillet N.: Hydrogen Peroxide Decomposition on Various Supported Catalysts Effect of Stabilizers, Journal of Propulsion and Power, Vol. 18, No.6, Nov-Dec 2002, pp. 1235-1241.

84   Bramanti, C., Cervone, A., Romeo, L., Torre, L., d'Agostino, L., Musker, A.J., Saccoccia, G.: Experimental Characterization of Advanced Materials for the Catalytic Decomposition of Hydrogen Peroxide, 42th AIAA/ASME/SAE/ASEE Joint Propulsion Conference and Exhibit, Sacramento, CA, 2006.

85   Ahuja L. D., Jareshwer D., Nagpal K.C.: Decomposition of Hydrogen Peroxide on Manganese Oxide Surfaces, Adv. in Catal. Sci. & Tech., Prasada Rao, Wiley, New Dehli 563, 1985.

86   Hasan, M.A., Zaki, M. I., Pasupulety, L., Kumari, K.: Promotion of the hydrogen peroxide decomposition activity of manganese oxide catalysts, Applied Catalysis A: General, Vol. 181, pp. 171-179, 1999.

87   Kappenstein C., Pirault-Roy L., Guerin M., Wahdan T., Ali A.A., Al-Sagheer F.A., Zaki M.I.: Monopropellant decomposition catalysts – V. Thermal decomposition and reduction of permanganates as models for the preparation of supported MnO_x catalysts, Applied Catalysis A: General, Vol. 234, No. 1, 2002, pp. 145-153.

88   Kappenstein C., Brahmi, R., Amariei, D., Batonneau, Y., Rossignol, S., Joulin, J.P.: Catalytic decomposition of energetic compounds – Influence of catalyst shape and ceramic substrate, 42th AIAA/ASME/SAE/ASEE Joint Propulsion Conference and Exhibit, Sacramento, CA, 2006.

89   Decker, G.: Structural Design of a miniaturized Bi-Propellant Thruster for the Position Control of Satellites, Master Thesis, Vienna University of Technology, 2011.

90   Pirault-Roy, L., Kappenstein, C., Guérin, M., Eloirdi, R., Pillet, N.: Hydrogen Peroxide Decomposition on Various Supported Catalysts Effect of Stabilizers, Journal of Propulsion and Power, Vol. 18, No.6, Nov-Dec 2002, pp. 1235-1241.

91   Davis, D.D., Dee, L.A., Hornung, S.D., McClure, M.B., Rathgeber, K.A.: Fire, Explosion, Compatibility and Safety Hazards of Hydrogen Peroxide, NASA/TM-2004-213151.

92   Sanford, G., McBride B.J.: Computer program for calculation of complex chemical equilibrium compositions, rocket performance, incident and reflected shocks and Chapman-Jouget detonations, NASA SP-273, 1971.

93   Miotti P., Scharlemann C., Seco F., Guraya C., Schiebl M., Keding M., Tajmar M.: TPF-MRE Final Report WP4100/WP4200/WP4300, Final Report, Seibersdorf, 2006.

94   Williams, F.A.: Combustion Theory, 2nd edition, Perseus BooksPublishing, Reading, Massachusetts, 1985.

95   Do, S.-H., Batchelor, B., Lee, H.-K., Kong, S.-H.: Hydrogen peroxide decomposition on manganese oxide (pyrolusite): Kinetics, intermediates, and mechanism, Chemosphere, Vol 75, 2009, pp. 8-12.

96   Corpening J. H., Heister S. D., Anderson W. E., Austin B. J.: A Model for Thermal Decompostion of Hydrogen Peroxide, 40th AIAA/ASME/SAE/ASEE Joint Propulsion Conference and Exhibit, Florida, 2004.

97   Baldridge, J., Villegas, Y.: Compatibility Studies of Hydrogen Peroxide and a New Hypergolic Fuel Blend, Technical Report, Marshall Space Flight Center, 2002.

98   Albers, R.E., Houterman, M., Verguns, T., Grolman, E., Moulijn, J.: Novel Monolithic Stirred Reactor, AIChE Journal, Vol. 44, No. 11, Nov 1998.

99   Ahuja, L. D., Jareshwer, D., Nagpal, K.C.: Decomposition of Hydrogen Peroxide on Manganese Oxide Surfaces, Adv. in Catal. Sci. & Tech., Prasada Rao, Wiley, New Dehli 563, 1985.

100 Kreutzer, M.T., Kapteijn, F., Moulijn, J.A., Heiszwolf, J.J.: Multiphase monolith reactors: Chemical reaction engineering of segmented flow in microchannels, Chemical Engineering Science 60, pp. 5895-5916, 2005.

101 Chung, P.M.-Y., Kawaji, M.: The effect of channel diameter on adiabatic two-phase flow characteristics in microchannels, International Journal of Multiphase Flow, Vol. 30, 2004, pp. 735-761.

102 Baehr, H.D., Stephan, K.: Wärme- und Stoffübertragung, Springer, Berlin, 2008.

103 Shao, N., Gavriilidis, A., Angeli, P.: Flow regimes for adiabatic gas-liquid flow in microchannels, Chemical Engineering Science 64, 2009, pp. 2749-2761.

104 Xu, J., Yi, F., Jiwen, C.: Transient flow patterns and bubble slug lengths in parallel microchannels with oxygen gas bubbles produced by catalytic reactions, International Journal of Heat and Mass Transfer 50, 2007, pp. 857-871.

105 Kind, M: Flow Boiling – An Introduction, in: VDI-Heat Atlas, Chap. H3, Springer Verlag, Berlin, pp. 793-795, 2010.

106 Krejci, D., Woschnak, A., Scharlemann, C.: Investigation of the Decomposition Chamber, Technical Report, TN7-ESA-22277/09/NL/RA, GSTP-4.

107 Woschnak, A., Krejci, D., Scharlemann, C.: Investigation of Catalytic Decomposition of Hydrogen Peroxide for Miniatureized Chemical Thrusters, Space Propulsion Conference 2010, San Sebastian, Spain, 2010.

108 National Institute of Standards and Technology: NIST Chemistry WebBook Standard Reference Database 69, http://webbook.nist.gov/chemistry/, 2008 (last accessed on 9.10.2009).

109 Padankar, S.V.: Numerical heat transfer and fluid flow, Hemisphere Publishing Corp. 1980.

110 Hewitt, G.F.: Boiling, in: Rohsenow Warren M., Hartnett James P., Cho Young I:: Handbook of Heat Transfer, 3rd Ed. McGraw-Hill, 1998, Ch. 15.

111 Grohmann, S.: Measurement and modeling of single-phase and flow-boiling heat transfer in microtubes, International Journal of Heat and Mass Transfer, Vol. 48, pp. 4073-4089, 2005.

112 Ventura, M., Wernimont, E.: Advancements in High Concentration Hydrogen Peroxide Catalyst Beds, AIAA-01-3250, 37th AIAA/ASME/SAE/ASEE Joint Propulsion Conference, Salt Lake City, Utah, 2001

113 Satterfield, C.N., Audibert, F.P.: Nucleate and film boiling in the catalytic decomposition of hydrogen peroxide, Ind. Eng. Chem. Fundamentals, 1963, pp.200-202.

114 Peng, Y., Richardson, J.T.: Properties of ceramic foam catalyst supports: one-dimensional and two-dimensional heat transfer correlations, Applied Catalysis A: General, Vol. 266, pp. 235-244, 2004.

115 Huzel, D.K., Huang, D.H.: Modern Engineering for Design of Liquid-Propellant Rocket Engines, Progress in Astronautics and Aeronautics, Vol. 147, 1992.

116 Marble, F. E.: Spacecraft Propulsion, Space Technology, Vol. 3, Jet Propulsion Laboratory, 20110008683, 1964.

117 Ju, Y., Maruta, K.: Microscale combustion: Technology development and fundamental research, Progress in Energy and Combustion Science, Vol. 36, Iss. 6, 2011, pp. 669-715.

118 Edwards, T.: Liquid Fuels and Propellants for Aerospace Propulsion: 1903-2003, Journal of Propulsion and Power, Vol. 19, No. 6, 2003, pp. 1089-1106.

119 Edwards, T., Maurice, L.Q.: Surrogate Mixtures to Represent Complex Aviation and Rocket Fuels, Journal of Propulsion and Power, Vol. 17, No. 2, 2001, pp. 461-466.

120 Shepherd, J.E., Nuyt, C.D., Lee, J.J.: Flash Point and Chemical Composition of Aviation Kerosene (Jet A), Explosion Dynamics Laboratory Report FM99-4, 2000.

121 Kazakov, A., Conley, J., Dryer, F.L.: Detailed modeling of an isolated, ethanol droplet combustion under microgravity conditions, Combustion and Flame, Vol. 134, 2003, pp. 301-314.

122 Rakopoulos, D.C., Rakopoulos, C.D., Papagiannakis, R.G., Kyritsis, D.C.: Combustion heat release analysis of ethanol of n-butanol diesel fuel blends in heavy-duty DI diesel engine, Fuel, Vol. 90, 2011, pp. 1855-1867.

123 Li, D.-g., Zhen, H., Xingcai, L., Wu-gao, Z., Jiang-guang, Y.: Physico-chemical properties of ethanol-diesel blend fuel and its effet on performance and emissions of diesel engines, Renewable Energy, Vol. 30, 2005, pp. 967-976.

124 Seiser, R., Humer, S., Seshadri, K., Pucher, E.: Experimental investigation of methanol and ethanol flames in nonuniform flows, Proceedings of the Combustion Institute, Vol. 31, 2007, pp. 1173-1180.

125 Yates, A., Bell, A., Swarts, A.: Insights relating to the autoignition characteristics of alcohol fuels, Fuel, Vol. 89, 2010, pp. 83-93.

126 Saxena, P., Williams, F.A.: Numerical and experimental studies of ethanol flames, Proceedings of the Combustion Institute, Vol. 31, 2007, pp. 1149-1156.

127 Spadaccini, C.M., Zhang, X., Cadou, C.P., Miki, N., Waitz, I.A.: Develoment of a catalytic silicon micro-combustor for hydrocarbon-fueled power MEMS, 15th IEEE International Conference on Micro Electro Mechanical Systems, 2002, pp. 228-231.

128 Plee, S.L., Mellor, A.M.: Characteristic time correlation for lean blowoff of bluff-body-stabilized flames, Combustion and Flame, Vol. 35, 1979, pp. 61-80.

129 Shanbhogue, S.J., Husain, S., Lieuwen, T.: Lean blowoff of bluff body stabilized flames: Scaling and dynamics, Progress in Energy and Combustion Science, Vol. 35, 2009, pp. 98-120.

130 Dagaut, P., Cathonnet, M.: The ignition, oxidation, and combustion of kerosene: A review of experimental and kinetic modeling, Progress in Energy and Combustion Science, Vol. 32, 2006, pp. 48-92.

131 Zukoski, E.E.: Flame Stabilization on Bluff Bodies at low and intermediate Reynolds numbers, PhD thesis, California Institute of Technology, Pasadena, CA, 1954.

132 Zukoski, E.E., and Marble, F.E.: Experiments Concerning the Mechanism of Flame Blowoff from Bluff Bodies, Proceedings of the Gas Dynamics Symposium on Aerothermochemistry, Evanston, Il, 1956.

133 Zukoski, E.E., Marble, F.E.: The Role of Wake Transition in the Process of Flame Stabilization on Bluff Bodies, Combustion Researches and Reviews, 1955, pp. 167-180.

134 Dean, A.J., Penyazkov, O.G., Sevruk, K.L., Varatharajan, B.: Autoignition of surrogate fuels at elevated temperatures and pressures, Proceedings of the Combustion Institute, Vol. 31, 2007, pp. 2481-2488.

135 Colket, Me.B. III, Spadaccini, L.J.: Scramjet Fuels Autoignition Study, Journal of Propulsion and Power, Vol. 17, Iss. 2, 2001.

136 Masri, A.R., Kalt, P.A.M., Barlow, R.S.: The compositional structure of swirl-stabilised turbulent non-premixed flames, Combustion and Flame, Vol. 137, 2004, pp. 1-37.

137 Kariuki, J., Dawson, J.R., Mastorakos, E.: Measurements in turbultent premixed bluff body flames close to blow-off, Combustion and Flame, 2012, IN PRESS.

138 Dagaout, P., Cathonnet, M.: The ignition, oxidation, and combustion of kerosene: A review of experimental and kinetic modeling, Progress in Energy and Combustion Science, Vol. 32, 2006, pp. 48-92.

139 Spalding, D.B.: Combustion in Liquid-Fuel Rocket Motors, Aero. Quaterly, Vol. 10, 1959, pp. 1-27.

140 Kryukov, A.P., Levashov, V. Yu., Sazhin, S.S.: Evaporation of diesel fuel droplets: kinetic versus hydrodynamic models, International Journal of Heat and Mass Transfer, Vol. 47, 2004, pp. 2541-2549.

141 Sazhin, S.S., Kristyadi, T., Abdelghaffar, W.A., Heikal, M.R.: Models for fuel droplet heating and evaporation: comparative analysis, fuel, Vol. 85, 2006, pp. 1612-1630.

142 Yang, W.M., Chou, S.K., Shu, C., Li, Z.W., Xue, H.: Combustion in micro-cylindrical combustors with and without a backward facing step, Applied Thermal Engineering, Vol. 22, 2002, pp. 1777-1787.

143 Zuo, B., Van den Bulck, E.: Fuel oil evaporation in swirling hot gas streams, Internatonal Journal of Heat and Mass Transfer, Vol. 41, Iss. 12, 1998, pp. 1807-1820.

144 Law, C.K.: Unsteady droplet combustion with droplet heating, Combustion and Flame, Vol. 26, 1976, pp. 17-22.

145 Law, C.K.: Multicomponent droplet combustion with rapid internal mixing, Combustion and Flame, Vol. 26, 1976, pp. 219-233.

146 Takahashi, F., Schmill, W. J., Strader, E.A., Belovich, V.M.: Supprssion of a Nonpremixed Flame Stabiized by a Backward-Facing Step, Combustion and Flame, Vol. 122, 2000, pp. 105-116.

147 Huang, Y., Yang, V.: Bifurcation of flame structure in a lean-premixed swirl-stabilized combustor: transition from stable to unstable flame, Combustion and Flame, Vol. 136, 2004, pp. 383-389.

148 Huang, Y., Yang, V.: Dynamics and stability of lean-premixed swirl-stabilized combustion, Progress in Energy and Combustion Science, Vol. 35, 2009, pp. 293-364.

149 Schiebl, M.: Analytical Evaluation of Auto-Ignition Conditions and Experimental Verification fo a Jet-A1/H_2O_2 μ-Propulsion System, Master Thesis, Vienna Universtiy of Technology, 2011.

150 Prior, R.C., Fowler, D.K., Mellor, A.M.: Engineering Design Models for Ramjet Efficiency and Lean Blowoff, Journal of Propulsion and Power, Vol. 11, Iss. 1, 1995, pp. 117-123.

151 Armaly, B.F., Durst, F., Pereira, J.C.F., Schönung, B.: Experimental and theoretical investigation of backward-facing step flow, Journal of Fluid Mechanics, Vol. 127, 1983, pp. 473-496.

152 Biswas, G., Breuer, M., Durst, F.: Backward-Facing Step Flows for Various Expansion Ratios at Low and Moderate Reynolds Numbers, Journal of Fluids Engineering, Vol. 126, 2004, pp. 362-374.

153 Avancha, R.V.R., Pletcher, R.H.: Large eddy simulation of the turbulent flow pas a backward-facing step wit hheat transfer and property variations, International Journal of Heat and Fluid Flow, Vol. 23, 2002, pp. 601-614.

154 Haque, A.-u., Ahmad, F., Yamada, S., Chaudhry, S. R.: Assessment of Turbulence Models for Turbulent Flow over Backward Facing Step, Proceedings of the World Congress on Engineering, London, UK, 2007.

155 Vaniershot, M., Van den Bulck, E.: The influence of swirl on the reattachment length in an abrupt axisymmetric expansion, International Journal of Heat and Fluid Flow, Vol. 29, 2008, pp. 75-82.

156 Liang, H., Maxworthy, T.: An experimental investigation of swirling jets, Journal of Fluid Mechanics, Vol. 525, 2005, pp. 115-159.

157 Ranga Dinesh, K.K.J., Kirkpatrick, M.P., Jenkins, K.W.: Investigation of the influence of swirl on a confined coannular swirl jet, Computers & Fluids, Vol. 39, 2010, pp. 756-767.

158 Wang, S., Hsieh, S.-Y., Yang, V.: Unsteady flow evolution in swirl injector with radial entry. I. Stationary conditions, Physics of Fluids, Vol. 17, 2005, pp. 045106 (13 pages).

159 Spencer, A., McGuirk, J.J., Midgley, K.: Vortex Breakdown in Swirling Fuel Injector Flows, Journal of Engineering for Gas Turbines and Power, Vol. 130, Iss. 2, 2008.

160 Zaichik, L.I., Pershukov, V.A., Kozelev, M.V., Vinberg, A.A.: Modeling of Dynamics, Heat Transfer, and combustion in Two-Phae Turbulent Flows: 1. Isothermal Flows, Experimental Thermal and Fluid Science, Vol. 15, 1997, pp. 291-310.

161 Mak, H., Balabani, S.: Near field characteristics of swirling flow past a sudden expansion, Chemical Engineering Science, Vol. 62, 2007, pp. 6726-6746.

162 Syred, N.: A review of oscillation mechanisms and the role of the precessing vortex core (PVC) in swirl combustion systems, Progress in Energy and Combustion Science, Vol. 32, 2006, pp. 93-161.

163 Zaichik, L.I., Pershukov, V.A., Kozelev, M.V., Vinberg, A.A.: Modeling of Dynamics, Heat Transfer, and combustion in Two-Phae Turbulent Flows: 2. Flows with heat Transfer and Combustion, Experimental Thermal and Fluid Science, Vol. 15, 1997, pp. 311-322.

164 Huang, Y., Sung, H.-G., Hsieh, S.-Y., Yang, V.: Large-Eddy Simulation of Combustion Dynamics of Lean-Premixed Swirl-Stabilized Combustor, Journal of Propulsion and Power, Vol. 19, Iss. 5, 2003, pp. 782-794.

165 Renard, P.-H., Thévenin, D., Rolon, J.C., Candel, S.: Dynamics of flame/vortex interactions, Progress in Energy and Combustion Science, Vol. 26, 2000, pp. 225-282.

166 Grinstein, F.F., Fureby, C.: LES Studies of the flow in a swirl gas combustor, Proceedings of the combustion Institute, Vol. 30, 2005, pp. 1791-1798.

167 Day, M., Tachibana, S., Bell, J., Lijewski, M., Beckner, V., Cheng, R.K.: A combined computational and experimental characterization of lean premixed turbulent low swirl laboratory flames I. Methane flames, Combustion and Flame, Vol. 159, 2012, pp. 275-290.

168 Zhao, Z., Yuen, D.W., Leung, C.W., Wong, T.T: Thermal performance of a premixed impinging circular flame jet array with induced-swirl, Applied Thermal Engineering, Vol. 29, 2009, pp. 159-166.

169 Spadaccini, L.J., TeVelde, J.A.: Autoignition characteristics of aircraft-type fuels, NASA CR-159886, 1980.

170 Edwards, T.: Liquid fuels and Propellants for Aerospace Propulsion: 1903-2003, Journal of Propulsion and Power, Vol. 19, Iss. 6, 2003.

171 Coordinating Research Concil: Handbook of Aviation Fuel Properties, society of Automotive Engineers, Warrendale, Pensilvania.

172 Walder, H., Broughton, L.W.: Thermal Ignition Tests of Hydrogen Peroxide and Kerosene in a 2200lb Thrust Rocket Motor, Royal Aircraft Establishment, Aug. 1952.

173 Walder, H.: An Investigation into the Thermal Ignition of Hydrogen Peroxide and Kerosine, Royal Aircraft Establishment, May. 1950.

174 Walder, H.: Further Investigations into the Thermal Ignition of Hydrogen Peroxide and Kerosine, Royal Aircraft Establishment, Dec. 1950.

175 Schiebl, M., Krejci, D., Woschnak, A., Winter, F., Lang, M., Scharlemann C.: Modeling and Experimental Verification of Auto-Ignition Processes for a Green Bi-Propellant Thruster, 61st International Astronautical Congress, CZ, 2010.

176 Sadov, V., Prokhorov, N.: Ignition of Kerosene and Hydrogen Peroxide in Combustion Chamber by Fire Jet, The 3rd International Conference on Green Propellant for Space Propulsion, Poitiers, France, 2006.

177 LaBry, Z.A., Shanbhogue, S.J., Speth, R.L., Ghoniem, A.F.: Flow structures in a lean-premixed swirl-stabilized combustor with microjet air injection, Proceedings of the Combustion Institute, Vol. 33, 2011, pp. 1575-1581.

178 Teng, H., Kinoshita, C.M., Masutani, S.M.: Prediction of Droplet Size from the Breakup of Cylindical liquid jets, International Journal of Multiphase Flow , Vol. 21, Iss. 1, 1995, pp. 129-136.

179 Glynne-Jones, P., Coletti, M., White, N.M., Gabriel, S.B., Bramanti, C.: A feasibility study on using inkjet technology, micropumps, and MEMs as fuel injectors for bipropellant rocket engines, Acta Astronautica, Vol. 67, 2010, pp. 194-203.

180 Li, T., Nishida, K., Hiryasu, H.: Droplet size distribution and evaporation characteristics of fuel spray by swirl type atomizer, Fuel, Vol. 90, 2011, pp. 2367-2376.

181 Kihm, K.D., Lyn, G.M., Son, S.Y.: Atomization of cross-injecting sprays into convective air stream, Atomization and Sprays, Vol. 5, 1995, pp. 417-433.

182 Siringnano, W.A, Mehring, C.: Review of theory of distortion and disintegration of liquid streams, Progress in Energy and Combustion Science, Vol. 26, 2000, pp. 609-655.

183 Liu, H.-F., Gong, X., Li, W.-F., Wang, F.-C., Yu, Z.-H.: Prediction of droplet size distribution in sprays of prefilming air-blast atomizers, Chemical Engineering Science, Vol. 61, 2006, pp. 1741-1747.

184 Sirignano, W.A., Mehring, C.: Review of theory of distortion and disintegration of liquid streams, Progress in Energy and Combustion Science, Vol. 26, 2000, pp. 609-655.

185 Jiang, X., Siamas, G.A., Jagus, K., Karayiannis, T.G.: Physical modeling and advanced simulations of gas-liquid two-phase jet flows in atomization and sprays, Progress in Energy and Combustion Science, Vol. 36, 2010, pp. 131-167.

186 Kim, S., Hwan, J.W., Lee, C.S.: Experiments and modeling on droplet motion and atomization of diesel and bio-diesel fuels in cross-flowed air stream, International Journal of Heat and Fluid Flow, Vol. 31, 2010, pp. 667-679.

187 Zeoli, N., Gu, S.: Numerical modeling of droplet break-up for gas atomization, Computational Materials Science, Vol. 38, 2006, pp. 282-292.

188 Aggarwal, S.K., Peng, F.: A Review of Droplet Dynamics and Vaporization Modeling for Engineering Calculations, Journal of Engineering for Gas Turbines and Power, Vol. 117, 1995, pp. 453-461.

189 Ortiz, C., Joseph, D.D., Beavers, G.S.: Acceleration of a liquid drop suddenly exposed to a high-speed airstream, International Journal of Mulitphase Flow, Vol. 30, 2004, pp. 217-224.

190 Peng, F, Aggarwal, S.K.: Droplet Motion under the Influence of Flow Nonuniformity and Relative Acceleration, 206th ACS National Meeting, 1993.

191 Kurdyumov, V.N., Fernández, E., Liñán, A.: Flame Flashback and Propagation of Premixed Flames near a Wall, Proceedings of the Combustion Institute, Vol. 28, 2000, pp. 1883-1889.

192 Yeh, L.K., Lin, C.A.: Turbulence Modelling of Strongly Swirling Flows, Computational fluid dynamics 2000: proceedings of the First International Conference on Computational Fluid Dynamics, Kyoto, Japan, 10-14 July 2000, pp. 779-782.

193 Ayinde, T.F.: A generalized relationship for swirl decay in laminar pipe flow, Sadhana, Vol. 35 (2), 2010, pp. 129-137.

194 Sheen, H. J., Chen, W. J., Jeng, S. Y., Huang, T. L.: Correlation of Swirl Number for a Radial-Type Swirl Generator, Experimental Thermal and Fluid Science, Vol. 12, 1996, pp. 444-451.

195 Valera-Medina, A., Syred N., Griffiths, A.: Visualisation of isothermal large coherent structures in a swirl burner, Combustion and Flame, Vol. 156, 2009, pp. 1723-1734.

196 Ko, J., Zahrai, S., Macchion, O., Vomhoff, H.: Numerical Modeling of Highly Swirling Flows in a Through-Flow Cylindrical Hydrocyclone, Fluid Mechanics and Transportation Phenomena, AIChE Journal, Vol. 52, No. 10, 2006, pp. 3334-3344.

197 Claypole, T. C., Syred, N.: The effect of swirl burner aerodynamics on NO_x formation, Symposium on Combustion, Vol. 18, Iss. 1, 1981, pp. 81-89.

198 Khanna, V. K.: A Study of the Dynamics of Laminar and Turbulent Fully and Partially Premixed Flames, PhD. Thesis, Virginia Polytechnic Institute and State University, 2001.

199 Chigier, N.A., Beér, J.M.: Velocity and Static-Pressure Distributions in Swirling Air Jets Issuing From Annular and Divergent Nozzles, Journal of Basic Engineering, Vol. 68, Iss. 4, 2964, pp. 788-797.

200 Yeh, L.K., Lin, C.A.: Turbulence Modelling of Strongly Swirling Flows, Computational fluid dynamics 2000: proceedings of the First International Conference on Computational Fluid Dynamics, Kyoto, Japan, 10-14 July 2000, pp. 779-782.

201 Moody, L.F.: Friction factors for pipe flow, Tans ASME, Vol. 66, Iss. 8, 1944, 671-684.

202 Kreith, F., Sonju, O.K.: The decay of a turbulent swirl in a pipe, Journal of Fluid Mechanics, Vol. 22, 1965, pp. 257-271.

203 Fokeer, S.: An investigation of geometrically induced swirl applied to lean phase pneumatic flows, PhD. Thesis, The University of Nottingham, 2006.

204 Majdalani, J., Halpenny, E.K.: The Bidirectional Vortex with Sidewall Injection, 44th AIAA/ASME/ SAE/ASEE Joint Propulsion Conference & Exhibit, Hartford, CT, AIAA 2008-5018, 2008.

205 Chang, F., Dhir, V. K.: Turbulent flow field in tangentially injected swirl flows in tubes, International Journal of Heat and Fluid Flow, Vol. 15, No. 4, 1994, pp. 346-356.

206 Moene, AaF.: Swirling pipe flow with axial strain, Experiment and Large Eddy Simulation, Ph.D. thesis, Technische Universiteit Eindhoven, 2003.

207 Steenbergen, W., Voskamp, J.: The rate of decay of swirl in turbulent pipe flow, Flow Measurement and Instrumentation, Vol. 9, 1998, pp. 67-78.

208 Jawarneh, Ali M.: Heat Transfer Enhancement in Swirl Annulus flows, 5th WSEAS Int. Conf. on Environmant, Ecosystems and Development, Tenerife, Spain, 2007, pp. 56-61.

209 Kioth, O.: Experimental study of turbulent swirling flow in a straight pipe, Journal of Fluid Mechanics, Vol. 225, 1991, pp. 445-479.

210 Ayinde, T.F.: A generalized relationship for swirl decay in laminar pipe flow, Sadhana Indian Academy of Sciences, Vol. 35, Part 2, 2010, pp. 129-137.

211 Serre, E., Bontoux, P.: Vortex breakdown in a three-dimensional swirling flow, Journal of Fluid Mechanics, Vol. 459, pp. 347-370.

212 Spencer, A., McGuirk, J.J.: Vortex Breakdown in Swirling Fuel Injector Flows, Journal of Engineering for Gas Turbines and Power, Vol. 130, Iss. 2, 2008, 021503, p. 8.

213 Spohn, A., Mory, M., Hopfinger, E.J.: Experiments on vortex breakdown in a confined flow generated by a rotating disc, Journal of Fluid Mechanics, Vol. 370, 1998, pp. 73-99.

214 Stein, O., Kempf, A.: LES of the Sydney swirl flame series: A study of vortex breakdown in isothermal and reacting flows, Proceedings of the Combustion Institute, Vol. 31, 2007, pp. 1755-1763.

215 Boerner, C.J., Sparrow, E.M., Scott, C.J.: Compressible Swirling Flow through Convergent-Divergent Nozzles, Wärme- und Stoffübertragung, Vol. 5, 1972, pp. 101-115.

216 Van Holten, T., Heiligers, M., Jaeken, A.: Chocking Phenomena in a Vortex Flow Passing a Laval Tube: An Analytical Treatment, Journal of Fluids Engineering, Vol. 131, 2009.

217 Hidding, B., Pfitzner, M.: Rocket-Propellant Characteristics of Silanes/O_2, Journal of Propulsion and Power, Vol. 22, 2006.

218 Nusca, M.J., Chen, C.-C-, McQuaid, M.J.: Modeling the Combustion Chamber Dynamics of Selectable-Thrust Rocket Motors, High Performance Computing Modernization Program Users Group Conference (HPCMP-UGC), Schaumburg, Il, June, 2010.

219 Hidding, B.: Untersuchung der Eignung von Silanen als Treibstoffe in der Luft- und Raumfahrt, Master thesis, Universität der Bundeswehr München and Heinrich-Heine-Universität Düsseldorf, 2004.

220 Back, L.H., Massier, P.F., Gier, H.L.: Convective heat transfer in a convergent-divergent nozzle, International Journal of Heat and Mass Transfer, Vol. 7, 1964, pp. 549-568.

221 Schacht, R.L., Quentmeyer, R.J., Jones, W.L.: Experimental Investigation of Hot-Gas Side Heat-Transfer Rates for a Hydrogen-Oxygen Rocket, NASA TN D-2832, 1965.

222 Howell, J.R., Strite, M.K., Renkel, H.E.: Analysis of heat-transfer effects in rocket nozzles operating with very high-temperature hydrogen, NASA TR R-220, 1965.

223 Wazzan, A.R., Robinson, L.B., Diem, H.G.: Heat transfer of gas-particle flow in a supersonic convergent-divergent nozzle, Applied Scientific Research, Vol. 18, 1967, pp. 288-308.

224 DeLise, J.C., Naraghi, M.H.N.: Comparative Studies of Convective Heat Transfer Models for Rocket Nozzles, 31st AIAA/ASME/SAE/ASEE Joint Propulsion Conference and Exhibit, San Diego, CA, 1995.

225 Bartz, D. R.: A simple equation for rapid estimation of rocket nozzle convective heat-transfer coefficients. Jet Propulsion, Vol. 27, 1957, pp. 49–51.

226 Truckenbrodt, E.: Fluidmechanik, Bd 2, Springer, Ch. 5, 2008.

227 Bayt, R. L.: Analysis, Fabrication and Testing of a MEMS-based Micropropulsion System, Ph.D. Thesis, Massachusstes Institute of Technology, 1999.

228 Elliott, D.G., Bartz, D.R., Silver, S.: Calculation of Turbulent Boundary-Layer Growth and Heat Transfer in Axi-Symmetric Nozzles, Technical Report 32-387, Jet Propulsion Laboratory, 1963.

229 Smith, D.M.: A Comparison of experimental heat-transfer coefficients in a nozzle with analytical predicitions from Bartz's methods for various combustion chamber pressures in a solid propellant rocket motor, Master Thesis, Noth Carolina Stat University, Raleigh, 1970.

230 Coles, D.: The Turbulent Boundary Layer in a Compressible Fluid, The Physics of Fluids, Vol. 7, No. 9, 1964, pp. 1403-1423.

231 Locke, J.M., Pal, S.P., Woodward, R.D.: Chamber Wall Heat Flux Measurements for a LOX/CH$_4$ Uni-element Rocket, 43rd AIAA/ASME/SAE/ASEE Joint Propulsion Conference & Exhibit, 8-11 July 2007, Cincinnati, OH, AIAA 2007-5547.

232 Zohir, A.E., Abdel Aziz, A.A. Habib, M.A.: Heat transfer characteristics in a sudden expansion pipe equipped with swirl generators, International Journal of Heat and Fluid Flow, Vol 32, 2011, pp. 352-361.

233 Bali, T.: Modelling of heat transfer and fluid flow for decaying swirl flow in a circular pipe, Int. Comm. Heat Mass Transfer, Vol. 25, No. 3, 1998, pp. 349-358.

234 Khalil, A., Zohir, A.E., Farid, A.M: Heat transfer characteristics and friction of turbulent swirling air flow through abrupt expansion, American Journal of Scientific and Instustrial Research, Vol. 1, Iss. 2, 2010, pp. 364-374.

235 Saha, S-K-, Dutta, A., Dhal, S.K.: Friction and heat transfer characteristics of laminar swirl flow through a circular tube fitted with regularly spaced twisted-tape elements, International Journal of Heat and Mass Transfer, Vol. 44, 2001, pp. 4211-4223.

236 Hedlund, C.R., Ligrani, P.M., Glezer, B., Moon, H.-K.: Heat transfer in a swirl chamber at different temperature ratios and Reynolds numbers, International Journal of Heat and Mass Transfer, Vol. 42, 1999, pp. 4081-4091.

237 Hedlund, C.R., Ligrani: Local Swirl Chamber Heat Transfer and Flow Structure at Different Reynolds Numbers, J. Turbomachinery, Vol. 122, 2000, pp. 375-385.

238 Richter, W., Görner, K.: K5 Heat Radiation in Furnaces, in: VDI-Heat Atlas, Springer Verlag, Berlin, pp. 1001- 1012, 2010.

239 Viskanta, R., Mengüç, M. P.: Radiation Heat Transfer in Combustion Systems, Prog. Energy Combust. Sci., Vol. 13, 1987, pp. 97-160.

240 Johansson, R., Leckner, B., Andersson, K., Johnsson, F.: Account for variations in the H$_2$O and CO$_2$ molar ratio when modelling gaseous radiative heat transfer with the weighted-sum-of-grey-gases model, Combustion and Flame, Vol. 158, 2011, pp. 893-901.

241 Watanabe, h., Suwa, Y., Matsushita, Y., Morozumi, Y., Aoki, H., Tanno, S., Miura, T.: Spray combustion simulation including soot and NO formation, Energy Conversion & Management, Vol. 48, 2007, pp. 2077-2089.

242 Byun, D., Baek, S.W.: Numerical investigation of combustion with non-gray thermal radiation and soot formation effect in a liquid rocket engine, Interanational Journal of Heat and Mass Transfer, Vol. 50, 2007, pp. 412, 422.

243 Modest, M.F., Zhang, H.: The Full-Spectrum Correlated-k Distribution for Thermal Radiation From Molecular Gas-Particulate Mixtures, Transactions of the ASME, Vol 124, 2002, pp. 30-38.

244 Cumber, P. S., Fairweather, M.: Evaluation of flame emission models combined with the discrete transfer method for combustion system simulation, International Journal of Heat and Mass Transfer, Wol. 48, 2005, pp. 5221-5239.

245 Porter, R., Liu, F., Pourkashanian, M., Williams, A., Smith, D.: Evaluation of solution methods for radiative heat transfer in gaseous oxy-fuel combustion environments, Journal of Quantitative Spectroscopy & Radiative Transfer, Vol. 111, 2010, pp. 2084-2094.

246 Viskanta, R.: Overview of convection and radiation in high temperature gas flows, International Journal of Engineering Science, Vol 36, 1998. pp. 1677-1699.

247 Kirchberger, C., Wagner, R., Kau, H.-P., Soler, S., Martin, P., Bouchet, M., Bonzom, C.: Prediction and Analysis of Heat Transfer in Small Rocket Chambers, 46th AIAA Aerospace Sciences Meeting and Exhibit, Reno, NV, AIAA2008-1260, 2008.

248 Vortmeyer, D., Kabelac, S.: Gas Radiation: Radiation from Gas Mixtures, in: VDI-Heat Atlas, Springer Verlag, Berlin, pp. 979- 988, 2010.

249 Hottel, H.C., Egbert, R.B.: Radiant heat transmission from water vapor, Transactions of the American Institute of Chemical Engineers, Vol. 38, 1943, pp. 531-568.

250 Paul, S.C., Paul, M.C.: Radiative heat transfer during turbulent combustion process, International Communications in Heat and Mass Transfer, Vol. 37,

251 Byun, D., Baek, S.W.: Numerical investigation of combustion with non-gray thermal radiation and soot formation effect in a liquid rocket engine, International Journal of Heat and Mass Transfer, Vol. 50, 2007, pp. 412-422.

252 Woschnak, A.: Untersuchung des Wärmeübergangs in regenerativ gekühlten Schubkammern kryogener Raketentriebwerke, Shaker Verlag, Aachen, 2009.

253 Scharlemann, C., Schiebl, M., Marhold, K., Tajmar, M., Miotti, P., Guraya, C., Seco, F., Kappenstein, C., Batonneau, Y., Brahmi, R., Lang, M.: Test of a Turbo-Pump Fed Miniature Rocket Engine, 42nd AIAA/ASME/SAE/ASEE Joint Propulsion Conference and Exhibit, Sacramento, CA, 2006.

254 Scharlemann, C., Schiebl, M., Amsüss, R., Tajmar, M.: Development of Miniaturized Green Propellant Based Mono- and Bipropellant Thrusters, 43rd AIAA/ASME/SAE/ASEE Joint Propulsion Conference and Exhibit, Cincinnati, OH, 2007.

255 Bates, R., Edwards, T., Meyer, M.L.: Heat transfer and Deposition Behavior of Hydrocarbon Rocket Fuels, AIAA Aerospace Sciences Conference, Reno, NV, 2003.

256 Reed, B.D., Biaglow, J.A., Schneider, S.J.: Iridium-coated rhenium radiation-cooled rockets, NASA Technical Memorandum TM-107453, 1997.

257 Wood, R.S.: Experiences with high temperature materials for small thrusters, 29th AIAA/ASME/SAE/ASEE Joint Propulsion Conference and Exhibit, Monterey, CA, 1993.

258 Schneider, S.J.: High temperature thruster technology for spacecraft propulsion, Acta Astronautica, Vol. 28, 1992, pp. 115-125.

259 Gimeno-Fabra, L.: Design, Manufacture and Properties of Cr-Re Alloys for Application in Satellite Thrusters, PhD. thesis, Universitat Politècnica de Catalunya, 2006.

260 Schoenman L.: 4000 F materials for low-thrust rocket engines, Journal of Propulsion and Power, Vol. 11, No. 6, 1995, pp. 1261-1267.

261 Young, K.J., Stewart, C.W., Moss, J.B.: Soot formation in turbulent non-premixed kerosene-air flames buring at elevated pressure: experimental measurement, Proceedings of the Combustion Institute, Vol. 25, 1995, pp. 609-617.

262 Crookes, R.J., Sivalingam, G., Nazha, M.A.A., Rajakaruna, H.: Prediction and measurement of soot particulate formation in a confined diesel fuel spray-flame at 2.1 MPa, International Journal of Thermal Sciences, Vol. 42, 2003, pp. 639-646.

263 Watanabe, H., Kurose, R., Komori, S., Pitsch, H.: Effects of radiation on spray flame characteristics and soot formation, Combustion and Flame, Vol. 152, 2008, pp. 2-13.

264 McCrain, L.L., Roberts, W.L.: Measurements of the soot volume field in laminar diffusion flames at elevated pressures, Combustion and Flame, Vol. 140, 2005, pp. 60-69.

265 Howell, J.R., Mengüc, M.P.: Radiation, in: Rohsenow, Warren M., Harnett, James P., Cho, Young I.: Handbook of Heat Transfer, McGraw-Hill, 1998, Chap.7.

266 Kain, S. C., Goel, T. C., Narayan, V.: Thermal conductivity of metals at high temperatures by the Jain and Krishnan method III. Platinum, Brit. J. Appl. Phys. (J. Phys. D.), Vol. 2, 1969.

267 Bradley, D, Entwistle, A. G.: Determination of the emissivity, for total radiation of small diameter platinum-10% rhodium wires in the temperature range 600-1450°C, Br. J. Appl. Phys. 12, 1971, pp. 708-711.

268 Barley, S., Palmer, P.L., Coxhill, I.: Evaluating the Miniaturisation of a Monopropellant Thruster, 4nd AIAA/ASMA/SAE/ASEE Joint Propulsion Conference & exhibit, Sacramento, CA, AIAA-2006-4549, 2006.

269 Musker, A. J.: Development of a 200 Newton Bipropellant Thruster Using Heterogeneous Catalytic Reduction of Hydrogen Peroxide, 4th European Converence for Aerospace Sciences (EUCASS), Saint Petersburg, Russia, 2011.

270 Bonifacio, S., Sapio, M.L., Festa, G., Russo Sorge, A.: Development and Testing of a Hydrogen Peroxide Fed Monopropellant Thruster, 4th European Converence for Aerospace Sciences (EUCASS), Saint Petersburg, Russia, 2011.

271 Su-Lim, L., Choong-Won, L.: Performance characteristics of silver catalyst bed for hydrogen peroxide, Aerospace Science and Technology, Vol. 13, 2009, pp. 12-17.

272 Blank, R.A., Pourpoint, T.L., Meyer, S.E.: Experimental Study of Flow Processes and Performance of a High Pressure Hydrogen Peroxide Catalyst Bed, 43rd AIAA/ASMA/SAE/ASEE Joint Propulsion Conference & exhibit, Cincinnati, OH, 8-11 July 2007.

273 Ponzo, J.: Small Envelope, High Flux 90% Hydrogen Peroxide Catalyst Bed, 43rd AIAA/ASMA/SAE/ASEE Joint Propulsion Conference & exhibit, Huntsville, AL, 20-23 July 2003.

274 Cen, J.W., Xu, J.L.: Performance evaluation and flow visualization of a MEMS based vaporization liquid micro-thruster, Acta Astronautica, Vol. 67, 2010, pp. 468-482.

275 Pirault-Roy L., Kappenstein C., Guérin M., Eloirdi R., Pillet N.: Hydrogen Peroxide Decomposition on Various Supported Catalysts Effect of Stabilizers, Journal of Propulsion and Power, Vol. 18, No.6, Nov-Dec 2002, pp. 1235-1241.

276 Blank, R.A., Pourpoint, T.L., Meyer, S.E.: Experimental Study of Flow Processes and Performance of a High Pressure Hydrogen Peroxide Catalyst Bed, 43th AIAA/ASME/SAE/ASEE Joint Propulsion Conference and Exhibit, Cincinnati, OH, AIAA 2007-5575, 2007.

277 Iarochenko, N., Dedic, V.: Hydrogen Peroxide as Monopropellant - Catalysts and Catalyst Beds – Experience from more than Thirty Years of Exploitation, 1st International Conference on Green Propellants for Space Propulsion, Noordwijk, The Netherlands, 2001.

278 Wilthan, B., Tanzer, R., Schützenhöfer, W., Pottlacher, G.: Thermophysical properties of the Ni-based alloy Nimonic 80A up to 2400 K, III, Thermochimica Acta, Vol. 465, 2007, pp. 83-87.

279 Muss, J.A., Johnson, C.W., Kruse, W., Cohn, R.K., 2003. The Performance of Hydrocarbon Fuels with H2O2 in a Uni-element Combustor, 39th AIAA/ASMA/SAE/ASEE Joint Propulsion Conference & Exhibit, Huntsville, AL, 20-23 July, AIAA 2003-4623.

280 Cohn, R.K., Danczyk, St.A., Bates, R.W.: A Comparison of the Performance of Hydrocarbon Fuels in a Uni-element Combustor, 39th AIAA/ASME/SAE/ASEE Joint Propulsion Conference & Exhibit, Huntsville, AL, AIAA 2003-4752, 2003.

281 Summerfield M, Foster C, Swan W: Flow separation in overexpanded supersonic exhaust nozzles, Jet Propulsion, Vol. 24, 1954, pp. 319–321

282 Stark, R.H.: Flow Separation in Rocket Nozzles, a Simple Criteria, 41st AIAA/ASME/SAE/ASEE Joint Propulsion Conference and Exhibit, Tucson, AZ, AIAA, 2005.

283 Östlund, J., Muhammad-Klingmann, B.: Supersonic Flow Seperation with Application to Rocket Engine Nozzles, Applied Mechanics Reviews, Vol. 58, 2005, pp. 143-177.

284 Leckner, B.: Spectral and Total Emissivity of Water Vapor and Carbon Dioxide, Combustion and Flame, Vol. 19, 1972, pp. 33-48.

Appendix

X.1. Turbulent boundary layer model integrals

The integrals appearing in the turbulent boundary model are, from Ref. 228:

$$a = \frac{T_w}{T}$$

$$b = \frac{T_0}{T_w} - 1$$

$$c = \left(\frac{\gamma - 1}{2} M^2 \right) \frac{T}{T_w}$$

$$I_1 = \int_0^1 \frac{s^7 (1-s)}{1 + bs/\zeta - cs^2} ds$$

$$I_2 = \int_0^1 \frac{s^7}{1 + bs/\zeta - cs^2} ds$$

$$I_3 = \int_0^\zeta \frac{s^6}{1 + bs/\zeta - c} ds$$

$$I_4 = \int_0^\zeta \frac{s^7 (1-s)}{1 + bs/\zeta - cs^2} ds$$

$$I_5 = \int_\zeta^1 \frac{s^7 (1-s)}{1 + b - cs^2} ds$$

$$I_6 = \int_0^\zeta \frac{s^7}{1 + bs/\zeta - cs^2} ds$$

$$I_7 = \int_\zeta^1 \frac{s^7}{1 + b - cs^2} ds$$

$$I_1' = \int_0^1 \frac{s^7 (1-s)}{1 + bs - c\zeta^2 s^2} ds$$

$$I_2' = \int_0^{1/\zeta} \frac{s^7 (1-s)}{1 + bs - c\zeta^2 s^2} ds$$

$$I_3' = \int_0^{1/\zeta} \frac{s^6 (1-s)}{1 + bs - c} ds$$

X.2. Synopsis on gas radiation

This section outlines the derivation of non-luminous gas radiation according to Ref. 248. This approach bases on the following assumptions:

- Uniform distribution of mixture components
- Only triatomic gases H_2O and CO_2 contribute significantly to radiation
- Uniform partial pressure distributions throughout the combustion chamber

Eq. (3.131) describes the incident radiative density as a function of equivalence layer thickness as outlined in section 3.7.3.1. Table 26 gives values found in literature and by Eq. (3.132) for geometries best resembling the cylindrical combustion chamber.

Table 26 Values for equivalent layer thickness for cylinder geometry

Cylinder	s_{eq}	Remark	Reference
$L_{CC} = 4r_{CC}$	$0.73 \cdot (2r_{CC})$	Finite value of optical density	[248, 239]
$L_{CC} = 4r_{CC}$	$0.8 \cdot (2r_{CC})$	Vanishing optical density	[248, 239]
Eq. (3.132)	$1.8 \cdot r_{CC} \cdot L_{CC}/(L_{CC}+r_{CC})$		[248]

Although Eq. (3.127) suggests that the emissivity is solely dependent on the product of partial pressure and equivalent layer thickness, this could not be confirmed experimentally. Instead, Hottel and Egbert [249] compiled diagrams containing emissivities for different gases from experimental data for different temperatures. The hemispherical total emissivity of CO_2 and H_2O are shown in Figure 177 and Figure 178 respectively. The product of partial pressure and equivalent layer thickness remains as important parameter.
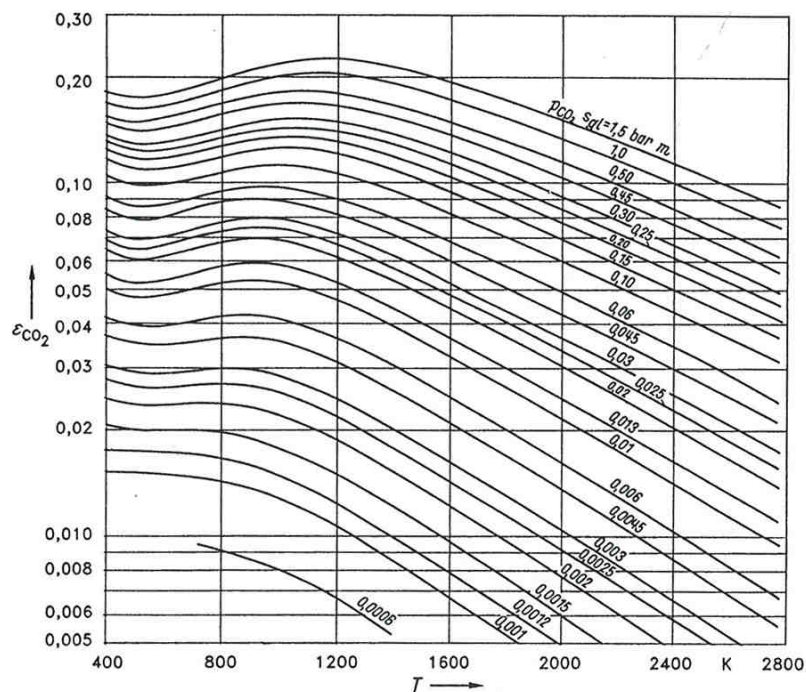
Figure 177 Total emissivity ε_{CO2} of carbon dioxide at pressure $p = 1$ bar, for $s_{eq} = s_{gl}$, from Ref. 239
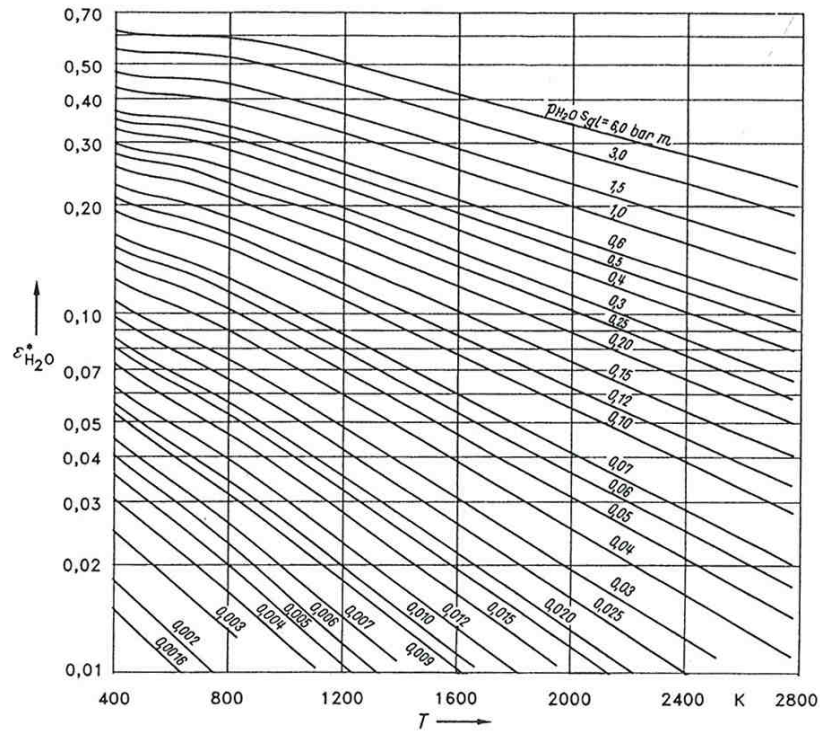
Figure 178 Total emissivity ε_{H2O} of carbon dioxide at pressure $p = 1$ bar ($p_{H2O} \to 0$ bar), for $s_{eq} = s_{gl}$, from Ref. 102

Since the data presented in the figures above is valid only for $p = 1$ bar, Ref. 248 introduces correction factors $f_{p,H2O}$ and $f_{p,CO2}$ which give reasonable results for $1 < p < 100$ bar

$$\varepsilon_{H_2O}(p) = f_{p,H_2O} \cdot \varepsilon'_{H_2O}(p_{H_2O} s_{eq}) \tag{8.1}$$

$$\varepsilon_{CO_2}(p) = f_{p,CO_2} \cdot \varepsilon'_{CO_2}(p_{CO_2} s_{eq}), \tag{8.2}$$

where $\varepsilon'_{H_2O}(p_{H_2O} s_{eq})$ and $\varepsilon'_{CO_2}(p_{CO_2} s_{eq})$ are found in Figure 177 and Figure 178 respectively. The correction factors are given(valid for $T_g > 750$ K), according to Ref. 248, by

$$f_{p,H_2O} = 1 + (A_{H_2O} - 1)\exp\left[-0.5\left(\log\left(\frac{0.132\left(T_g/1000\right)^2}{p_{H_2O} s_{eq}}\right)\right)^2\right] \tag{8.3}$$

$$A_{H_2O} = \frac{\left(1888 - 2053\log\left(\frac{T_g}{1000}\right)\right) p\left(1 + 4.9\frac{p_{H_2O}}{p}\left(\frac{273}{T_g}\right)^{1/2}\right) + 1.1\left(\frac{T_g}{1000}\right)^{-1.4}}{0.888 - 2053\log\left(\frac{T_g}{1000}\right) + p\left(1 + 4.9\frac{p_{H_2O}}{p}\left(\frac{273}{T_g}\right)^{1/2}\right) + 1.1\left(\frac{T_g}{1000}\right)^{-1.4}} \tag{8.4}$$

.

If $f_{p,H_2O} > A_{H_2O}$, the correction factor is calculated by $f_{p,H_2O} = A_{H_2O}$

The correction factor for CO_2 is given (valid for $T_g > 700$ K), according to Ref. 248, by

$$f_{p,CO_2} = 1 + (A_{CO_2} - 1)\exp\left[-0.5\left(\log\left(\frac{0.225(T_g/1000)}{100\,p_{CO_2}s_{eq}}\right)\right)^2\right],$$ (8.5)

$$A_{CO_2} = \frac{\left[0.1\left(\frac{T_g}{1000}\right)^{-1.45} + 1\right]p\left(1 + 0.28\frac{p_{CO_2}}{p}\right) + 0.23}{0.1\left(\frac{T_g}{1000}\right)^{-1.45} + p\left(1 + 0.28\frac{p_{CO_2}}{p}\right) + 0.23}.$$ (8.6)

Again, if $f_{p,CO_2} > A_{CO_2}$, the correction factor is calculated by $f_{p,CO_2} = A_{CO_2}$

The net flow rate density of thermal radiation energy between a gas volume and the surrounding wall at the wall surface is given by

$$\dot{q}_{rad} = \sigma\frac{\varepsilon_w}{1 - (1 - \varepsilon_w)(1 - A_V)}\left(\varepsilon_g T_g^4 - A_V T_w^4\right),$$ (8.7)

where the quantities of the gas mixture ε_g and A_v are given by

$$\varepsilon_g = \varepsilon_{H_2O} + \varepsilon_{CO_2} - (\Delta\varepsilon)_g$$ (8.8)

$$A_V = A_{V,\varepsilon_{H_2O}} + A_{V,\varepsilon_{CO_2}} - (\Delta\varepsilon)_w,$$ (8.9)

with the correction factor evaluated at the gaseous and wall temperature respectively. The correction factor, accounting for the overlap of absorption spectrum lines, is given in Figure 179 for 920 °C. Figure 180 shows the correction factor accounting for overlapping spectral bands as a function of path length for a variety of temperatures, including high temperature range. Although this data represents a gaseous mixture with higher carbon dioxide fraction than in the investigated case (which would yield $p_{H2O}/(p_{H2O}+p_{CO2}) \approx 0.84$), the general behavior of the correction factor points to a vanishing value for the small equivalent layer thickness of the given combustion chamber.
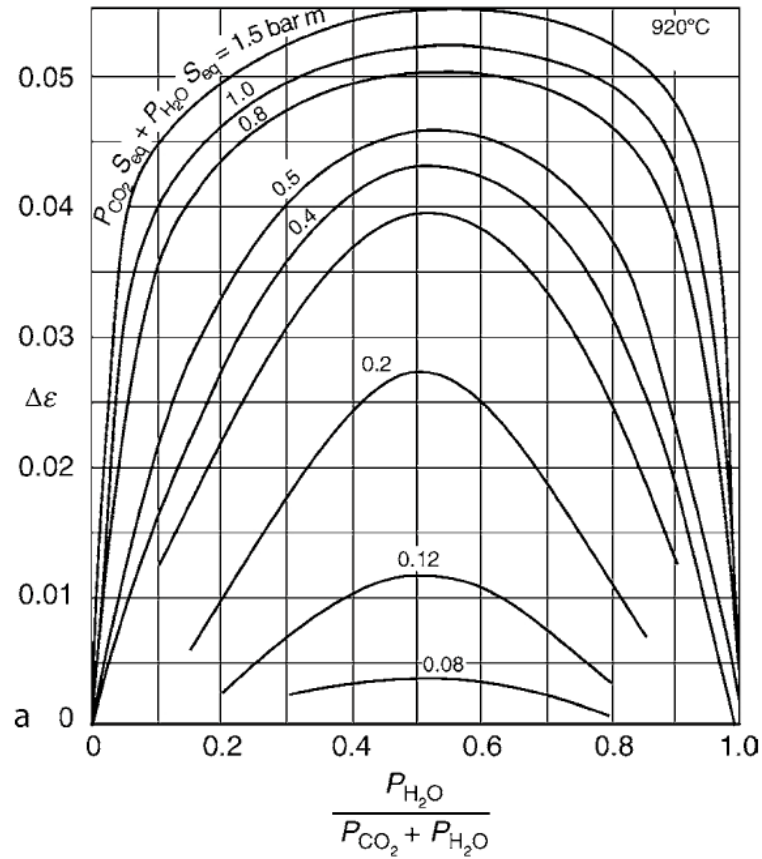
Figure 179 Correction $\Delta\varepsilon$ for mixtures of H_2O and CO_2, from Ref. 248
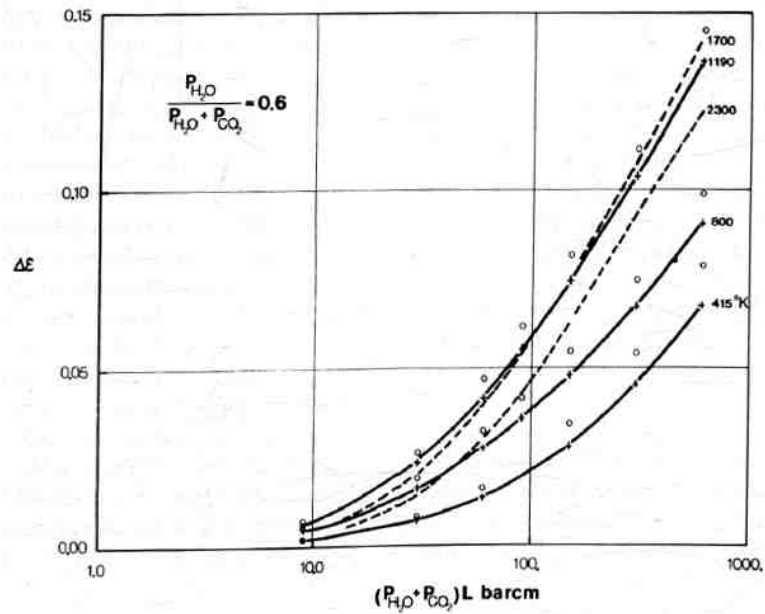
Figure 180 Correction $\Delta\varepsilon$ for given mixture of H_2O and CO_2 as function of partial pressures and path-length from Ref. 284

The emissivities in Eq. (8.8) are determined by Figure 177 to Figure 178 as a function of pressure, temperature and the product of partial pressure with equivalent layer thickness.

The absorptance appearing in Eq. (8.9) is additionally dependent on the temperature of the enclosing wall T_w. Thus, the emissivities appearing in the equations below are determined for the wall temperature and for a partial pressure corrected by the wall temperature as indicated (Ref. 248):

$$A_{V,\varepsilon_{H_2O}} = f_{p,H_2O} \left(\frac{T_g}{T_w} \right)^{0.45} \varepsilon_g (T_w; s_{eq} \cdot p_{H_2O} \cdot T_w / T_g) \qquad \text{for} \quad p > 1 \text{ bar} \qquad (8.10)$$

$$A_{V,\varepsilon_{CO_2}} = f_{p,CO_2} \left(\frac{T_g}{T_w} \right)^{0.65} \varepsilon_g (T_w; s_{eq} \cdot p_{CO_2} \cdot T_w / T_g) \qquad \text{for} \quad p > 1 \text{ bar} , \qquad (8.11)$$

with the correction factors for elevated pressures given by Eq. (8.3) and (8.5) for H_2O and CO_2 respectively.

Calculating net heat flux from gas radiation in combustion chamber

The radiative net heat flux from combustion gases in the combustion chamber is calculated based on the assumption that the cylindrical part of the combustion chamber is homogeneously filled by readily combusted exhaust gases at ideal combustion temperature. This is an approximation for an adiabatic chamber with a thin flame front close to the injector, which constitutes an upper limit for the radiation heat flux in the combustion chamber. This calculation thus results in an upper limit for the radiative heat flux to the chamber walls.

The parameters for combusted exhaust gases given in Table 27 were derived by CEA code [92]. Table 27 also lists the input parameters for combustion calculation.

Table 27 Parameters for H_2O_2 .Jet A-1 combustion

Parameter	Value	Dimension
Input for Combustion		
Mixture Ratio O/F	7.33	-
H_2O injected	0.71965	mole fraction
O_2 injected	0.28035	mole fraction
T_{H2O} injected T_{O2} injected	941.5	K
p_{CC}	10	bar
Properties of combusted Gases		
T_g	2623.25	K
x_{H2O}	0.75634	mole fraction
x_{CO2}	0.14160	mole fraction
x_{CO}	0.04418	mole fraction
x_{H2}	0.03615	mole fraction
x_{OH}	0.01380	mole fraction
x_{O2}	0.00482	mole fraction

Due to the dominant convective heat flux at the throat region, the radiation heat flux contribution is only relevant in the cylindrical and in the convergent region with large area aspect ratio. Therefore, only the region upstream of the throat is chosen as radiation surface. In order to match this geometry to a cylinder for evaluation of the equivalence layer thickness, the length of the corresponding cylinder is chosen so that the surface of the cylinder matches the surface of the actual geometry including the convergent section of the combustion chamber while the radius of the actual chamber remains equal to the cylindrical radius. The area of the combustion chamber cylindrical section plus the converging section is $A_{CC} \approx 750$ mm². For the equivalent cylinder with radius equal to the actual combustion chamber, the length becomes:

$$L_{cyl} = \frac{A_{CC}}{2r_{CC}\pi} - r_{CC} \approx 26\,\text{mm}\,. \tag{8.12}$$

Employing Eq. (3.132), the equivalent layer thickness becomes $s_{eq} \approx 0.0062128$ m.

Evaluation of Eq. (8.1) to (8.11) gives $\varepsilon_g \approx 0.0257$ for Pt-20%Rh as chamber material and the net flow rate density of thermal radiation energy between a gas volume and the surrounding wall at the wall surface can be calculated by Eq. (8.7) to:

$$\begin{aligned} \dot{q}_{rad} &= 31.37\,\text{kW m}^{-2} \\ Q_{rad} &= 26.07\,\text{W}\,. \end{aligned} \tag{8.13}$$

X.3. Propellant specifications

Specification of diluted H₂O₂

H₂O₂ Batch 1

Werkszeugnis

nach EN 10 204-2.2

Seite 1   SerialNr: 239252

⊜ EVONIK
INDUSTRIES

Evonik Degussa GmbH
Untere Kanalstr. 3
79618 Rheinfelden

AIT Austrian Institute of Technolog
GmbH

Postfach:
AT   2444   Seibersdorf

Material:	**PROPULSE (TM)** **875 HTP**
Material-Nr.:	22.1125.8700.99
Spez.-Nr.:	1132/01
Gültig ab:	01.08.2008
Kunden-Nr.:	0000643537
Auftrags-Nr.:	31855842 /10
Lieferbeleg-Nr.:	44193172 /10
Lieferdatum:	10.07.2009
Versandbedingung:	Lkw Stückgut
Menge:	28 KG
Kundenbestell-Nr.:	4510074651

Warenempfänger
AIT
Austrian Institute of Technology
Wareneingang-Zentralmagazin

Kontroll/Lot-Nr.:   4322

AT   2444   Seibersdorf
Österreich

Produktspezifikation

Merkmale und Prüfmethoden		Einheiten	Sollwerte (Grenzen)	Istwerte
600/WM11	H2O2-Gehalt	g/100 g	87,0-88,0	86,7
600/WM21	Zersetzungsrate (96°C/16h)	%	<=2,0	0,4
600/WM40	Säuregehalt [meq/l]	-	<=1,0	0,5
600/WN20	Glührückstand	mg/l	<=30	15
600/WO91	Natriumnitrat (NaNO3)	mg/l	12,0-20,0	16,2
600/WO21	Zinn (Sn)	ppm	5,00-9,00	6,40
600/WO13	Phosphat (als PO4)	ppm	<=0,50	<0,10
600/WO15	Sulfat (als SO4)	ppm	<=5,00	
600/WO10	Chlorid (Cl)	ppm	<=2,00	
600/WP40	Aluminium (Al)	ppm	<=1,00	
600/WO30	Kohlenstoff (C)	mg/l	<=100	

07/09/2009 03.11.26 PM

gez. Uttenweiler, FAX 07623/91-7346
Qualitätssicherung

Dieses Dokument wurde maschinell erstellt, daher keine Unterschrift.

Die vorstehenden Angaben geben die Ergebnisse unserer Qualitätsprüfungen wieder. Sie bedeuten keine rechtliche Zusicherung bestimmter Eigenschaften des Produkts oder seiner Eignung für einen konkreten Einsatzzweck. Wir gewährleisten die vertragsgemäße Beschaffenheit unseres Produkts im Rahmen unserer "Allgemeinen Verkaufs- und Lieferbedingungen". Alle Werte gelten bei Verlassen des Lieferwerks.

H₂O₂ Batch 2

Werkszeugnis

nach EN 10 204-2.2

Seite 1   SerialNr: 256564

⊚ EVONIK
INDUSTRIES

Evonik Degussa GmbH
Untere Kanalstr. 3
79618 Rheinfelden

AIT Austrian Institute of Technolog
GmbH

Postfach:
AT   2444   Seibersdorf

Material:	**PROPULSE (TM)**
	875 HTP
Material-Nr.:	22.1125.8700 .99
Spez.-Nr.:	1132/01
Gültig ab:	06.12.2009
Kunden-Nr.:	0000643537
Auftrags-Nr.:	31968401 /10
Lieferbeleg-Nr.:	44325356 / 10
Lieferdatum:	02.03.2010
Versandbedingung:	Lkw Stückgut
Menge:	20 KG
Kundenbestell-Nr.:	per e-mail Herr Dr.

Warenempfänger
AIT
Austrian Institute of Technnology
Warencingang-Zentralmagazin

AT   2444   Seibersdorf
Österreich

Kontroll/Lot-Nr.:   5275

Produktspezifikation

Merkmale und Prüfmethoden		Einheiten	Sollwerte (Grenzen)	Istwerte
600/WM11	**H2O2-Gehalt**	g/100 g	87,0-88,0	87,7
600/WM21	**Zersetzungsrate (96°C/16h)**	%	<=2,0	0,3
600/WM40	**Säuregehalt [meq/l]**	-	<=1,0	0,5
600/WN20	**Glührückstand**	mg/l	<=30	15
600/WO91	**Natriumnitrat (NaNO3)**	mg/l	12,0-20,0	15,5
600/WO06	**Zinn (Sn)**	mg/l	5,00-9,00	6,25
600/WO08	**Phosphat (als PO4)**	mg/l	<=0,50	0,10
600/WO07	**Sulfat (als SO4)**	mg/l	<=5,00	<0,10
600/WO09	**Chlorid (Cl)**	mg/l	<=2,00	0,10
600/WP78	**Aluminium (Al)**	mg/l	<=1,00	0,48
600/WO30	**Kohlenstoff (C)**	mg/l	<=100	68

03/01/2010 03.31.12 PM

gez. Uttenweiler, FAX 07623/91-7346
Qualitätssicherung

Dieses Dokument wurde maschinell erstellt, daher keine Unterschrift.

Die vorstehenden Angaben geben die Ergebnisse unserer Qualitätsprüfungen wieder. Sie bedeuten keine rechtliche Zusicherung bestimmter Eigenschaften des Produkts oder seiner Eignung für einen konkreten Einsatzzweck. Wir gewährleisten die vertragsgemäße Beschaffenheit unseres Produkts im Rahmen unserer "Allgemeinen Verkaufs- und Lieferbedingungen". Alle Werte gelten bei Verlassen des Lieferwerks.

H₂O₂ Batch 3

Werkszeugnis

nach EN 10 204-2.2

Seite 1   SerialNr. 269641

Evonik Degussa GmbH
Untere Kanalstr. 3
79618 Rheinfelden

AIT Austrian Institute of Technolog.
GmbH

Postfach:
AT   2444   Seibersdorf

Material:	**PROPULSE (TM)**
	875 HTP

Material-Nr.:	22.1125.8700.99
Spez.-Nr.:	1132/01
Gültig ab:	06.12.2009
Kunden-Nr.:	0000643537
Auftrags-Nr.:	32050631 /10
Lieferbeleg-Nr.:	44418764 / 10
Lieferdatum:	26.07.2010
Versandbedingung:	Lkw Stückgut
Menge:	KG
Kundenbestell-Nr.:	Herr Dr. Scharlemann

Warenempfänger
AIT
Austrian Institute of Technology
Wareneingang-Zentralmagazin

Kontroll/Lot-Nr.:	5275

AT   2444   Seibersdorf
Österreich

Produktspezifikation

Merkmale und Prüfmethoden		Einheiten	Sollwerte (Grenzen)	Istwerte
600/WM11	H2O2-Gehalt	g/100 g	87,0-88,0	87,7
600/WM21	Zersetzungsrate (96°C/16h)	%	<=2,0	0,3
600/WM40	Säuregehalt [meq/l]	-	<=1,0	0,5
600/W820	Glührückstand	mg/l	<=30	15
600/W091	Natriumnitrat (NaNO3)	mg/l	12,0-20,0	15,5
600/W00E	Zinn (Sn)	mg/l	5,00-9,00	6,25
600/W008	Phosphat (als PO4)	mg/l	<=0,50	0,10
600/W007	Sulfat (als SO4)	mg/l	<=5,00	<0,10
600/W009	Chlorid (Cl)	mg/l	<=2,00	0,10
600/WF76	Aluminium (Al)	mg/l	<=1,00	0,48
600/W030	Kohlenstoff (C)	mg/l	<=100	68

07/26/2010 09.46.37 AM

gez. Uttenweiler, FAX 07623/91-7346
Qualitätssicherung

Dieses Dokument wurde maschinell erstellt, daher keine Unterschrift.

Die vorstehenden Angaben geben die Ergebnisse unserer Qualitätsprüfungen wieder. Sie bedeuten keine rechtliche Zusicherung bestimmter
Eigenschaften des Produkts oder seiner Eignung für einen konkreten Einsatzzweck. Wir gewährleisten die vertragsgemäße Beschaffenheit unseres
Produkts im Rahmen unserer "Allgemeinen Verkaufs- und Lieferbedingungen". Alle Werte gelten bei Verlassen des Lieferwerks.

Specification Jet A-1

R E F I N E R Y   C E R T I F I C A T E   O F   Q U A L I T Y   JET A-1

Embodying the most stringent requirements of the following specifications (latest editions) as they are stated / qualified
in the "Aviation Fuel Quality Requirements for Jointly Operated Systems"   ISSUE 24 (October 2008)

OMV

TEST CERTIFICATE no   **3629**

BATCH no   **3064/63**   * Batch amount **4841**   m³   **Tank no   T-4728**   Sampling Date   **07.08.2009**

Methods	Properties		Units	Results	Limits
A P P E A R A N C E					
Visual				passed	Clear, bright and visually free from solid matter and undissolved water at ambient temperature
ASTM D 156	Colour			+30	
ASTM D 5452	Particulate Contamination		mg/l	0,1	1,0 max.
IP 565	Particle counts	Particle counts > = 4 µm(c)	counts/ml	54.7	Report
		Particle counts > = 6 µm(c)	counts/ml	11.1	Report
		Particle counts > = 14 µm(c)	counts/ml	2.0	Report
		Particle counts > = 21 µm(c)	counts/ml	0.4	Report
		Particle counts > = 25 µm(c)	counts/ml	0.3	Report
		Particle counts > = 30 µm(c)	counts/ml	0.1	Report
		ISO-Code		13/11/08/06/05/04	Report
C O M P O S I T I O N					
ASTM D 3242	Total Acidity		mg KOH/g	0,005	0,015 max.
ASTM D 6379	Total aromatics		% vol	15,0	26,5 max.
ASTM D 5453	Sulfur, Total		% mass	0,0190	0,30 max.
ASTM D 3227	Sulfur, Mercaptan		% mass	0,0001	0,0030 max.
	Hydroprocessed components		% vol	58,0	Report
	Severely hydroprocessed components		% vol	0,0	Report
V O L A T I L I T Y					
ASTM D 86	Distillation:	Initial Boiling Point	°C	151,8	Report
		10 % vol. rec.	°C	168,9	205,0 max.
		50 % vol. rec.	°C	191,3	Report
		90 % vol. rec.	°C	225,5	Report
		Final Boiling Point	°C	255,1	300,0 max.
		Residue	% vol	1,3	1,5 max.
		Loss	% vol	0,9	1,5 max.
ASTM D 3828	Flash Point		°C	43,0	38,0 min.
ASTM D 4052	Density at 15°C		kg/m³	795,0	775,0 min. 840,0 max.
F L U I D I T Y					
ASTM D 7153	Freezing Point		°C	-55.6	-47,0 max
ASTM D 445	Viscosity at -20°C		mm2/s	3,605	8,000 max.
C O M B U S T I O N					
ASTM D 3338	Specific energy, net		MJ/kg	43,33	42,80 min.
ASTM D 1322	Smoke Point		mm	25,1	19,0 min.
ASTM D 1840	Naphthalenes		% vol.	0,58	3,00 max.
C O R R O S I O N					
ASTM D 130	Corrosion, Copper (2h at 100°C)		Classification	1a	1 max.
T H E R M A L S T A B I L I T Y					
ASTM D 3241	JFTOT Control temp. 260°C: Filter pressure difference		mm Hg	0.2	25,0 max.
	Tube rating (visual)			<1	<3, no 'Peacock' or 'abnormal' colour deposits
C O N T A M I N A N T S					
ASTM D 381	Existent Gum		mg/100 ml	<1.0	7 max.
ASTM D 3948	Microseparometer ratings (with SDA)		MSEP	90	70 min.
A D D I T I V E S					
	Antioxidant hydroprocessed components total		mg/l	19,6	17,0 min. 24,0 max.
*	Antioxidant hydroprocessed components	RDE/A/607	mg/l	19,6	17,0 min. 24,0 max.
	Antioxidant hydroprocessed components	NIL	mg/l	0,0	17,0 min. 24,0 max.
	Antioxidant hydroprocessed components	NIL	mg/l	0,0	17,0 min. 24,0 max.
	Antioxidant unhydroprocessed components	NIL	mg/l	0,0	24,0 max.
*	Static Dissipator Additive	RDE/A/621	mg/l	0,6	3,0 max.
C O N D U C T I V I T Y					
ASTM D 2624	electrical conductivity		pS/m at °C	230/24	50 min. 600 max.

We certify that the product complies with the specifications detailed above.

Dr. M. Zahora
Head of Department Quality Control
LIMS_Zertifikat_Jet_A1.rpt Rev 13

* data from Tank farm

Refinery Schwechat / Quality Control
10.08.2009 Mannswörtherstrasse 28, A 2320 Schwechat
Date   Tel: 004314044042216

Specification Ethanol

AustrAlco Agrar-Alkohol Handelsges.m.b.H.   2104-Spillern, Bahnstrasse 16

Analysendatum:	24.03.2009
Charge:	AAAH- 5020- 07025 -240309
Datum:	24.03.2009
Tank:	07025

Kunde:	Lactan
Laborant:	Heil Johannes
Produkt:	Ethanol 99%
Version:	AAAH-LZ-P99-003

Ph. Eur.& USP   Spezifikation   Resultate

			Spezifikation			Resultate		
	Rel. Dichte	20°C	0,7900-0,7930			0,7908		
Gehaltsbestimmung mittels Alkoholimetrischer Tabelle:			>99,5	vol%		99,98	vol%	
	B) Absorption		340-270nm	260-250nm	240nm	340-270nm	260-250nm	240nm
			max 0,10	max 0,30	max 0,40	0,017	0,122	0,303
	C)Farbe Blau		Blau			entspricht		
	D)Gelber Niederschlag		gelber Niederschlag			entspricht		
Aussehen:	Klarheit und Opaliszenz		klar			entspricht		
	Farbe		farblos			entspricht		
Säure oder Basengehalt:	A) rosa Färbung		max. 30ppm Säure			entspricht		
GC:	Methanol		<200ppm(V/V)	ppm		1,0	ppm	
	Acetaldehyd		<10ppm(V/V)	ppm		< 3,0	ppm	
	Benzol		<2ppm(V/V)	ppm		n.n.	ppm	
	Rest. Verunreinigungen		Summe Rest Ver. <300ppm	ppm		< 2,0	ppm	
Verdampfungsrückstand:			<25	mg/l		<10,0	mg/l	

Seite 1/2

246

X.4. NASA Chemical Equilibrium and Applications (CEA) code

A sample analysis performed using NASA Chemical Equilibrium and Applications (CEA) code [92] is presented in this section. The analysis shown here corresponds to the input parameters of the long duration DM firing test presented in Figure 166 and Figure 167. Input parameters of oxidizer to fuel mass flow ratio, injection temperatures and combustion chamber pressure where determined by averaging as outlined in section 4.5.3. The output shown summarizes the input parameters, then lists all species considered in the analysis and gives the calculated combustion performance parameters at the bottom. All calculated parameters such as combustion gas temperature, characteristic velocity, chamber pressure as well as the thruster performance related parameters such as specific impulse are given at different flow stations, corresponding to the combustion chamber (vanishing velocity corresponds to infinite volume of the combustion chamber), at throat and at the specified nozzle exit area, matching the nozzle expansion ratio of the DM thruster. The final composition of the product gas mixture is given at the end of the analysis output file.

```
*******************************************************************************

         NASA-GLENN CHEMICAL EQUILIBRIUM PROGRAM CEA2, MAY 21, 2004
                  BY  BONNIE MCBRIDE AND SANFORD GORDON
      REFS: NASA RP-1311, PART I, 1994 AND NASA RP-1311, PART II, 1996

 *******************************************************************************



problem     o/f=4.9463657,
    rocket  frozen  nfz=2  tcest,k=3800
  p,bar=8.5112111,
  sup,ae/at=96.4,
react
  oxid=H2O moles=0.71668  t,k=704.85
  oxid=O2 moles=0.28332  t,k=704.85
  fuel=Jet-A(L) moles=1  t,k=293.15
output  massf
    plot p t rho h u g s m mw cp gam son cf
end

OPTIONS: TP=F  HP=F  SP=F  TV=F  UV=F  SV=F  DETN=F  SHOCK=F  REFL=F  INCD=F
RKT=T  FROZ=T  EQL=F  IONS=F  SIUNIT=T  DEBUGF=F  SHKDBG=F  DETDBG=F  TRNSPT=F

TRACE= 0.00E+00  S/R= 0.000000E+00  H/R= 0.000000E+00  U/R= 0.000000E+00

Pc,BAR =      8.511211

Pc/P =

SUBSONIC AREA RATIOS =

SUPERSONIC AREA RATIOS =     96.4000

NFZ=  2  Mdot/Ac= 0.000000E+00  Ac/At= 0.000000E+00

    REACTANT              MOLES     (ENERGY/R),K   TEMP,K  DENSITY
         EXPLODED FORMULA
O: H2O              0.716680  -0.273560E+05   704.85  0.0000
         H  2.00000  O  1.00000
O: O2               0.283320   0.152267E+04   704.85  0.0000
         O  2.00000
F: Jet-A(L)         1.000000  -0.367002E+05   293.15  0.0000
         C 12.00000  H 23.00000

 SPECIES BEING CONSIDERED IN THIS SYSTEM
```

```
 (CONDENSED PHASE MAY HAVE NAME LISTED SEVERAL TIMES)
  LAST thermo.inp UPDATE:    9/09/04

  g 7/97  *C              tpis79 *CH             g 4/02 CH2
  g 4/02  CH3             g11/00 CH2OH           g 7/00 CH3O
  g 8/99  CH4             g 7/00 CH3OH           srd 01 CH3OOH
  tpis79  *CO             g 9/99 *CO2            tpis91 COOH
  tpis91  *C2             g 6/01 C2H             g 1/91 C2H2,acetylene
  g 5/01  C2H2,vinylidene g 4/02 CH2CO,ketene    g 3/02 O(CH)2O
  srd 01  HO(CO)2OH       g 7/01 C2H3,vinyl      g 6/96 CH3CO,acetyl
  g 1/00  C2H4            g 8/88 C2H4O,ethylen-o g 8/88 CH3CHO,ethanal
  g 6/00  CH3COOH         srd 01 OHCH2COOH       g 7/00 C2H5
  g 7/00  C2H6            g 8/88 C2H5OH          g 7/00 CH3OCH3
  srd 01  CH3O2CH3        g 8/00 C2O             tpis79 *C3
  n 4/98  C3H3,1-propynl  n 4/98 C3H3,2-propynl  g 2/00 C3H4,allene
  g 1/00  C3H4,propyne    g 5/90 C3H4,cyclo-     g 3/01 C3H5,allyl
  g 2/00  C3H6,propylene  g 1/00 C3H6,cyclo-     g 6/01 C3H6O,propylox
  g 6/97  C3H6O,acetone   g 1/02 C3H6O,propanal  g 7/01 C3H7,n-propyl
  g 9/85  C3H7,i-propyl   g 2/00 C3H8            g 2/00 C3H8O,1propanol
  g 2/00  C3H8O,2propanol g 7/88 C3O2            g tpis *C4
  g 7/01  C4H2,butadiyne  g 8/00 C4H4,1,3-cyclo- n10/92 C4H6,butadiene
  n10/93  C4H6,1butyne    n10/93 C4H6,2butyne    g 8/00 C4H6,cyclo-
  n 4/88  C4H8,1-butene   n 4/88 C4H8,cis2-buten n 4/88 C4H8,tr2-butene
  n 4/88  C4H8,isobutene  g 8/00 C4H8,cyclo-     g10/00 (CH3COOH)2
  n10/84  C4H9,n-butyl    n10/84 C4H9,i-butyl    g 1/93 C4H9,s-butyl
  g 1/93  C4H9,t-butyl    g12/00 C4H10,n-butane  g 8/00 C4H10,isobutane
  g 8/00  *C5             g 5/90 C5H6,1,3cyclo-  g 1/93 C5H8,cyclo-
  n 4/87  C5H10,1-pentene g 2/01 C5H10,cyclo-    n10/84 C5H11,pentyl
  g 1/93  C5H11,t-pentyl  n10/85 C5H12,n-pentane n10/85 C5H12,i-pentane
  n10/85  CH3C(CH3)2CH3   g 2/93 C6H2            g11/00 C6H5,phenyl
  g 8/00  C6H5O,phenoxy   g 8/00 C6H6            g 8/00 C6H5OH,phenol
  g 1/93  C6H10,cyclo-    n 4/87 C6H12,1-hexene  g 6/90 C6H12,cyclo-
  n10/83  C6H13,n-hexyl   g 6/01 C6H14,n-hexane  g 7/01 C7H7,benzyl
  g 1/93  C7H8            g12/00 C7H8O,cresol-mx n 4/87 C7H14,1-heptene
  n10/83  C7H15,n-heptyl  n10/85 C7H16,n-heptane n10/85 C7H16,2-methylh
  n 4/89  C8H8,styrene    n10/86 C8H10,ethylbenz n 4/87 C8H16,1-octene
  n10/83  C8H17,n-octyl   n 4/85 C8H18,n-octane  n 4/85 C8H18,isooctane
  n10/83  C9H19,n-nonyl   g 3/01 C10H8,naphthale n10/83 C10H21,n-decyl
  g 8/00  C12H9,o-bipheny g 8/00 C12H10,biphenyl g 6/97 *H
  g 1/01  HCO             g 6/01 HCCO            g 4/02 HO2
  tpis78  *H2             g 5/01 HCHO,formaldehy g 6/01 HCOOH
  g 8/89  H2O             g 6/99 H2O2            g 6/01 (HCOOH)2
  g 5/97  *O              g 4/02 *OH             tpis89 *O2
  g 8/01  O3              n 4/83 C(gr)           n 4/83 C(gr)
  n 4/83  C(gr)           g11/99 H2O(cr)         g 8/01 H2O(L)
  g 8/01  H2O(L)

 O/F =    4.946366


                       EFFECTIVE FUEL    EFFECTIVE OXIDANT      MIXTURE
 ENTHALPY                  h(2)/R              h(1)/R            h0/R
 (KG-MOL)(K)/KG       -0.21935307E+03     -0.87245919E+03   -0.76262637E+03

 KG-FORM.WT./KG           bi(2)              bi(1)             b0i
  *H                 0.13746853E+00     0.65220643E-01    0.77370566E-01
  *O                 0.00000000E+00     0.58393534E-01    0.48573496E-01
  *C                 0.71722711E-01     0.00000000E+00    0.12061605E-01

 POINT ITN      T            H          O          C
   1    21   2195.569     -9.775    -19.931    -14.029
 Pinf/Pt = 1.768982
   2     3   1997.798     -9.889    -21.170    -13.676
 Pinf/Pt = 1.773528
   2     2   1996.937     -9.890    -21.176    -13.674




          THEORETICAL ROCKET PERFORMANCE ASSUMING FROZEN COMPOSITION
                           AFTER POINT 2


 Pin =   123.4 PSIA
 CASE =

             REACTANT                         MOLES        ENERGY      TEMP
                                                           KJ/KG-MOL     K
```

```
OXIDANT      H2O                                0.7166800   -227451.958    704.850
OXIDANT      O2                                 0.2833200     12660.242    704.850
FUEL         Jet-A(L)                           1.0000000   -305144.062    293.150


O/F=    4.94637  %FUEL= 16.816995  R,EQ.RATIO= 1.293061  PHI,EQ.RATIO= 1.663721


                CHAMBER   THROAT     EXIT
Pinf/P           1.0000   1.7735  1989.01
P, BAR           8.5112   4.7990  0.00428
T, K            2195.57  1996.94   467.56
RHO, KG/CU M    9.1820-1 5.6945-1 2.1686-3
H, KJ/KG        -6340.86 -6847.59 -10100.7
U, KJ/KG        -7267.81 -7690.34 -10298.0
G, KJ/KG        -34568.5 -32521.5 -16112.0
S, KJ/(KG)(K)   12.8566  12.8566  12.8566

M, (1/n)         19.694   19.702   19.702
Cp, KJ/(KG)(K)   2.6167   2.5192   1.7419
GAMMAs           1.1958   1.2026   1.3198
SON VEL,M/SEC    1052.8   1006.7    510.3
MACH NUMBER       0.000    1.000    5.374


PERFORMANCE PARAMETERS

Ae/At                     1.0000   96.400
CSTAR, M/SEC              1484.7   1484.7
CF                        0.6781   1.8470
Ivac, M/SEC              1843.8   2814.2
Isp, M/SEC              1006.7   2742.2


MASS FRACTIONS

*CO         0.18074   *CO2        0.24685   *H         0.00001
*H2         0.01568   H2O         0.55661   *OH        0.00011

 * THERMODYNAMIC PROPERTIES FITTED TO 20000.K


   PRODUCTS WHICH WERE CONSIDERED BUT WHOSE MASS FRACTIONS
   WERE LESS THAN 5.000000E-06 FOR ALL ASSIGNED CONDITIONS
```

Curriculum Vitae

Title/Name:	Dipl. Ing. Mag. David Krejci
Date of birth:	Nov. 3, 1982, Wels / Upper Austria

Education

1993 – 2001	High School „Gymnasium der Abtei Schlierbach", Upper Austria
2003 – 2008	Studies of Technical Physics at Vienna University of Technology
2004 – 2012	Studies of Political Science at University Vienna
since Oct. 1, 2008	PhD. Studies Mechanical Engineering at Institute for Energy Systems and Thermodynamics, Vienna University of Technology

Additionally:

Aug.– Dez., 2007	„Aerospace Engineering" at Illinois Institute of Technology, Chicago

Grants and Scholarships

2006	Undergraduate research grant of University of Natural Resources and Applied Life Sciences Vienna
2007	American-European Engineering Exchange (Global AE3 Joint Study) Grant
2008	Performance Scholarship of Faculty of Physics, TU Vienna
2010	Grants from FFG and ESA for attendance of Summer School Alpbach 2010 „New Space Missions for Understanding Climate Change" and Post-Alpbach Seminar
2011	ESA Conference Grant, 1st IAA Conference on University Satellite Missions, Rome, Jan. 2011.

Relevant Work Experience

2002 - 2003	Civilian service in Jacobina / Brazil and Vrbovéc / Croatia
2006 - 2007	Research assistant and physics tutor at Department of Materials Sciences and Process Engineering, University of Natural Resources and Applied Life Sciences Vienna
Jan. – Jul., 2008	Diploma student at Austrian Research Centers (ARC) Seibersdorf, Space Propulsion and Advanced Concepts
Since Aug., 2008	PhD. candidate at Austrian Institute of Technology (AIT) Seibersdorf, Space Propulsion and Advanced Concepts, Since Jan, 1, 2011: Fotec GmbH, Aerospace Engineering

Selected Publications and Conference Proceedings

2012

Krejci, D., Woschnak, A., Scharlemann, C., Ponweiser, K.: Performance assessment of a 1N bipropellant thruster using green propellants H_2O_2/Kerosene, Journal of Propulsion and Power, working paper.

Krejci, D., Woschnak, A., Scharlemann, C., Ponweiser, K.: Structural Impact of Honeycomb Catalysts on Hydrogen Peroxide Decomposition for Micro Propulsion, Chemical Engineering Research and Design, In Press, DOI: 10.1016/j.cherd.2012.05.015.

Woschnak, A., Krejci, D., Schiebl, M., Scharlemann, C.: Development Model of a Green 1N Bi-Propellant Thruster for Attitude Control, Space Propulsion Conference, Bordeaux, 7-10. May 2012.

Hoffmann, A., Clifford, D., Aulinas, J., Carton, J.G., Deconinck, F., Esen, B., Hüsing, J., Kern, K., Kox, S., Krejci, D., Krings, T., Lohrey, S., Romano, P., Topham, R., Weitnauer, C.: A Novel Satellite Mission Concept for Upper Air Water Vapour, Aerosol and Cloud Observation Using Integrated Path Differential Absorption LiDAR Limb Sounding, Remote Sensing, Vol. 4, Iss. 4, 2012, pp. 867-910.

Selva, D., Krejci, D.: A survey and assessment of the capabilities of Cubesats for Earth observation, Acta Astronautica, Vol. 74, 2012, pp. 50-68.

2011

Scharlemann, C., Tajmar, M., Vasiljevich, I., Buldrini, N., Krejci, D., Seifert, B.: Investigation of Nanosatellite Propulsion Systems, 62nd International Astronautical Congress, Cape Town, South Africa, IAC-11-C4.4.3, 3-7 Oct. 2011.

Scharlemann, C., Tajmar, M., Vasiljevich, I., Buldrini, N., Krejci, D., Seifert, B.: Propulsion for Nanosatellites, 32nd International Electric Propulsion Conference, Wiesbaden, GER, 11-15 Sep. 2011.

Krejci, D., Woschnak, A., Scharlemann, C., Ponweiser, K.: Hydrogen Peroxide Decomposition for Micro Propulsion: Simulation and Experimental Verification, 47th AIAA/ASME/SAE/ASEE Joint Propulsion Conference & Exhibit, San Diego, CA, 3. Jul - 3 Aug. 2011.

Woschnak, A., Krejci, D., Schiebl, M., Scharlemann, C.: Development of a Green Bi-Propellant Hydrogen Peroxide Thruster for Attitude Control on Satellites, 4th European conference for Aerospace Sciences EUCASS, St. Petersburg, RUS, 4-8 July 2011.

Krejci, D., Seifert, B., Scharlemann, C.: Thrust Measurement of a Micro Pulsed Plasma Thruster for Cubesats, 1st IAA Conference on University Satellite Missions and CubeSat Workshop, Rome, IT, 24-29 Jan. 2011.

Pottinger, S., Krejci, D., Scharlemann, C.: Pulsed plasma thrusters performance for miniaturised electrode configurations and low energy operation, Acta Astronautica, Vol. 68, 2011, pp. 1996-2004.

2010 and earlier

Krejci, D., Seifert, B.: Miniaturized Pulsed Plasma Thrusters for Cubesats: Modelling and Direct Thrust Measurement, 61st International Astronautical Congress, Prague, CZ, 27 Sep. -1 Oct. 2010.

Schiebl, M., Krejci, D., Woschnak, A., Winter, F., Lang, M., Scharlemann, C.: Modeling and Experimental Verification of Auto-Ignition Processes for a Green Bi-Propellant Thruster, 61st International Astronautical Congress, Prague, CZ, 27 Sep. -1 Oct. 2010.

Woschnak, A., Krejci, D., Scharlemann, C.: Investigation of Catalytic Decomposition of Hydrogen Peroxide for Miniaturized chemical Thrusters, Space Propulsion Conference, San Sebastian, ES, 3-6 May 2010.

Krejci, D., Scharlemann, C.: Analytic model for the Assessment of the Electrode Configuration of a μPPT, 45th AIAA/ASME/SAE/ASEE Joint Propulsion Conference & Exhibit, Denver, CO, 21-23 July 2009.

Pottinger, S., Krejci, D., Scharlemann, C.: Development of a μPPT for CubeSat Applications, 44th AIAA/ASME/SAE/ASEE Joint Propulsion Conference & Exhibit, Hartford, CT, 21-23 July 2008.

Book chapter:

Woschnak, A., Krejci, D., Schiebl, M., Scharlemann, C.: Development of a Green Bi-Propellant Hydrogen Peroxide, in: Deluca, L., Bonnal, C., Haidn, O.J., Frolov, S.M. (Eds.): Progress in propulsion physics - Volume 4, Advances in AeroSpace Sciences, Edp Sciences, 2012.